HOLOGRAPHIC OPTICAL ELEMENTS FOR SPECTRUM-SPLITTING PHOTOVOLTAIC SYSTEMS

by

Benjamin D. Chrysler

A Dissertation Submitted to the Faculty of the

JAMES C. WYANT COLLEGE OF OPTICAL SCIENCES

In Partial Fulfillment of the Requirements

For the Degree of

DOCTOR OF PHILOSOPHY

In the Graduate College

THE UNIVERSITY OF ARIZONA

2021

THE UNIVERSITY OF ARIZONA
GRADUATE COLLEGE

As members of the Dissertation Committee, we certify that we have read the dissertation prepared by: Benjamin D Chrysler, titled: Holographic Optical Elements for Spectrum-Splitting Photovoltaic Systems,

and recommend that it be accepted as fulfilling the dissertation requirement for the Degree of Doctor of Philosophy.

Raymond K. Kostuk — Date: 8/6/2021
Raymond K. Kostuk

Robert A. Norwood — Date: 8/6/21
Robert Norwood

Pierre-A. Blanche — Date: 08/06/2021
Pierre Blanche

Yuzuru Takashima — Date: 8/6/21
Yuzuru Takashima

Final approval and acceptance of this dissertation is contingent upon the candidate's submission of the final copies of the dissertation to the Graduate College.

I hereby certify that I have read this dissertation prepared under my direction and recommend that it be accepted as fulfilling the dissertation requirement.

Raymond Kostuk — Date: 8/6/2021
Raymond K. Kostuk
Dissertation Committee Chair
James C. Wyant College of Optical Sciences

Signature: Robert A. Norwood
Email: rnorwood@optics.arizona.edu

Signature:
Email: pablanche@optics.arizona.edu

Signature: Raymond Kostuk
Email: kostuk@arizona.edu

Signature: Yuzuru Takashima
Email: ytakashima@optics.arizona.edu

Acknowledgments

Many have played a direct or indirect role in helping me write this dissertation and I would like to acknowledge their support and contributions here. First, I would like to thank my advisor, Ray Kostuk, for years of hard work, teaching, and dedication as an advisor. I have good memories in the lab and will look back fondly on these years. I would also like to thank each of my committee members, Pierre Blanche, Robert Norwood, and Yuzuru Takashima for their valuable input on this dissertation.

I couldn't achieve this without my parents, Jim and Leslie Chrysler, for teaching me the dedication, persistence, and independence needed for academic growth and teaching me how to face new challenges even when they seem overwhelming. My grandparents, Leslie and Joan Peterson and Alden and Susanne Chrysler, have been another source of constant encouragement and support. And I couldn't go without thanking my older brothers, Andy and Josh Chrysler, for always being an inspiration to me.

There are many things to thank my wife, Siwei "Alice" Wu, for, but just to name one: she has taught me how to approach my life with a type of confidence that is not based on perfection or comparison, but a clearer understanding of myself and others. This approach has helped clear my mind and improve my work as a researcher. This also extends to my new parents, Jiahong Shi and Xiantong Wu, for their support, understanding, and encouragement.

Thanks to all my fellow students in Optical Sciences and Electrical Engineering for helpful conversations and collaboration of all sorts, especially those I've worked with in the Photonics Systems Laboratory: Shelby Vorndran, Silvana Ayala-Pelaez, Yuechen Wu, Jianbo Zhao, Sam Tan, Jilian Nguyen, and Eli Salay.

I would also like to thank those who have supported my research in various ways: Zachary Holman, Christiana Honsberg, Zhengshan Yu, and Sean Shaheen. And thanks to many others have invested in me and helped me grow throughout the course of graduate school: Nathan Hagen, Yukitoshi Otani, Roger Angel, Bob Breault, and Russell Chipman.

Lastly, I would like to thank the National Science Foundation and those who have contributed to the Optical Science FoTO Scholarship fund for financial support of my graduate education.

Table of Contents

List of Figures

List of Tables

Abstract

Spectrum-splitting is a technique for increasing the conversion efficiency of a photovoltaic system. In a spectrum-splitting system, an optical element such as a dichroic filter or a diffraction grating is used to divide the solar spectrum between a set of laterally separated photovoltaic cells with different energy bandgaps. In the past, one of the main challenges for spectrum splitting systems was a lack of inexpensive photovoltaic cells at a variety of energy bandgaps. However, the recent development of perovskite solar cells opens up new opportunities for spectrum splitting systems. Perovskite solar cells are efficient and inexpensive and have been developed at a variety of bandgap energies ranging from 1.25eV to 2.3eV.

In literature, perovskite solar cells are arranged in a vertical stack and achieve spectral separation through absorptive filtering. However, this approach is limited since each perovskite cell parasitically absorbs 10% to 20% of the incident light before transmitting to the underlying cells. One of the main questions considered in this dissertation is what the optimal cell arrangement is for spectrum splitting systems with two, three, and four energy bandgaps. This question is approached by designing and comparing a variety of spectrum splitting systems. First, a particular approach for lateral spectral separation using volume holographic lens arrays is selected and developed in depth for a two-bandgap system. Next, the approach is extended for a three-bandgap system by designing and simulating a cascaded volume holographic lens array. Lastly, a hybrid cell arrangement is proposed which combines both vertically stacked and laterally separated cell arrangements. Three- and four- bandgap systems are designed in the hybrid cell arrangement and are shown to have greater conversion efficiency than either cell arrangement individually.

A variety of issues related to the design and fabrication of volume holographic lens arrays are also addressed. First, the environmental stability of Covestro Bayfol HX is shown to be insufficient for solar applications due to yellowing of the film after only several weeks of exposure. However, the other holographic material candidate, dichromated gelatin (DCG), is difficult to work with and is well known for yielding different results when processed in different atmospheric conditions. A reproducibility study is conducted and it is found that the variation in the measured spectral diffraction efficiency is reduced by a factor of six when the humidity is regulated at 65% during the drying stage of the film preparation process. Lastly, a replication system for volume

holographic lens arrays is proposed that is suitable for mass manufacturing. In the replication method, the object beam, reference beam, and aperture of the copy hologram are all recorded in a composite master hologram and replayed by illuminating with a single laser beam aligned at normal incidence. This replication system is used to fabricate a 9.6cm by 6.0cm volume holographic lens array with 36 elements that each have greater than 95% diffraction efficiency.

Chapter 1

Introduction

Lateral spectrum-splitting is technique for increasing the conversion efficiency of a photovoltaic system by dividing the solar spectrum between a set of laterally separated photovoltaic cells with different energy bandgaps. One approach for lateral spectral separation that balances a variety of design considerations is the use of a volume holographic lens array. In this dissertation, this approach is used to meet new opportunities and challenges stemming from recent developments in photovoltaic cell technologies, such as perovskite and bifacial silicon cells. In addition to design and analysis, a variety of issues related to the fabrication and implementation of volume holographic lens arrays are also addressed. In this chapter, some of the recent developments in the photovoltaic industry are discussed that motivate the research topics in this dissertation.

1.1 Photovoltaic Industry

One of the main goals in photovoltaics (PV) research is to develop technologies that increase the converted electrical energy yield and reduce the overall system cost [1]. The energy yield is a measure of the total electrical energy produced by a PV system over the course of the year. The energy yield depends on the power conversion efficiency (PCE) as well as the ability to convert diffuse sunlight scattered from the atmosphere and light reflected from the ground surface. The

overall cost of a utility scale PV system includes the cost of individual components and cells as well as fixed costs such as land, installation, maintenance, and loans.

For many decades the PV market grew rapidly due to a steady reduction in the cost of silicon PV cells and a gradual increase in conversion efficiency. However, in recent years the cost of a silicon PV module has become relatively small compared to the fixed costs and the decreasing cost of silicon alone is not sufficient to continue the rapid growth of the industry [2], [3]. For these reasons, the PV industry has a new focus: namely to improve the overall system energy yield [1].

One way to improve the energy yield is by increasing the conversion efficiency of individual silicon cells. However, this approach may only provide a short-term solution as the conversion efficiency is already approaching the detailed balance limits first described by Shockley and Quiesser [4]. The theoretical conversion efficiency limit for a single-junction solar cell is 33% but reduces to 29.4% [5] for the material properties specific to silicon. A practical efficiency limit for silicon is believed to be closer to 27.1% [6]. Given that a silicon cell has already been demonstrated with an efficiency of 26.7% [6] there is limited room for increasing the conversion efficiency of silicon cells.

Fortunately, another avenue exists for increasing the conversion efficiency of a PV system beyond the Shockley-Quisser limit. The detailed balance limit increases for systems that utilize multiple photovoltaic semiconductor junctions with different energy bandgaps [7], [8]. Each photovoltaic junction is also referred to as a “subcell”. In a multijunction system, each subcell has a different spectral response and converts light in its optimal solar spectral band. The number of subcells determines the theoretically attainable conversion efficiency of the system. While a single-junction system has a conversion efficiency limit of 33%, a multijunction system with two

subcells has a limit of 42%. The limit further increases to 49% with three subcells. Calculations have shown that with twenty subcells the limit increases to 65% [7]. Despite the higher power conversion efficiency of multijunction systems, designing a system with an energy yield to cost ratio that is high enough to outperform conventional silicon modules in the marketplace remains a challenge.

1.2 Multijunction Photovoltaic Systems

Interest in developing a multijunction PV system has been an ongoing area of research for more than 30 years [9] and a variety of system designs and cell arrangements have been proposed. Initially, most effort was focused on developing tandem multijunction PV cells [10]. A tandem multijunction PV cell incorporates each subcell on a single, monolithic substrate by depositing III-V semiconductor materials layer by layer with epitaxial growth. This approach has yielded multijunction cells with up to six subcells and efficiencies as high as 47.1% under solar concentration [11]. However, the cost of a III-V multijunction cell is very high and is typically designed for use with solar concentration systems (Fig. 1.1a) that focus sunlight by factors of several hundred to reduce the material usage costs [11], [12]. The use of high concentrating power leads to other problems such as the inability to convert diffuse sunlight that is scattered from the atmosphere and incompatibility with single-axis sun tracking systems that are commonly installed in other utility scale PV power plants. These factors led to many multijunction cell manufacturers closing their plants or canceling projects for expanding their facilities [13].

The challenges faced by the multijunction cell industry also led to increased interest in an alternative method for implementing multiple subcells called “lateral spectrum splitting” [14]. In a lateral spectrum-splitting photovoltaic (SSPV) system, each subcell is laterally arranged and an

optical element such as a volume hologram [15], surface relief grating [16], or dichroic filter [17] divides the solar spectrum between laterally separated subcells (Fig. 1.1b). Spectrum-splitting avoids many complications arising in the design of multijunction cells. Furthermore, SSPV systems are designed at much lower concentration ratios ranging between 1X and 10X and as a result convert diffuse sunlight and in many designs are compatible with single-axis sun tracking. One of the main limitations in the development of SSPV systems is a lack of inexpensive single-junction solar cells that have different energy bandgaps.

Recent developments in the PV industry have potential for filling the need for inexpensive and efficient PV cells. A new class of PV cell called perovskite solar cells (PSCs) [18] has potential for use in spectrum splitting systems [19]. There are three main characteristics of PSCs that make them suitable candidates for use in SSPV systems. First, PSCs have been demonstrated with conversion efficiencies (25.2%) [20], [21] quickly approaching the conversion efficiency of silicon cells (26.7%) [6], [21]. Second, PSCs use low energy manufacturing processes and have potential for costs even lower than silicon cells [22]. Third, PSCs have been experimentally demonstrated with a wide range of energy bandgaps spanning 1.25eV to 2.3eV [23]–[27]. One of the remaining challenges for the commercialization of perovskite solar cells is the lifetime stability [28], [29]. However, continual progress has been made in this area with many devices having lifetimes of several months [30] and some having lifetimes greater than one year [31], [32], In addition to PSCs, the efficiency and stability of other inexpensive thin-film solar cells such as CIGS, CZTS, CdTe, and MgCdTe [21], [33]–[35] have progressed in recent years and also have potential for use in spectrum-splitting systems.

Although the development of perovskite cells creates a new opportunity for lateral spectrum splitting, system designs should be evaluated in comparison with a “vertically stacked” cell

arrangement which is also suitable for use with PSCs [36]. In this arrangement, single-junction perovskite cells are vertically stacked and mechanically connected (Fig. 1.1c). Each PSC is "semi-transparent" and transmits light below the bandgap energy to the underlying cells. Until this point, researchers have mostly assumed the use of a vertically stacked cell arrangement and have not designed lateral spectrum splitting systems for use with perovskite solar cells.

One of the main reasons that researchers have designed perovskite systems in a vertically stacked cell arrangement is due to the greater simplicity of the design compared to lateral spectrum splitting. However, one of the main limitations in the conversion efficiency of a perovskite cell stack is parasitic absorption [23], [36]–[40]. Transparent conductive oxides (TCO) have high levels of parasitic absorption and are typically used as electrical contacts in semi-transparent perovskite cells. For this reason, a semi-transparent perovskite cell typically absorbs 10% to 20% of the light below the bandgap energy. The total parasitic absorption is even greater as the number of subcells increases since light is transmitted through a large number of semi-transparent cells with each absorbing some of the incident light.

As the photovoltaic industry progresses, it is expected that the number of subcells in a stack will increase over time [1]. However, one of the main issues that needs to be solved, especially for greater numbers of subcells, is that of parasitic absorption [40]. Lateral spectrum splitting has potential for alleviating the problem of parasitic absorption in multijunction perovskite systems since the cells do not need to be semi-transparent. In this dissertation, it is found that when the parasitic absorption of semi-transparent perovskite cells is greater than 18% lateral spectrum splitting systems have higher power conversion efficiency. A potentially more significant result is also explored in this dissertation. When the lateral and vertical cell arrangements are combined in a "hybrid" cell arrangement, the overall conversion efficiency is higher than either configuration

individually even when the parasitic absorption is as low as 6%. The relative advantages of the hybrid spectrum splitting designs increase as the number of subcells increases since the optical element separates the spectrum into fewer spectral bands compared with a lateral cell arrangement and light transmits through fewer subcells compared with a vertical cell arrangement. In addition to the energy yield advantage, a preliminary cost estimate in Appendix A shows the potential for many of the systems described in this dissertation to reduce the levelized cost of energy (LCOE) by up to 15%.

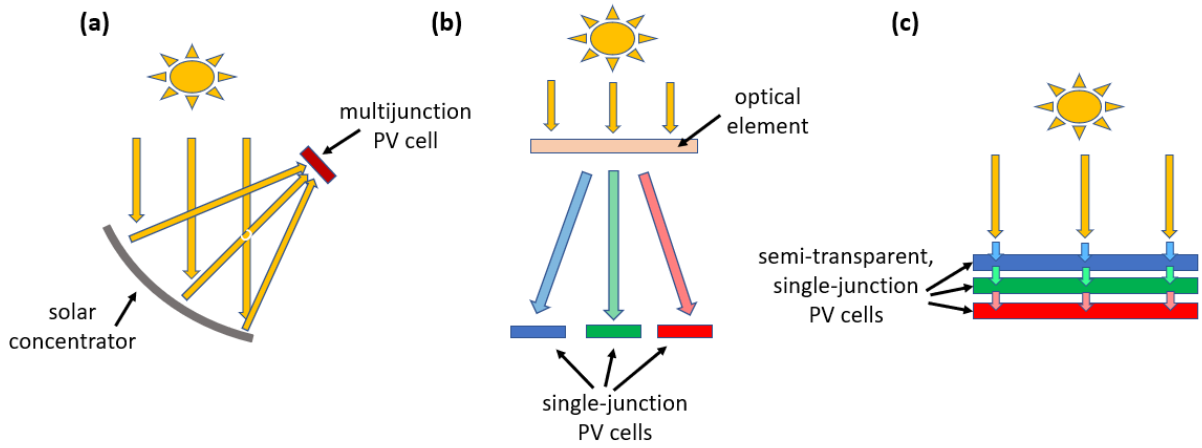

Figure 1.1: Three different configurations for multijunction photovoltaic (PV) systems. (a) a solar concentrator focuses light onto a small multijunction cell. In a multijunction cell, each PV cell junction is grown on a single monolithic substrate. (b) In a lateral spectrum-splitting configuration an optical element divides the solar spectral among laterally separated single-junction PV cells. (c) In a vertically stacked cell configuration, semi-transparent, single-junction PV cells convert sunlight and act as absorptive optical filters for underlying cells.

1.3 Outline

In Chapter 2, a detailed design procedure, optimization, and analysis for a two-junction lateral spectrum splitting system that uses volume holographic lenses is presented. Many of the techniques presented in this chapter serve as a foundation for subsequent chapters. In Chapter 3, the design and analysis is extended for lateral spectrum splitting in three spectral bands. Spectrum-

splitting in three spectral bands is accomplished by stacking volume holographic lens arrays in a "cascaded" configuration. A diffraction model for cascaded gratings is presented that calculates the cross-coupled interactions between all diffracted modes. The model is then used in an analysis of the spectrum splitting system. In Chapter 4, the designs from Chapters 2 and 3 are extended for use in a "hybrid" cell arrangement that combines vertically stacked and lateral cell arrangements. Hybrid system designs with three and four bandgap junctions are designed and compared with vertical and lateral spectrum splitting designs. It is found that the hybrid cell arrangement has the highest conversion efficiency of all three configurations.

One of the primary metrics used to compare the designs in Chapters 2 through 4 is the power conversion efficiency. However, this is a standardized metric and the actual energy yield varies depending on the illumination conditions. In Chapter 5, a simple method for calculating the energy yield for different illumination conditions is presented. A method for enhancing the energy yield using bifacial silicon solar cells is also presented.

In Chapter 6, the focus shifts from the system design and analysis to the holographic materials used to perform the spectral separation. Two candidate holographic materials are identified and evaluated. It is found that under prolonged solar exposure that Covestro Bayfol HX degrades and is not suitable for solar energy systems. Another material candidate, dichromated gelatin, has many excellent optical properties. However, it is known for being difficult work with and obtain reproducible results. The causes of the observed variability in dichromated gelatin holograms are investigated and a method for improving the repeatability is developed.

In Chapter 7, different techniques for fabricating holographic optical elements are discussed. A demonstration spectrum splitting system is developed using a stitching method with sequential exposures. This method requires different optical setups to be set up and aligned after each

exposure and is very time consuming, inaccurate, and unrepeatable. To help overcome these difficulties, a new replication technique is developed which is more suitable for the fabrication of volume holographic lens arrays. In this technique, the object beam, reference beam, and aperture of the copied hologram are all recorded in a composite master hologram. The composite master hologram is replayed with a single reference beam aligned at normal incidence.

1.4 Dissertation Contributions

Several contributions in the fields of photovoltaics and holography are made in this dissertation and some of the highlights are listed below:

1. Detailed design, optimization, and analysis of spectrum-splitting systems that use volume holographic lens arrays are presented.
2. A spectrum splitting system that divides the solar spectrum between three perovskite solar cells is designed.
3. A diffraction model for cascaded volume holographic lens arrays based on rigorous coupled wave analysis is developed.
4. Three and four junction photovoltaic systems with “hybrid” cell arrangements are proposed and shown to have potential for higher conversion efficiency than vertically stacked or lateral cell arrangements.
5. A bifacial spectrum splitting system is proposed that enhances the energy yield by converting light reflected from the ground surface.

6. A film preparation process for dichromated gelatin is developed that enhances the reproducibility and a statistical analysis is presented which shows the underlying variation of the holographic element parameters.

7. A replication technique and system is proposed which simplifies the fabrication of volume hologram arrays.

1.5 Publications

Much of the work in this dissertation is included in the following peer-reviewed and conference publications completed during my PhD program:

1. Chrysler, Benjamin D., and Raymond K. Kostuk. “A comparison of spectrum-splitting configurations for high-efficiency photovoltaic systems with perovskite cells” (manuscript in preparation)

2. Chrysler, Benjamin D., Sean Shaheen, Raymond K. Kostuk, “Lateral Spectrum Splitting System with Perovskite Photovoltaic Cells” (manuscript in preparation)

3. Chrysler, Benjamin D., Elias J. Salay, and Raymond K. Kostuk. “Reproducibility of a Dichromated Gelatin Mold-Coating Film Preparation Process” (manuscript in preparation)

4. Chrysler, Benjamin D., and Raymond K. Kostuk. "High energy yield bifacial spectrum-splitting photovoltaic system." Applied Optics 59, no. 22 (2020): G8-G18.

5. Chrysler, Benjamin D., and Raymond K. Kostuk. "Holographic spectrum-splitting photovoltaic system using bifacial cells." In Photonics for Solar Energy Systems VIII, vol. 11366, p. 113660P. International Society for Optics and Photonics, 2020.

6. Chrysler, Benjamin D., Xuessen Tan, Jianbo Zhao, and Raymond K. Kostuk. "Spectrum-splitting photovoltaic system using bifacial cells for high energy yield." In New Concepts in Solar and Thermal Radiation Conversion II, vol. 11121, p. 111210B. International Society for Optics and Photonics, 2019.

7. Chrysler, Benjamin D., Elias J. Salay, and Raymond K. Kostuk. "Improving the repeatability of the spectral bandwidth and diffraction efficiency of holograms formed in dichromated gelatin." In Photosensitive Materials and their Applications, vol. 11367, p. 1136718. International Society for Optics and Photonics, 2020.

8. Chrysler, Benjamin D., and Raymond K. Kostuk. "Volume hologram replication system for spectrum-splitting photovoltaic applications." Applied optics 57, no. 30 (2018): 8887-8893.

9. Chrysler, Benjamin D., and Raymond K. Kostuk. "Volume hologram replication system for photovoltaic applications." In New Concepts in Solar and Thermal Radiation Conversion and Reliability, vol. 10759, p. 107590W. International Society for Optics and Photonics, 2018.

10. Chrysler, Benjamin D., and Raymond K. Kostuk. "Volume hologram replication system." In Optics and Photonics Japan, p. 31aAJ5. Optical Society of America, 2018.

Some of the work described in this dissertation was performed during my M.S. program:

1. Chrysler, Benjamin D., Yuechen Wu, Zhengshan Yu, and Raymond K. Kostuk. "Volume holographic lens spectrum-splitting photovoltaic system for high energy yield with direct and diffuse solar illumination." In Next Generation Technologies for Solar Energy

Conversion VIII, vol. 10368, p. 103680G. International Society for Optics and Photonics, 2017.

2. Chrysler, Benjamin D., Silvana Ayala Pelaez, Yuechen Wu, Shelby D. Vorndran, and Raymond K. Kostuk. "Environmental stability study of holographic solar spectrum splitting materials." In Next Generation Technologies for Solar Energy Conversion VII, vol. 9937, p. 99370N. International Society for Optics and Photonics, 2016.

Other work was completed during a research stay at Utsunomiya University in Japan but did not directly contribute to the work in this dissertation:

1. Chrysler, Benjamin D., Kazuhiko Oka, Yukitoshi Otani, and Nathan Hagen. "Dynamic calibration for enhancing the stability of a channeled spectropolarimeter." Applied Optics 59, no. 30 (2020): 9424-9433.

2. Chrysler, Benjamin D., Yukitoshi Otani, and Nathan Hagen. "Dynamic calibration of a channeled spectropolarimeter for extended temperature stability." In Polarization Science and Remote Sensing IX, vol. 11132, p. 111320P. International Society for Optics and Photonics, 2019.

Chapter 2

Holographic Spectrum Splitting

In this dissertation, volume holographic lens arrays are used for dividing the solar spectrum into spectral bands. The design procedures for a two-junction spectrum splitting photovoltaic system are discussed in this chapter including the photovoltaic cell selection, optimization of the hologram for performance during reconstruction, simulation, and analysis. The concepts and designs that are presented provide a foundation for spectrum splitting designs with more than two energy bandgaps in subsequent chapters of this dissertation.

2.1 Introduction

Several types of optical elements are used in lateral spectrum-splitting systems with the most common being dichroic filters [17], [41], surface relief gratings [16], and volume holographic optical elements (VHOEs) [15]. The use of a dichroic filter is attractive since they are able to reflect broad spectral bandwidths (200 nm) with high efficiency and have well-developed manufacturing processes. For this reason, spectrum-splitting systems with dichroic filters have achieved high conversion efficiency (40%) in a laboratory setting [42], [43]. However, dichroic filters are reflective which makes it difficult to design modules with form factors comparable to conventional flat-panel modules. On the other hand, surface relief gratings also have broad spectral

bandwidth and well-developed commercial manufacturing processes and can be designed in transmission geometries. However, it is difficult to simultaneously achieve high spatial frequencies (500lp/mm to 2000lp/mm), encapsulation, focusing power, and low cost with surface relief gratings. Similarly, VHOEs can be also designed with broad spectral bandwidth in transmission geometries [15]. However, focusing power can be incorporated directly into the element which avoids the need for an additional lens or mirror [44]. Holographic materials such as dichromated gelatin are able to be manufactured with costs as low as 3$/m^2 [45], [46]

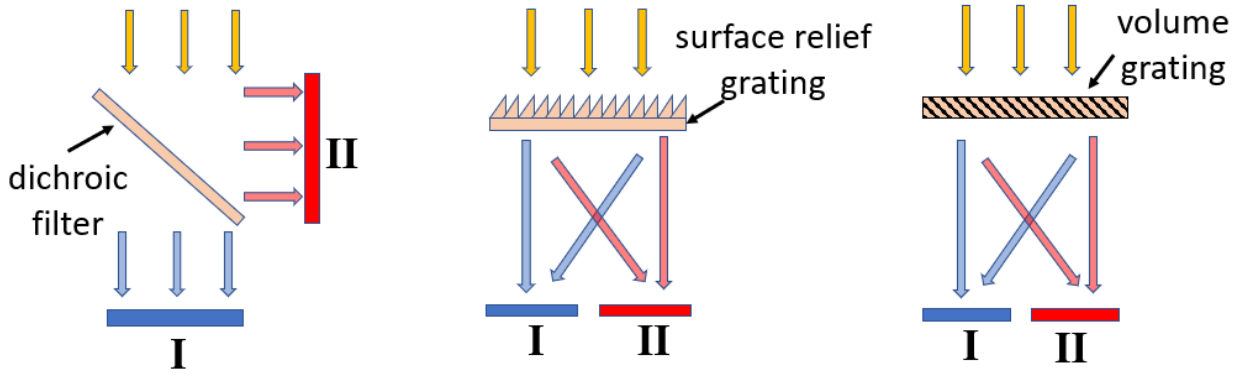

Figure 2.1: Three different approaches for dividing the solar spectrum between photovoltaic cells 'I' and 'II' that have different energy bandgaps. The first uses a reflective dichroic filter, the second uses a surface relief diffraction grating, and the third uses a volume grating.

Based on the considerations above, VHOEs are selected for use in the spectrum splitting designs in this dissertation. The two main approaches for implementing VHOEs in a spectrum splitting system can be broadly classified as grating-over-lens configurations [47], [48] and volume holographic lens (VHL) configurations [44], [49] (Fig. 2.2). In a grating-over-lens configuration a VHOE diffracts and disperses light which is then focused by a lens onto the PV cells. The light that is not diffracted (0^{th} order) is also focused by the lens to an underlying PV cell. One of the downsides of this configuration is that it only converts a fraction of the diffuse sunlight. This is because grating-over-lens systems typically use smaller PV cells that do not cover the entire

surface area of the module. Another downside of this approach is that it typically requires dual-axis solar tracking systems. The VHL approach combines both the diffractive power of the grating and the focusing power of the lens in a single holographic element which has two main advantages over the grating-over-lens approach. First, combining the focusing and dispersive powers in a single element reduces the system complexity and allows for module form factors comparable to conventional flat-panel modules. Second, a greater quantity of diffuse sunlight is collected. This is because the 0^{th} order light does not come to a focus and the module is designed with a greater surface area covered by PV cells. In addition, this type of module is compatible with single-axis solar tracking if the VHLs are recorded with cylindrical lenses.

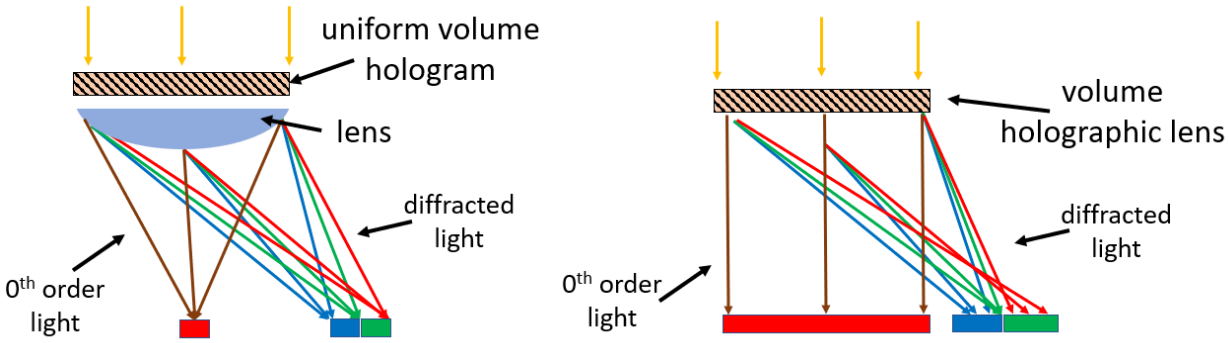

Figure 2.2: Two different approaches for using volume holographic optical elements in a spectrum splitting system. (left) In a grating-over-lens approach a volume hologram diffracts light which is uniformly dispersed and focused by a lens. The diffracted light comes to a focus at the PV cell plane. The light that is not diffracted (0^{th} order) is also focused by the lens. In a volume holographic lens approach a volume grating has a spatially varying grating period and light diffracts and comes to a focus. The 0^{th} order light does not come to a focus.

A specific implementation of the VHL approach was proposed by Vorndran et al [49]. This implementation is analyzed in depth in this chapter and is used as a foundation for many of the designs in this dissertation. A VHL spectrum-splitting system consists of an array of unit cells as depicted in Fig. 2.3. The holographic element in a unit cell consists of four VHLs which are

denoted by the numbers ‘1’, ‘2’, ‘3’ and ‘4’. The VHL array is separated from an array of PV cells by an encapsulant material of thickness ‘t’. The encapsulant material is assumed to be glass with an index of n = 1.5 but can also be a plastic such as PMMA or air. There are two different PV cell energy bandgaps, or “subcells”, denoted by the roman numerals ‘I’ and ‘II’. An example of the spectral conversion efficiency for the two subcells is shown in Fig. 2.4. The subcells are rectangular in shape with total widths of W_I and W_{II} per unit cell. The subcells are arranged in an alternating configuration between wide-bandgap (‘I’) and narrow-bandgap (‘II’).

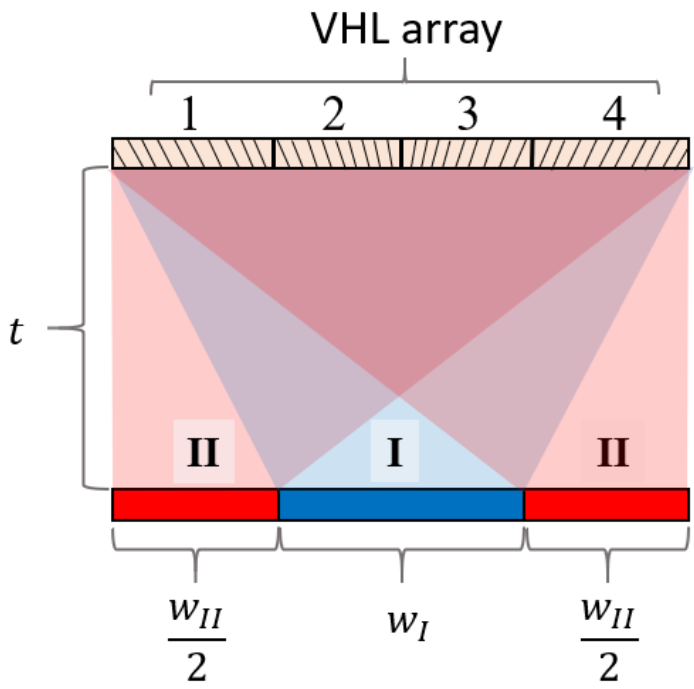

Figure 2.3: Unit cell for a spectrum-splitting system using a volume holographic lens array for lateral spectral separation. PV cell ‘I’ is a wide bandgap cell and is optimized for converting light at shorter wavelengths and PV cell ‘II’ is a narrow-bandgap cell and is optimized for converting light at longer wavelengths.

Each VHL diffracts and focuses light at a “transition” wavelength λ_t (green arrows in Fig. 2.4) to the boundary between PV cells ‘I’ and ‘II’. The transition wavelength is selected to be equal to the bandgap wavelength of the wide-bandgap cell ‘I’. VHLs ‘1’ and ‘4’ are positioned above

narrow-bandgap cell ‘II’ and are tuned to diffract normally incident light with peak efficiency at wavelength λ_{p1} (diffracted blue arrows in Fig. 2.4). The remaining light outside the spectral diffraction range is transmitted without diffraction to PV cell ‘I’ (transmitted blue arrows in Fig. 2.4). VHLs ‘2’ and ‘3’ are positioned above wide-bandgap cell ‘I’ and are tuned to diffract normally incident light with peak efficiency at wavelength λ_{p2} in the optimal spectral band of PV cell ‘II’ (diffracted red arrows in Fig. 2.4). The remaining light outside the spectral diffraction range is transmitted without diffraction to PV cell ‘II’ (transmitted red arrows in Fig. 2.4). The widths of the VHLs are selected to match the widths of the underlying PV cells. Therefore, VHLs ‘1’ and ‘4’ have a width of $W_{II}/2$ and VHLs ‘2’ and ‘3’ have a width of $W_I/2$.

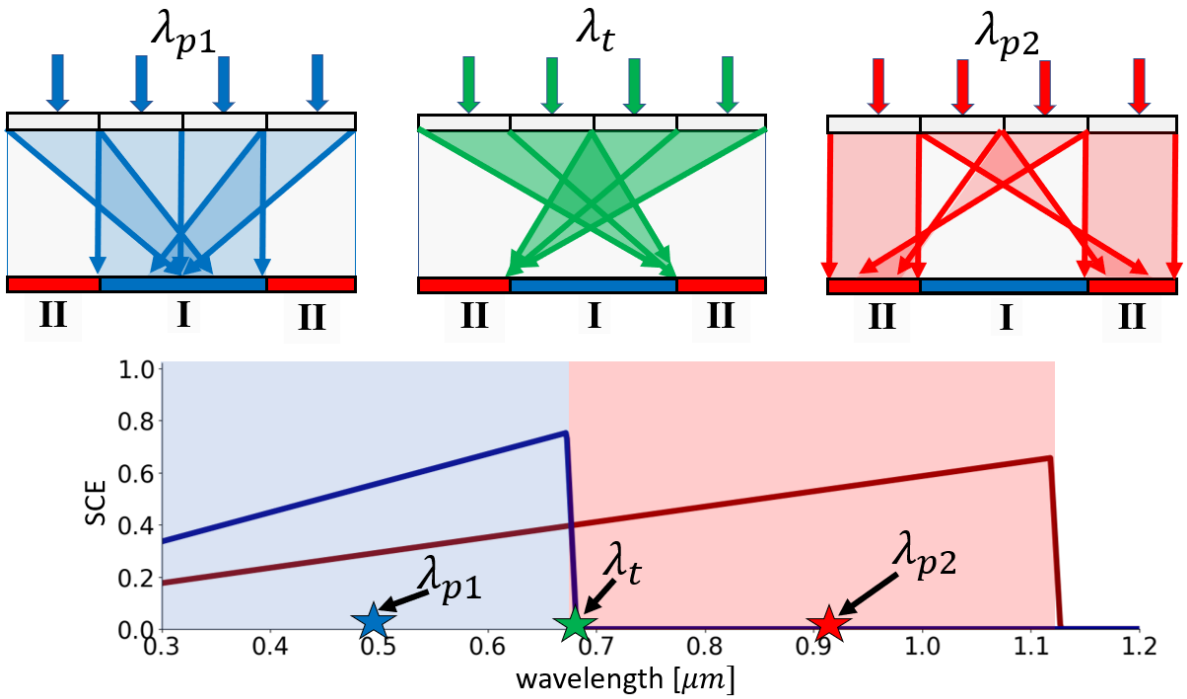

Figure 2.4: Spectral conversion efficiency (SCE) of a wide-bandgap PV cell (blue line) and a narrow-bandgap PV cell (red line). Three wavelengths λ_t, λ_{p1}, λ_{p2} are also indicated. The diffraction of each of these three wavelengths by the volume holographic lens array are illustrated. The selection of λ_t provides spectral separation between PV cells and the selection of λ_{p1} and λ_{p2} matches the diffracted spectral band with the spectral response of the PV cells.

2.2 Photovoltaic Cell Selection

One important factor affecting the power conversion efficiency (PCE) of a SSPV module is the combination of energy bandgaps. The following analysis is used to select the PV cells for the two-, three-, and four- junction system designs in this dissertation. The two-junction system designs are evaluated later in this chapter while the three- and four-junction system designs are evaluated in subsequent chapters.

The first step in the process is determining the energy bandgap combinations for "ideal" PV cells. Assumptions are made about the bandgap energy of certain cells in order to more closely match the availability of experimental PV cells. In a "silicon/PSC" combination, the narrow-bandgap cell is assumed to be a 1.1eV silicon cell [50] and the remaining cells are assumed to be perovskite solar cells (PSCs) with bandgaps ranging between 1.25eV to 2.3eV [23]–[27]. In an "all-PSC" combination, each of the cells are assumed to be perovskite cells with bandgap energies ranging between 1.25eV to 2.3eV. In addition to the silicon/PSC and all-PSC cell combinations, a "silicon/III-V" combination is also considered for two- and three- junction systems.

One of the ways to characterize the performance and a PV cell is with the spectral conversion efficiency (SCE) [14]. The SCE(λ) is a function that describes the conversion efficiency as a function of wavelength. The SCE(λ) of ideal PV cells is determined as a function of the bandgap energy using a detailed balance analysis [4], [8]. In addition to the individual PV cell spectral conversion efficiency, the overall PCE of the module depends on the spectral optical efficiency SOE(λ). The spectral optical efficiency $SOE_j(\lambda)$ for the jth PV cell is the ratio of the spectrum incident on the jth PV cell $E_j(\lambda)$ divided by the total global solar spectrum $E_{AM1.5G}(\lambda)$ [51] illuminating the unit cell:

$$SOE_j(\lambda) = \frac{E_j(\lambda)}{E_{AM1.5G}(\lambda)} \tag{2.1}$$

where 'j' is the index of the bandgap energy and is represented by roman numerals. The roman numeral 'I' indicates the widest bandgap and increases in the order of decreasing bandgap energy for a given cell combination. The PCE of the system is calculated by multiplying the $E_{AM1.5G}(\lambda)$ spectrum by the $SCE_j(\lambda)$ and $SOE_j(\lambda)$ of the jth PV cell, integrating over all wavelengths, dividing by the total incident power, and summing the power generated by each PV cell [14]:

$$PCE = \sum_j \frac{\int E_{AM1.5G}(\lambda) \cdot SOE_j(\lambda) \cdot SCE_j(\lambda) \cdot \mathrm{d}\lambda}{\int E_{AM1.5G}(\lambda) \cdot d\lambda} \tag{2.2}$$

When determining energy bandgap combinations, the system is assumed to have "perfect" optical filtering. In a system with perfect optical filtering, the $SOE_j(\lambda)$ is equal to one within the spectral band of the jth PV cell. The spectral band of the jth PV cell is defined as the range of wavelengths between the bandgap wavelengths of the jth and (j-1)th PV cells. For example, the spectral bands for the PV cells in Fig. 2.4 range from 0.3μm to 0.69μm for PV cell 'I' and from 0.69μm to 1.13μm for PV cell 'II'.

The power conversion efficiency of different cell bandgap combinations is calculated using Eq. 2.2. The power conversion efficiency of a two-bandgap combination is shown in the contour plot in Fig. 2.5a. In this plot, the bandgap of cell 'I' is varied along the horizonal axis and the bandgap of cell 'II' is varied along the vertical axis of the plot. The plot looks like a triangle since only cell combinations are considered in which the bandgap of cell 'I' is greater than the bandgap of cell 'II'. Dotted red lines are plotted in the horizontal direction that indicate the power conversion efficiency of cell combinations with a 1.1eV silicon bottom cell (cell 'II' = 1.1eV) [50] and cell combinations with a 1.25eV perovskite bottom cell (cell 'II' = 1.25eV) [23]. The most

efficient bandgap combination using a 1.1eV silicon cell (cell ‘II’) is indicated by one of the two red circles (I: 1.84eV, II: 1.1eV) and the most efficient bandgap combination using a 1.25eV perovskite cell is indicated by the other red circle (I: 1.92eV, II: 1.25eV).

For three-bandgap cell combinations, the narrow-bandgap cell is fixed at either 1.1eV for silicon/perovskite combinations or 1.25eV for all-perovskite combinations. The power conversion efficiency is then shown in the contour plots (Fig. 2.5b,c) with the bandgaps of cells ‘I’ and ‘II’ varied along the horizontal and vertical axes. The most efficient bandgap combinations are marked on the contour plots with the red circles. The most efficient all-perovskite bandgap combination is: I: 2.27eV, II: 1.68eV, III: 1.25eV and the most efficient silicon/perovskite bandgap combination is: I: 2.17eV, II: 1.55eV, III: 1.1eV.

For four-bandgap cell combinations, the narrow-bandgap cell, cell ‘IV’, is fixed at either 1.1eV (silicon/perovskite) or 1.25eV (all-perovskite) as is done for three-bandgap cell combinations. However, the bandgap of the wide-bandgap cell, cell ‘I’, is also fixed at 2.3eV. This value is selected since 2.3eV is the largest bandgap which has been experimentally demonstrated for perovskite photovoltaic cells with significant conversion efficiency [27]. Without fixing cell ‘I’ at this value, the bandgap optimization would yield values greater than 2.3eV which have not yet shown potential for high conversion efficiency. The power conversion efficiency of the four-bandgap cell combinations are shown in the contour plots in Fig. 2.5d,e. The energy bandgap of cell ‘II’ is plotted along the horizontal axis and the energy bandgap of cell ‘III’ is plotted along the vertical axis. The most efficient bandgap combinations are marked by the red circles. The most efficient silicon/perovskite bandgap combination is: I: 2.3eV, II: 1.87eV, III: 1.46eV, IV: 1.1eV, and the most efficient all-perovskite bandgap combination is: I: 2.3eV, II: 1.87eV, III: 1.54eV, IV: 1.25eV.

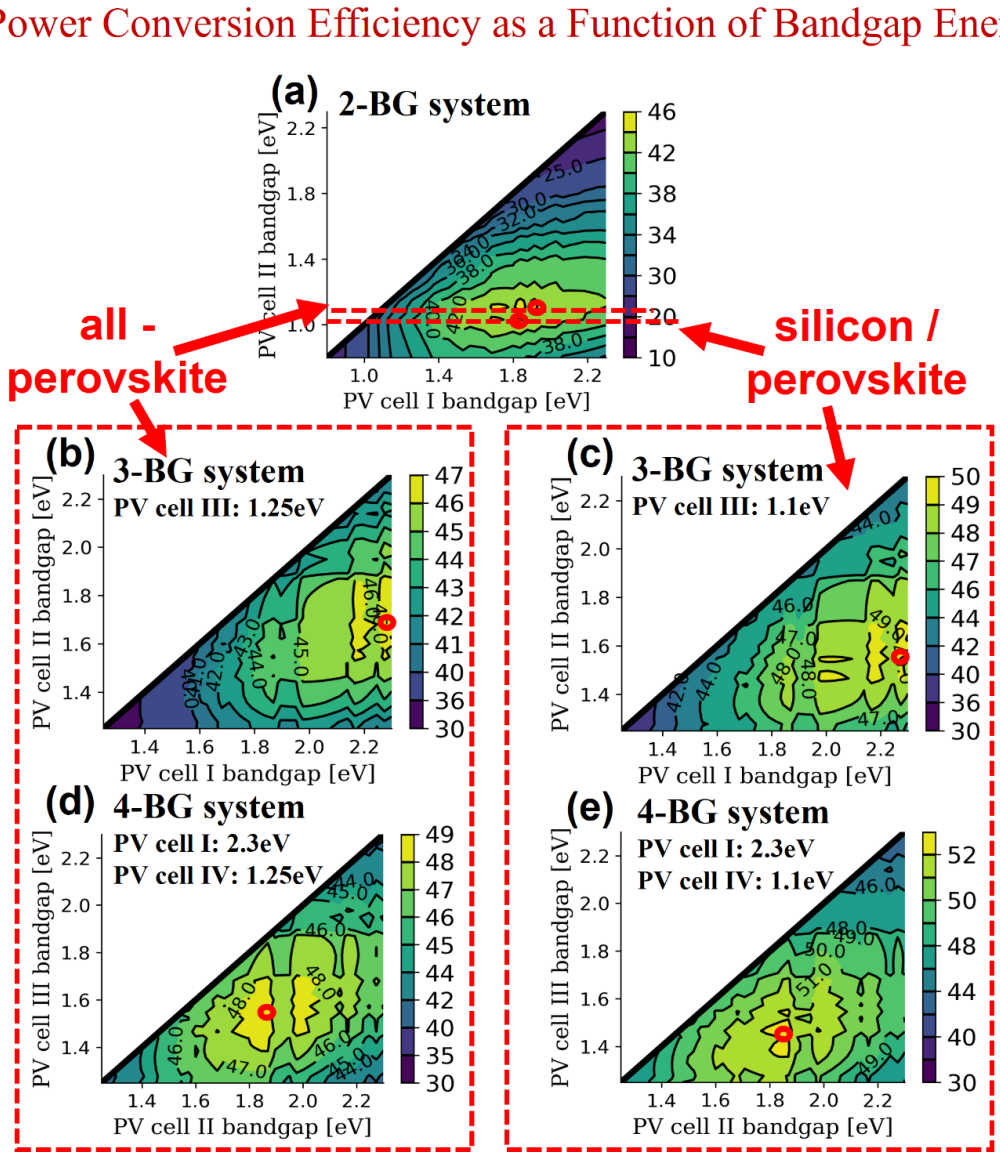

Figure 2.5: Contour plot of the power conversion efficiency for different cell bandgap combinations. The energy bandgaps of two different PV cells are varied along the horizontal and vertical axes. The bandgap of the remaining PV cells in the 3- or 4- bandgap systems are set at the fixed values indicated on the plot. The bandgap combination with highest power conversion efficiency is marked by the red 'o' symbol. (a) A cell combination with two bandgaps. (b) An all-perovskite cell combination with three bandgaps. The bandgap of cells 'I' and 'II' are varied and the bandgap of cell 'III' is fixed at 1.25eV. (c) A silicon/perovskite cell combination with three bandgaps. The bandgap of cells 'I' and 'II' are varied and the bandgap of cell 'III' is fixed at 1.1eV. (d) An all-perovskite cell combination with four bandgaps. The bandgap of cells 'II' and 'III' are varied while the bandgap of cell 'IV' is fixed at 1.25eV and the bandgap of cell 'I' is fixed at 2.3eV. (e) A silicon/perovskite cell combination with four bandgaps. The bandgap of cells 'II' and 'III' are varied while the bandgap of cell 'IV' is fixed at 1.1eV and the bandgap of cell 'I' is fixed at 2.3eV.

The bandgap combinations that give the highest power conversion efficiency are listed in Table 2.1 and are briefly summarized here. The highest attainable PCE for a SSPV module with ideal cells ranges from 42.0% for a 2-junction all-perovskite combination to 52.5% for a 4-junction silicon/perovskite combination. In general, a 3-junction combination has a 5% advantage over a 2-junction combination and a 4-junction combination has a 2% advantage over a 3-junction combination. For a given number of bandgaps the silicon/PSC cell combinations have a 2% to 3% advantage compared with all-PSC combinations. The SCE(λ) curves generated from detailed balance calculations [4], [8] for each of the ideal cells is plotted in Fig. 2.6a. Experimental cells are also selected from the literature that have actual bandgap values near the ideal bandgap values. The experimental bandgap combinations are also listed in table 2.1. The SCE(λ) data for each of these cells is taken from literature and plotted in Fig. 2.6b.

In addition to silicon-PSC and all-PSC combinations, silicon/III-V cell combinations are also shown. These combinations are further from the ideal bandgap values since few single-junction cells have been developed with these materials and are available for use. However, this combination is valuable for analysis for the following reasons. First, PV cells based on III-V materials are extremely efficient with GaAs cells reaching 28.8% conversion efficiency [52], [53] and a GaInP cell being the first cell measured with a fill factor greater than 90% [54]. The combination of III-V cells and silicon cells show the upper limits of spectrum-splitting conversion efficiency that is possible with current cell technology. However, the high cost of III-V cells may limit the commercial potential for these combinations.

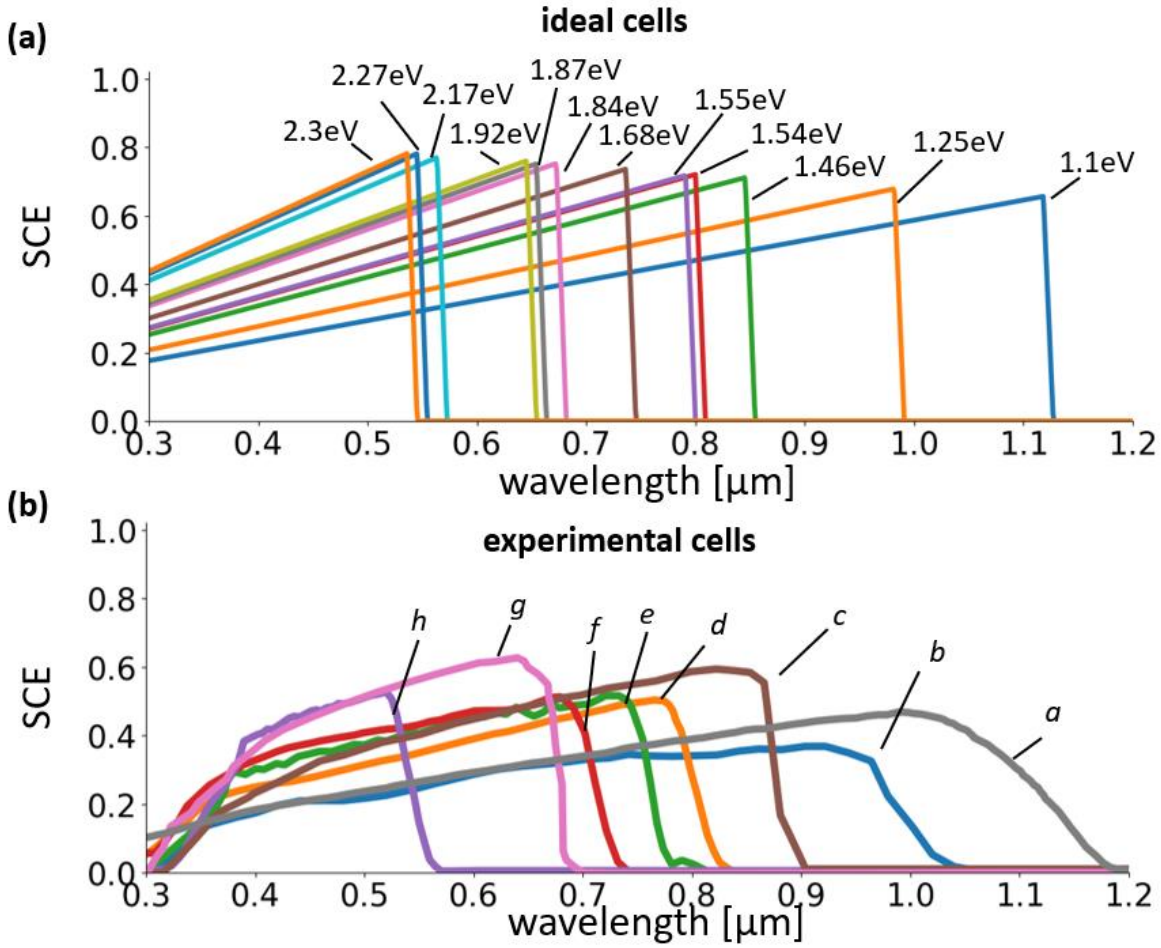

Figure 2.6: Spectral conversion efficiency (SCE) of different photovoltaic cells. (a) ideal cell spectral responses for the bandgap energies in Table 2.1. (b) experimental cells with energy bandgaps match the ideal cell bandgap combinations. *a:* 1.1eV silicon [50], *b:* 1.25eV Sn-Pb perovskite [23], *c:* 1.41eV GaAs [53], *d:* 1.55eV iodide management perovskite [24], *e:* 1.63eV rubidium cation [25], *f:* 1.72eV 2D/3D heterostructure perovskite [26], *g:* 1.84eV GaInP [54], *h:* 2.3eV $CH_3NH_3PbBr_3$ perovskite [27].

Table 2.1: Ideal and experimental cell bandgap energy combinations and the maximum power conversion efficiency (PCE).

Ideal cells obtained from detailed balance

	all-perovskite					silicon/perovskite				
	I	II	III	IV	PCE	I	II	III	IV	PCE
2-junction	1.92eV	1.25eV			42.0%	1.84eV	1.1eV			44.4%
3-junction	2.27eV	1.68eV	1.25eV		46.8%	2.17eV	1.55eV	1.1eV		49.6%
4-junction	2.3eV	1.87eV	1.54eV	1.25eV	48.9%	2.3eV	1.87eV	1.46eV	1.1eV	52.5%

Experimental cells reported in literature

	all-perovskite					silicon/perovskite				
	I	II	III	IV	PCE	I	II	III	IV	PCE
2-junction	1.72eV (f)	1.25eV (b)			28.90%	1.72eV (f)	1.1eV (a)			33.40%
3-junction	2.3eV (h)	1.63eV (e)	1.25eV (b)		31.50%	2.3eV (h)	1.55eV (d)	1.1eV (a)		34.90%
4-junction	2.3eV (h)	1.72eV (f)	1.55eV (d)	1.25eV (b)	32.30%	2.3eV (h)	1.72eV (f)	1.55eV (d)	1.1eV (a)	36.50%

	Silicon/III-V				
	I	II	III	IV	PCE
2-junction (GaAs)	1.41eV (c)	1.1eV (a)			34.78%
2-junction (GaInP)	1.84eV (g)	1.1eV (a)			37.3%
3-junction	1.84eV (g)	1.41eV (c)	1.1eV (a)		41.6%
4-junction	--	--	--	--	

(a) 25.6% efficient 1.1eV silicon heterojunction [50]

(b) 20.4% efficient 1.25eV Sn-Pb perovskite [23]

(c) 28.8% efficient 1.41eV GaAs [53]

(d) 21.25% efficient 1.55eV iodide management perovskite [24]

(e) 21.6% efficient 1.63eV rubidium cation perovskite [25]

(f) 19.8% efficient 1.72eV 2D/3D heterostructure perovskite[26]

(g) 22.0% efficient 1.84eV GaInP [54]

(h) 10.4% efficient 2.3eV $CH_3NH_3PbBr_3$ perovskite [27]

2.3 Volume Holographic Lens Design

There are four volume holographic lenses (VHLs) in each unit cell as depicted in Fig. 2.7 and denoted by the indices '1', '2', '3' and '4'. Each VHL is designed to achieve efficient lateral spectral separation upon reconstruction which is achieved by the selection of three parameters λ_t, R_f, and λ_p. The first parameter, the transition wavelength λ_t, is selected to be equal to the bandgap wavelength of PV cell 'I' to provide a sharp spectral transition between the PV cells. Normally incident light with wavelength λ_t is diffracted and focused to a position specified by the second parameter, R_f. The focus position R_f is located at the boundary between PV cell 'I' and PV cell 'II' and is measured with respect to the center of the VHL. The third parameter is the Bragg wavelength λ_p. The Bragg wavelength is the wavelength with highest diffraction efficiency for normally incident light. The Bragg wavelength tunes the spectral diffraction range for the VHL and is selected to match the spectral band of the targeted PV cell. For VHLs '1' and '4' the target PV cell is PV cell 'I' and for VHLs '2' and '3' the target PV cell is PV cell 'II'.

After selecting the three reconstruction parameters λ_t, R_f, and λ_p the K-vector $\vec{K}(x)$ is selected. The K-vector determines the direction and frequency of the modulation of the index of refraction in a volume hologram as depicted in Fig. 2.8. First, the "target" K-vector $\vec{K}_t(x)$ is selected which meets the desired reconstruction conditions specified by λ_t, R_f, and λ_p for all positions 'x' along the aperture of the VHL. As will be seen later in the discussion, in the spectrum-splitting application the K-vector cannot be fabricated with exact accuracy using conventional fabrication methods. For this reason, the target K-vector $\vec{K}_t(x)$ is used as an intermediate design parameter in determining the optimal construction geometry for the VHL.

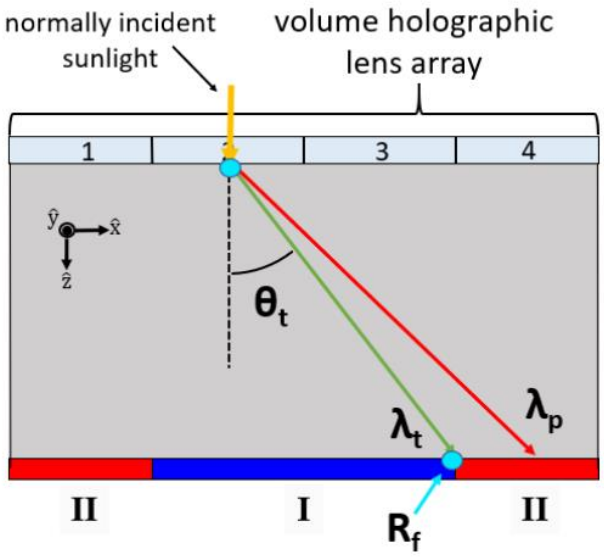

Figure 2.7: The unit cell aperture is divided into four volume holographic lenses '1', '2', '3', and '4'. The reconstruction parameters λ_t, R_f, and λ_p are used to calculate the ideal K-vector. The ideal K-vector diffracts light with wavelength λ_t to the position R_f and is tuned for highest diffraction efficiency at the Bragg wavelength λ_p.

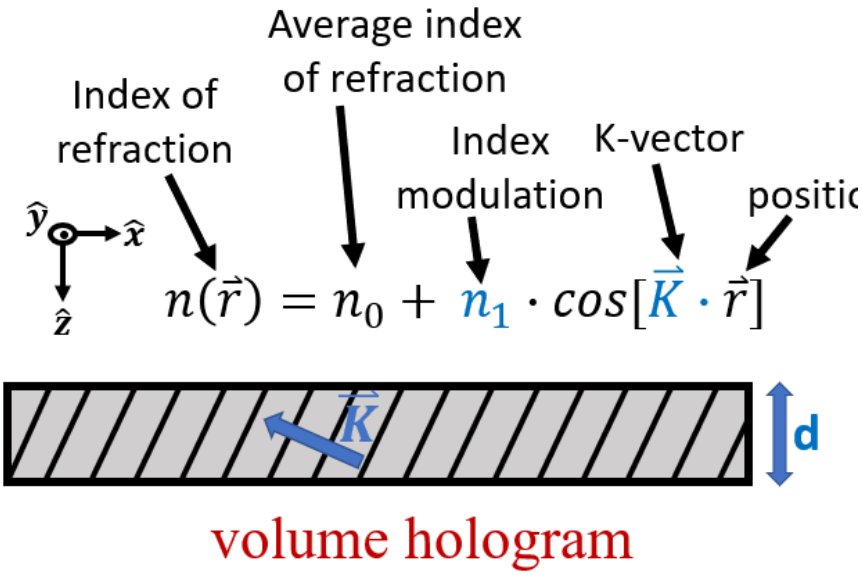

Figure 2.8: Illustration of a volume hologram. The three main design parameters affecting the spectral and angular diffraction characteristics are highlighted in blue: K-vector $\vec{K}$, the index modulation n_1, and the film thickness d. In a volume holographic lens, the K-vector varies along the aperture of the element and is a function $\vec{K}(x)$.

The target K-vector $\vec{K}_t(x)$ of a VHL is calculated using K-vector closure methods as a function of the design parameters specified in the previous paragraph [55], [56]. First, the transverse component of the target K-vector $\vec{K}_{t,x}(x)$ is calculated to satisfy the diffraction geometry specified by λ_t and R_f. An additional parameter θ_t is used for this calculation and is the angle between a given position 'x' on the VHL aperture and the focus position R_f. The value of the transverse component of the K-vector can then be calculated using the grating equation:

$$K_{x,t}(x) = \beta_t \cdot \sin\big(\theta_t(x)\big) \tag{2.3}$$

where $\beta_t = 2\pi n/\lambda_t$ is the wavenumber for light with wavelength λ_t. At this point the longitudinal component of the K-vector $\vec{K}_{t,z}(x)$ remains a free parameter. Next, an equation is derived for $\vec{K}_{t,z}(x)$ that tunes the hologram for maximum diffraction efficiency at the wavelength λ_p. The equation is derived based on the reconstruction geometry in Fig. 2.9b:

$$K_{z,t}(x) = \beta_p - \sqrt{{\beta_p}^2 - K_{x,t}(x)^2}, \tag{2.4}$$

where $\beta_p = 2\pi n/\lambda_p$ is the wavenumber for light with wavelength λ_p.

Unfortunately, the "target" K-vector $\vec{K}_t(x)$ cannot be recorded in a hologram with exact precision using a conventional "two point source" fabrication method. This method can be used to fabricate a volume holographic lens in which the tuning wavelength λ_p, transition wavelength λ_t, and construction wavelength λ_c are all equal. In this case, these wavelengths all have different values [57], [58] and there is no combination of point sources in which the interfering wavefronts perfectly match the target K-vector $\vec{K}_t(x)$ of the designed holographic lens. Errors in the K-vector result in aberrations in the reconstructed wavefront that decrease the quality of the lateral spectral

separation and reduce the diffraction efficiency across the aperture of the VHL. To overcome this limitation, a robust algorithm is developed for determining the optimal hologram construction geometry.

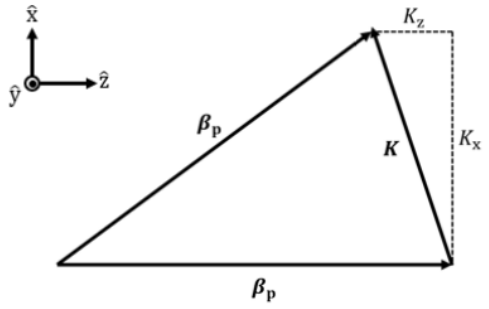

Figure 2.9: K-vector closure diagram for normally incident light with wavenumber $\beta_p = 2\pi n/\lambda_p$. The transverse component of the K-vector $K_{x,t}(x)$ is determined using the grating equation. An equation for the longitudinal component $K_{z,t}(x)$ is derived based on the K-vector closure geometry.

In practice, holograms are fabricated using a "two point source" construction geometry as illustrated in Fig. 2.10 [56]. For VHLs in the spectrum splitting application, the focusing only occurs in one dimension, so each "point source" is actually a one-dimensional "line source", which can be generated by focusing light with a cylindrical lens. The hologram is constructed with laser light at the construction wavelength λ_c. The grating K-vector $\vec{K}(x, P_1, P_2)$ produced when a photopolymer material is illuminated with light from two point sources P_1 and P_2 is given by:

$$\vec{K}(x, P_1, P_2) = \vec{k}_1(x, P_1) - \vec{k}_2(x, P_2), \tag{2.5}$$

where $\vec{k}_1(x, P_1)$ and $\vec{k}_2(x, P_2)$ are the wavevectors of light at a point 'x' on the surface of the hologram emanating from point sources P_1 and P_2 respectively. The point source locations are determined by minimizing the total error $\Delta(x)$ between the constructed K-vector $\vec{K}(x, P_1, P_2)$ and

the target K-vector $\vec{K}_t(x)$. In order to include the effects of both the transverse and longitudinal components of the K-vector the error is calculated using the L^2 norm [59]:

$$\Delta(\mathrm{x}) = \sqrt{\left[\vec{K}_x(x, P_1, P_2) - \vec{K}_{x,t}(x)\right]^2 + \left[\vec{K}_z(x, P_1, P_2) - \vec{K}_{z,t}(x)\right]^2} \tag{2.6}$$

The minimization is performed as a function of P_1 and P_2 in Python using the *optimize.minimize* function in the SciPy package [60]. The point sources returned by the minimization algorithm are then used to obtain the K-vector. This process is repeated for each VHL in the unit cell array.

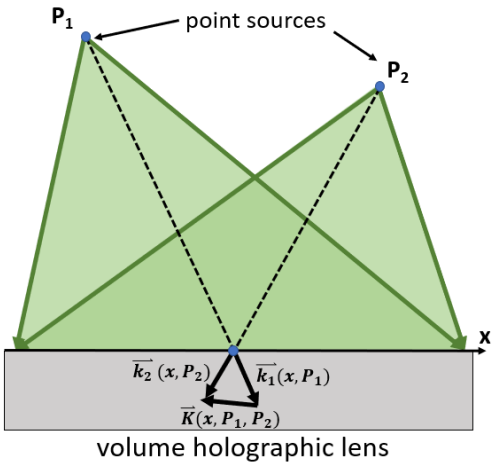

Figure 2.10: Volume holographic lenses are formed through interference of two point sources of monochromatic light. The grating K-vector varies as a function of the position along the aperture, x, and the position of the two point sources P_1 and P_2. The position of the point sources are optimized to maximize diffraction efficiency and minimize aberrations.

An example of the target K-vector $\vec{K}_t(x)$ and the K-vector constructed with optimized point sources $\vec{K}(x, P_1, P_2)$ is shown in Fig. 2.11. In this example, the hologram is an off-axis holographic lens with an F/# of 2.8 that focuses light along an axis that is oriented at an angle of 24.9° with respect to the z-axis. The target K-vector was constructed with a transition wavelength λ_t of

0.705μm, a focus position of $R_f = \langle 5.4mm, 10mm \rangle$ and a Bragg wavelength λ_p of 0.55μm. In Figs. 2.11a,b the difference between target K-vector and the K-vector constructed with point sources P_1 and P_2 appears very small with deviations observed at the edges of the lens aperture. The errors in the x and the z components of the K-vector are shown in Fig. 2.11c. The error crosses the zero axis at two points along the aperture of the element indicating that the point source locations are optimized.

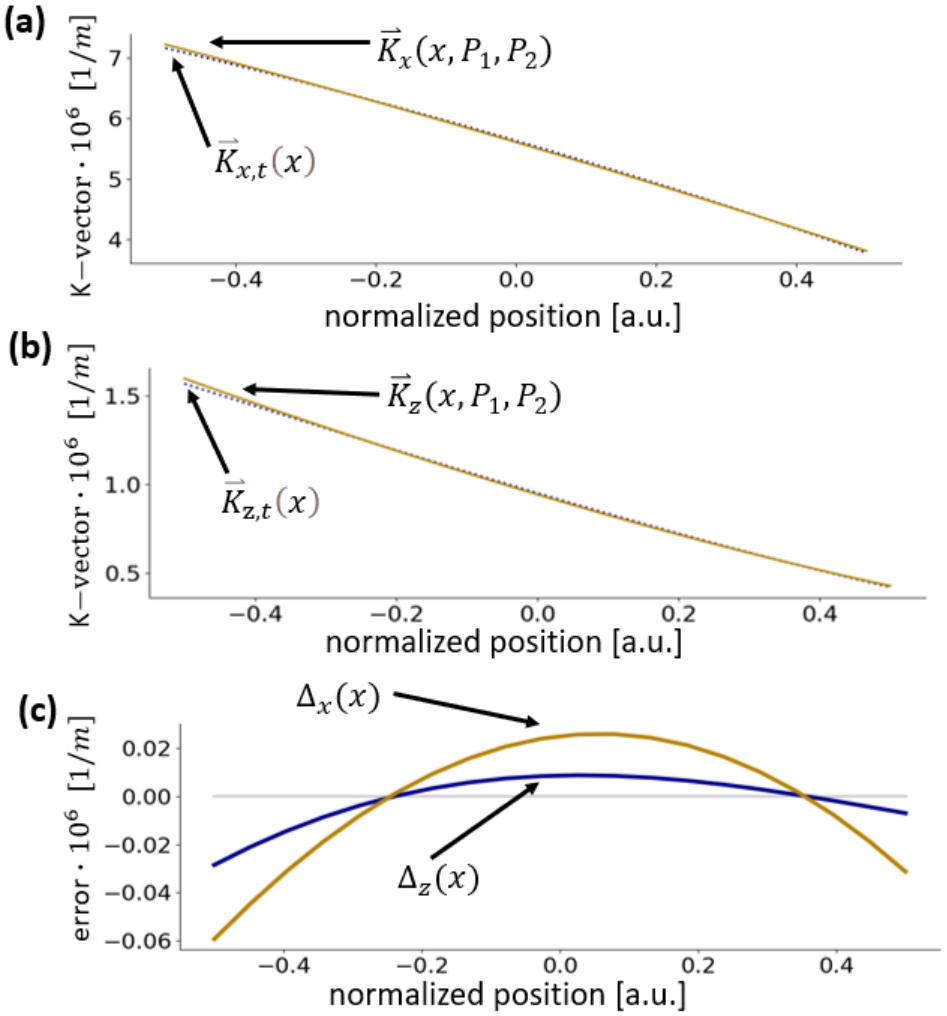

Figure 2.11: Plot showing the target K-vector and the K-vector constructed with optimal point sources for an off-axis volume holographic lens. The horizontal axis is the position x along the aperture normalized to the width of the hologram. (a) Lateral component of the target K-vector (dotted blue line) and constructed K-vector (solid yellow). (b) Longitudinal component of the target K-vector (dotted blue line) and constructed K-vector (solid yellow). (c) Error between the target K-vector and two-point source constructed K-vector.

The final two VHL parameters that need to be determined are the film thickness ‘d’ and index modulation ‘n_1’. The film thickness determines the spectral and angular bandwidth of the hologram. In general, thick holograms have a narrow bandwidth and thin holograms have a broad bandwidth. For spectrum splitting applications broad spectral bandwidths are usually desirable and thin film thickness values are preferable. However, if the film thickness is too thin, a significant amount of light is diffracted in higher orders which reduces the overall conversion efficiency of the system. Additionally, thinner holograms require higher index modulation values and may exceed the capability of the material. The film thickness values are initially determined through diffraction efficiency simulations to balance the competing effects of bandwidth and higher order diffraction. In subsequent sections, an optimization method is discussed for directly optimizing the power conversion efficiency as a function of the film thickness. After selecting the film thickness, the index modulation value is determined. The index modulation affects the diffraction efficiency of a hologram but does not significantly affect the bandwidth or higher order diffraction. Therefore, the index modulation is selected to maximize the diffraction efficiency. The film thickness and index modulation values are selected within a range that can be manufactured in dichromated gelatin [61]–[64]. The film thickness is selected in a range between 2μm and 30μm and the index modulation is selected in a range between 0.01 to 0.10. The dichromated gelatin recording material is discussed in more depth in Chapter 6.

2.4 Simulation Method

After determining the K-vector, film thickness, and index modulation of the volume holographic lenses, the spectral diffraction efficiency is calculated as a function of position along the aperture of the element. One challenge in simulating a spatially varying hologram is that

coupled wave models require the element to be periodic. The approach used in this dissertation for simulating spatially varying holograms is to divide the VHOE into smaller sections which are locally approximated as being periodic [49], [65]. The diffraction efficiency of each of the smaller sections is then simulated using coupled wave methods.

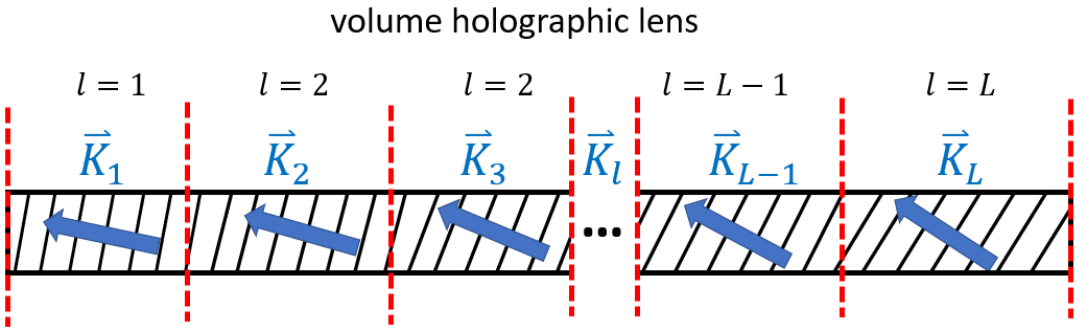

Figure 2.12: depiction of a spatially varying volume holographic lens divided into 'L' sections for simulation purposes. Each section is approximated as being periodic with a K-vector $\vec{K}_l$ where 'l' is the index number of the section.

The diffraction efficiency of each section is simulated using rigorous coupled wave analysis (RCWA) in this dissertation [66]. RCWA is an exact solution to Maxwell's equations for optical elements with periodic modulation in the index of refraction or absorptivity. RCWA is advantageous for its ability to calculate an arbitrary number of diffraction orders, unlike approximate models which only calculate a transmitted order and a single diffracted order [55]. For spectrum-splitting applications RCWA is the preferred model to use since thin, broad bandwidth elements typically diffract light in higher orders. The RCWA methods discussed in this chapter are used in the majority of this dissertation. An extension of this method is developed for cascaded gratings in Chapter 3.

Two different implementations of RCWA are used. The first implementation is using a commercial simulation software package, RSOFT [67]. RSOFT is used when arbitrary angles of incidence in 3D space are required or transverse magnetic (TM) polarization is needed for

accuracy. However, in many cases simulating the diffraction efficiency as a function of the in-plane angle of incidence is sufficient and for most spectrum-splitting geometries the difference between TE and TM polarizations is small. Additionally, the calculation time with RSOFT can take hours or days and is not suitable for optimizations that may require tens or hundreds of iterations.

With these considerations in mind, an alternative implementation is developed by directly implementing the RCWA equations in Python. The formulation used was described in a 1981 paper by Moharam and Gaylord for gratings with sinusoidal index modulation [66]. Although this formulation is more limited and less accurate than layered [68] or 3D approaches [69] it is suitable for simulating volume holograms in many applications. One of the modifications that is made to improve the numerical stability of the model is to remove the evanescent waves from the calculation. When evanescent waves are included in the model they result in terms with extremely large or extremely small values. These terms then reduce the numerical stability during the evaluation of the boundary conditions. While evanescent terms are important to include in certain types of gratings such as those with absorption modulation, the differences are small in the cases examined in this dissertation.

A comparison of the spectral diffraction efficiency computed with RSOFT and the in-house Python code is shown in Fig. 2.13. The elements being simulated are volume holographic lenses and the light is assumed to be normally incident. Some small deviations are seen but in general the agreement is very good. The power conversion efficiency (PCE) for a spectrum splitting system computed using the in-house Python code is 0.01% less than the PCE computed using RSOFT. A comparison of the spectral diffraction efficiency for TE and TM polarized light computed with RSOFT is shown in Fig. 2.14. The difference between the two polarizations is relatively small for

this geometry. The PCE when computed with TE modes is 0.03% higher than when computed with TM modes.

To summarize, the difference in power conversion efficiency for the TE and TM modes is 0.03% and the difference between the RSOFT calculation and the in-house code is 0.01%. However, the in-house code is 50X faster than the RSOFT code. For this reason, the in-house code is used for most of the calculations in this dissertation. Unless otherwise noted, it is assumed the diffraction efficiency is computed in Python.

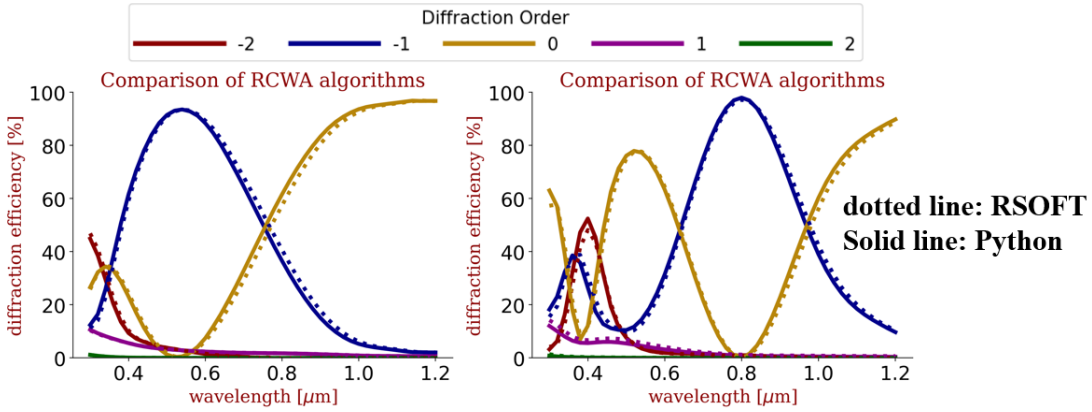

Figure 2.13: A comparison of RCWA calculations for two volume holographic lenses performed using RSOFT software and in-house code written in Python. Some small deviations are seen in the curves but the agreement is very close.

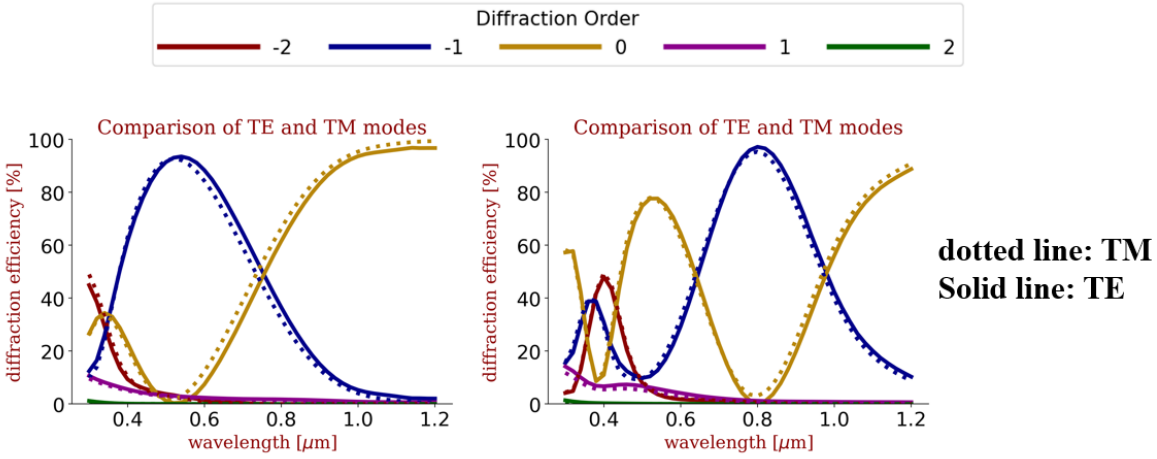

Figure 2.14: A comparison of transverse electric (TE) and transverse magnetic (TM) modes for volume holographic lenses.

An example of the RCWA diffraction efficiency of a spectrum splitting VHL array computed in Python is shown in Fig. 2.15 and Fig. 2.16. The VHL array is designed using the methods in the previous section to divide the solar spectrum between a 1.25eV perovskite cell and a 1.72eV perovskite cell. For this cell combination the first spectral band ranges between I: 0.300μm to 0.705μm and the second spectral band ranges between II: 0.705μm to 0.990μm. In this example, each VHL is divided into a total of L=20 sections. The spectral diffraction efficiency of each section is simulated independently and plotted in Fig. 2.15. It is observed that the spectral bandwidth and higher order diffraction increases from the left side of the aperture (l=1) to the right side of the aperture (l=20) since the grating vector varies as a function of position. The diffraction efficiency of section is then averaged for each VHL and plotted in Fig. 2.16b.

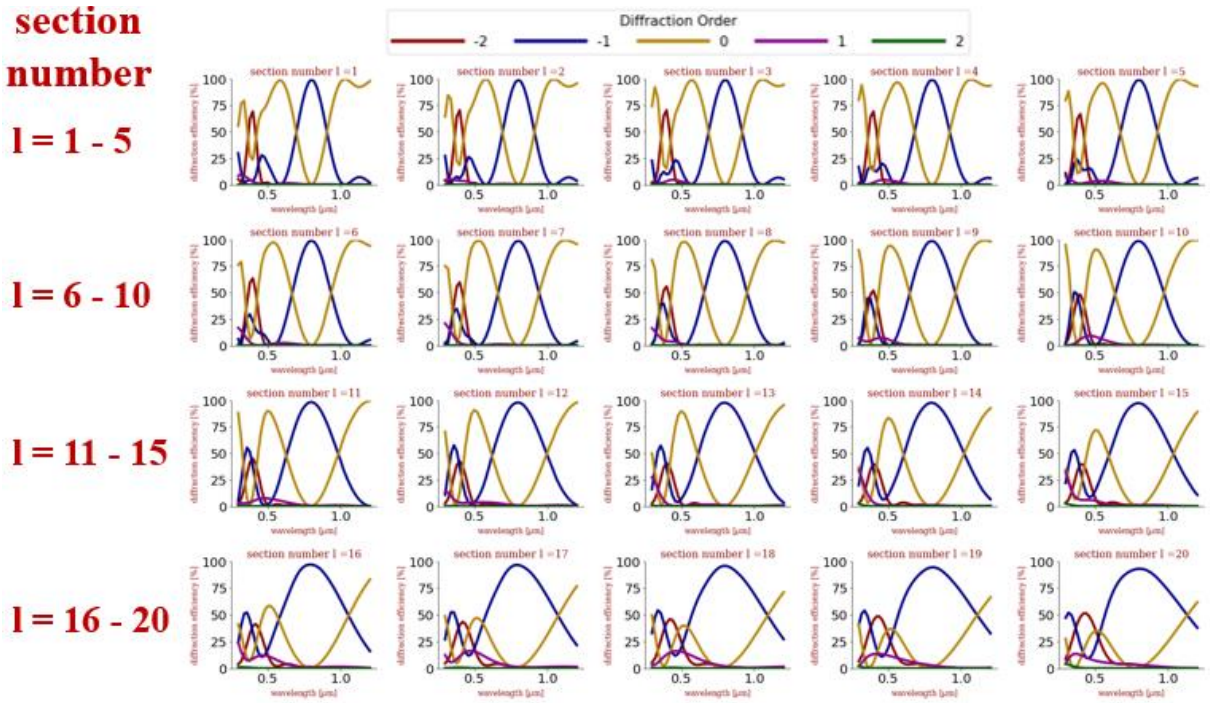

Figure 2.15: Spectral diffraction efficiency across the aperture of a volume holographic lens split into 20 different sections for simulation. The Bragg wavelength stays constant, but the bandwidth and higher order diffraction significantly increases from the left side of the lens (l = 1) to the right side of the lens (l=20). The average diffraction efficiency across this lens is plotted in Fig. 2.16b.

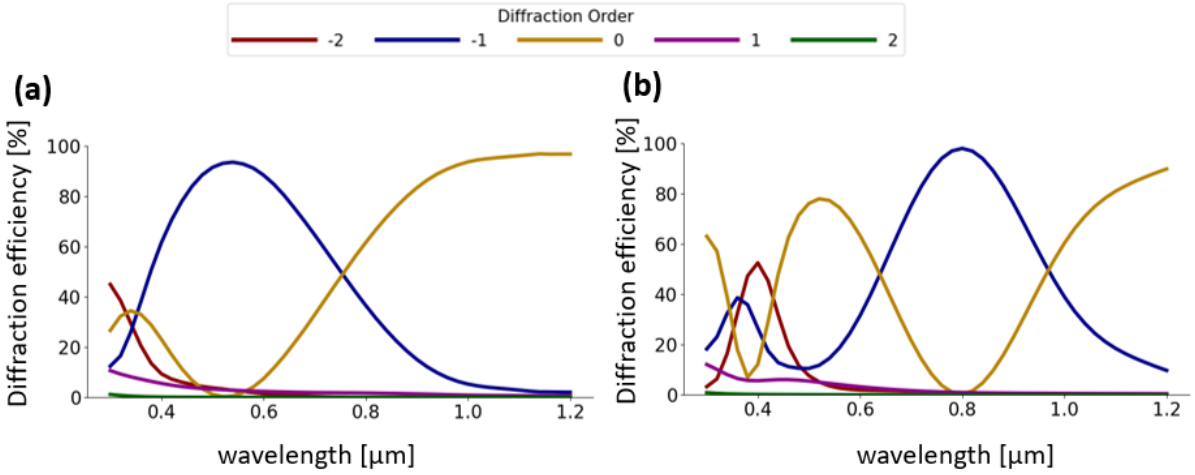

Figure 2.16: Spectral diffraction efficiency for two volume holographic lenses (VHLs) when illuminated at normal incidence. Each VHL is divided into 20 smaller sections and simulated with RCWA. The data shown here is the average spectral diffraction efficiency across the aperture. (a) The spectral diffraction efficiency of the 'mth' diffraction order of VHL '1' $\{\eta_m(\lambda)\}^{(1)}$, (b) The spectral diffraction efficiency of the 'mth' diffraction order of VHL '2' $\{\eta_m(\lambda)\}^{(2)}$. Due to symmetry, the spectral diffraction efficiency of the '-mth' diffraction order of VHL '4' $\{\eta_{-m}(\lambda)\}^{(4)}$ is equal to $\{\eta_m(\lambda)\}^{(1)}$. For the same reason, the spectral diffraction efficiency of the '-mth' order of VHL '3' $\{\eta_{-m}(\lambda)\}^{(3)}$ is equal to $\{\eta_m(\lambda)\}^{(2)}$.

After determining the spectral diffraction efficiency, the next step in the simulation is to determine the spectral optical efficiency $SOE(\lambda)$ using equation 2.1. In order to use this equation, the spectrum $E_j(\lambda)$ incident on each PV cell needs to be determined through a raytracing simulation. Two different raytracing approaches are implemented to achieve this. In earlier work, the non-sequential raytracing software FRED [70] is implemented. When using FRED, each grating section is modeled as a "linear grating" and the diffraction efficiency of each grating is entered in a diffraction efficiency table. A set of rays with wavelengths spanning across the solar spectrum is traced through the VHL array in a Monte Carlo simulation and then further traced to the PV cell plane. As the ray intersects with the VHOE it diffracts into one of the diffraction orders specified in the RCWA calculation. The probability that a ray is diffracted into a given order is equal to the diffraction efficiency of the order. The spectrum $E_j(\lambda)$ on each PV cell is then

determined using the spectral analysis function in FRED. This process is automated through command line scripts called from Python so that all data analysis and optimization can be performed in a high-level programming language.

In more recent work, a different raytracing method is implemented in which the ray propagation is directly computed in Python. In this approach, each ray is modeled as an object with attributes such as wavelength, position, and direction. Each ray also has a ray history which records the history of interactions with VHLs as well as the diffraction order. The direction of diffraction of a ray is computed using the grating equation and the flux of a ray is weighted by the RCWA diffraction efficiency. The results of this raytracing implementation agree strongly with the results of the FRED raytrace. A number of advantages are realized by directly implementing the raytracing model in Python. The first advantage is the increased productivity and ease when working entirely in a single programming language. For example, the way data is transferred between FRED and Python is through intermediate text files. This requires scripts in FRED and Python to read and write data in a specific format. While this approach is adequate once the scripts are set up, the format for the data exchange needs to be tailored to a particular optical system. Therefore, any changes in the optical system may also require changes in the read/write scripts. By implementing the raytrace directly in Python, the data exchange scripts can be eliminated entirely which increases the versatility of the approach. Another advantage of raytracing in Python is that more data is recorded about the diffraction history of a ray. This property is useful for sorting rays according to the diffraction order and is used in subsequent analyses to determine the source of optical losses.

After tracing the rays to the PV cells, the spectrum $E_j(\lambda)$ on each cell is obtained and the spectral optical efficiency is calculated using Eq. 2.1. The spectral optical efficiency for the system

in the previous example (Fig. 2.16) is shown in Fig. 2.17. Clear transitions between spectral bands can be seen. Lower spectral optical efficiency is seen for PV cell 'I' for wavelengths between 0.35 μm and 0.45 μm. In a subsequent section it is shown that this loss is due to higher order diffraction.

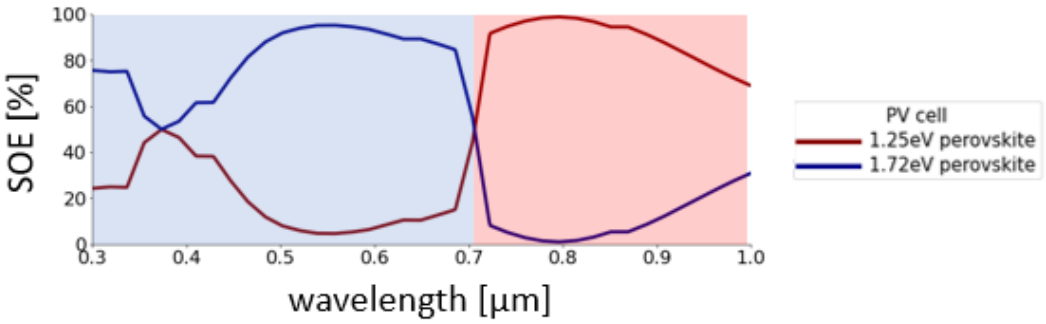

Figure 2.17: Spectral optical efficiency (SOE) for a volume holographic lens array splitting the solar spectrum between 1.25eV and 1.72eV perovskite solar cells. The color of the background indicates the spectral bands of the PV cells.

Lastly, the spectral optical efficiency is used to calculate the power conversion efficiency with direct sunlight PCE_d by multiplying the direct SMARTS2 solar spectrum $E_{AM1.5D}(\lambda)$ [51] by the $SOE_j(\lambda)$ and the $SCE_j(\lambda)$ for the jth PSC, integrating over all wavelengths, and summing the contribution from each solar cell [14]:

$$PCE_d = \sum_j \frac{\int E_{AM1.5D}(\lambda) \cdot SOE_j(\lambda) \cdot SCE_j(\lambda) \cdot \mathrm{d}\lambda}{\int E_{AM1.5D}(\lambda) \cdot d\lambda} \tag{2.7}$$

The power conversion efficiency for direct sunlight for the example above is 26.3%. However, one important factor that is not included in this result is the effect of diffuse sunlight. Diffuse sunlight is light that is scattered from the atmosphere and is assumed to be uniformly scattered over 2π steradians. The spectrum of the diffuse sunlight is blue-shifted and is assumed to be equal to the ASTM standard diffuse spectrum $E_{AM1.5F}(\lambda)$ [51]. The direct, diffuse, and global solar spectra are plotted in Fig. 2.18.

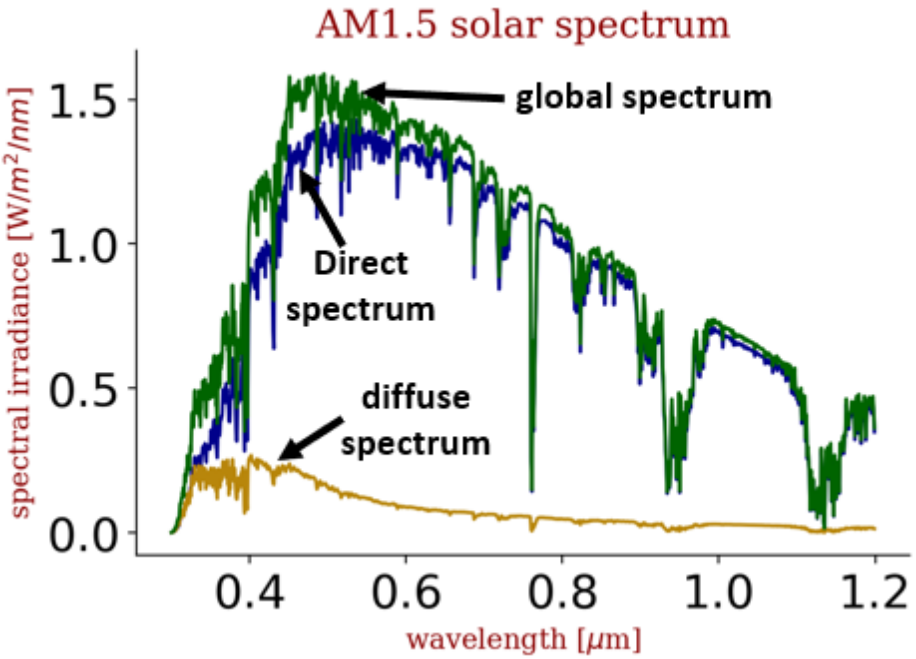

Figure 2.18: Plot of the AM1.5 standard solar spectrum. The green line shows the global spectrum. The global spectrum is a weighted sum of the direct and diffuse spectra.

The different spectral and angular characteristics of diffuse sunlight also result in a different spectral optical efficiency function $SOE_{F,j}(\lambda)$ since the diffraction of a volume hologram is sensitive to the wavelength and angle of incidence. However, it is shown here that the spectral optical efficiency for diffuse sunlight can be estimated as the ratio of the width of the j^{th} PV cell W_j divided by the total unit cell width W_u:

$$SOE_{F,j}(\lambda) = \frac{W_j}{W_u} \tag{2.8}$$

The reason this approximation can be made is explained based on the symmetry of a transmission volume hologram as a function of the angle of incidence. A volume hologram has two "Bragg angles" which diffract light into the m = +1 and the m = -1 orders. The angular diffraction efficiency profiles of the two Bragg angles are centered about the slant angle of the fringes. Light incident at one of Bragg angles is diffracted in the direction of the other Bragg angle

and vice versa. In section 2.3 the volume holographic optical element is designed so that one of the two Bragg angles diffracts normally incident sunlight towards the optimal solar cell. Therefore, a second Bragg angle exists off-axis that diffracts light away from the optimal solar cells. For a Lambertian source, the m = +1 and m = -1 orders effectively cancel out and there is little net change in the angular intensity distribution of diffuse sunlight as it propagates through the hologram. The spatial distribution of the diffuse spectrum on the surface of the solar cells is therefore uniform and does not depend on the wavelength. Therefore, the $SOE_{F,j}(\lambda)$ for a given PV cell is only dependent on the fraction of the total surface area that it covers in the unit cell aperture (Eq. 2.8).

This can also be explained by computing the power conversion efficiency for in-plane incidence angles ranging from -90 degrees to +90 degrees (Fig. 2.19). For incidence angles within the angular bandwidth of the system (~ +/-10^o) the power conversion efficiency is greater than the average efficiency of the PV cells (gray line). However, for angular bands ranging between -40^o and -10^o and between 10^o and 40^o the power conversion efficiency is actually lower than the average efficiency of the two cells. This corresponds to the second, off-axis Bragg angle of the holograms which diffracts light away from the optimal solar cells, resulting in an "inverse" spectrum splitting. The average power conversion efficiency over the entire range of angles is 20.4%. In comparison the average efficiency of the two cells (20.4% and 19.8%) is 20.1%. In this case, the power conversion efficiency of the system averaged over a full 180 degree range is close to the weighted average of the individual solar cell efficiency. This property is also verified for other cell combinations. Since simulating the system for angles ranging from -90 degrees to 90 degrees is time consuming, the spectral optical efficiency for diffuse sunlight is calculated using Eq. 2.8.

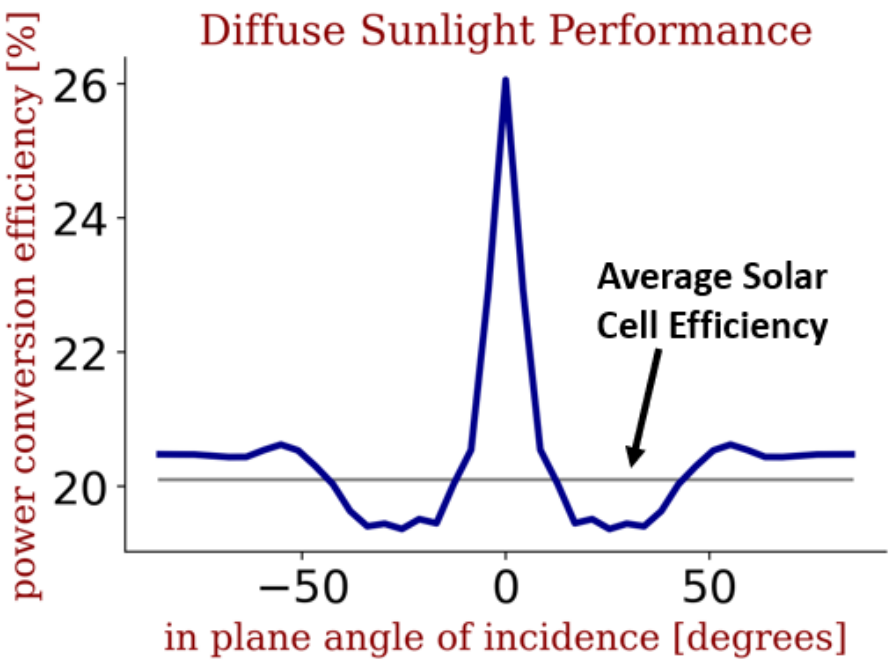

Figure 2.19: Power conversion efficiency calculated for in-plane incidence angles ranging from -90 degrees to +90 degrees. The system has high conversion efficiency for incidence angles near normal incidence but has lower conversion efficiency for angles between -40° and -10° and between 10° and 40°.

After determining the $SOE_{F,j}(\lambda)$ for each cell using Eq. 2.8, the power conversion efficiency for diffuse sunlight (PCE_F) can be calculated:

$$PCE_F = \sum_j \frac{\int E_{AM1.5F}(\lambda) \cdot SOE_{F,j}(\lambda) \cdot SCE_j(\lambda) \cdot \mathrm{d}\lambda}{\int E_{AM1.5F}(\lambda) \cdot d\lambda} \tag{2.9}$$

Using Eq. 2.9 the PCE_F for the perovskite example is calculated to be 23.6%. This value is greater than the diffuse power conversion efficiency calculated in the previous discussion since the system is simulated using a diffuse solar spectrum instead a direct solar spectrum. The diffuse solar spectrum is blue-shifted and nearly all of the incident spectrum is at wavelengths within the spectral response range of the PV cells. Therefore, the power conversion efficiency for diffuse

sunlight is typically higher than the power conversion efficiency computed for direct sunlight because of the blue shift of the spectrum.

According to the ASTM standard [51], the total power in the direct solar spectrum is equal to 90% of the total power in the global solar spectrum and the total power in the diffuse solar spectrum is equal to 10% of the total power in the global solar spectrum (Fig. 2.18). For this reason the total power conversion efficiency is calculated as the weighted sum of the direct and diffuse power conversion efficiencies:

$$PCE = 0.90 \cdot PCE_d + 0.10 \cdot PCE_F \tag{2.10}$$

The ASTM standard is used in Chapters 2 through 4 of this dissertation since it is the most prevalent metric for comparing photovoltaic cells and modules. However, the ratio of diffuse sunlight is greater in realistic illumination conditions (15% to 40%) due to cloud coverage and other atmospheric effects [71]. The effect of more realistic illumination conditions is analyzed using the energy yield metric in Chapter 5. Using Eq. 2.10, the overall power conversion efficiency for the combination of two perovskite cells is calculated to be 26.1%.

2.5 Hologram Optimization

One of the important parameters in optimizing the power conversion efficiency (PCE) of a spectrum splitting system is the holographic film thickness ‘d’. In literature the holographic film thickness is selected to limit higher order diffraction based on the “Q-parameter” [48], [49], [55]. The Q-parameter describes the combination of grating parameters in which an approximate coupled wave model is accurate and there is not significant diffraction in higher orders. This design approach is used since higher order diffraction reduces the conversion efficiency of a spectrum splitting system. However, the spectral bandwidth is also determined by the holographic film

thickness and affects the power conversion efficiency. By selecting the film thickness based on the Q-parameter, the spectral bandwidth is also limited and may in turn limit the power conversion efficiency. For this reason, the Q-parameter is not considered in this optimization. Instead, the power conversion efficiency is used as a merit function for selecting the film thickness.

In addition to the benefit of increased power conversion efficiency, the algorithm described in this section can be automated. This allows for an additional design analysis to be performed in the next section that is time consuming when manually selecting film thickness and index modulation values. In that analysis, the effect of the system geometrical parameters on the power conversion efficiency is determined. However, the optimal film thickness also varies significantly as a function of the system geometrical parameters. In order to determine the optimal power conversion efficiency as a function of the system geometrical parameters, the holographic film thickness is treated as an intermediate parameter that is automatically selected before calculating the power conversion efficiency.

In the film thickness optimization, the power conversion efficiency is calculated using the methods in section 2.4 for holographic film thicknesses ranging between 1μm and 30μm. For each holographic film thickness, the index modulation value is selected that gives the highest diffraction efficiency. The index modulation is selected within a range between 0.01 to 0.1. The combination of film thickness and index modulation values that give the highest power conversion efficiency are selected as the optimal parameter values.

The film thickness of each volume holographic lens (‘1’, ‘2’, ‘3’, and ‘4’) is assumed to be different and the optimization for each is performed separately. This improves the power conversion efficiency since each VHL has a different optimal film thickness. This assumption is

also compatible with manufacturing methods used in industry. For example, Prism Solar manufactured volume holograms on narrow strips of film before inserting them in a photovoltaic module [45], [46].

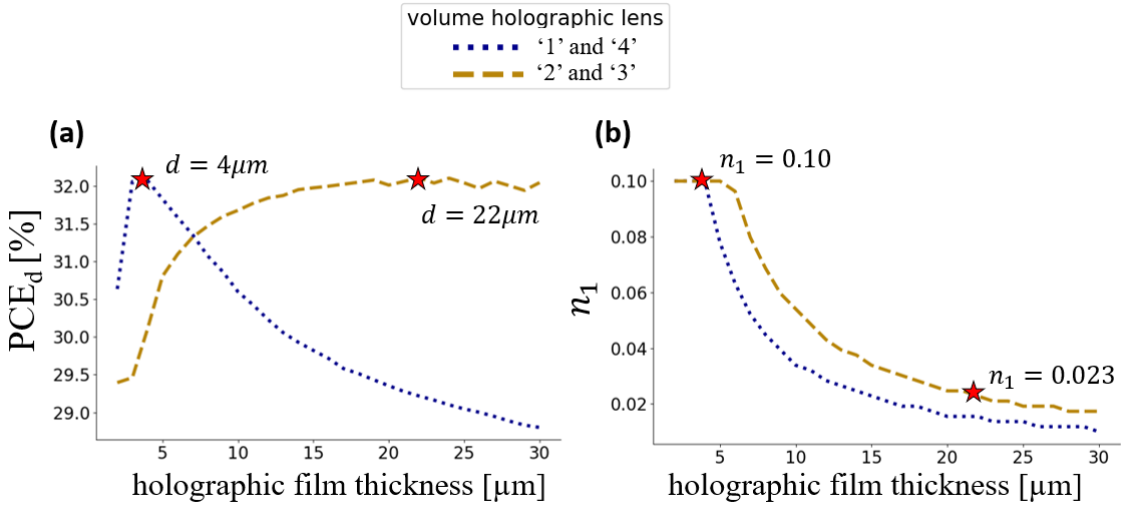

Figure 2.20: Plots showing the effect of the volume holographic lens array parameters on the conversion efficiency for spectrum splitting between a 28.8% efficient GaAs cell and a 22.5% efficient silicon cell. The dotted blue lines correspond to VHLs with indices '1' and '4' and the dashed yellow lines correspond to VHLs with indices '2' and '3'. (a) Plot of the power conversion efficiency for direct sunlight (PCE_d) as a function of the holographic film thickness 'd'. (b) Plot of the index modulation values that give the highest diffraction efficiency for each of the film thickness values.

The results of an optimization for a combination of 28.8% efficient GaAs and 22.5% efficient silicon solar cells is shown in Fig. 2.20. In Fig. 2.20a the power conversion efficiency for direct sunlight is shown as a function of the holographic film thickness 'd'. The optimal film thickness values are determined to be 4µm for VHLs '1' and '4' and 22µm for VHLs '2' and '3'. The index modulation value n_1 that has the highest diffraction efficiency is plotted as a function of holographic film thickness in Fig. 2.20b. The index modulation value for VHLs '1' and '4' is 0.1 and the index modulation value for VHLs '2' and '3' is 0.023.

This procedure can be automated by selecting the film thickness value and index modulation value that give the highest power conversion efficiency. This procedure is used in the next section for different geometrical layouts before computing the power conversion efficiency.

2.6 System Geometrical Parameters

Another important aspect of the spectrum splitting system design is the effect of the system geometrical parameters on the achievable power conversion efficiency. The dimensions of the unit cell are defined by the width of the PV cells W_I and W_{II} and the distance t between the hologram and PV cells (Fig. 2.3). Each of these parameters affect the design of the volume holographic lenses and therefore also affect the dispersion, spectral bandwidth, and uniformity of the diffraction. As a result, the power conversion efficiency should be optimized as a function of the unit cell geometry. In the following analysis the dimensions of the unit cell layout (Fig. 2.3) are parametrized. The first parameter is the concentration ratio (CR) and is defined as the ratio of the width of the unit cell $W_I + W_{II}$ divided by the width of wide-bandgap cell W_I:

$$CR = \frac{W_I + W_{II}}{W_I} \tag{2.11}$$

The second parameter is the front aspect ratio (FAR) and is defined as the distance t between the holograms and the PV cells divided by the width of the unit cell:

$$FAR = \frac{t}{W_I + W_{II}} \tag{2.12}$$

The concentration ratio and front aspect ratio are important parameters since they impact the power conversion efficiency as well as the cost, size, and weight of the system. In some spectrum splitting systems the wide-bandgap PV cells are assumed to be made from III-V materials since

these cells have been demonstrated with high conversion efficiency and are manufactured commercially. Unfortunately, III-V cells are expensive compared to silicon cells and in some cases it is desired to minimize the usage of these cells. For this reason, it is worthwhile analyzing the tradeoffs between the conversion efficiency and the concentration ratio. Similarly, the front aspect ratio affects the thickness of the glass or plastic material layer between the hologram and the PV cells. A thinner glass slab is more desirable for reducing the weight and bulkiness of the system but can come at the cost of reducing the conversion efficiency.

The power conversion efficiency for two different cell combinations is simulated as a function of the concentration ratio and the front aspect ratio in Fig. 2.21. The first cell combination consists of a silicon cell with a conversion efficiency of 22.5% and a GaAs cell with a conversion efficiency of 28.8%. In the second cell combination the GaAs cell is replaced with a hypothetical 1.8eV MgCdTe cell with a conversion efficiency of 21.1% [72]. For each point that is plotted on the figure the volume holographic lenses are designed, simulated, and optimized using the techniques discussed previously. Since some of the geometrical layouts have much higher diffraction angles than typically considered, RSOFT is used for simulating both the TE and TM modes of the hologram. For the GaAs/silicon cell combination, the maximum power conversion efficiency is 31.4% for an ideal concentration ratio of 1.55. For this value of the concentration ratio, the GaAs cell covers 60% of the module. However, it can also be seen that for a concentration ratio of 4, the power conversion efficiency still exceeds 30% even though the surface coverage of the GaAs cell is reduced to 25%. Even when the surface coverage of the GaAs cell is reduced to just 10%, the power conversion efficiency (26.6%) of the system is still significantly greater than the conversion efficiency of the silicon cell individually (22.5%). Based on this analysis the higher cost of a wide-bandgap cell may be able to be partially compensated by increasing the concentration ratio. For

the range of concentration ratio values considered (<10X), the effect of heat on the conversion efficiency is minimal and is not considered [73].

The power conversion efficiency also varies significantly as a function of the front aspect ratio. For the GaAs/silicon cell combination the power conversion efficiency is maximized for a front aspect ratio ranging between 0.75 and 1.5. For each value of the concentration ratio that is simulated the front aspect ratio increases starting from the minimum value (0.25) until it begins to plateau at a value between 0.5 and 0.75. In many cases a thinner system is more desirable to reduce weight and glass material costs. Although a front aspect ratio of 1.0 has the highest conversion efficiency in this simulation (31.4%), a front aspect ratio of 0.5 simultaneously provides high conversion efficiency (30.3%) and a thinner module form factor.

Another factor that affects the optimal concentration ratio and the front aspect ratio is the specific PV cell combination used. As can be seen in Figures 2.21c,d the results for the MgCdTe/silicon cell combination are different than the results for the GaAs/silicon combination. One of the most notable differences is the optimal concentration ratio which is much higher (3.5 for MgCdTe/Si) compared to the GaAs/silicon cell combination (1.55). This difference is believed to be a result of the differing bandgap energy and efficiency of the MgCdTe and GaAs cells. Since the GaAs cell has a narrower bandgap energy than the MgCdTe cell (1.4eV compared to 1.8eV) and a much higher efficiency (28.8% compared to 21.1%), the optimal unit cell layout for the GaAs/silicon cell combination favors greater surface coverage of the GaAs cell. However, the converse is true in the MgCdTe/silicon design and favors greater surface coverage of the silicon cell.

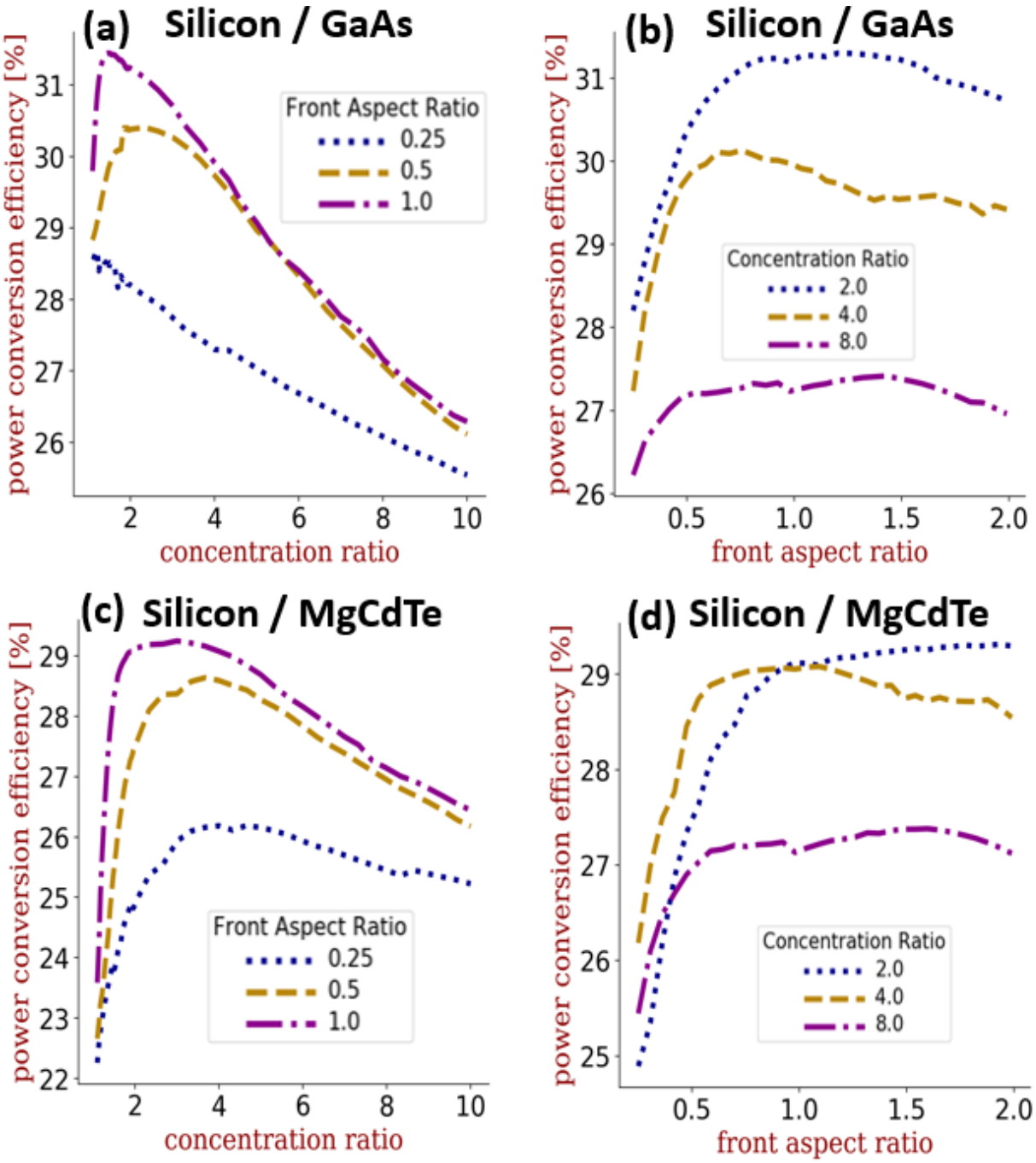

Figure 2.21: Power conversion efficiency (PCE) as a function of different system geometric parameters for two different PV cell combinations. (a) concentration ratio, GaAs and silicon (b) front aspect ratio, GaAs and silicon, (c) concentration ratio, MgCdTe and silicon, (d) front aspect ratio, MgCdTe and silicon.

2.7 Loss Analysis

Another aspect of the spectrum splitting system analysis is quantifying the different optical losses that reduce the power conversion efficiency. With a perfect optical filter all light is directed to the solar cell that has the optimal spectral response. However, in actual designs some light diffracted in the main diffraction order (m = -1 or m = +1 depending on the direction of diffraction) is dispersed across a PV cell boundary onto a non-optimal PV cell. These losses are categorized as a "dispersion losses". Another optical loss occurs when light that is designed to be diffracted is instead transmitted through the hologram without diffraction (m = 0) and is incident on a non-optimal cell. This loss is categorized as "low diffraction efficiency loss" and occurs for two reasons. The first reason is because of the non-ideal spectral diffraction efficiency profile of a volume hologram (Fig. 2.16) and the second reason is the spatially varying diffraction efficiency of a volume holographic lens (Fig. 2.15). The last kind of optical loss occurs when light diffracted in a higher order (m = +/-2, +/-3, +1 or -1) reaches a non-optimal solar cell. This loss is categorized as "higher order diffraction loss". Other loss mechanisms include reflections and absorption and are briefly discussed after the analysis. In the following example, a loss analysis is performed for a spectrum splitting system with a 1.25eV perovskite cell and a 1.72eV perovskite cell.

Each of the loss mechanisms are analyzed after the raytrace simulation by sorting rays according to their wavelength, position, and diffraction order. First, the spatial distribution of light on the PV cells from all the diffraction orders combined is obtained by sorting the rays into two different spectral bands. For the solar cells in this example the spectral bands range between 0.3μm to 0.705μm and from 0.705μm to 0.99μm. The spatial distribution of light within each spectral band is plotted in Fig. 2.22a. Sharp transitions between spectral bands are observed on the edges

of the PV cells and exemplify the effectiveness of the design procedures described in previous sections.

Next, an additional filter is used to sort rays based on the diffraction order. Light from the primary diffraction order (m = -1 or m = +1) is plotted in Fig. 2.22b. Clear transitions between spectral bands are observed at the edges between PV cells ‘I’ and ‘II’ and nearly all of the light reaches the intended PV cell. For this reason the dispersion losses are almost negligible for two-bandgap VHL spectrum splitting systems. Next, the light that is transmitted without diffraction (m = 0) is plotted in Fig. 2.22c. Most of this light reaches the optimal PV cell. However, some of the light that is ideally diffracted to another cell is instead transmitted to the underlying cell. Lastly, the spatial distribution of light diffracted into higher orders (m = +/-2, +/-3, +1 or -1) is plotted in Fig. 2.22d. A significant amount of light is diffracted in higher orders and does not reach the intended PV cells.

The relative contribution of each type of loss is calculated by integrating the flux located outside of the intended PV cells for each diffraction order. Each type of loss is displayed as a fraction of the total loss in the pie chart in Fig. 2.22e. The greatest loss is low diffraction efficiency (50.2%), followed by higher orders (45.4%), and dispersion (4.3%). Each type of loss is a function of the VHL parameters and cannot individually be isolated and corrected. For example, higher order diffraction can be reduced by increasing the thickness of the holographic film. However, this will also narrow the bandwidth and increase the losses due to low diffraction efficiency.

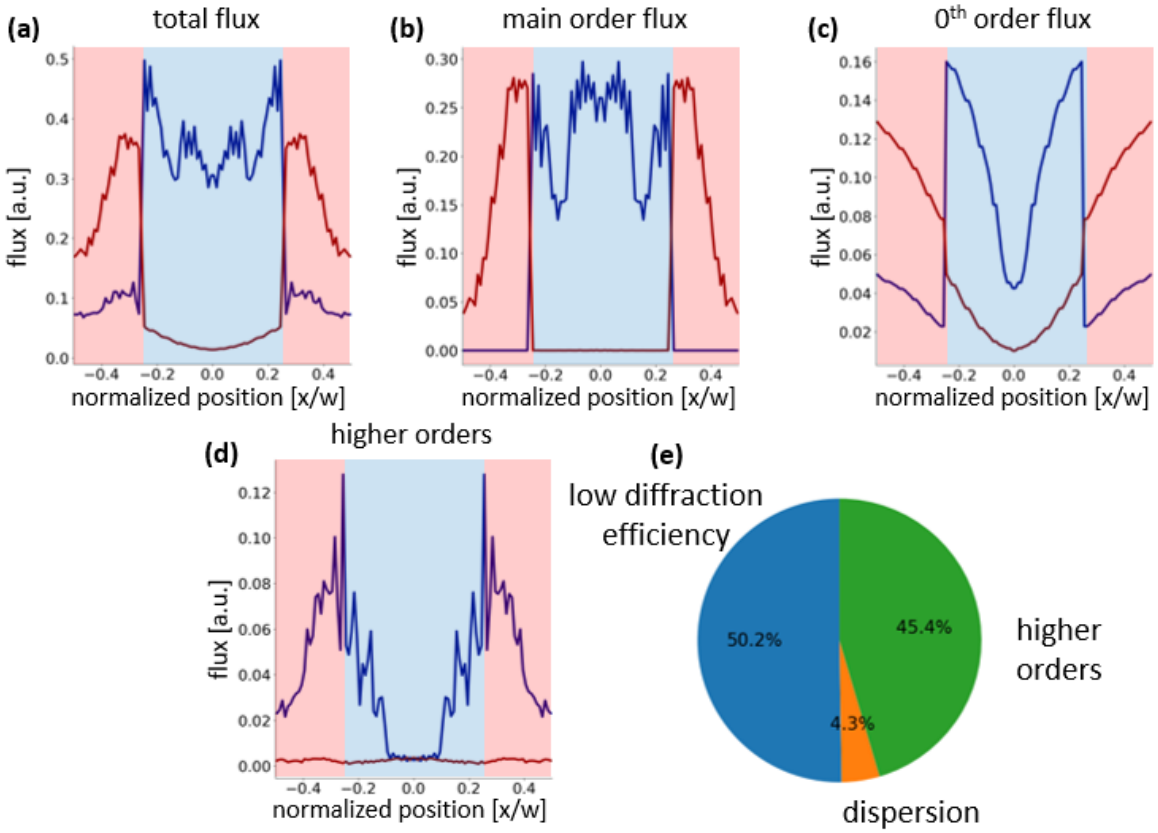

Figure 2.22: Plots showing the spatial distribution of light within two spectral bands 'I' and 'II' (blue lines, I: 0.30µm to 0.705µm and red lines: II: 0.705µm to 0.99µm) on the surface of the PV cells. The horizontal axis is the position along the unit cell aperture normalized to the width of the unit cell. The ray flux contained in each analysis bin is plotted in the vertical axis. There are 100 analysis bins across the unit cell, 100 ray starting positions and 50 wavelengths spanning 0.3um to 1.2um. The initial flux of each ray is 1/100 so that the total integrated flux for a given wavelength is equal to 1. The color of the background indicates the position of PV cells 'I' and 'II'. (a) all diffraction orders, (b) main diffraction order (m = +1 or -1 depending on direction of diffraction), (c) directly transmitted order (m = 0), (d) higher diffraction orders (m = +/-2, +/-3,1 or -1), (e) optical losses contributed from each diffraction order.

In addition to the loss mechanisms described above, reflections also reduce the conversion efficiency of the module. Reflections occur at the interface between the PV cell and the glass slab and between the glass slab and the atmosphere. The reflection between the PV cell and the glass slab is controlled within 1% to 3% using antireflection coatings and surface texturing [74]–[76]. The effect of this reflection is already accounted for in the experimental PV cell data and doesn't reduce the conversion efficiency beyond what is reported here. However, the reflection between

the glass slab and the atmosphere is not accounted for in the experimental PV cell data and significantly reduces the conversion efficiency. An uncoated glass surface with an index of refraction of 1.5 has a reflection of 4% while the reflection of anti-reflective solar glass such as Pilkington Sunplus is as low as 3% [77]. As an example, for a module calculated to have a power conversion efficiency of 30.0% without reflections, the efficiency is reduced to 29.1% for a glass-air reflection of 3%. This reflection is not specific to spectrum-splitting systems and is one of the reasons that the highest recorded conversion efficiency of a silicon solar module is only 24.4% despite the individual cell efficiency being much higher (26.7%) [21].

Another factor that has potential to reduce the power conversion efficiency is absorption and scattering in the holographic recording material. The transparency of the dichromated gelatin recording material is very high (98% in laboratory measurements for 20μm film between 400nm and 900nm) but more detailed studies should be conducted to optimize the scattering in DCG film and determine the exact effect on the conversion efficiency of the module.

In addition to analyzing the sources of optical losses it is also important to quantify the overall effect of the optical losses on the system conversion efficiency. In this dissertation a metric known as the spectrum splitting efficiency (SSE) is used [78]. The SSE is the ratio of the power conversion efficiency for a system with actual optical filters PCE_a divided by the power conversion efficiency for a system with ideal optical filters PCE_i

$$SSE = \frac{PCE_a}{PCE_i}, \tag{2.13}$$

where an ideal optical filter is assumed to direct all light in a given spectral band to the optimal PV cell and an actual optical filter is the simulated or experimental filter. A system with an SSE of one reaches the maximum possible conversion efficiency for a given cell combination. These

maximum values are listed in Table 2.1 for a variety of experimental and ideal cell combinations. A lower SSE value means that the optics are not ideal and the system only attains a fraction of the maximum power conversion efficiency possible for a given cell combination. The SSE value can therefore be interpreted as a weighted optical efficiency measuring the ability of the optical system to reach the maximum conversion efficiency for a given cell combination. The maximum possible conversion efficiency for the cell combination in the example above is 28.9% (Table 2.1) and the conversion efficiency with the simulated VHLs is 26.1%. Therefore, the SSE is 90.0%.

2.8 Comparison of Cell Combinations

Due to the recent development of perovskite photovoltaic cells, a variety of cell combinations are possible for use in spectrum-splitting photovoltaic systems. In this section several different cell combinations are simulated and compared. The simulated cell combinations are listed in Table 2.1. The VHL array is designed with the techniques described in Section 2.3 and simulated with the methods in Section 2.4. The design parameters for each of the volume holographic lens arrays are listed in Appendix B.

The spectral optical efficiency (SOE) for each cell combination is plotted in Fig. 2.23 and the corresponding ideal power conversion efficiency (PCE_i), spectrum splitting efficiency (SSE), and actual power conversion efficiency (PCE_a) are listed in Table 2.2. The silicon and GaInP cell combination has the highest power conversion efficiency (PCE_a = 32.9%) and the silicon and GaAs cell combination has the highest spectrum splitting efficiency (SSE = 92.8%).

The power conversion efficiency of a new PV cell combination can be estimated in a simple way without simulating the diffraction of the hologram if the spectral conversion efficiency of each cell is known. First the maximum power conversion efficiency PCE_i for the combination is

calculated using Eq. 2.2. Next the PCE_i is multiplied by the average of the SSE values listed in Table 2.2 (90.2%). This method can be used since the variation in SSE values is relatively low. The minimum value for these cell combinations is 88.2% and the maximum value is 92.8%.

$$PCE = PCE_i \cdot 0.902, \tag{2.14}$$

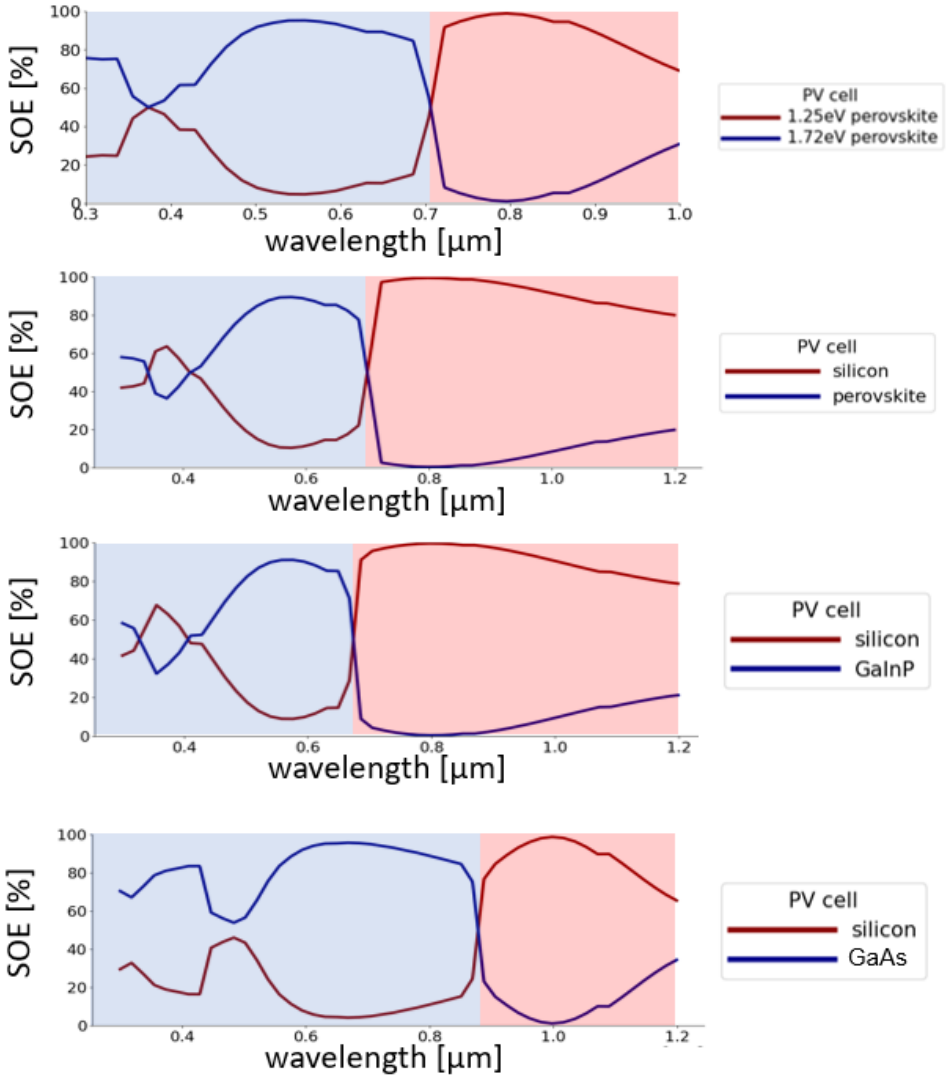

Figure 2.23: Spectral optical efficiency (SOE) for four different photovoltaic cell combinations. The color of the background indicates the optimal spectral bands for each PV cell (a) 1.25eV and 1.72eV perovskite cells. (b) 1.1eV silicon and 1.72eV perovskite cells. (c) 1.1eV silicon and 1.84eV GaInP cells, (d) 1.1eV and 1.41eV GaAs cells.

Table 2.2: Table of performance metrics for different PV cell combinations. The power conversion efficiency with ideal optical filters (PCE_i), spectrum splitting efficiency (SSE), and actual power conversion efficiency (PCE_a) are listed.

Cell combination	PCE_i	SSE	PCE_a
Perovskite 1.25eV & Perovskite 1.72eV	28.9%	90.0%	26.1%
Silicon 1.1eV & perovskite 1.72eV	33.4%	89.8%	30.0%
Silicon 1.1eV & GaInP 1.84eV	37.3%	88.2%	32.9%
Silicon 1.1eV & GaAs 1.41eV	34.8%	92.8%	32.3%

2.9 Conclusion

In this chapter, the detailed design, simulation, optimization, and analysis of a two-junction spectrum-splitting photovoltaic system using volume holographic lens arrays is presented. One of the strengths of this design procedure is that each step can be automated and evaluated over a wide range of parameters. This allows for a variety of design tradeoffs to be considered. For example, the effect of the concentration ratio and the front aspect ratio on the power conversion efficiency is analyzed. This analysis may be used to help reduce the thickness of the front glass slab and reduce the surface area of more expensive PV cells. The design procedure also allows a variety of cell combinations to be simulated and compared. It is found that a combination of 1.25eV perovskite and 1.72eV perovskite cells has potential for reaching a conversion efficiency of 26.1% and a combination of 1.1eV silicon and 1.84eV GaInP cells has a potential for reaching a conversion efficiency of 32.9%. On average, the conversion efficiency of the two-bandgap spectrum-splitting system with simulated volume holograms reaches 90.2% of the maximum possible conversion efficiency with perfect optical filters.

Chapter 3

Spectrum Splitting in Three Spectral Bands

In this chapter, the design techniques that are described in Chapter 2 are extended for lateral spectrum splitting photovoltaic systems with three cells that have different energy bandgaps. One of the main developments is a cascaded volume holographic lens array designed to minimize "cross-coupling" or light that is diffracted by an upper layer hologram and subsequently diffracted by a lower hologram in the stack of holograms. A diffraction model is developed for calculating the cross-coupling between all diffraction orders including the higher orders. The photovoltaic system has potential for higher conversion efficiency than the two-bandgap design in Chapter 2 and provides a foundation for spectrum-splitting systems with four or more energy bandgaps in Chapter 4.

3.1 Introduction

As discussed in previous chapters of this dissertation, a new class of PV cell has recently been developed based on perovskite materials [18]. Perovskite solar cells (PSCs) have been demonstrated with bandgap energies ranging between 1.25eV to 2.3eV [23]–[27] making them candidates for use in lateral spectrum splitting photovoltaic systems. In addition to a variety of energy bandgaps, PSCs are inexpensive [22] and have conversion efficiencies up to 25.2% [20].

PSCs are typically implemented in a vertically stacked cell arrangement as depicted in Fig. 3.1. The top cell converts the shorter wavelength light and transmits the longer wavelength light to the underlying cells. A tandem module using the vertically stacked cell arrangement was recently demonstrated with a conversion efficiency of 24.2% using 1.22eV and 1.77eV perovskite subcells [21], [79].

One of the reasons that PSCs have been designed in vertically stacked cell arrangements is simplicity [36]. However, there are advantages of a lateral spectrum splitting arrangement. When compared with a tandem cell arrangement one of the benefits of lateral spectrum splitting is reduced parasitic absorption. In a tandem arrangement each PSC is designed to transmit light with energy less than the bandgap to the underlying cells. This constraint requires cells to be "semi-transparent" which limits the design of the electrical contact [40]. For example, many PV cells use reflective metal materials, but this approach cannot be used in semi-transparent cells. Instead, transparent conductive oxides (TCOs) are used in perovskite cells since they are both conductive and transparent. One downside to using this material is that PSCs only transmit 80% to 90% of the light below the bandgap energy [23], [36]–[40]. Most of the remaining light is parasitically absorbed in the TCO. A lateral spectrum splitting system avoids this problem since light is directly sent to each cell without transmitting through multiple TCO layers.

A second advantage of a lateral spectrum splitting configuration is fewer constraints on the solar cell design. In a vertically stacked cell arrangement, several aspects of the top cell design affect the transmission of light and the spectrum received by the bottom cell [40]. Some of these factors include the electrodes, antireflections coatings, rear reflector, and absorber thickness. The requirement for the cell to be "semi-transparent" therefore limits the design of the top cells. In a lateral spectrum splitting arrangement, each PSC can be independently designed and optimized for

conversion efficiency without considering the transmitted spectrum. For example, as mentioned previously semi-transparent perovskite cells do not use reflective metal materials in the electrical contact. However, the use of these materials increases electrical conductivity and the absorption of sunlight and can be used in a lateral spectrum splitting system. The TCO material selection also has fewer design constraints in a lateral spectrum-splitting system. TCO materials with parasitic absorption at infrared wavelengths reduce light transmitted to lower cells in the stack making the system less efficient [39], [80]. However, this is not a problem for lateral spectrum-splitting systems. Another example is the antireflection coating which can be optimized for individual spectral bands in lateral spectrum splitting systems without the need to cover the entire spectrum as is required for stacked cell arrangements.

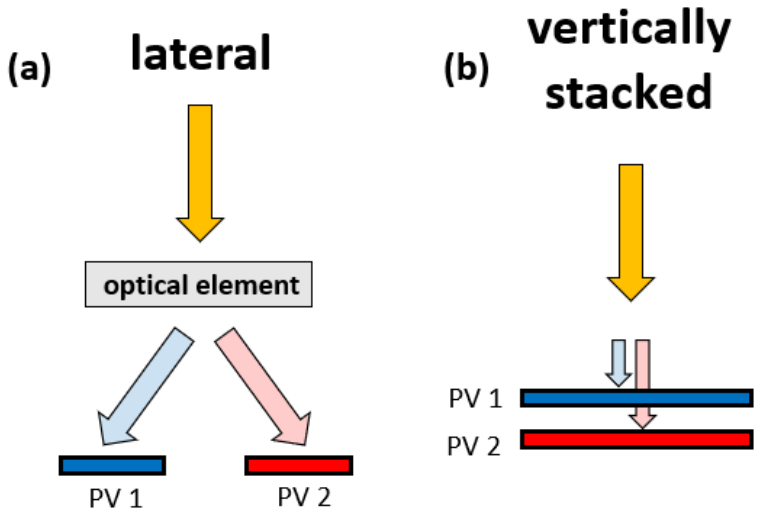

Figure 3.1: Illustration of two different cell arrangements for multiple bandgap photovoltaic systems (a) lateral spectrum splitting, (b) vertically stacked tandem.

Another advantage of the lateral spectrum splitting approach is that the overall usage of PV cell material is lower. In a vertically stacked cell arrangement, the surface area of each subcell covers the entire aperture of the module. The total PV cell surface area is therefore equal to the number of subcells times the aperture of the module. In a lateral spectrum splitting system, the

total PV cell usage is equal to or less than the aperture area of the module. Therefore, the PV cell material usage can be reduced by a factor equal to the number of subcells, yielding potential cost savings.

Despite the potential advantages of lateral spectrum splitting systems it remains a challenge to design systems with more than two energy bandgaps. Although a variety of two-junction spectrum splitting designs have been proposed [15], [44], [47], [49], fewer lateral spectrum splitting designs with three or more bandgaps have been proposed [16], [48], [78]. One of the main reasons for this is a lack of solar cells with the different required energy bandgaps necessary for an effective three-junction module. However, the emergence of PSCs has opened new options in the design of three-junction lateral spectrum splitting systems [19].

In this Chapter, a lateral spectrum splitting system is proposed that uses a cascaded volume holographic lens array (CVHLA) for dividing the solar spectrum between three PV cells. The module consists of an array of unit cells as depicted in Fig. 3.2a. The CVHLA is positioned over an array of rectangular shaped PV cells. The material between the PV cells and the CVHLA is assumed to be glass with an index of 1.5, but can also be PMMA, air, or any other transparent material. The three PSCs (Table 3.1) used in this design example are determined based on the analysis in Section 2.2 and have experimental values taken from the literature. PSC 'I' has a bandgap of 2.3eV and a conversion efficiency of 10.4% [27], PSC 'II' has a bandgap of 1.63eV and a conversion efficiency of 21.6% [25], and PSC 'III" has a bandgap of 1.25eV and a conversion efficiency of 20.4% [23]. Each PSC is assumed to be electrically independent. The spectral conversion efficiency (SCE) of each PSC is shown in Fig. 3.2b. The spectral bands for the three PSCs 'I', 'II', and 'III' are $0.3\mu m<\lambda\leq 0.535\mu m$, $0.535\mu m<\lambda\leq 0.76\mu m$, and $0.76\mu m<\lambda\leq 1.05\mu m$, respectively.

With ideal optical filters this combination of PV cells can reach 31.5% conversion efficiency as indicated in Table 2.1. However, a variety of optical losses in the CVHLA exist that reduce the conversion efficiency from 31.5% to 26.7%. In the rest of this chapter a diffraction model for a cascaded volume holographic lens is developed and then used to analyze the optical losses for this photovoltaic system.

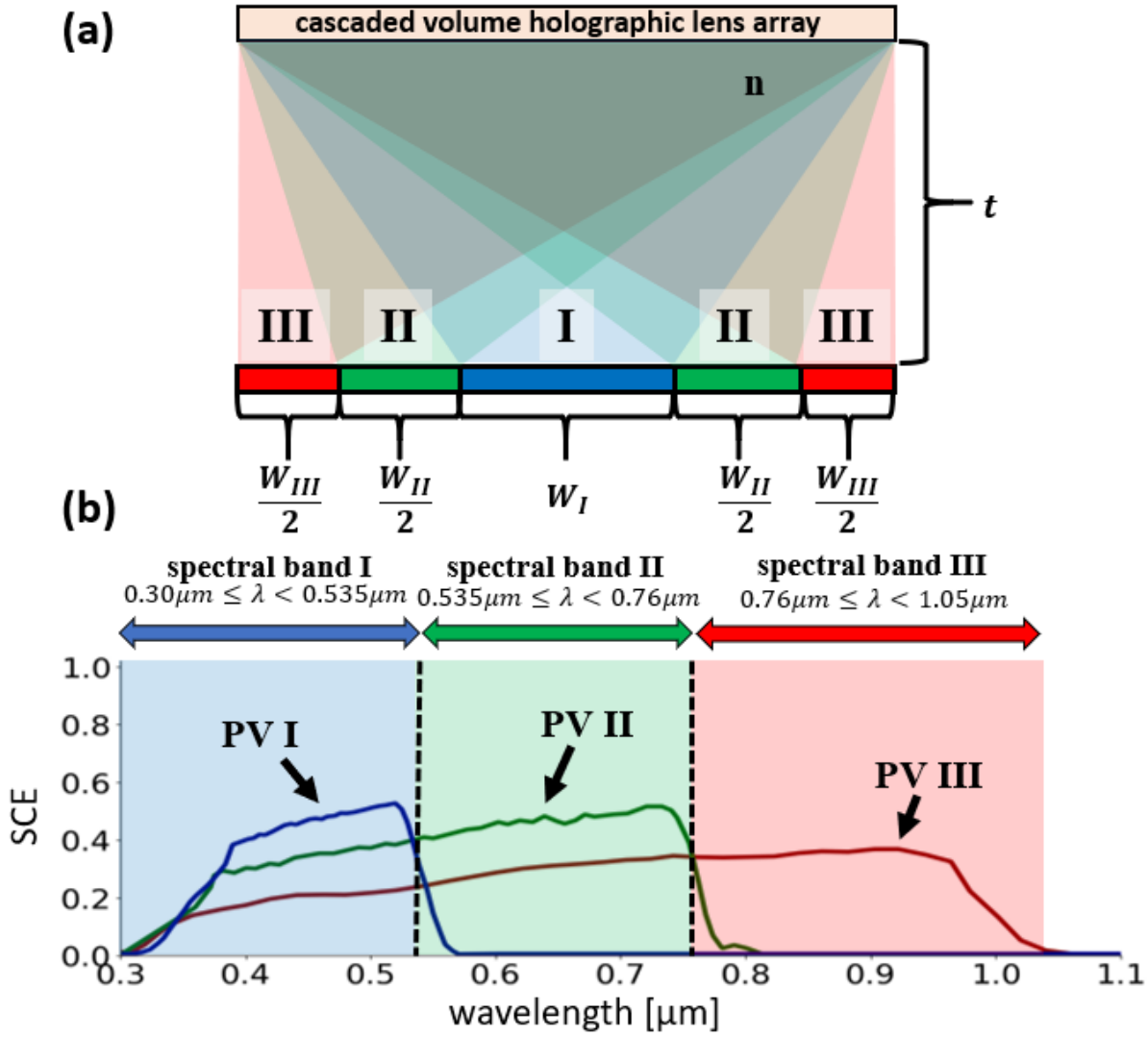

Figure 3.2: (a) Unit cell for a three-bandgap lateral spectrum-splitting system. The spectral separation is attained with cascaded volume holographic lens array (b) Spectral conversion efficiency for the three perovskite solar cells used in the design example.

Table 3.1: List of perovskite PV cells for a three-bandgap spectrum splitting system. The values are pulled from Table 2.1.

Index Number	Perovskite Cell Composition	Bandgap	Spectral Band	Efficiency
I	$CH_3NH_3PbBr_3$ perovskite [27]	2.3eV	$0.3\mu m < \lambda \leq 0.535\mu m$	10.4%
II	rubidium cation perovskite [25]	1.63eV	$0.535\mu m < \lambda \leq 0.76\mu m$	21.6%
III	Sn-Pb perovskite [23]	1.25eV	$0.76\mu m < \lambda \leq 1.05\mu m$	20.4%

3.2 Cascaded Volume Holographic Lens Array

A more detailed illustration of the cascaded volume holographic lens array (CVHLA) is shown in Fig. 3.3. The CVHLA consists of two VHL arrays that are separated by a thin glass substrate. The upper VHL array is denoted as layer 'A' and the lower VHL array is denoted as layer 'B'. The hologram array consists of six different VHLs that each have widths corresponding to the solar cells underneath them. For each cascaded VHL, the hologram in the upper layer is designed to diffract light in one of three spectral bands 'I', 'II', or 'III' to one of the PV cells corresponding to that spectral band (e.g. the VHL diffracts spectral band 'I' to PV cell 'I'). Ideally, all light within that spectral band is diffracted and directed to the intended PV cell. The hologram in the lower layer is then designed to diffract light into one of the other two spectral bands. Light in the third spectral band is matched to the spectral band of the underlying PV cell and is directly transmitted without diffraction.

The design procedures and design parameters for each VHL are similar to those described in Section 2.3. One difference is that instead of a single transition wavelength λ_t, there exist two different transition wavelengths $\lambda_{t,I}$ or $\lambda_{t,II}$ corresponding to the energy bandgaps of the wide-bandgap and mid-bandgap PV cells. The diffracted light comes to a focus at the position $\vec{R}_f$ at the boundary between two adjacent PV cells. Incident solar illumination with wavelengths longer than

the transition wavelength is dispersed across the PV cell with the narrower bandgap and light at shorter wavelengths is dispersed across the PV cell with the wider bandgap. The specific transition wavelength is selected based on the energy bandgaps of the two adjacent PV cells. For example, if the two adjacent cells are PV cells 'I' and 'II', then the transition wavelength $\lambda_{t,I} = 0.535\mu m$ is selected to provide a sharp transition between spectral bands 'I' and 'II'. In the case where the adjacent cells are PV cells 'II' and 'III' the transition wavelength $\lambda_{t,II} = 0.76\mu m$ is selected. In addition to the transition wavelength each VHL also has a Bragg wavelength λ_B. The Bragg wavelength is selected to tune the diffracted spectral band to match the optimal spectral band of the PV cell. For example, a VHL diffracting light towards PV cell 'III' may have a Bragg wavelength of $\lambda_B = 0.85\mu m$ to maximize diffraction efficiency in spectral band 'III' and have a transition wavelength $\lambda_{T,II} = 0.76\mu m$ to provide a sharp spectral cutoff between spectral bands 'II' and 'III'.

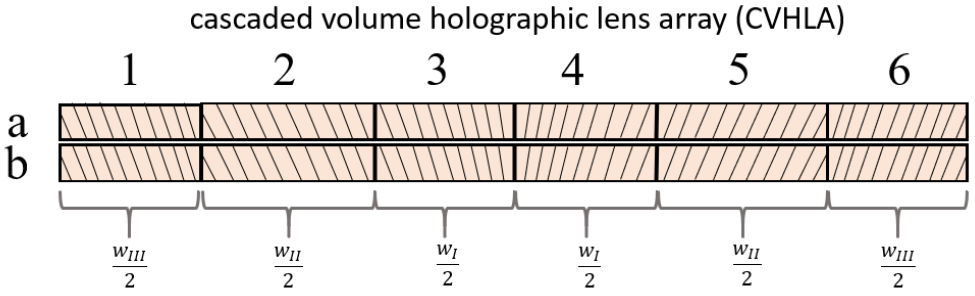

Figure 3.3: Cascaded volume holographic lens array (CVHLA) used in a three-bandgap lateral spectrum-splitting module. The numbers '1' through '6' denote the VHL indices and 'a' and 'b' denote the VHL layer.

Alternative designs are possible with different combinations of the parameters λ_T, $\vec{R}_f$, and λ_B to accomplish lateral spectral separation. The specific combination used in this thesis is determined based on simulation and optimization to minimize optical losses. For cascaded VHLs, Cross-coupling reduces the amount of light diffracted in the main diffraction order and reduces the

conversion efficiency [48], [78], [81]. Cross-coupling is an effect that occurs when light diffracted by the upper VHL array is subsequently diffracted by the lower VHL array. Cross-coupling is mitigated by designing mismatch between the diffracted spectral and angular bands of the upper hologram and the spectral and angular acceptance bands of the lower hologram. The simplest way to separate the diffracted spectral and angular bands is to design the cascaded VHL pair to diffract light in opposite (right/left) directions [45]. This method is used in the CVHLA design to reduce the cross-coupling.

An illustration of the diffracted spectral bands for each VHL and the intended PV cells is shown in Fig. 3.4. In Fig. 3.4a the diffracted spectral bands for VHLs '1' and '6' are shown. These VHLs are located on the edges of the unit cell. Normally incident light from the upper VHL 'unit cell 1, element 6' diffracts light in the green spectral band (II: $0.535\mu m<\lambda\leq 0.76\mu m$) towards the left and the lower VHL 'element 6' diffracts light in the blue spectral band (I: $0.30\mu m<\lambda\leq 0.535\mu m$) towards the right. VHLs '2' and '5' are shown in Fig. 3.4b and unlike other VHLs do not diffract in opposite directions. However, there is still sufficient angular and spectral separation to suppress most of the cross-coupling. Another consideration for these VHLs is the suppression of higher diffraction orders. The upper VHL is selected to diffract light in spectral band 'I' and the lower VHL is selected to diffract light in the red spectral band (III: $0.76\mu m<\lambda\leq 1.05\mu m$). This arrangement suppresses higher order diffraction by reducing the overlap between the transmitted 0^{th} order of the upper VHL and the spectral diffraction range of the 2^{nd} order of the lower VHL. Lastly, VHLs '3' and '4' are shown in Fig. 3.4c and like elements '1' and '6' diffract light in opposite directions to minimize cross-coupling.

An illustration of the transition wavelengths and focus positions for each VHL is shown in Fig. 3.5. The cyan colored light indicates that the VHL has a transition wavelength of $\lambda_{t,I}$ and the

yellow light indicates the VHL has a transition wavelength of $\lambda_{t,II}$. The focus position R_f is located on the diagram where the diffracted light comes to a focus. VHLs '1' and '6' shown in Fig. 3.5a both have a transition wavelength equal to $\lambda_{t,I}$. VHLs '2' and '5' are shown in Fig. 5b. The VHL in the upper layer has a transition wavelength of $\lambda_{t,I}$ and the VHL in the lower layer has a transition wavelength of $\lambda_{t,II}$. VHLs '3' and '4' are shown in Fig. 3.5c. The VHL in the upper layer has a transition wavelength of $\lambda_{t,II}$ and the VHL in the lower layer has a transition wavelength of $\lambda_{t,I}$.

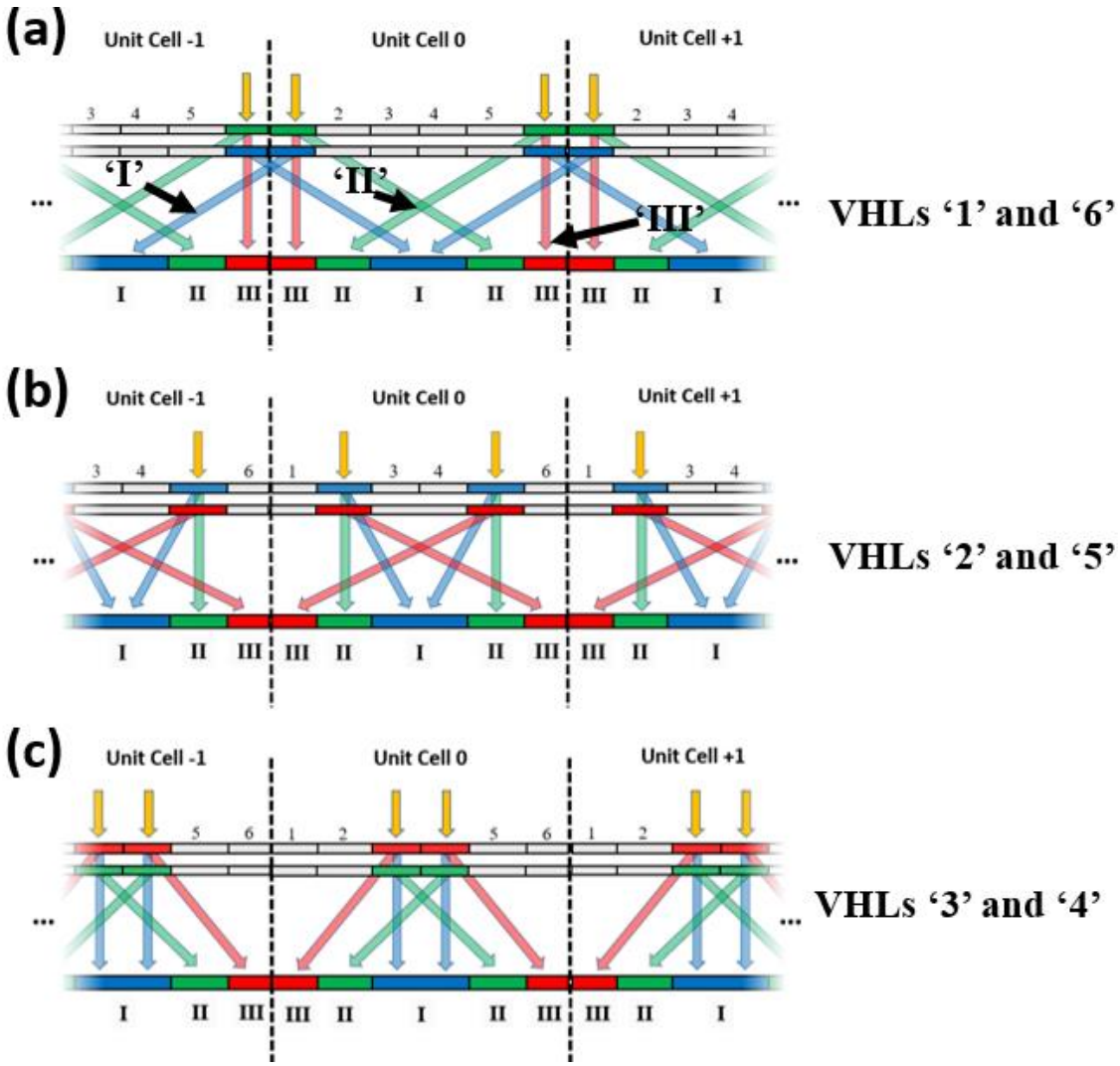

Figure 3.4: Illustration showing the diffracted spectral bands for each VHL and the intended PV cells. Neighboring unit cells are also shown in the diagram. Blue colored arrows indicate spectral band 'I', green colored arrows indicate PV spectral band II, and red colored arrows indicate spectral band III. (a) VHLs '1' and '6' (b) VHLs '2' and '5'. (c) VHLs '3' and '4'.

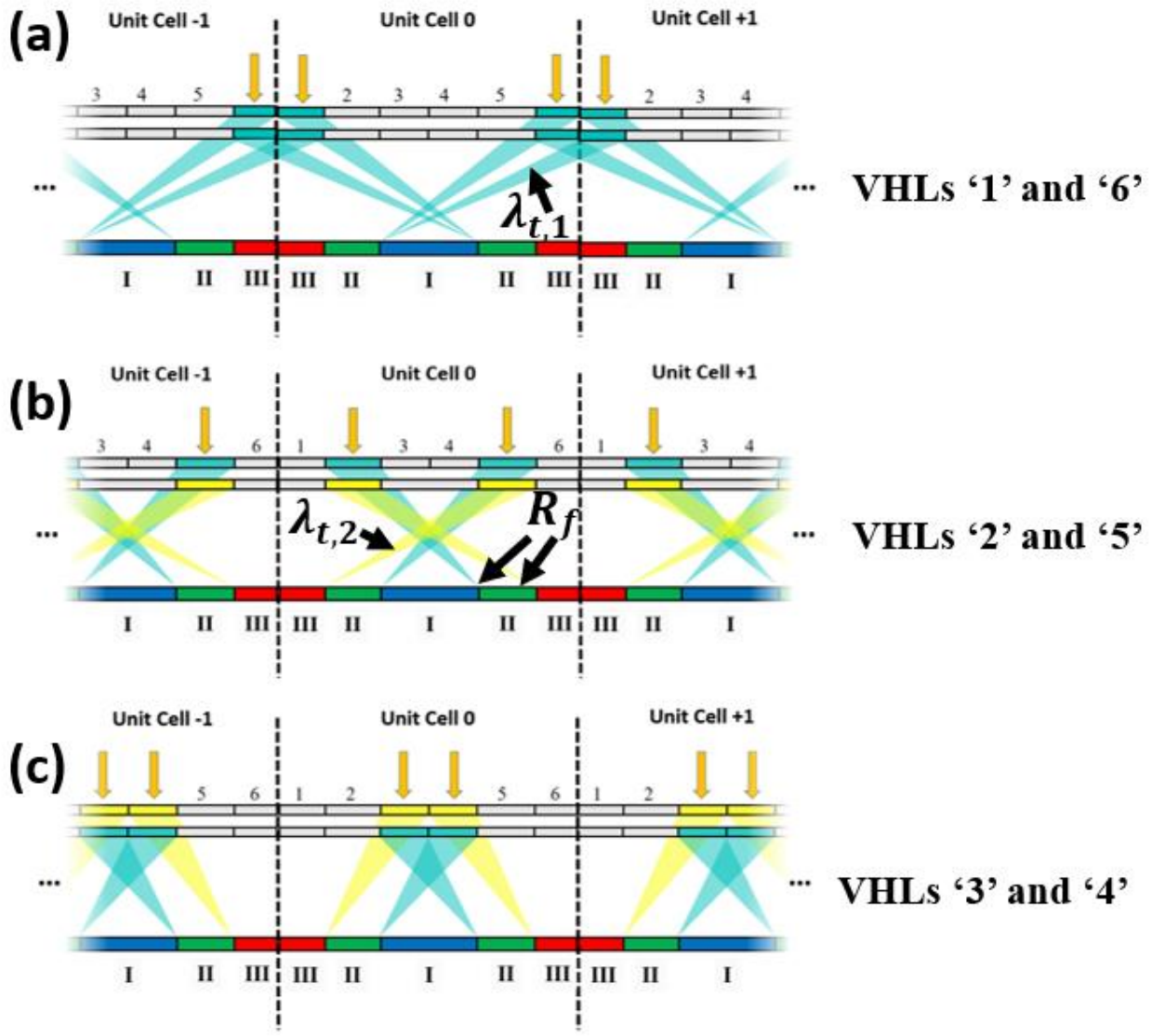

Figure 3.5: Illustration showing the transition wavelength and focus position for each VHL. Neighboring unit cells are also shown. The cyan light indicates the transition wavelength $\lambda_{T,I}$ and the yellow light indicates the transition wavelength $\lambda_{T,II}$. The point that the beam comes to a focus is the focus position $\vec{R}_f$ (a) VHLs '1' and '6' (b) VHLs '2' and '5'. (c) VHLs '3' and '4'.

The parameters λ_t, $\vec{R}_f$, and λ_B are used to determine an optimal pair of point sources $\vec{R}_1$ and $\vec{R}_2$ for constructing the holographic lenses. The method for determining the construction point sources is described in detail in Section 2.3. The holographic film thickness 'd' and index modulation 'n_1' are also selected for maximizing the diffraction efficiency and spectral bandwidth

as described in Section 2.3. The CVHLA parameters for the PSC design example are listed in Appendix B. The design values are selected assuming a separation thickness between the holographic optical element and PV cells of $t = 10mm$ and a total unit cell width of $w_u = 10mm$. The dimensions of the unit cell can be proportionately scaled without changing the power conversion efficiency or the diffraction efficiency analysis in the proceeding sections. To scale the dimensions of the unit cell, the VHL widths, PSC widths, and VHL construction points sources are also scaled but the film thickness and index modulation values do not change from the design values.

3.3 Modeling a Cascaded Volume Holographic Element

Even though the cascaded volume holographic lens array (CVHLA) is designed to mitigate cross-coupling, it cannot be entirely eliminated. For this reason it is important to use a diffraction efficiency model that includes the effect of cross-coupled light. In this section a technique for modeling cascaded volume holographic lenses is developed that extends approaches found in literature in two ways. First, existing models compute the cross-coupling between the +1 and the -1 diffraction orders but not between higher diffraction orders [48], [81]. The effect of higher order diffraction cannot be neglected since, as seen in the loss analysis in Section 2.7, nearly half of the optical losses are due to higher order diffraction. In this section, the cross-coupling between all computed diffraction orders is calculated including the cross-coupling between higher orders. Second, existing models for hologram cross-coupling have been applied to spatially uniform holograms but the model developed in this chapter is applied to spatially varying volume holographic lenses.

The first step in simulating a cascaded volume hologram is to calculate the diffraction efficiency of the upper hologram using the RCWA techniques described in Section 2.4. The diffraction efficiency in the l^{th} diffraction order of the upper hologram is denoted as $\eta_l(\theta_i, \lambda)$ where θ_i is the angle of incidence and λ is the wavelength of light. The lower hologram is also simulated using RCWA but the input parameters are modified to account for the effect of the light diffracted from the upper hologram before reaching the lower hologram (Fig. 3.6). The angle of incidence for the lower hologram is equal to the angle of light diffracted from the upper hologram θ_d and varies as a function of wavelength and diffraction order. This angle is calculated using the grating equation:

$$\sin[\theta_d] = \sin[\theta_i] - \frac{K_x}{2 \cdot \pi \cdot n/\lambda} \cdot l, \tag{3.1}$$

where $\boldsymbol{K_x}$ is the lateral component of the grating vector, and $\boldsymbol{n}$ is the index of refraction. The diffraction efficiency of the lower hologram in the $\boldsymbol{k}^{\text{th}}$ diffraction order is denoted as $\boldsymbol{\eta_k(\theta_d, \lambda)}$ and is calculated by inserting Eq. 3.1 into the argument:

$$\eta_k(\theta_d, \lambda) = \eta_k\left(\arcsin\left[\sin[\theta_i] - \frac{K_x}{2 \cdot \pi \cdot n/\lambda} \cdot l\right], \lambda\right) \tag{3.2}$$

The combined diffraction efficiency of the cascaded hologram $\eta_m(\theta_i, \lambda)$ can now be calculated where $m = l, k$ is the order of light first diffracted in order l and subsequently diffracted in order k. This expression is obtained by multiplying $\eta_l(\theta_i, \lambda)$ by Eq. 3.2:

$$\eta_m(\theta_i, \lambda) = \eta_l(\theta_i, \lambda) \cdot \eta_k\left(\arcsin\left[\sin[\theta_i] - \frac{K_x}{2 \cdot \pi \cdot n/\lambda} \cdot l\right], \lambda\right) \tag{3.3}$$

This method is suitable for simulating the diffraction efficiency of a planar cascaded hologram. The diffraction efficiency of a spatially varying cascaded hologram is modeled by dividing the

aperture into ‘L’ different sections (Fig. 2.12), as is done in Chapter 2 for single-layer volume holographic lenses. In this case, each section is locally approximated as a planar cascaded hologram and simulated using the cascaded RCWA technique just described.

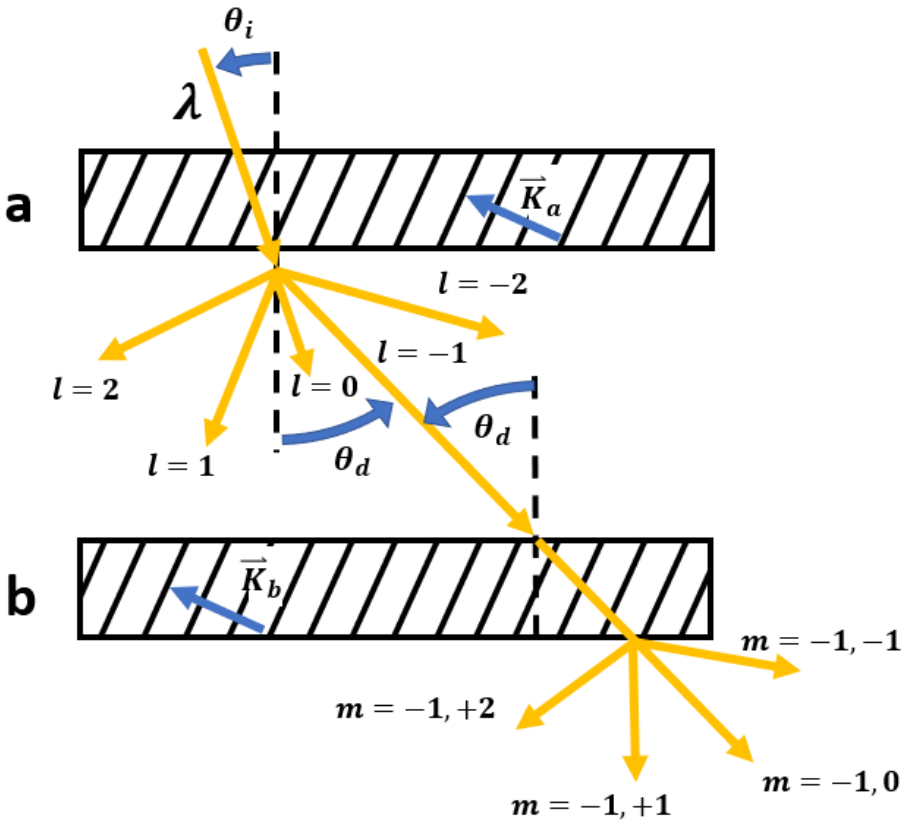

Figure 3.6: Illustration of the diffraction orders and geometry in a cascaded hologram. The angle of light diffracted by the upper hologram is equal to the angle of incidence for the lower hologram. Only the light first diffracted in the $l = -1$ and then diffracted by the lower hologram are shown, but all combinations of orders can be calculated with the cascaded RCWA method.

The diffraction model is verified by measuring the diffraction efficiency of an experimental cascaded volume hologram. The holograms are constructed by exposing 16μm thick Covestro Bayfol HX photopolymer film with light from a 0.457μm DPSS laser. The upper hologram is formed with beams at angles of 0° and 30° and the lower hologram is formed with beams at angles

of 0º degrees and 25º. The photopolymer is exposed with an energy dosage of 8.4 J/cm^2 and then cured by exposing the film to sunlight for several minutes.

First, the diffraction efficiency of the upper and lower holograms is measured separately and compared to an RCWA model. The RCWA model assumes that each hologram is formed with the construction angles listed above, has a film thickness of 16μm, and has an index modulation n_1 = 0.01. The experimental diffraction efficiency of the individual holograms and the computed diffraction efficiency using RCWA are in close agreement (Fig. 3.7). Next, the upper hologram is placed in contact with the substrate of the lower hologram to form the cascaded hologram as pictured in Fig. 3.8. The gap between the two elements is filled with an index matching fluid to reduce surface reflections. The diffraction efficiency of the cascaded hologram is measured as a function of incidence angle for the $\boldsymbol{m = +1, 0}$, $\boldsymbol{m = 0}$, $\boldsymbol{+1}$, $\boldsymbol{m = 0, 0}$ and $\boldsymbol{m = +1}$, $\boldsymbol{-1}$ orders. The measured diffraction efficiency is then compared to the simulated diffraction efficiency using the cascaded RCWA model. Each measured order shows agreement with the model. Other diffraction orders are also seen in Fig. 3.9 besides the main orders that are plotted. These orders are measured to have a diffraction efficiency less than 1% and are believed to be the $\boldsymbol{m = -1, 0}$, $\boldsymbol{m = 0, -1}$, and $\boldsymbol{m = -2, +1}$ orders.

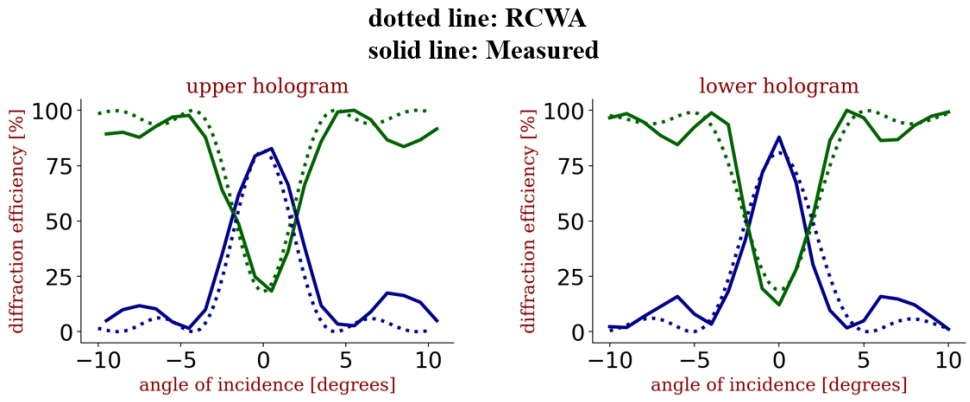

Figure 3.7: Measured and simulated diffraction efficiency of the upper and lower holograms that are later placed in a cascaded configuration and measured in Fig. 3.9.

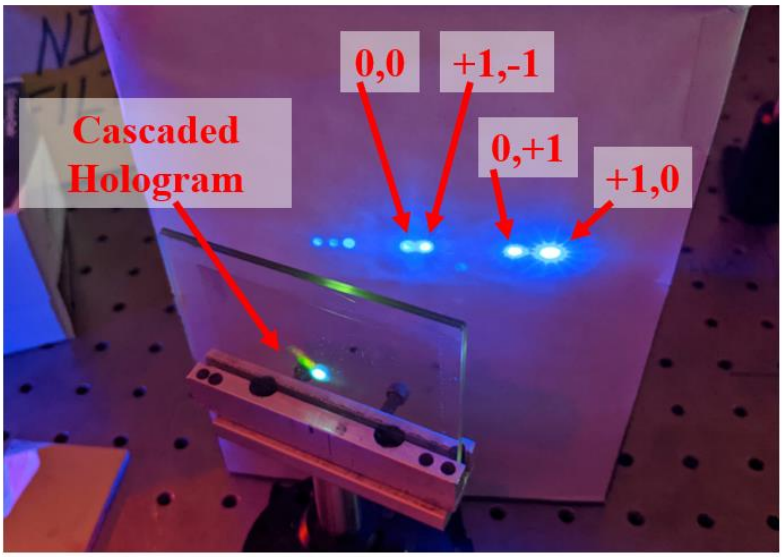

Figure 3.8: picture of a cascaded hologram diffracting light into various orders. The orders that are identified in the text blocks are measured and plotted in Fig. 3.10. The other orders that are visible but not identified are the $m = -1,0$, $m = 0,-1$, and $m = -2,+1$ orders and have less than 1% diffraction efficiency.

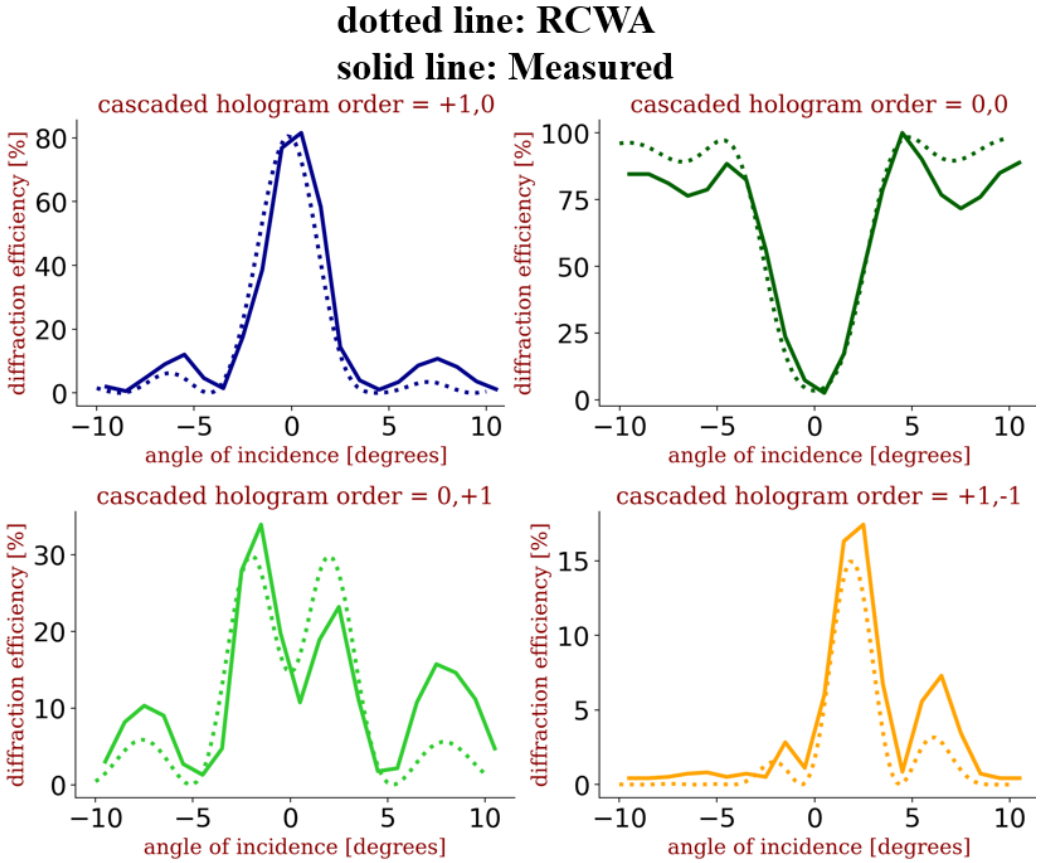

Figure 3.9: Measured and simulated diffraction efficiency of a cascaded volume hologram.

The diffraction efficiency of the cascaded volume holographic lens array (CVHLA) designed in Section 3.2 is modeled using the techniques described above. The spatial variation of the CVHLA is simulated by dividing the element into 120 sections along the aperture of the unit cell. The average diffraction efficiency across the aperture of each VHL is plotted in Fig. 3.10. Each VHL diffracts light into one of the main two diffraction orders (-1 diffracts to the right and +1 diffracts to the left) with high efficiency in spectral band 'I', 'II', or 'III'. The plot shows the main orders ($\mathbf{m = +1, 0}$; $\mathbf{m = -1, 0}$; $\mathbf{m = 0, +1}$; $\mathbf{m = 0, -1}$) each diffracting in one of the three spectral bands along with several other diffraction orders that have significant power. Cascaded VHL pairs '1' and '6' have the least diffracted power in cross-coupled or higher diffraction orders (Fig. 3.10a). Cascaded VHL pairs '2' and '5' (Fig. 3.10b) have the most diffracted power in cross-coupled orders ($\mathbf{m = -1, -1}$; $\mathbf{m = -1, +1}$). Cascaded VHL pairs '3' and '4' (Fig. 3.10c) have the most diffracted power in higher orders ($\mathbf{m = +2, 0}$; $\mathbf{m = 0, -2}$).

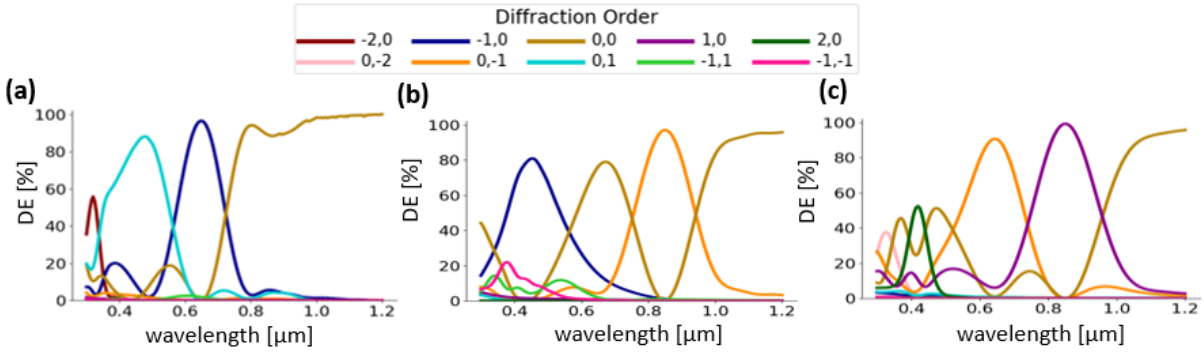

Figure 3.10: Average spectral diffraction efficiency of each cascaded volume holographic lens (a) VHL '1' (b) VHL '2' (c) VHL '3'. VHLs '4', '5', and '6' have the same diffraction efficiency as VHLs '3', '2', and '1' in the oppositely signed diffraction orders.

3.4 System Analysis

After computing the diffraction efficiency, a raytrace simulation is used to determine the spectral flux on the surface of the PV cells. The effect of different optical losses that reduce the

conversion efficiency of the system is analyzed in a similar way as done for two-bandgap systems in Section 2.7. Each ray is sorted into one of the three different spectral bands and plotted as a spatial distribution in Fig. 3.11a. The horizontal axis corresponds to the position on the PV cell plane and is normalized to the unit cell width (+0.5 is the right edge of the unit cell and -0.5 is the left edge). The blue, green, and red colored background indicates the position of PV cells 'I', 'II' and 'III' respectively. Ideally, all light diffracted from the CVHLA is located on corresponding PV cell. For example, all flux in spectral band 'I' should be located on PV cell 'I' without any flux reaching PV cells 'II' or 'III'. The spatial distribution validates the CVHLA design by showing that most of the light within each spectral band reaches the intended PV cell. Sharp transitions between spectral bands are observed on the edges of the PV cells and validate the design procedure. It is also observed that some of the light is directed to unintended solar cells. The source of this "misallocated" light is analyzed in the following discussion.

In order to analyze the sources of the misallocated light, each ray is sorted based on the diffraction order from the CVHLA. Light from the main diffraction order ($l = +1;\ l = -1;\ k = +1;\ k = -1$ depending on the direction of diffraction) is plotted in Fig. 3.11b. Most of this light reaches the intended PV cell but some is diffracted across the edge to an adjacent PV cell. Losses from the main diffraction order are classified as dispersion losses since they occur when light from the main order is dispersed onto a non-optimal solar cell. The dispersion loss is observed in spectral band 'I' on the edge between PV cell 'I' and PV cell 'II'. Next, the light that is transmitted without diffraction ($m = 0, 0$) is plotted in Fig. 3.11c. As stated in the design procedure, one of the spectral bands is designed to be transmitted through the hologram without diffraction to the optimal cell. This is clearly observed on PV cell 'III' where spectral band 'III' contributes a significant fraction of the total flux. However, some of the light that is ideally diffracted is instead transmitted in the

0^{th} order. This loss is classified as a low diffraction efficiency loss. The low diffraction efficiency loss results from non-uniform spectral diffraction efficiency (Fig. 3.10) and the variation of diffraction efficiency across the VHL aperture. The distribution of cross-coupled light is plotted in Fig. 3.11d. As mentioned previously, cross-coupling can significantly reduce the light reaching the intended solar cells. However, cross-coupling is specifically addressed in the design of the CVHLA and consequently has a relatively small flux. Lastly, the distribution of light diffracted into higher orders (l and k up to the third order) is shown in Fig. 3.11e. Very little light from the higher diffraction orders reach the intended PSCs. Almost all of the light diffracted in a higher diffraction order is in spectral band 'I' and is distributed across PV cells 'II' and 'III'. Most of the higher order diffraction is in spectral band 'I' because shorter wavelengths are more likely to diffract into a higher diffraction order than longer wavelengths [55].

The relative contribution of each loss is shown as a fraction of the total loss in the pie chart in Fig. 3.11f. The relative loss is calculated by dividing the misallocated flux for a given diffraction order by the total misallocated flux. The greatest loss is low diffraction efficiency (42.6%) followed by dispersion (22.8%), higher orders (19.8%), and cross-coupled orders (14.7%).

Next, the spectral optical efficiency $SOE(\lambda)$ of the system is calculated as is discussed in more detail in Section 2.4. The spectrum incident on the j^{th} PV cell $E_j(\lambda)$ is calculated by summing the flux on each PV cell as a function of wavelength. The $SOE_j(\lambda)$ is then calculated by dividing $E_j(\lambda)$ by the total incident direct solar spectrum $AM1.5D(\lambda)$ [51] illuminating the unit cell:

$$SOE_j(\lambda) = \frac{E_j(\lambda)}{AM1.5D(\lambda)} \tag{3.4}$$

The $SOE(\lambda)$ for the perovskite design example is plotted in Fig. 3.12 and shows a clear transition between spectral bands. The $SOE(\lambda)$ for PV cell 'I' is lower than for the other PV cells due to increased higher order diffraction and cross-coupled diffraction at shorter wavelengths. The power conversion efficiency for diffuse sunlight is also calculated using the methods in Section 2.4. Based on this analysis the overall power conversion efficiency for this spectrum-splitting system is 26.7%.

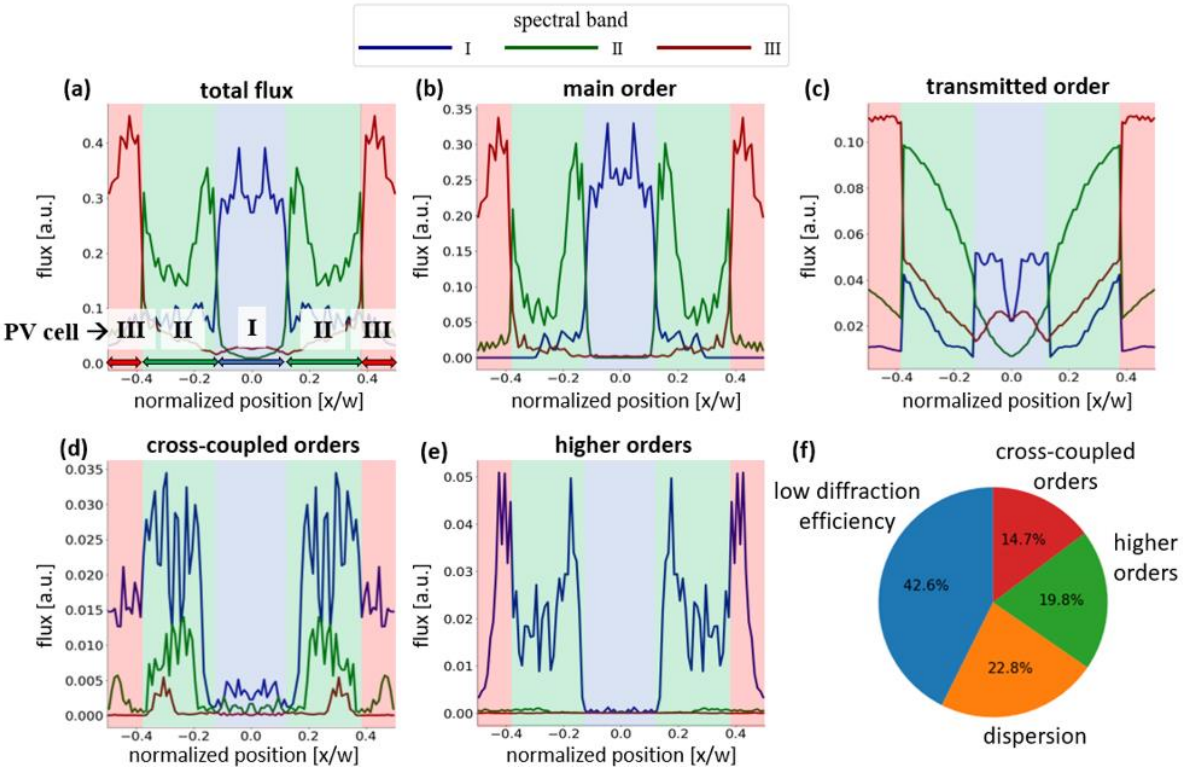

Figure 3.11: Plot of the spatial distribution of light within spectral bands 'I', 'II', and 'III' on the surface of the PV cells. The flux on the PV cell plane from the different diffraction orders are plotted separately. The horizontal axis is the position along the unit cell aperture normalized to the width of the unit cell. The ray flux contained in each analysis bin is plotted in the vertical axis. There are 100 analysis bins across the unit cell, 100 ray starting positions and 50 wavelengths spanning 0.3um to 1.2um. The initial flux of each ray is 1/100 so that the total integrated flux for a given wavelength is equal to 1. The blue, green, and red background colors indicates the position of PV cells 'I', 'II' and 'III' respectively. (a) Total irradiance from all diffraction orders. (b) Diffraction from the main order. (c) Light that is transmitted without being diffracted. (d) Light that is cross-coupled. (e) Light that is diffracted in a higher order. (f) Pie chart indicating the percentage of optical losses caused by low diffraction efficiency, cross-coupled light, dispersion, and higher order diffraction.

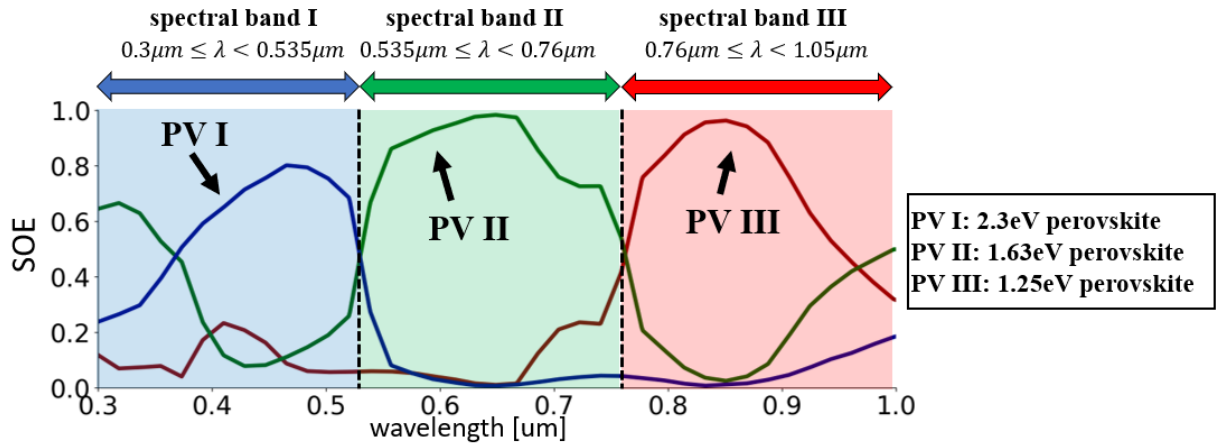

Figure 3.12: Plot of the spectral optical efficiency for a perovskite photovoltaic system showing the fraction of light reaching each PV cell as a function of wavelength. The optimal spectral bands are shown by the colored arrows on the top.

Another aspect of the spectrum-splitting design that is considered is the effect of the conversion efficiency of the individual PV cells and the diffraction efficiency of the VHL array on the overall power conversion efficiency. The effect of the conversion efficiency of the individual perovskite cells is analyzed by computing the power conversion efficiency for five different sets of hypothetical perovskite cells (Table 3.2). For each hypothetical perovskite cell, the experimentally measured $SCE(\lambda)$ curve is scaled to reach a higher conversion efficiency. The effect of the diffraction efficiency is analyzed by simulating the system for different values of the maximum diffraction efficiency (MDE). The MDE is the diffraction efficiency for normally incident light at the Bragg wavelength λ_B. The design parameters used in the analysis so far have assumed an MDE near 100% since this is theoretically attainable [55]. However, in practice the MDE varies between 85% to 95% [62]. In the following analysis the diffraction efficiency is reduced from 100% to the value of the MDE by decreasing the index modulation. For example, VHL '3' in the upper layer has an index modulation of 0.014. By reducing the index modulation to 0.010 the MDE is decreased from 100% to 80%.

The overall power conversion efficiency (PCE) is computed as a function of the MDE for each of the five sets of perovskite cells. The PCE is plotted in Fig. 3.13 and the results are tabulated in Table 3.3. The PCE data shows minimal degradation (0.3%) when reducing the MDE from 100% to 90%. The drop in performance is more than twice as much (0.7%) when the MDE decreases from 90% to 80% and an additional reduction of 0.5% occurs when the MDE decreases from 80% to 70%. The degradation rate is non-linear since the effect of the MDE is different for each of the optical losses discussed in the previous section. Not surprisingly as the diffraction efficiency is reduced the "low diffraction efficiency" losses increase. However, the higher order losses and cross-coupling losses actually decrease and offset some of the loss seen in diffraction efficiency. The overall effect is a non-linear decrease in PCE as the diffraction efficiency is decreased. An MDE value of 90% avoids the highest rate of degradation between 90% and 80% and can be achieved in practice. Based on this analysis, a manufacturing target for the CVHLA is to have an MDE greater than 90%.

The final aspect of the analysis that is considered is the effect of the individual perovskite cell conversion efficiencies. Fig. 3.13 shows that a set of perovskite cells with conversion efficiencies of 12.0%, 24.8%, and 23.5% can attain a conversion efficiency of 30.4% when combined with a CVHLA that has a diffraction efficiency greater than 90%. The most efficient PSC on record has a conversion efficiency of 25.2% and a bandgap (1.55eV) [23] that is similar to the bandgap of PV cell 'II' (1.63eV). This shows that the necessary perovskite cell conversion efficiency for exceeding a system conversion efficiency of 30% may be attainable in practice. Significantly less research has been conducted on PSCs with 1.25eV and 2.3eV bandgaps. With improvements in the conversion efficiency of PSCs at these bandgaps a lateral SSPV system with a conversion efficiency greater than 30% is possible.

Table 3.2: Five sets of perovskite solar cells (PSC) with conversion efficiencies scaled relative to the experimentally measured values.

PSC	Set 1	Set 2	Set 3	Set 4	Set 5
I	10.4%	10.92%	11.44%	11.96%	12.48%
II	21.6%	22.68%	23.76%	24.84%	25.92%
III	20.4%	21.42%	22.44%	23.46%	24.48%

Table 3.3: Power conversion efficiency for each of the perovskite cell sets in Table 3.2 and for different values of the maximum diffraction efficiency (MDE).

MDE	Set 1	Set 2	Set 3	Set 4	Set 5
80%	25.7%	27.0%	28.2%	29.5%	30.8%
90%	26.4%	27.7%	29.1%	30.4%	31.7%
100%	26.7%	28.0%	29.4%	30.7%	32.0%

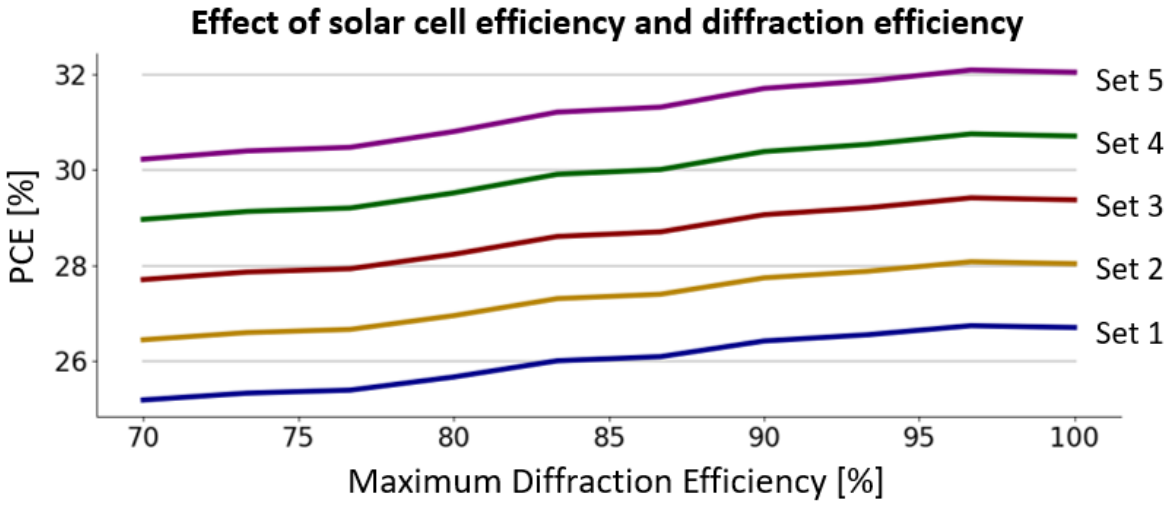

Figure 3.13: Power conversion efficiency (PCE) as a function of the maximum diffraction efficiency (MDE) for the perovskite cell sets listed in Table 3.2.

3.5 Comparison of Cell Combinations

In this section, a III-V/silicon cell combination is simulated and compared with the perovskite cell combination. The spectral optical efficiency is plotted for both cell combinations in Fig. 3.14 and is the highest within the optimal spectral bands of each PV cell. The ideal power conversion efficiency (PCE_i), spectrum splitting efficiency (SSE), and actual power conversion efficiency (PCE_a) for each cell combination is listed in Table 3.4. These metrics are discussed in more detail in Section 2.7. The silicon/III-V cell combination has the highest power conversion efficiency (PCE_a = 35.4%) and a slightly higher SSE (85.1%) than the all-perovskite combination (84.8%).

The power conversion efficiency of new PV cell combinations can be estimated in a simple way without simulating the holograms if the spectral conversion efficiency of each cell is known. First the ideal power conversion efficiency PCE_i is calculated using Eq. 2.2. Next, the PCE_i is multiplied by the average value of the SSE (85.0%):

$$PCE = PCE_i \cdot 0.850, \tag{3.5}$$

Table 3.4: Table of performance metrics for different PV cell combinations. The power conversion efficiency with ideal optical filters (PCE_i), spectrum splitting efficiency (SSE), and actual power conversion efficiency (PCE_a) are listed.

Cell combination	PCE_i	SSE	PCE_a
Perovskite 1.25eV & Perovskite 1.63eV & Perovskite 2.3eV	31.5%	84.8%	26.7%
Silicon 1.1eV & GaAs 1.41eV & GaInP 1.83eV	41.6%	85.1%	35.4%

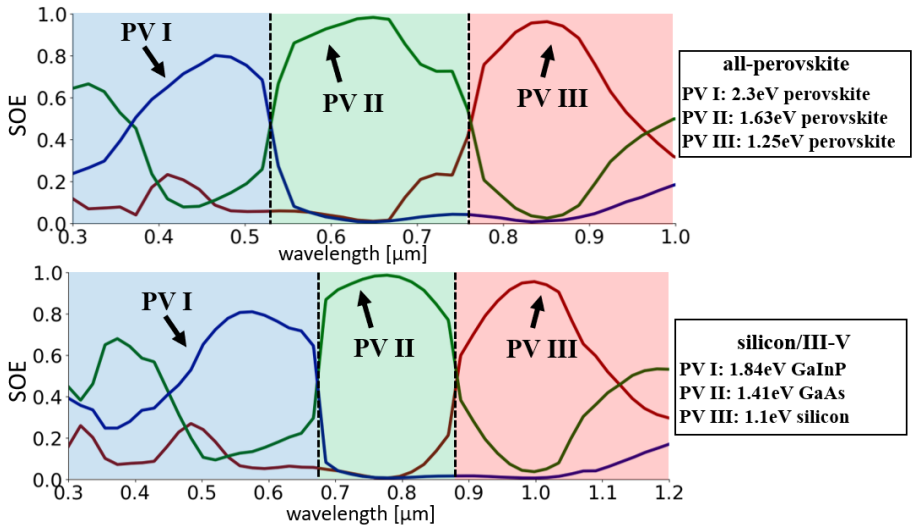

Figure 3.14: Spectral optical efficiency (SOE) for an all-perovskite cell combination and for a silicon/III-V cell combination.

3.6 Conclusion

In this chapter a lateral spectrum-splitting photovoltaic system is proposed that divides the solar spectrum between three solar cells with different energy bandgaps. Spectral separation is accomplished using a cascaded volume holographic lens array. An RCWA diffraction model for the cascaded holographic element is developed that calculates the cross-coupled diffraction between the computed diffraction orders. The optical losses in the system are analyzed and it is determined that a combination of losses due to low diffraction efficiency, higher order diffraction, dispersion, and cross-coupled orders all contribute to reduced spectral optical efficiency. The system is able to attain to a power conversion efficiency of 26.7% when using perovskite cells. This is an improvement of 0.6% compared with the two-bandgap system described in Chapter 2. However, the spectrum-splitting efficiency is significantly lower for the three-way splitter (85.0%) compared with the two-way splitter (92.0%). In the next chapter, this limitation is addressed by introducing a technique that simultaneously increases the spectrum-splitting efficiency and the number of energy bandgaps.

Chapter 4

Spectrum-Splitting Systems with Hybrid Cell Arrangements

In this chapter a “hybrid” cell arrangement for multijunction photovoltaic systems is proposed which combines both lateral and vertically stacked cell configurations. The hybrid cell arrangement is suitable for use with semi-transparent photovoltaic cells including perovskite solar cells. Three- and four- bandgap hybrid designs are proposed that use the lateral spectrum splitting techniques from Chapters 2 and 3 to divide the spectrum between a set of semi-transparent top cells while longer wavelength light is transmitted to an underlying narrow-bandgap cell. Each hybrid system has a greater conversion efficiency and a greater spectrum splitting efficiency than equivalent systems implemented with just lateral or vertical cell arrangements. These observations may be useful for implementation in next-generation photovoltaic systems in which three, four, or more energy bandgaps are used to increase the conversion efficiency.

4.1 Introduction

Increasing the power conversion efficiency (PCE) of photovoltaic (PV) solar energy systems is expected to be a major driver of the PV market over the next several decades [1]. As discussed

in previous chapters, spectrum splitting systems attain high conversion efficiency by dividing the incident solar spectrum between a set of PV cells with different bandgap energies [14]. Multijunction photovoltaic systems can be implemented with different cell arrangements. One of the most common configurations is the “vertically stacked” cell arrangement. In this arrangement subcells are placed on top of each other (Fig. 4.1a) and spectrum splitting is accomplished through absorptive filtering. The top cell absorbs and converts the shorter wavelength light and transmits the longer wavelength light to the underlying cells. Spectrum splitting systems in this configuration are commonly referred to as ‘tandem modules’ or ‘tandem stacks’ but also classify as spectrum splitting systems since they divide the solar spectrum between subcells with different bandgap energies. In a ‘lateral’ configuration, cells are laterally arranged and an optical element such as a diffraction grating or dichroic filter directs light within each spectral band to the optimal solar cells (Fig. 4.1b). In a ‘hybrid’ configuration, some cells are laterally arranged and other cells are vertically stacked (Fig. 4.1c). Sunlight is divided into spectral bands using an optical element and further subdivided through absorptive filtering in a cell stack.

In the literature, perovskite solar cells (PSCs) have been implemented in the vertically stacked arrangement. A two-junction system using only perovskite cells was demonstrated with an efficiency of 24.2% [21], [79] and a two-junction system using a combination of a silicon and perovskite cells reached an efficiency of 29.2% [21]. A recent industry roadmap suggests that two-junction systems based on a combination of silicon cells and either PSCs or other thin-film cells will occupy a growing market share by the end of the decade [82]. Beyond this point, advances in conversion efficiency are expected to be obtained by integrating three or more bandgaps with a potential shift away from silicon towards the middle of the century [1].

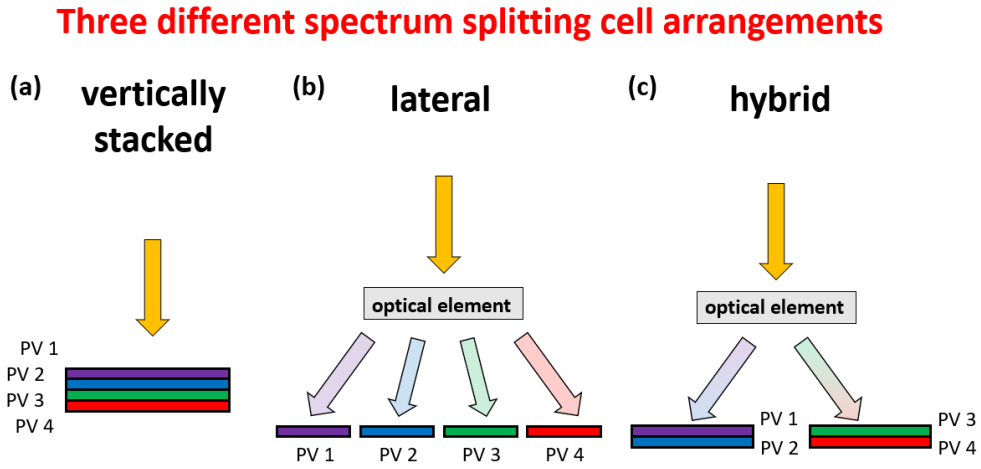

Figure 4.1: Depictions of three different cell arrangements for spectrum splitting photovoltaic systems. (a) vertically stacked, (b) lateral, (c) hybrid. In general, cells can be connected in series, series-parallel combinations, or electrically-independent configurations.

One of the challenges faced when integrating a greater number of energy bandgaps in a spectrum splitting system is the effect that the electrical contacts and electrical wiring configurations have on the overall design flexibility and conversion efficiency. In the past, the use of monolithically integrated multijunction cells limited many multijunction systems to be connected in a series configuration. However, PSCs are typically fabricated on independent substrates with independent sets of electrical contacts composed of transparent conductive oxides (TCOs). This provides extra design flexibility since PSCs in a spectrum splitting module can be wired in series, series-parallel combinations, or in electrically-independent configurations [36]. While flexibility in wiring configurations can be an advantage for PSC-based systems, the use of TCOs also results in parasitic absorption of incident sunlight (10-20%) [23], [36]–[40]. The effect of parasitic absorption is especially important for vertically stacked systems with more than two perovskite subcells since transmission through each subcell successively absorbs light that would otherwise be converted into electricity. For example, the bottom cell in a four-bandgap vertically

stacked system only receives 66% of the total light within its optimal spectral band when the overlying PSCs each absorb 10% of the light.

In this chapter, a “hybrid” cell arrangement is proposed as a solution for reducing the parasitic light absorption in multijunction systems using semi-transparent photovoltaic cells, such as perovskite cells. This arrangement is advantageous because for a given number of bandgap energies it simultaneously reduces the number of spectral bands divided by the optical element and the number of cells in the vertical stack. As a result, simpler optical elements are used compared with a lateral spectrum splitting system and the parasitic absorption is reduced compared with a vertically stacked system. Similar arrangements have been proposed in literature for laterally dividing the solar spectrum between a set of multijunction cells. When more than one multijunction cell is incorporated in a hybrid system, the current matching, lattice matching, and dark saturation current constraints are reduced compared to a system consisting of a single multijunction cell [83]. Two hybrid mini-modules were demonstrated with conversion efficiencies of 38.5% [42] and 40.6% [43]. In both cases the mini-modules used a dichroic filter to split sunlight in two spectral bands. Each band was then sent to either a multijunction cell or a silicon cell. The multijunction cells further subdivided the spectral bands for a total of four spectral bands. In another paper, Darbe et. al [78] used a volume holographic optical element to divide the solar spectrum between four laterally separated dual-junction PV cells. The dual-junction cells further subdivided each band into two additional bands for a total of eight spectral bands. The authors proposed the design with the initial goal of reaching 50% conversion efficiency. Recently, a paper by Lan et al. [83] proposed a hybrid system consisting of two multijunction cells with distributed Bragg reflectors. In this design multijunction cells are positioned so that Bragg reflectors in one of the multijunction cells direct a set of spectral bands to the optimal subcells in the other

multijunction cell. Based on their calculations, this design has potential for exceeding 51% conversion efficiency at a solar concentration of 300 suns.

Although each of these studies showed some of the potential benefits of a hybrid cell arrangement, they focused on dividing the solar spectrum between monolithic multijunction cells and did not focus on integrating semi-transparent, single-junction cells such as perovskite solar cells. In this chapter, two different hybrid spectrum splitting systems are proposed and compared with vertically stacked and lateral systems. Each system consists of an array of unit cells as illustrated in Fig. 4.2. The energy bandgaps of the PV cells are indicated by the roman numerals and range from widest bandgap (‘I’) to narrowest bandgap (‘IV’). Each module has a cell combination consisting entirely of PSCs or a combination of PSCs and silicon cells. Each bandgap is assumed to be connected in an electrically-independent configuration. Each of the lateral modules are implemented with a volume holographic lens (VHL) array for dividing the spectrum into two spectral bands (Fig. 4.2c, Chapter 2) or a cascaded volume holographic lens array for dividing the spectrum into three spectral bands (Fig. 4.2d, Chapter 3). The hybrid designs are an extension of the lateral designs by vertically stacking the unit cell layout on top of an additional narrow-bandgap cell (Fig. 4.2e,f). The VHL array divides the shorter wavelength spectral bands between the top cells. A longer wavelength spectral band is transmitted through the top cells to the underlying narrow-bandgap PV cell. The power conversion efficiency for each of the modules in Fig. 4.2 is computed using experimental and ideal cell spectral efficiency values calculated in Section 2.2. A comparison shows that a hybrid cell arrangement results in the highest conversion efficiency when the transmission through the PSCs is less than 93%. Given that PSCs have been demonstrated with transmission values ranging between 80% to 90%, a hybrid cell arrangement

may attain greater power conversion efficiency than comparable systems that use only vertically stacked or laterally separated cell arrangements.

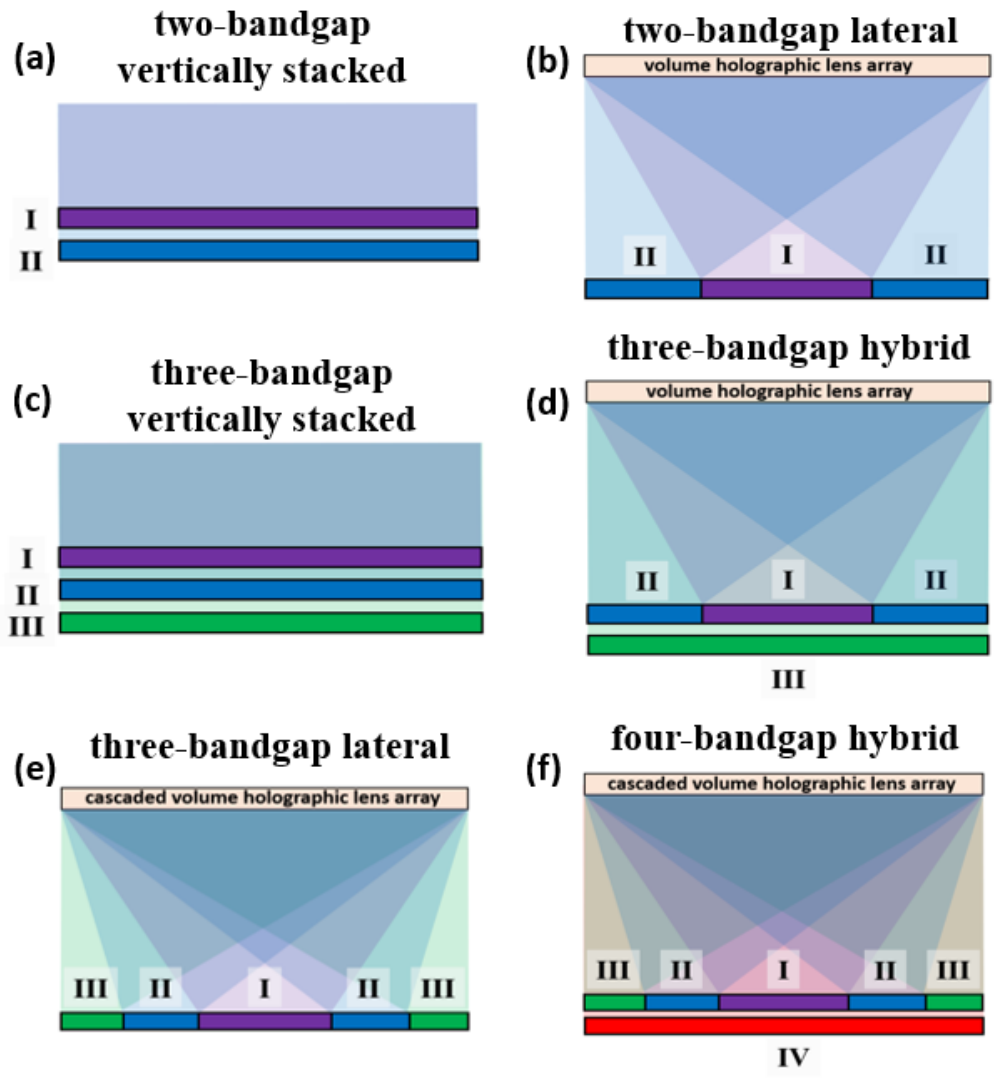

Figure 4.2: Unit cell layout for six spectrum-splitting systems with different cell arrangements. In each unit cell layout, cells are arranged in a stacked, lateral, or hybrid configuration and the solar spectrum is split between two, three, or four subcells. The roman numerals 'I', 'II', 'III', and 'IV' indicate the bandgap of the cell. (a) two-junction vertically stacked (b) two-junction lateral (c) three-junction vertically stacked (d) three-junction hybrid (e) 3-junction lateral (f) 4-junction hybrid.

4.2 Simulation Method

4.2.1 Modeling Vertically Stacked Systems

The spectral optical efficiency $SOE_j(\lambda)$ for the j[th] cell in a vertically stacked system depends on the bandgap energy and the light 'T' transmitted through a perovskite cell. Ideally the transmission value is equal to one, but in most PSCs the value ranges between 80% to 90%. The transmission value is primarily reduced due to parasitic light absorption in the TCO contacts. Other effects such as reflections or parasitic absorption in other parts of the cell also contribute but to a smaller degree [40]. In this chapter, transmission through a cell is modeled as a step function with a tapered step. The taper models the gradual increase in transmission near the band edge in experimental cells. λ_j^+ is the "upper" edge of the bandgap and is measured as the wavelength that the spectral conversion efficiency $SCE(\lambda)$ falls to zero. λ_j^- is the "lower" edge of the bandgap and is measured as the wavelength in which the $SCE(\lambda)$ begins to decrease. In experimental cells, the taper has a finite spectral width that typically ranges between 10nm to 20nm but can be as high as 150nm for silicon. In ideal cells there is no taper and there is an abrupt increase in transmission at the bandgap ($\lambda_j^+ = \lambda_j^-$). The $SOE_j(\lambda)$ for light incident on the top cell 'I' is equal to one since the incident spectrum is equal to the solar spectrum. The $SOE_j(\lambda)$ for the j[th] cell is calculated by multiplying the $SOE_{j-1}(\lambda)$ for the overlying cell by the tapered transmission function for cell 'j-1':

$$SOE_j(\lambda) = SOE_{j-1}(\lambda) \cdot \begin{cases} 0, & \lambda < \lambda_{j-1}^- \\ T \cdot \dfrac{(\lambda - \lambda_{j-1}^-)}{(\lambda_{j-1}^+ - \lambda_{j-1}^-)}, & \lambda_{j-1}^- \le \lambda \le \lambda_{j-1}^+ \\ T, & \lambda > \lambda_{j-1}^+ \end{cases} \tag{4.1}$$

The $SOE(\lambda)$ for a two-bandgap vertically stacked system splitting light between 1.25eV and 1.72eV perovskite cells is shown in Fig. 4.3a. The $SOE(\lambda)$ for a three-bandgap vertically stacked spectrum splitting system that divides light between a set of 1.25eV, 1.55eV, and 2.3eV perovskite cells is shown in Fig. 4.3b. In this plot it is observed that the $SOE(\lambda)$ for PV cell 'III' in spectral band 'III' is lower than the $SOE(\lambda)$ for PV cell 'II' in spectral band 'II' because light is transmitted through an additional PSC and has greater transmission losses.

4.2.2 Modeling Lateral Systems

The design and simulation of the lateral spectrum splitting systems (Fig. 4.2c,d) is performed using the techniques described in Chapters 2 and 3. The parameters used for each of the holographic optical elements are listed in Appendix B. The $SOE(\lambda)$ for a lateral spectrum splitting system that divides the solar spectrum between 1.25eV and 1.72eV perovskite cells is shown in Fig. 4.3c. The $SOE(\lambda)$ for a three-bandgap lateral system dividing the spectrum between 1.25eV, 1.63eV, and 2.3eV PSCs is shown in Fig. 4.3d. Some of the differences between lateral and vertically stacked cell arrangements can be seen by comparing the $SOE(\lambda)$ curves (Fig. 4.3a-d). The spectral optical efficiency for each of the PV cells in the vertically stacked systems are uniform within the corresponding spectral bands. In contrast, the spectral optical efficiency for the PV cells in the lateral systems vary as a function of wavelength since the spectral diffraction efficiency of a hologram is not uniform. However, the $SOE(\lambda)$ of a lateral system can exceed that of a vertically stacked system for wavelengths that are diffracted with high diffraction efficiency. For example, the $SOE(\lambda)$ of PV cell 'II' in spectral band 'II' is greater for a two-bandgap lateral system compared with a vertically stacked system for wavelengths ranging between 0.725μm and 0.925μm.

4.2.3 Modeling Hybrid Systems

The $SOE(\lambda)$ for a hybrid cell arrangement is calculated using a combination of the methods previously described for vertically stacked and lateral configurations. The three-junction hybrid design (Fig. 4.2e) consists of a two-junction lateral design (Fig. 4.2c) vertically stacked on top of a narrow-bandgap PV cell. The four-junction hybrid design (Fig. 4.2f) consists of a three-junction lateral design (Fig. 4.2d) stacked on top of a narrow-bandgap PV cell. The first step in calculating the $SOE(\lambda)$ of a hybrid cell arrangement is to simulate the holographic optical element using the methods from Chapters 2 and 3. The simulation result gives the $SOE(\lambda)$ for each of the top cells. Next, the $SOE(\lambda)$ for the bottom cell is calculated by modifying Eq. 4.1 to account for the light transmitted through each of the top cells:

$$SOE_N(\lambda) = \sum_{j}^{N-1} SOE_j(\lambda) \cdot \begin{cases} 0, & \lambda < \lambda_j^- \\ T \cdot \dfrac{(\lambda - \lambda_j^-)}{(\lambda_j^+ - \lambda_j^-)}, & \lambda_j^- \le \lambda \le \lambda_j^+ \\ T, & \lambda > \lambda_j^+ \end{cases}, \qquad (4.2)$$

where N is the total number of energy bandgaps in the system and $SOE_N(\lambda)$ is the spectral optical efficiency of the bottom cell. The $SOE(\lambda)$ for a three-bandgap hybrid system dividing sunlight between 1.25eV, 1.63eV, and 2.3eV perovskite cells is shown in Fig. 4.3e and the $SOE(\lambda)$ for a four-bandgap hybrid system dividing the spectrum between 1.25eV, 1.55eV, 1.72eV, and 2.3eV perovskite cells is plotted in Fig. 4.3f.

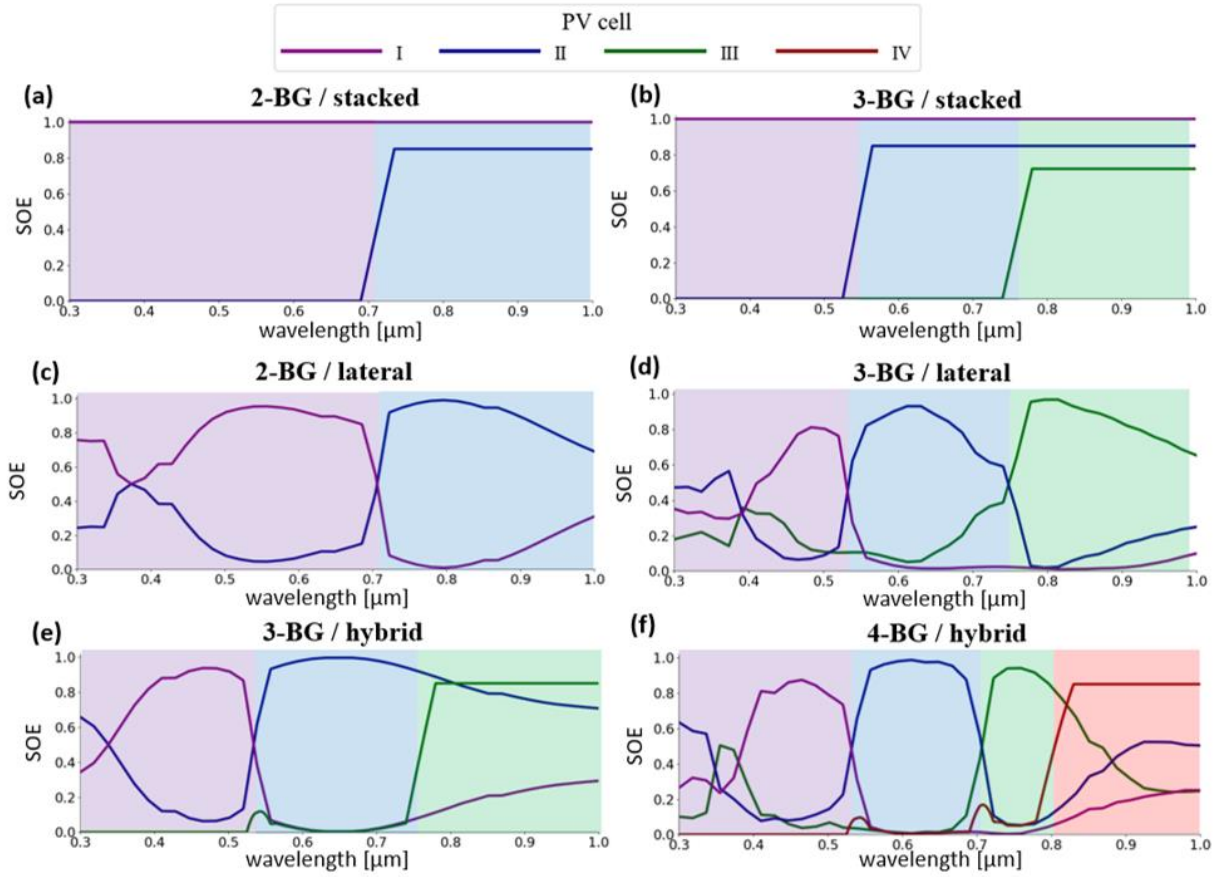

Figure 4.3: The spectral optical efficiency $SOE(\lambda)$ for vertically stacked, lateral, and hybrid spectrum splitting systems. The color of the SOE curve indicates the PV cell energy bandgap and the color of the background indicates the ideal spectral bands for each solar cell. The transmission value, T, is assumed to be 85%. (a) 2-bandgap stacked, (b) 3-bandgap stacked, (c) 2-bandgap lateral, (d) 3-bandgap lateral, (e) 3-bandgap hybrid, (f) 4-bandgap hybrid.

4.2.4 Modeling Performance with Diffuse Sunlight

The effect of diffuse sunlight is also calculated for each of the systems. As discussed in previous chapters, diffuse sunlight is assumed to be scattered uniformly from the atmosphere over a full hemisphere (2π steradians) and has a blue-shifted spectrum $AM1.5F(\lambda)$ [51]. The diffuse sunlight analysis for lateral spectrum splitting systems is discussed in Section 2.4 and is applied in this analysis as well. However, in vertically stacked systems the absorptive filtering is not angularly selective. For this reason, the spectral optical efficiency for diffuse sunlight is also calculated using Eq. 4.1. For hybrid systems, the spectral optical efficiency for diffuse sunlight is

calculated using the diffuse sunlight analysis in Section 2.4 for the top cells. However, the spectral optical efficiency for the bottom cell is still calculated using Eq. 4.2. The overall power conversion efficiency (PCE) is then calculated by weighting the conversion efficiency for direct sunlight by 90% and weighting the conversion efficiency for diffuse sunlight by 10% (Eq. 2.10) [51].

4.3 Comparison of System Configurations

The PCE for each of the system designs in Fig. 4.2 is computed for a variety of cell combinations listed in Table 2.1 in Chapter 2. The ideal cell combinations are determined using a detailed balance analysis and the experimental cell combinations are selected to closely match the ideal cell bandgap combinations.

The transmission value ‘T’ is an important parameter in determining the power conversion efficiency (PCE) of vertically stacked and hybrid systems. The PCE is computed as a function of the transmission value and plotted in Fig. 4.4. The vertically stacked systems have the highest PCE of any system design for transmission values ranging between 95% to 100%. As the transmission value is decreased below 93% the hybrid spectrum splitting systems have the highest PCE. Below this range, the performance of the hybrid systems is greatest and is only outperformed by lateral systems when the transmission value is well below 75%. Although lateral spectrum splitting systems have the lowest PCE values in most cases, they are more efficient than vertically stacked modules for transmission values less than 75% to 82% depending on the specific designs.

The PCE for each of the system designs is listed in Table 4.1 assuming a transmission value of 85%. The four-bandgap hybrid system has the highest PCE of any module and reaches a power conversion efficiency of 30.0% using experimental spectral conversion efficiency values for perovskite solar cells. For systems with a silicon bottom cell, the PCE of the three- and four-

bandgap hybrid systems are computed to be 32.0% and 33.5% efficient, respectively. As discussed in Chapter 3, the PCE of the overall system will also increase as advances in the perovskite cell technology increase the efficiency of individual cells. The maximum conversion efficiency that is possible for these system designs is determined based on the conversion efficiency of ideal cell combinations. The PCE for modules with ideal cell combinations is 10% to 14% higher than for modules with experimental cells.

With no transmission losses the vertical cell stacks are more efficient than any other cell arrangement. However, the transmission losses in the TCOs reduce the conversion efficiency to a range in which hybrid systems have greater conversion efficiency. The effect of the TCO losses increase as the number of bandgaps increase since light needs to transmit through every cell in the stack to reach the lowest cell. This effect is apparent when comparing three- and four- bandgap vertically stacked and hybrid systems. A three-bandgap vertically system requires a transmission value greater than 93% to exceed the efficiency of a three-bandgap hybrid module. This value increases to 95% when comparing a four-bandgap stacked module with a four-bandgap hybrid module. The increasing requirement on the perovskite cell transmission as the number of energy bandgaps increases may mean that a hybrid cell arrangement is preferable for systems with three, four, or more perovskite photovoltaic cells.

The effectiveness of each module configuration is also evaluated using the spectrum-splitting efficiency SSE metric as described in Chapter 2 [78]. The SSE compares the power conversion efficiency of a photovoltaic system with ideal optical filters (PCE_i) and simulated or experimental optical filters (PCE_a):

$$SSE = \frac{PCE_a}{PCE_i}, \tag{4.3}$$

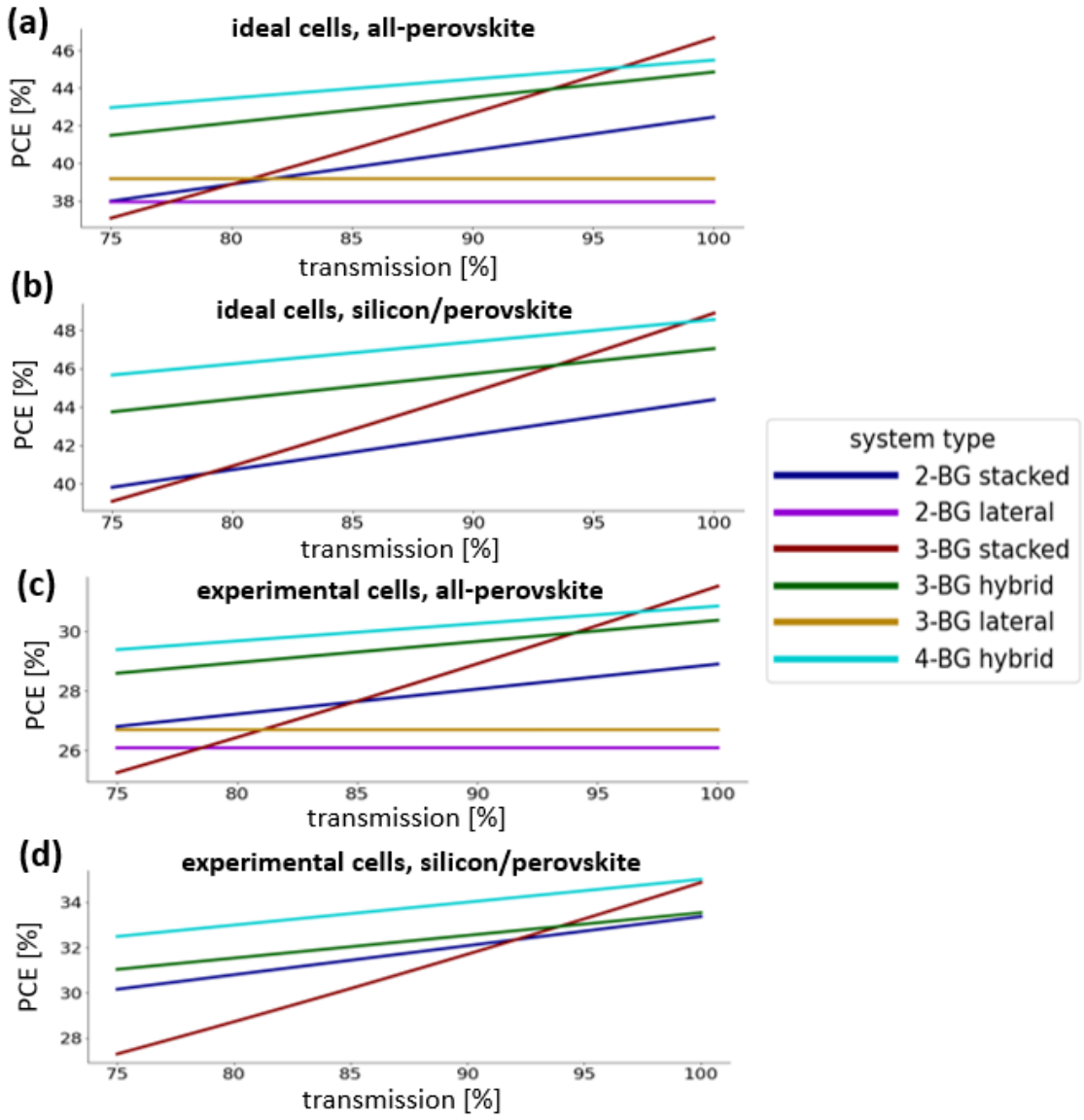

Figure 4.4: Power conversion efficiency (PCE) as a function of the transmission value. The transmission value is the percent of light transmitted through a semi-transparent perovskite cell. The PCE is plotted for each of the system configurations in Fig. 4.2 for cell combinations listed in Table 2.1. (a) Ideal, all-perovskite cells (b) Ideal, silicon/perovskite cells (c) experimental, all-perovskite cells, and (d) experimental, silicon/perovskite cells.

The SSE is the preferred metric for comparing optical designs in this dissertation since it directly shows the effect of the spectral optical filter on the attainable power conversion efficiency. Other metrics, such as the optical efficiency do not account for the non-uniformity of the solar spectrum or the spectral conversion efficiency of the PV cells. Another metric, the improvement

over best bandgap (IOBB) [14], is useful for comparing optical designs for a given cell combination but can be misleading when comparing different cell combinations. If one cell in a set of PV cells has a very high conversion efficiency and another cell has a relatively low conversion efficiency, the IOBB will be relatively low even if the optical filter is close to ideal.

The SSE values are listed in Table 4.2 and are calculated for both the ideal and experimental cell combinations assuming a transmission value of 85%. The two-junction vertically stacked system has the highest SSE (94.7%). However, a 3-junction hybrid system has a considerably higher SSE (91.5%) than a three-junction stacked system (87.0%) and a three-junction lateral system (83.7%). The data in the table shows that the high power conversion efficiency of a hybrid system results from both greater spectrum splitting efficiency as well as a greater number of bandgaps. For example, a three-bandgap lateral spectrum splitting system has a conversion efficiency of 26.7% and a four-bandgap hybrid spectrum splitting system has a conversion efficiency of 30.0%. The difference might seem to be mostly due to the higher detailed balance limit for a system with four bandgaps. However, the four-junction hybrid system also has a much higher SSE value (92.9% compared to 84.8%). One of the reasons for the greater SSE can be attributed to the ability of the bottom cell to convert some of the light that is misallocated on the top cells. In a system with just lateral spectrum splitting some of the misallocated light is greater than the bandgap wavelength and is not converted at all. This results in a big loss that is partially recovered by the bottom cell in a hybrid system.

Another characteristic of the hybrid SSPV module configuration is a lower marginal decrease in spectrum-splitting efficiency when increasing the number of energy bandgaps. When increasing the number of bandgaps from two to three, the SSE value decreased from 94.7% to 87.0% for vertically systems and from 90.5% to 83.7% for lateral systems. In contrast, when increasing the

number of bandgaps from three to four, the SSE value in the hybrid systems only decreased from 91.5% to 90.0%. For experimental cell combinations the SSE barely changed or even increased. More research needs to be done, but if this trend continues, then the advantage of hybrid cell arrangements may be even greater for systems with more than four bandgaps.

Table 4.1: List of power conversion efficiency values for various cell combinations and system configurations.

system configuration	all-perovskite		silicon/perovskite	
	ideal cells	experimental cells	ideal cells	experimental cells
2-bandgap, stacked	39.8%	27.6%	41.7%	31.4%
3-bandgap, stacked	40.7%	27.7%	42.8%	30.2%
2-bandgap, lateral	38.0%	26.1%	-	-
3-bandgap, lateral	39.2%	26.7%	-	-
3-bandgap, hybrid	42.8%	29.3%	45.1%	32.0%
4-bandgap, hybrid	44.0%	30.0%	46.8%	33.5%

Table 4.2: Spectrum-splitting efficiency SSE for each system design, where SSE is the ratio of power conversion efficiency (PCE) values using the simulated optical filters (Table 4.1) with a transmission value of 85% compared with the PCE using ideal optical filters (Table 2.1).

system configuration	all-perovskite		silicon/perovskite	
	ideal cells	experimental cells	ideal cells	experimental cells
2-bandgap, stacked	94.7%	95.5%	93.9%	94.0%
3-bandgap, stacked	87.0%	87.9%	86.2%	86.5%
2-bandgap, lateral	90.5%	90.3%	-	-
3-bandgap, lateral	83.7%	84.8%	-	-
3-bandgap, hybrid	91.5%	93.0%	90.9%	91.6%
4-bandgap, hybrid	90.0%	92.9%	89.1%	91.8%

4.4 Conclusion

In this chapter a “hybrid” photovoltaic spectrum splitting system is proposed that combines both lateral and vertically stacked cell arrangements. The cell arrangement is suitable for use with semi-transparent solar cells including many perovskite solar cells. The lateral spectrum splitting designs in Chapters 2 and 3 are used as a foundation for three- and four- bandgap hybrid system designs. It is shown that the conversion efficiency and the spectrum splitting efficiency are both higher for the hybrid system designs. The main reason the hybrid systems are more efficient than vertically stacked systems is because they reduce the losses from parasitic absorption in the transparent conductive oxide layers of perovskite solar cells. A general observation is made that for each additional energy bandgap the spectrum splitting efficiency decreases for each cell arrangement that is considered. However, the reduction in spectrum splitting efficiency is much lower for hybrid cell arrangements since the sensitivity of the optical design on the cell transparency and lateral spectral separation are more relaxed compared to systems with just vertically stacked or lateral cell arrangements. For these reasons it is concluded that hybrid cell arrangements may be useful for high efficiency photovoltaic systems with three, four or more energy bandgaps.

Chapter 5

Energy Yield Analysis and Bifacial Spectrum Splitting

In previous chapters the design and simulation of several different spectrum splitting systems is presented. The main metric used in these designs is the power conversion efficiency. In this chapter the focus is shifted from power conversion efficiency to energy yield. A design that enhances the energy yield of a spectrum splitting system by converting light reflected from the ground surface using bifacial silicon cells is presented. The effect of different illumination conditions and solar tracking systems is also analyzed.

5.1 Introduction

In the previous chapters, several system designs are analyzed that have high power conversion efficiency. The power conversion efficiency is a standardized metric [51] and is useful for system design and comparison. However, a more important performance metric is the annual energy yield. The annual energy yield is the total electrical energy converted by a photovoltaic system throughout the course of a year and varies depending on a variety of factors [84]. In this chapter,

a technique for analyzing the energy yield is developed and the effect of bifacial light collection, local illumination conditions, and solar tracking is analyzed.

An example that illustrates the importance of energy yield in photovoltaic system design comes from the concentrating photovoltaic (CPV) industry. As discussed in Chapter 1, CPV systems focus direct sunlight onto small multijunction solar cells that have high conversion efficiency [11], [12]. Since multijunction cells are manufactured using slow epitaxial growth processes, the cells are expensive and CPV systems must have high levels of solar concentration to be cost effective. As a result of the solar concentration, CPV systems do not typically convert a significant fraction of diffuse sunlight and the energy conversion efficiency is much lower than the power conversion efficiency [13], [85]. While diffuse sunlight only consists of 10% of the standardized AM1.5 spectrum, it accounts for 15% to 40% of actual solar illumination even in characteristically sunny locations [71]. The inability to convert diffuse sunlight is an important reason why the CPV industry has declined in the last few years [13]. Another aspect of the CPV design that is an obstacle for commercial success is the requirement for dual-axis solar tracking. Dual-axis solar tracking systems are typically bulky and expensive and are not used in conventional photovoltaic systems.

One of the advantages of lateral spectrum splitting systems is that the difference between the energy conversion efficiency and power conversion efficiency is not as large as for CPV systems. In most locations the energy conversion efficiency is only slightly lower than the power conversion efficiency. When bifacial solar cells are used, the energy conversion efficiency can exceed the power conversion efficiency. Lastly, volume holograms are relatively insensitive to changes in the out-of-plane incidence angle. As a result, spectrum splitting systems can be mounted with single-

axis solar tracking with negligible losses in the energy yield due to the angular sensitivity of the hologram.

5.2 Energy Yield Analysis

In this section a methodology for calculating the expected annual energy yield (EY) of a photovoltaic system is presented. One of the primary assumptions made in this analysis is that the voltage of the PV cells is constant and does not vary as a function of irradiance. This assumption may not hold for very low irradiance levels. However, the total insolation for very low irradiance levels is much smaller than for typical irradiance levels. By making this assumption the energy yield can be decomposed into direct, diffuse, and ground reflected components which are denoted by the abbreviations EY_d, EY_f, and EY_r respectively:

$$EY = EY_d + EY_f + EY_r \tag{5.1}$$

The direct and diffuse components of the energy yield are calculated based on the power conversion efficiency for direct and diffuse sunlight which are denoted as PCE_d and PCE_f, respectively:

$$EY_d = PCE_d \cdot E_d, \tag{5.2}$$

$$EY_f = PCE_f \cdot E_f, \tag{5.3}$$

where E_d and E_f are the direct and diffuse solar insolation from the Typical Meteorological Year (TMY3) database at a specific location [71]. TMY3 is a database that contains the solar insolation that can be expected statistically for any given time of day for a variety of locations in the US. The direct solar insolation E_d is the “direct normal” data added up over the entire course of the year

and the diffuse insolation E_f is the "diffuse horizontal" data added up over the entire course of the year. The ground reflected component of the energy yield can be computed using the formula:

$$EY_r = \chi \cdot \left(E_d + E_f\right) \cdot PCE_r, \tag{5.4}$$

where PCE_r is the power conversion efficiency for the rear side of the module and $E_d + E_f$ is the total combined insolation on the front side of the panel, and χ is the irradiance factor given by:

$$\chi = \frac{E_r}{E_d + E_f} \tag{5.5}$$

The irradiance factor therefore represents the fraction of insolation on the rear side of the module E_r divided by the insolation on the front side of the module. Modeling the rear illumination is a challenging task that depends on factors related to the module spacing, ground clearance, tilt angle, and albedo [86]–[91]. In the literature, results are not typically reported in terms of the irradiance factor, but instead reported in terms of the bifacial gain (BG):

$$BG = \chi \cdot \phi, \tag{5.6}$$

where ϕ is bifacial factor. The bifacial factor is the ratio of the conversion efficiency of the rear side of the cell divided by the conversion efficiency of the front side of the cell [92]. The irradiance factor used in literature can be obtained by dividing the bifacial gain by the bifacial factor. In many cases, the bifacial factor is assumed to be one, so the bifacial gain is equivalent to the irradiance factor. In this Chapter the irradiance factor is calculated using an empirical formula by Kutzer et al. [86]:

$$\chi = \alpha \cdot 0.95 \cdot \left[1.037 \cdot \left(1 - \sqrt{gcr}\right) \cdot \left(1 - e^{-8.691 \cdot h \cdot gcr}\right) + 0.125 \cdot \left(1 - gcr^4\right)\right], \tag{5.7}$$

where α is the albedo, h is the length of the module, and gcr is the ground coverage ratio, or the ratio of the module length over the distance between modules. According to this model, the irradiance factor varies between 7.3% and 18.4% when the albedo varies between 20% and 50% for a fixed module height of h = 0.3m and ground coverage ratio of gcr = 0.5. In Pelaez et al. [87] the irradiance factor varies between 10% and 20%. Some studies show that the irradiance factor can be increased even further to 30% by elevating the modules 1m off the ground [88] and 50% for standalone modules [91]. In this analysis, an irradiance factor of 15% is assumed except when otherwise noted.

One other way to express the energy yield that is used in this Chapter is the energy conversion efficiency (ECE). The energy conversion efficiency is the fraction of the total energy yield EY over the total insolation incident on the front-side of the module:

$$ECE = \frac{EY}{E_d + E_f} \tag{5.8}$$

This expression provides a convenient comparison of the energy yield of systems in different locations and illumination conditions and provides a convenient metric for comparing monofacial and bifacial systems. For example, a monofacial silicon module with cell conversion efficiency η_s = 22.5% also has an ECE of 22.5%. A bifacial silicon module with the same cell efficiency and with a bifacial gain of 15% has an ECE of 25.9%. This example shows that a monofacial module must have a PV cell conversion efficiency of η_s=25.9% to achieve the same energy yield as the bifacial module.

5.3 Rear-side light collection

In this section, the design of a bifacial spectrum-splitting photovoltaic (BF-SSPV) system is proposed that combines spectrum splitting and bifacial approaches for increasing the energy yield. The conversion of ground-reflected light using bifacial photovoltaic (BFPV) cells is a technique for increasing the energy yield in a fixed collection region [92]. BFPV systems have received greater interest in recent years and are expected to surpass 30% of the total PV market share by 2025 [93]. BFPV systems use bifacial silicon solar cells that have electrical contact grids and PN-junctions designed to allow conversion from both the front and rear sides of the cell. The energy yield of a module with bifacial cells can be improved by 10% to 50% depending on the characteristics of the ground surface and the module array configuration as discussed in the previous section [86]–[91].

The basic layout of the BF-SSPV system is similar to the one discussed in Chapter 2. The unit cell design for the system is depicted in Fig. 5.1. One of the main differences between this design and previous designs is that the silicon cells are bifacial and convert light reflected from the ground surface. The wide-bandgap cell is assumed to be monofacial and a diffuser is located on the rear side of this cell to increase the collection of light that would otherwise not be converted. The diffuser increases the collection efficiency by scattering light from the rear surface of the monofacial cell towards the rear glass surface which, in turn, is reflected through total internal reflection onto the surface of the bifacial silicon cell and converted.

The spectrum splitting design, optimization, and simulation is performed using the methods described in Chapter 2. In the design example, the narrow-bandgap cell is a bifacial silicon cell that has an efficiency of 22.5% and a 1.1eV bandgap. The wide-bandgap cell is a monofacial GaAs

cell that has an efficiency of 28.8% and a 1.4eV bandgap. The shorter wavelength light is dispersed onto the GaAs cell and the longer wavelength light is dispersed onto the bifacial silicon cell. An additional geometrical parameter is used in this design that affects the rear-side light collection. The rear aspect ratio (RAR) is ratio of the thickness of the rear glass H_r divided by the total width of the unit cell $W_I + W_{II}$:

$$RAR = \frac{H_r}{W_I + W_{II}}, \tag{5.9}$$

where W_I is the width of the monofacial wide-bandgap cell and W_{II} is the width of the bifacial narrow-bandgap cell. In the design example provided here, PV cell 'I' is the monofacial GaAs cell and PV cell 'II' is the bifacial silicon cell. Another important aspect of the design is the concentration ratio (CR) which is discussed in Chapter 2 but is repeated here again:

$$CR = \frac{W_I + W_{II}}{W_I}, \tag{5.10}$$

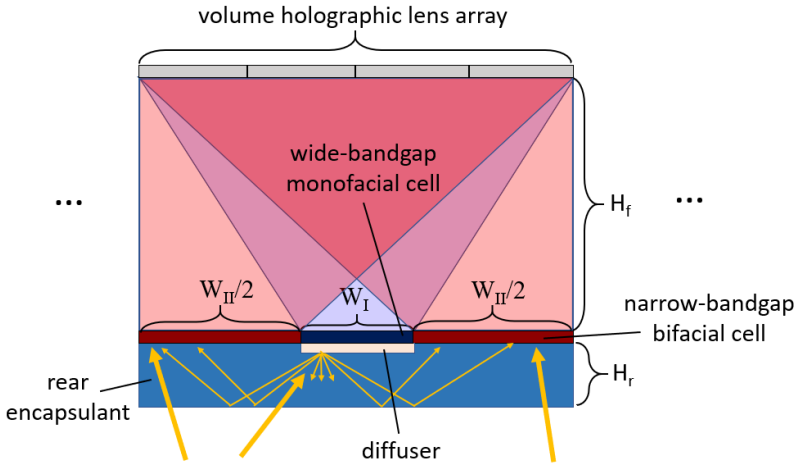

Figure 5.1: Illustration of a bifacial spectrum-splitting photovoltaic system. A volume holographic lens array focuses and disperses light onto a bifacial narrow-bandgap cell (cell 'II') and a monofacial wide-bandgap cell (cell 'I'). The energy yield is enhanced by converting light reflected from the ground surface with the bifacial cells. A diffuser on the rear side of the monofacial wide-bandgap cell increases rear-side light collection by scattering additional light onto the bifacial silicon cell.

Since the BF-SSPV system shares many aspects of the design in common with the systems discussed in previous chapters the main aspect of the design that needs to be addressed is the rear-side collection efficiency. The power conversion efficiency for the rear side of the module PCE_r is simulated with the non-sequential raytracing software FRED [70]. The FRED model is set up based on the unit cell geometry of the rear side of the module in Fig. 5.1. First, a 96% reflective Lambertian scattering surface is placed underneath PV cell 'I' to enhance light collection by the bifacial cell. Next, a glass slab with thickness, H_r, is placed underneath the PV cells. Lastly a source with total flux, G_r, is placed underneath the glass slab to simulate the ground reflected light. The source is assumed to be uniform for all angles in the hemisphere (2π steradians). The collection factor (CF) is determined by tracing rays from the source until they either escape from total internal reflection or are collected by the bifacial cell:

$$CF = \frac{I}{G_r}, \tag{5.11}$$

where I is the flux collected on the bifacial cell. The power conversion efficiency for the rear side of the module is now determined by multiplying the collection factor by the conversion efficiency for the bifacial cell, which in this design example is $\eta_s = 22.5\%$:

$$PCE_r = CF \cdot \eta_s, \tag{5.12}$$

The collection factor is plotted as a function of the concentration ratio and the rear aspect ratio in Fig. 5.2. The collection factor varies as a function of the concentration ratio since the system only converts light in the area covered by bifacial cells and does not convert light in the area filled by the monofacial cell. The collection factor depends upon the rear aspect ratio since this parameter affects the average number of scattering interactions a ray needs to experience before reaching the

bifacial cell. Each pass through the diffuse surface loses a percentage of light through the total internal reflection escape cone, so the rear aspect ratio needs to exceed a certain value to maximize the collection efficiency. With a RAR of 0.2, the collection factor is enhanced by up to 25% compared with a non-scattering surface. In the remaining parts of this analysis, a RAR value of 0.2 is assumed.

As mentioned previously the rear side collection efficiency varies as a function of the concentration ratio. As a result, the concentration ratio that gives the maximum energy yield is different than the concentration ratio that gives the maximum power conversion efficiency. The effect of the irradiance factor χ on the optimal concentration ratio is seen by plotting the power conversion efficiency as a function of the concentration ratio for $\chi = 0\%$ and $\chi = 15\%$ in Fig. 5.3. When the value of χ is equal to 0% the optimal concentration ratio is CR is 1.55 but when the value of χ is equal to 15% the optimal concentration ratio increases to 2.33. This changes the total surface area covered by bifacial cells from 40% to 60% of the module. For systems that use a more expensive wide-bandgap cell this change in concentration ratio may help increase the cost-benefit of the system. The change in optimal concentration ratio can be explained from the following reasoning. The irradiance factor is the fraction of solar insolation on the rear side of the module divided by the front side of the module. When the irradiance factor is high there is a greater rear side insolation E_r available for the module to convert with bifacial cells. This situation favors a greater surface area to be covered by the bifacial cell and less surface area covered by the monofacial cell.

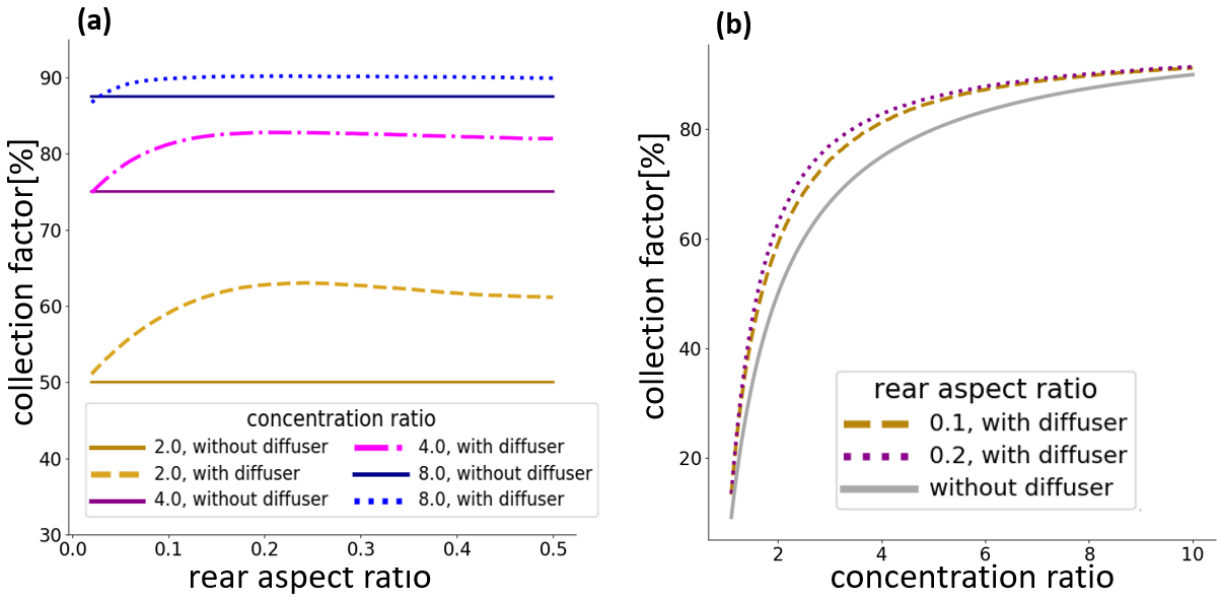

Figure 5.2: Fraction of the total rear-side insolation incident on the bifacial silicon cell, also referred to as the "collection factor". The collection factor is plotted as a function of (a) rear aspect ratio, and (b) concentration ratio. The results indicate the diffuser provides optimal enhancement when the rear aspect ratio is 0.2 and when the concentration ratio is near 2.

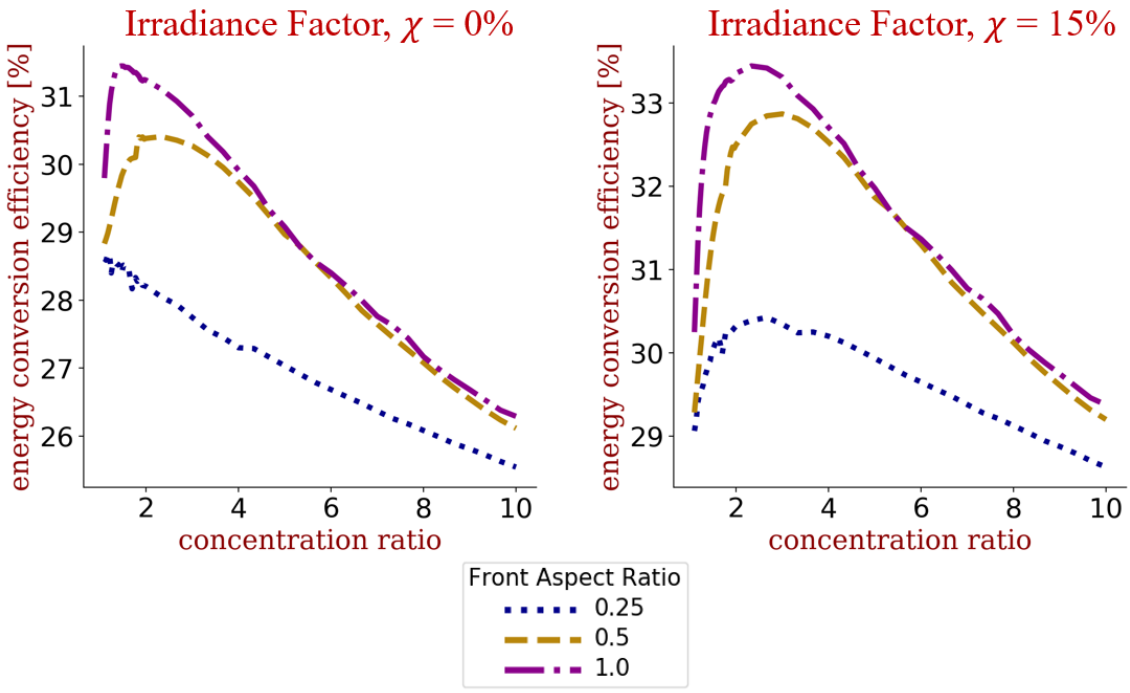

Figure 5.3: Plots showing the energy conversion efficiency as a function of the concentration ratio for a system with no illumination reflected from the ground surface (left) and a system with an irradiance factor of 15% (right). The optimal concentration ratio shifts from 1.55 to 2.33 between the two different illumination conditions and favors a greater surface area for the bifacial cell.

5.4 Illumination Analysis

Different locations, ground surface characteristics, and module array geometries result in varying illumination conditions and module performance. To analyze the performance of the module, the energy yield is computed for different illumination conditions and plotted in terms of the energy conversion efficiency in Fig. 5.4. On the horizontal axis, the ratio of diffuse insolation divided by front-side insolation is plotted. On the vertical axis the irradiance factor is plotted, which is the ratio of rear-side insolation divided by total front-side insolation. The percentage of diffuse illumination for different locations and for the standardized STC conditions are also indicated [51].

The energy conversion efficiency of the BF-SSPV system in the AM1.5 illumination condition without any rear-side illumination is 31.4%. For an irradiance factor (7.3%) corresponding to a surface albedo of 20%, the energy conversion efficiency increases to 32.2%. For an irradiance factor (18.4%) corresponding to a surface albedo of 50%, the energy conversion efficiency is further increased to 34.0%. However, these energy conversion efficiency values do not factor in the varying performance in actual illumination conditions in which there is a greater percentage of diffuse sunlight [71]. The ratio of diffuse sunlight to direct sunlight for three different locations in the US is marked on the horizontal axis of the plot. The most arid location that is marked is Tucson where 17% of the solar insolation is diffuse. In this condition the spectrum splitting module converts 31.0% of the total annual solar insolation without considering any ground reflected light. In Dallas, the diffuse ratio increases to 26% and the energy conversion efficiency decreases to 30.5%. The final location considered is Seattle where 34% of the solar insolation is diffuse and the energy conversion efficiency is 30.1%.

The actual energy yield for each of these locations varies considerably more than the energy conversion efficiency. In Tucson, the annual energy yield is $955\frac{kw \cdot hr}{yr \cdot m^2}$, compared to $525\frac{kw \cdot hr}{yr \cdot m^2}$ in Seattle. The primary reason for the large difference in energy yield is the difference in total solar insolation which ranges from $3080\frac{kw \cdot hr}{yr \cdot m^2}$ in Tucson to $1750\frac{kw \cdot hr}{yr \cdot m^2}$ in Seattle. A secondary reason for the decreased energy yield is the decreased energy conversion efficiency which decreases from 31.0% in Tucson to 30.1% in Seattle.

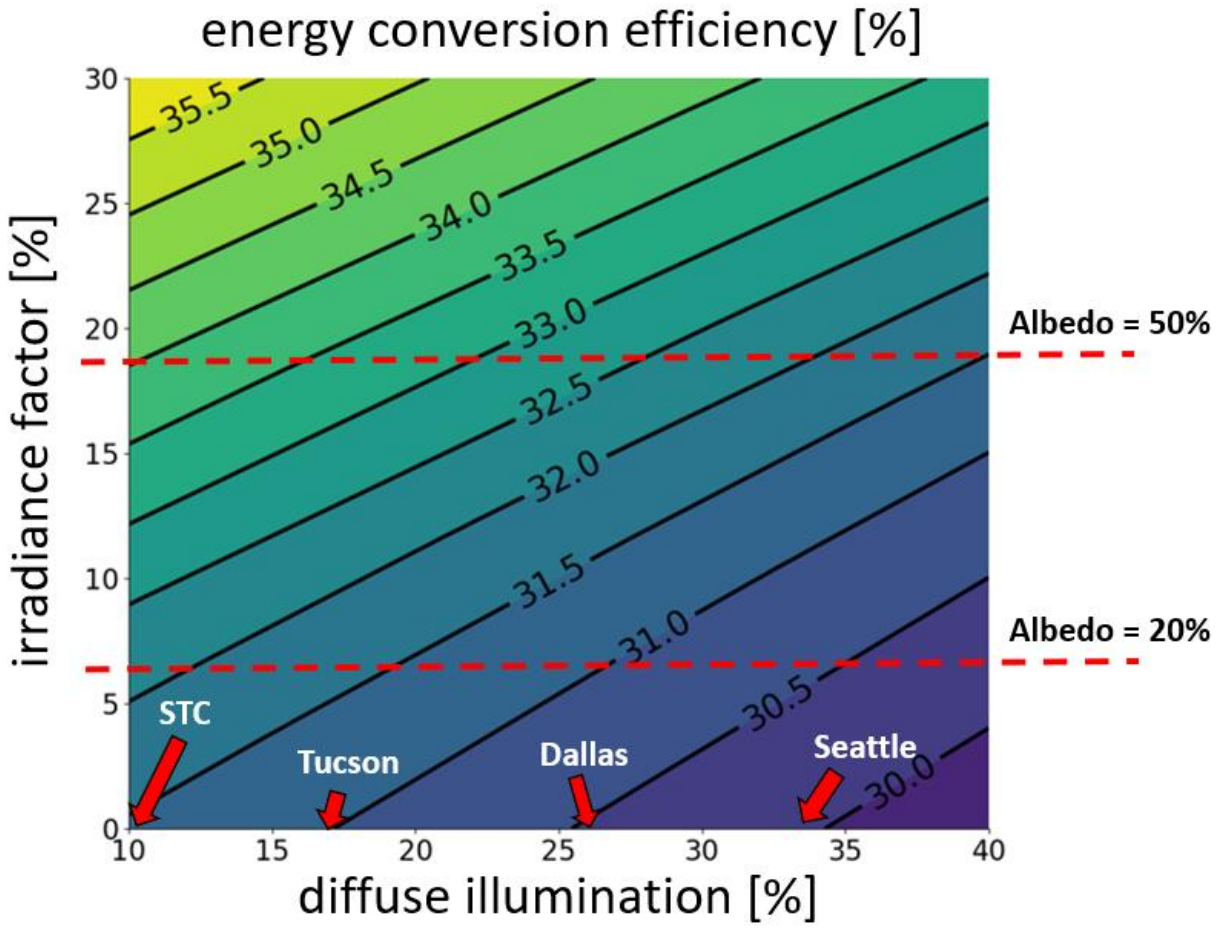

Figure 5.4: Contour plot of the energy conversion efficiency for different illumination conditions. The fraction of diffuse insolation divided by direct insolation is plotted on the horizontal axis. The irradiance factor χ, or the fraction of rear-side insolation divided by the total front-side insolation is plotted on the vertical axis. The percentage of diffuse illumination for Tucson, Dallas, and Seattle are marked as well as the standardized STC condition.

5.5 Solar Tracking

The diffraction efficiency of a volume hologram is sensitive to the angle of incidence of light [55]. In the previous calculations it is assumed that sunlight is normally incident and the angular selectivity of the holograms is not considered. This assumption is valid when the photovoltaic system is mounted with dual-axis solar tracking but is not valid for single-axis tracking or for modules on a fixed mount without solar tracking. Fortunately, the angular selectivity of a volume hologram is far lower for out-of-plane incidence angles compared with in-plane incidence angles (Fig. 5.5). Holographic spectrum splitting modules are compatible with single-axis solar tracking by orienting the hologram fringes in the direction of the daily movement of the sun [45], [94]. In this orientation, the only variation in the incidence angle of sunlight occurs in the out-of-plane direction as the position of the sun varies between seasons. As is seen in the following analysis the seasonal variation of the sun (+/-23.5 degrees) is lower than the acceptance angle of the spectrum splitting system.

The power conversion efficiency for direct sunlight is computed over a range of incidence angles for a combination of a 22.5% efficient silicon cell and a 28.8% efficient GaAs cell. The diffraction efficiency simulation is performed in RSOFT for both TE and TM modes. The power conversion efficiency is plotted in Fig. 5.6. The in-plane incidence angle is plotted on the horizontal axis and ranges between -2 degrees and +2 degrees. The out-of-plane incidence angle is plotted on the vertical axis and ranges between -25 degrees and +25 degrees. The power conversion efficiency decreases from 32.0% to 31.7% when increasing the out-of-plane incidence angle from 0^o to 23.5^o. This reduction in power conversion efficiency is caused by the seasonal variation of the sun. Another potential reduction in the power conversion efficiency occurs for systems with imperfect tracking accuracy. In Fig. 5.6 a box is marked that indicates the range of

incidence angles that are possible over the course of the year for a single-axis solar tracking system with +/- 0.5 degree accuracy [94], [95]. The average power conversion efficiency inside this box is 31.9%. This is a decrease of only 0.1% and does not a significantly decrease they energy yield of the system.

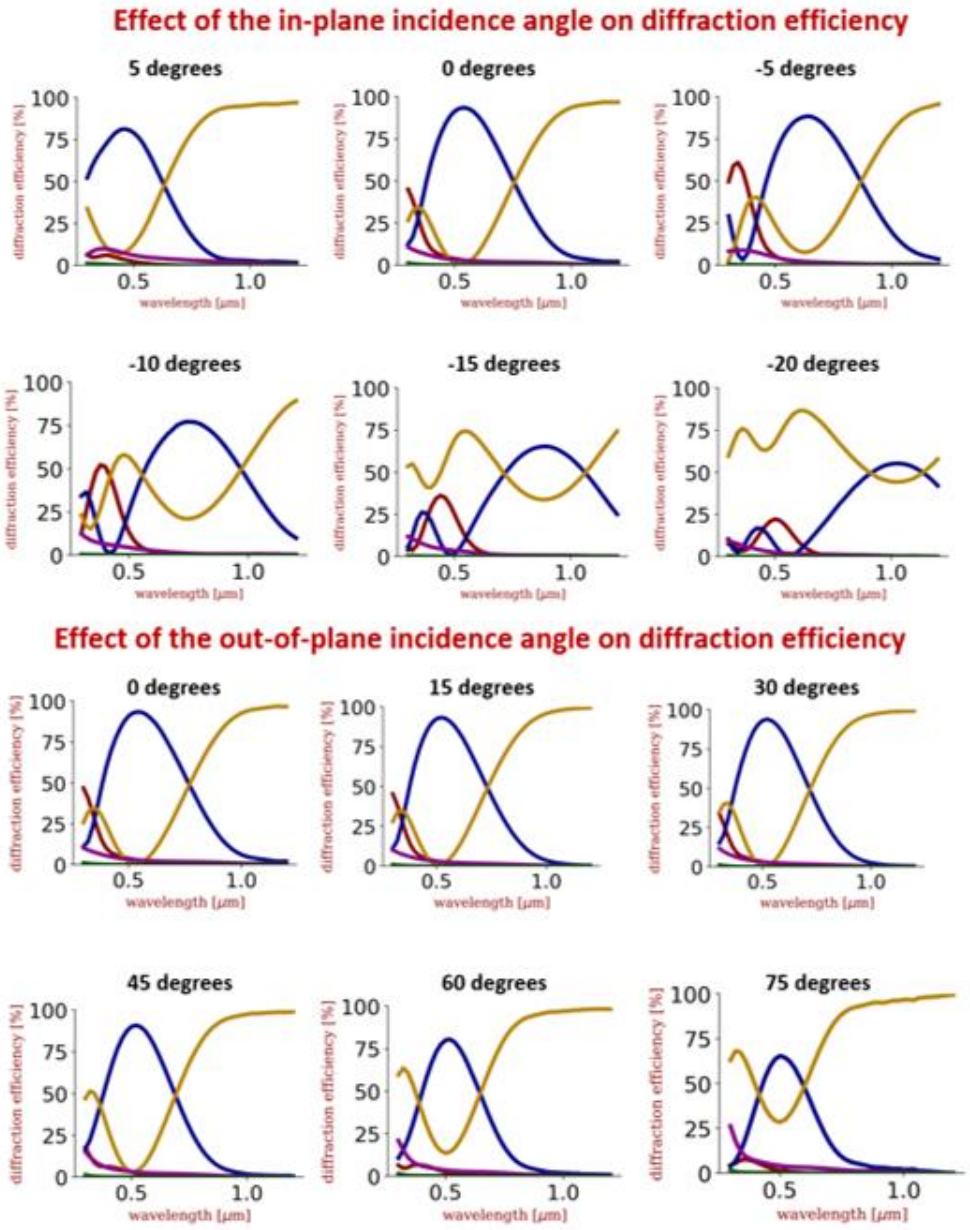

Figure 5.5: Spectral diffraction efficiency for in-plane incidence angles ranging from 5^{o} to -20^{o} and for out-of-plane incidence angles ranging from 0^{o} to 75^{o}.

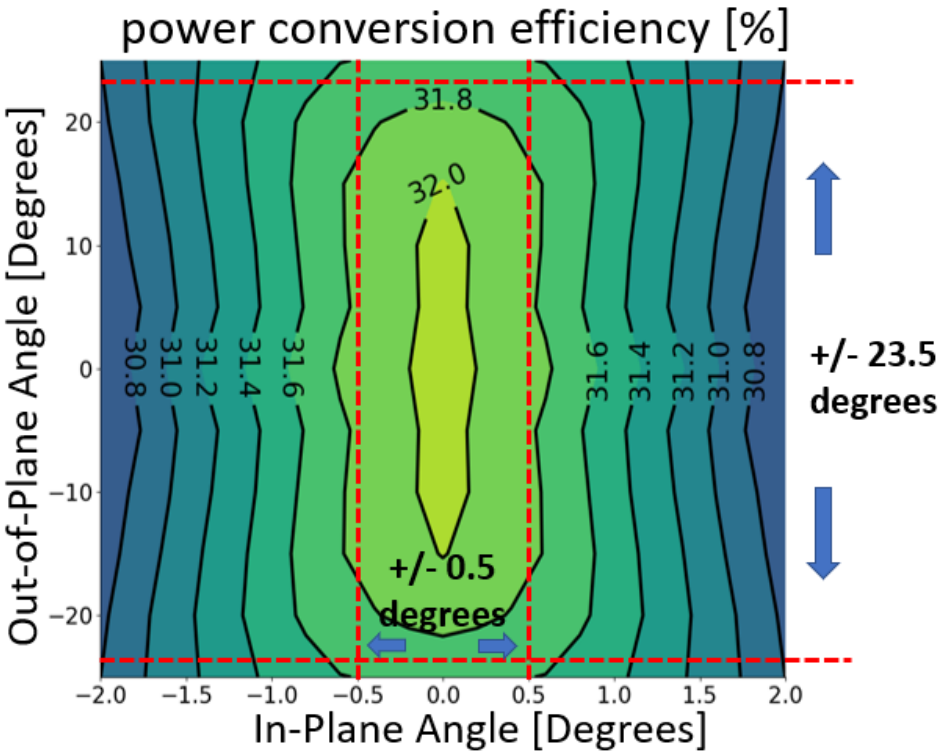

Figure 5.6: Contour plot showing the effect of the in-plane incidence angle and the out-of-plane incidence angle on power conversion efficiency for direct sunlight. This plot is generated for a combination of a silicon cell with a conversion efficiency of 22.5% and a GaAs cell with a conversion efficiency of 28.8%.

The tracking efficiency for a combination of 1.25eV and 1.72eV perovskite cells is also plotted for different in-plane and out-of-plane incidence angles in Fig. 5.7. One way the angular bandwidth can be measured is the range of angles in which the overall power conversion efficiency is greater than the average conversion efficiency of the individual PV cells. For this cell combination the average cell efficiency is 20.1%. Using this metric, it can be seen that the in-plane angular bandwidth is +/-12^{o} and the out-of-plane angular bandwidth is greater than the +/-75^{o} angular range that was simulated. Finally, the in-plane tracking efficiency is calculated for the three-bandgap lateral spectrum splitting system designed in Chapter 3. The average PV cell efficiency of this combination is 17.5%. This system has a lower angular bandwidth of +/-8^{o}. One of the reasons for this is a lower average cell efficiency (17.5%) compared with the two-bandgap system (20.1%).

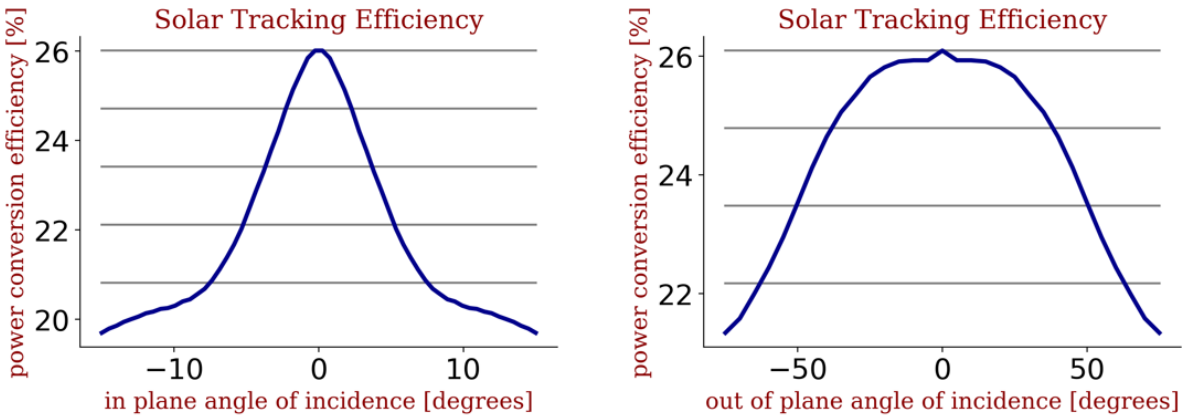

Figure 5.7: power conversion efficiency for in-plane and out-of-plane incidence angles for a combination of 1.25eV and 1.72eV perovskite cells. The grey lines are marked at intervals of 5% reductions from the maximum power conversion efficiency.

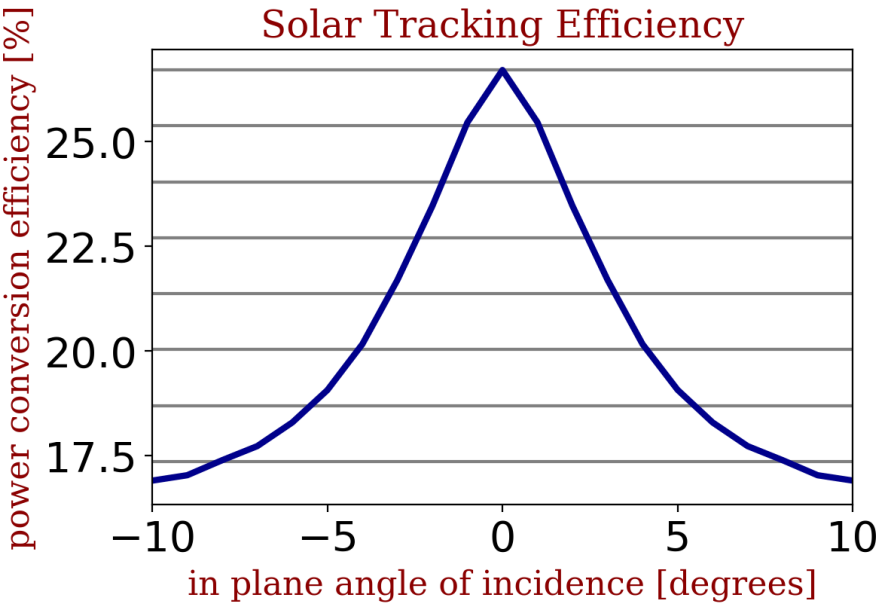

Figure 5.8: Power conversion efficiency as a function of the in-plane incidence angle for a three-bandgap lateral spectrum splitting system with 1.25eV, 1.63eV, and 2.3eV perovskite solar cells.

5.6 Conclusion

In this Chapter an energy yield analysis is presented for spectrum splitting systems. The analysis accounts for the effect of single-axis solar tracking and the varying illumination conditions

in different locations of the US. The effect of single-axis solar tracking for a system with +/- 0.5 degree accuracy reduces the power conversion efficiency for direct sunlight from 32.0% to 31.9% over the course of the year. When accounting for the effect of diffuse illumination, the energy conversion efficiency decreases from 31.4% in ASTM standardized conditions to 31.0% in Tucson AZ and further to 30.1% in Seattle WA. A spectrum splitting design is also proposed which uses bifacial cells to increase the energy yield. In this design, the energy conversion efficiency is increased from 31.4% to 32.2% for surfaces with an albedo of 20% and further to 34.0% for surfaces with an albedo of 50%.

Chapter 6

Holographic Materials

Several spectrum-splitting designs are designed and analyzed in the previous chapters of this dissertation. Each of these systems use volume holographic optical elements to provide spectral separation. However, there are a number of challenges related to the use of holographic materials in spectrum splitting systems which are addressed in this chapter. The first aspect that is addressed is the environmental stability of volume holograms. Unfortunately, it is found that a common holographic material photopolymer Covestro Bayfol HX degrades significantly when exposed to sunlight for a period of several weeks. Another common holographic material, dichromated gelatin, has been used in commercial photovoltaic systems that passed lifetime testing. However, this material is very sensitive to environmental parameters during the fabrication process. For this reason a reproducibility study is conducted and it is found that controlling the humidity during the drying stage of the film preparation process helps reduce the variability in the measured spectral transmission.

6.1 Introduction

There are several requirements for holographic materials to be suitable for use in solar energy applications. The first requirement is that the material has sufficient spectral bandwidth and

diffraction efficiency. Two common materials that satisfy this constraint are Covestro Bayfol HX [96], [97] and dichromated gelatin (DCG) [61]–[63]. Both materials can be manufactured with film thickness sufficiently thin to provide spectral bandwidths ranging between 200nm and 500nm. Additionally, each material has been demonstrated with diffraction efficiencies greater 95%.

A second requirement is that the material can withstand more than 30 years of solar and environmental exposure. Solar panel temperatures can rise in excess of 80^{o}C and cycle during day/night and seasonal variations. In this chapter an experiment is presented that shows that Bayfol HX degrades significantly over the course of just 16 weeks in outdoor solar exposure conditions. The Covestro samples are an older formulation (HX 102) but show the potential risk of using photopolymer materials in solar energy applications. In the DCG samples, there is minimal degradation until they are exposed to moisture. With proper edge sealing DCG has potential for high environmental stability. This is supported by the fact that DCG holographic solar concentrators from Prism Solar passed accelerated lifetime testing and were certified for operational durations in excess of 25 years (Fig. 6.1) [46].

A third requirement for use in spectrum splitting photovoltaic systems is that the hologram fabrication process is reproducible and there is little variation in the spectral diffraction efficiency. Although a number of experiments and commercial applications using DCG have indicated it is possible to achieve repeatable results [62], [98], [99], it is well known for being extremely sensitive to environmental parameters [100], [101]. Surprisingly, there is little information in the literature on the specific parameters and processes that are most sensitive, methods for improving the reproducibility, and the underlying variability in the hologram fringe structure that causes the observed differences in diffraction efficiency. In this chapter a reproducibility study is conducted and it is shown that the material is most sensitive to humidity while the film is drying during the

film preparation process. It is shown that by regulating the humidity at 65% the variability in the spectral diffraction efficiency is reduced by a factor of six. It is also shown that one of the most important reasons for the observed variability in the diffraction efficiency is due to changes in the film swelling and shearing which shift the slant angle of the fringes.

Figure 6.1: Holographic solar concentrator modules made by Prism Solar that use dichromated gelatin holographic material.

6.2 Environmental Stability

6.2.1 Experimental Design

Transmission and Reflection holograms are prepared in both DCG and Covestro photopolymer materials. DCG holograms are prepared using a mold coating procedure that is explained in more depth in Section 6.3. The resulting film thickness for the DCG holograms is 20μm. The other set of holograms are fabricated in a 16μm thick commercial photopolymer Covestro Bayfol HX 102. The "102" formulation is several years old and is no longer available for purchase but shares many characteristics in common with the current Bayfol HX 200 formulation including film thickness and index modulation.

The DCG transmission holograms are formed with construction angles of -25^o and -5^o relative to the film normal and exposed with 250mJ/cm^2 of 532nm laser light (Fig. 6.2). Bayfol HX transmission holograms are formed with construction angles of -5^o and 15^o and exposed with 24mJ/cm^2 at 532nm. After processing, the Bragg angles for the samples are -5^o and 15^o for Bayfol HX and -20^o and 0^o for DCG.

DCG reflection holograms in this study are formed with construction angles of 10^o and 170^o relative to the film normal and exposed with 650mJ/cm^2 of 532nmm laser light. After the chemical film processing the holograms are measured to have a spectral bandwidth of 135nm. Bayfol HX reflection holograms in this study are formed with construction angles of 20^o and 160^o and exposed with 200mJ/cm^2 of 532nm laser light. After processing they had a bandwidth of 18nm. The difference in spectral bandwidth between the two holograms is due to non-linear film swelling in DCG [102].

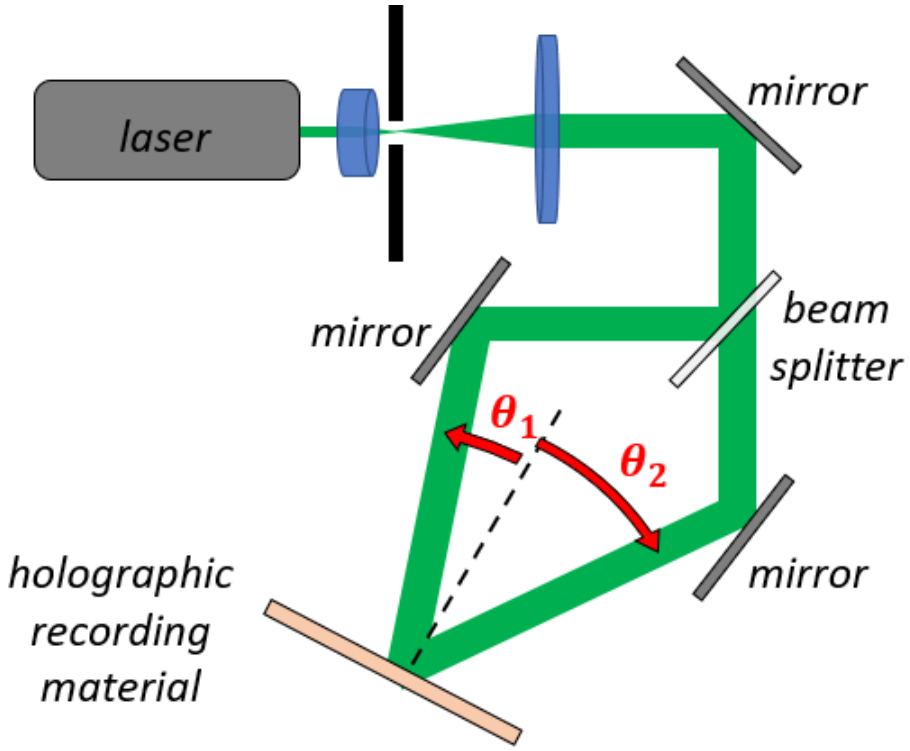

Figure 6.2: Optical setup for fabricating transmission volume holograms.

Each sample is encapsulated and sealed with Sylgard Silicon Elastomer 184 and a cover glass for protection against water vapor, precipitation, and abrasive particles. The glue is intended for use in PV modules, and is hydrophobic and water resistant. No visible degradation of the seal is observed over the course of the study. A picture of a sealed Covestro transmission hologram is shown in Fig. 6.3a.

Two groups of holograms are prepared: one as an exposure group and one as a control group. Each group consists of a total of 10 test samples, consisting of two transmission and two reflection holograms each for DCG and Bayfol HX materials and two samples without any holographic material. The experimental group is attached to a silicon photovoltaic panel as pictured in Fig. 6.3b and placed in an unobstructed area in Tucson, AZ. The panel faces towards the south and is tilted at approximately 30^o to maximize the solar insolation. The control group is placed in a dark cabinet

in a climate-controlled building. The experimental group is exposed to solar illumination for periods of four weeks at a time. In between each period the spectral transmittance and the angular diffraction efficiency are measured. The cover glass and substrate for each sample is cleaned before the measurement to eliminate differences due to dirt accumulated on the exposed samples.

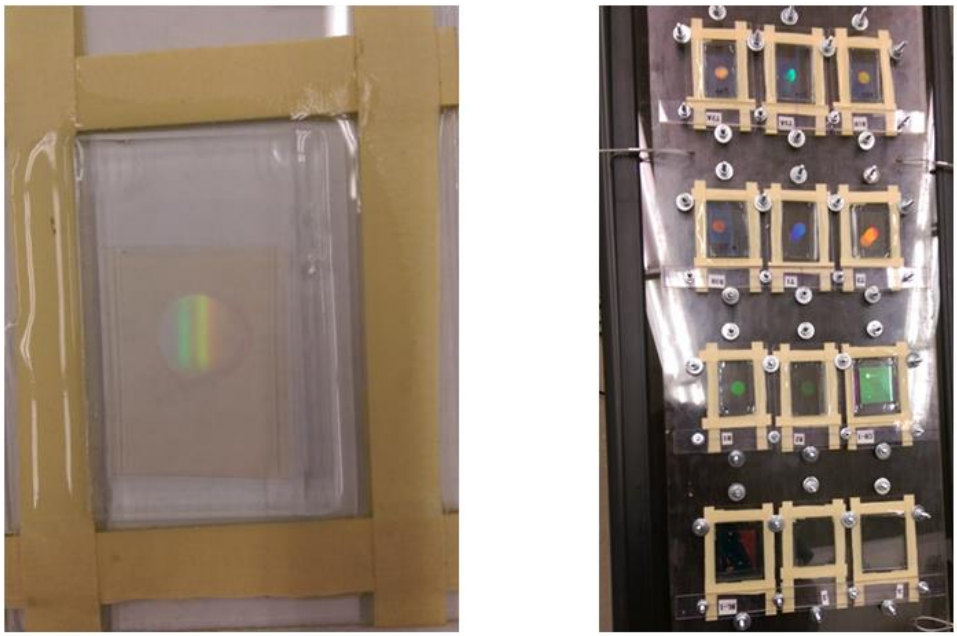

(a) (b)

Figure 6.3: (a) Sealed Bayfol HX transmission hologram. (b) Experimental group samples attached to silicon PV panel.

6.2.2 Experimental Results

The exposed holograms are evaluated by measuring the diffraction efficiency as a function of angle of incidence. Bayfol HX holograms are measured at the recording wavelength of 532nm for both transmission and reflection holograms. DCG transmission holograms are also measured with a 532nm laser light but the reflection holograms are measured with 632.8nm laser light to better match the spectral acceptance range of the hologram. The diffraction efficiency η as a function of angle θ is the ratio of diffracted light to the total light transmitted into the film:

$$\eta(\theta) = \frac{P_{diff}(\theta)}{P_{inc} - P_{refl}(\theta)}, \tag{6.1}$$

where P_{diff} is the measured power of the diffracted beam, P_{inc} is the measured power of the incident beam, and P_{refl} is the power of the beam reflected from the hologram.

The hologram is illuminated with a light from a collimated tungsten halogen lamp with an incident spectrum of $P_{inc}(\lambda)$. The hologram is rotated to the Bragg angle before measuring the transmitted spectrum $P_{trans}(\lambda)$ with a USB2000+ Ocean Optics spectrometer. The spectral transmittance $T(\lambda)$ is:

$$T(\lambda) = \frac{P_{trans}(\lambda)}{P_{inc}(\lambda) - P_{refl}(\lambda)}, \tag{6.2}$$

where $P_{refl}(\lambda)$ is the reflected spectrum. The transmittance of the holographic material is also measured in the area where there is no grating to determine the absorption and scattering in the material. No discernable changes in the measurements or visual appearance of the control group are detected.

The average spectral transmittance of the Bayfol HX film is shown after each 4-week period in Fig. 6.4a. A consistent reduction in the transmittance of the film is observed over the entire spectral range and is due to increased levels of absorption. After the full 16 weeks of sun exposure, a 43% increase in absorption was measured for a wavelength of 400nm. The absorption also causes a distinct yellowing of the film as pictured in Fig. 6.5.

The angular diffraction efficiency of a Bayfol HX transmission hologram and Bayfol HX reflection hologram are plotted in Figs. 6.4b,c. The peak diffraction efficiency for the transmission holograms reduced by 22% and by 26% for the reflection holograms. An 8^{o} degree shift in the

Bragg angle is measured for the reflection holograms. This shift indicates that the material swells by a factor of 4% over time as it is exposed to heat and sunlight. This swelling value is also expected to shift the slant angle of the transmission hologram from 5.0^{o} to 4.8^{o}. Since the resolution of the measurement is only +/- 1^{o} it cannot be confirmed if the same swelling occurs for the transmission hologram.

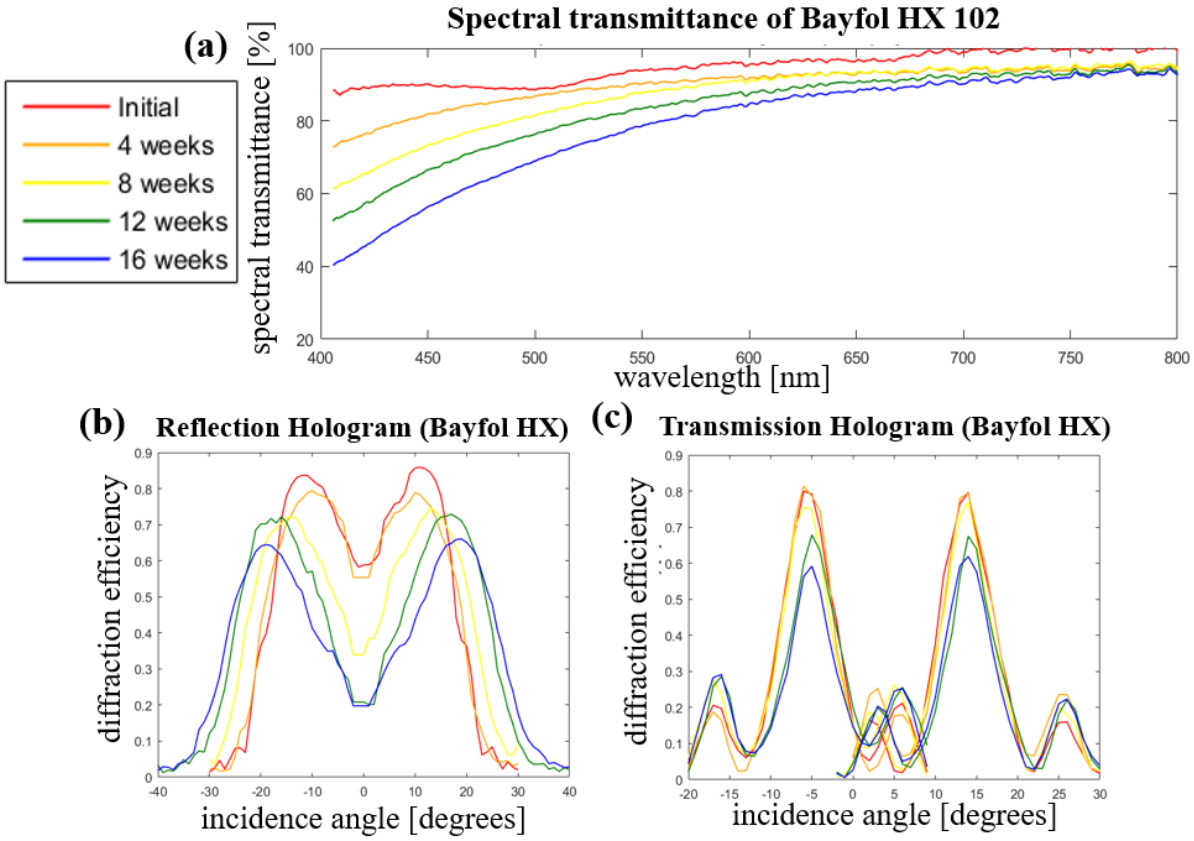

Figure 6.4: Measurements of Bayfol HX 102 after 4-week intervals of sun exposure for a total of 16 weeks. (a) Spectral transmittance of the film. A strong increase in absorption is observed that causes yellowing of the film. (b) Angular diffraction efficiency for a transmission hologram. (c) Angular diffraction efficiency for a reflection hologram. (d) Spectral transmittance of a reflection hologram.

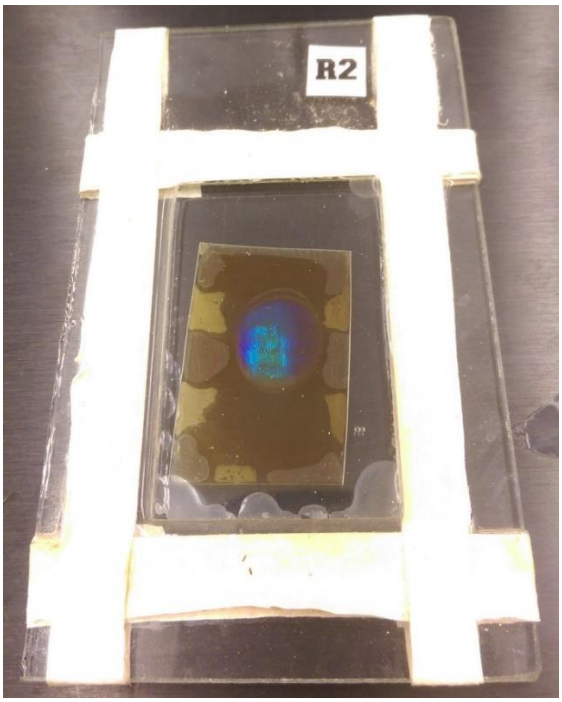

Figure 6.5: Picture of the Covestro Bayfol HX 200 after 16 weeks of sun exposure. A distinct yellowing of the film is observed.

The angular diffraction efficiency of a DCG transmission hologram and a DCG reflection hologram are plotted in Figs. 6.6a,b. The transmission holograms show a 3% reduction in peak diffraction efficiency over the 16 weeks of exposure and the reflection holograms show a reduction of 2%. A reduction in angular bandwidth is also observed for the reflection hologram. This is caused by film shrinkage which can be verified based on the blue-shift observed in the spectral transmittance of the reflection hologram (Fig. 6.6c).

After the monsoon rains, pockets of moisture are observed to slowly diffuse through the edges of the seal towards the DCG gratings (Fig. 6.7). Once the moisture reaches the grating the diffraction efficiency quickly drops to zero. Aside from the film shrinkage, this is the main effect observed in the DCG material. By properly sealing the edges of the film with desiccant materials, the environmental stability of the material may be improved and reach the levels required for commercial applications such as the holographic solar concentrator from Prism Solar (Fig. 6.1).

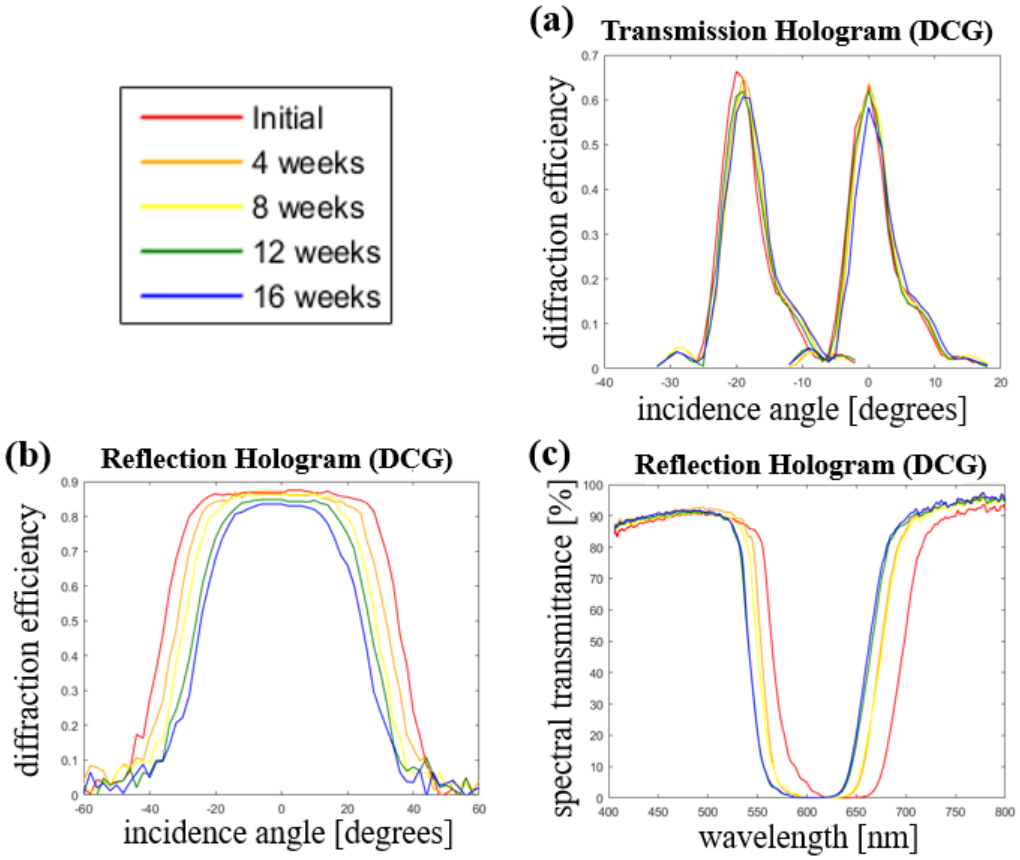

Figure 6.6: DCG samples after 4-week intervals of sun exposure for a total of 16 weeks. (a) Angular diffraction efficiency of a transmission hologram. (b) Angular diffraction efficiency of the reflection hologram. (c) Spectral transmission of the reflection hologram.

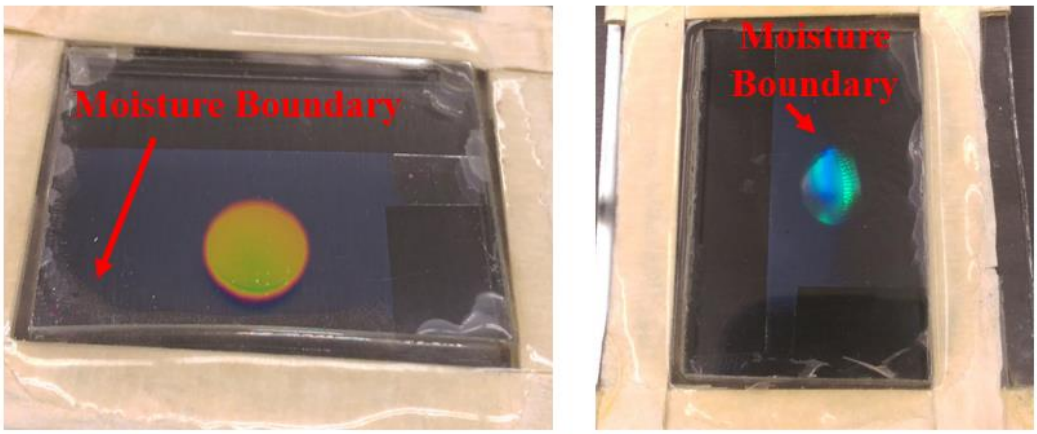

Figure 6.7: Picture of a DCG reflection hologram and a DCG transmission hologram after more than 20 weeks of sun exposure. After the monsoon season brought rain, moisture began to diffuse from the edges of the seal towards the hologram. Once the moisture reached the hologram the diffraction efficiency quickly dropped to zero. In the left picture the moisture has not yet reached the grating. In the picture on the right the moisture has partially engulfed the grating.

6.3 Reproducibility in Dichromated Gelatin

Dichromated gelatin (DCG) is a holographic material that was developed in the 1960s and is still used today [61], [64]. DCG has a number of excellent qualities including low cost ($3/m^2), high index modulation capacity (>0.1), and optical transparency (>98%) [45], [103]. DCG holograms can be made with basic laboratory equipment through a variety of film deposition and chemical development processes. In addition to the excellent optical qualities, the chemical development process can be modified to provide increased spectral and angular bandwidth by imparting a non-linear modulation of the index of refraction [49], [102]. Despite its advantageous qualities, it is difficult to obtain consistent or "repeatable" results in holograms recorded in dichromated gelatin. In comparison, Covestro Bayfol HX photopolymer has a simple and reliable development process which has led to greater commercial success.

Even though the problem with reproducibility of DCG is well known, there is little information in literature available on the causes of the observed variations and solutions for improving it. Stojanoff noted that the humidity and temperature are important environmental parameters for attaining repeatable results [62] but did not quantify the observed variations, identify which processing step is the most critical to control, or specify the optimal environmental conditions for achieving the most reproducible results. Neither did they specify which hologram parameter (film thickness, index modulation, K-vector etc.) varies that causes the measured changes in the diffraction efficiency.

In this section, the humidity during the film drying stage is identified as a critical environmental parameter for achieving reproducible results using a mold coating film preparation process. A clear reduction in the variability of the spectral transmittance is observed for a set of DCG holograms

that are dried with an environmental humidity of 65%. Furthermore, it is determined that the most important factor in the reproducibility of dichromated gelatin is the variability in the slant angle of the hologram fringes. Another factor that affects the reproducibility are variations in the index modulation. However, it is determined that the variations in film thickness are less than 1μm and do not significantly affect the reproducibility.

6.3.1 Film Preparation Process

In this experiment DCG film is prepared using a mold coating process. Some of the parameters used in the film preparation process are listed in Table 6.1. First, a gelatin solution is formed by mixing 25 grams of water with 3 grams of 300 bloom strength type-A gelatin (Sigma-Aldrich [104]) for 45 minutes or until the gelatin is fully dissolved. The gelatin solution is placed in a 50^{o}C bath to increase the solubility. Next, 0.5 grams of ammonium dichromate is mixed into the gelatin solution for 20 minutes or until it is fully dissolved.

Once the solution is fully dissolved 2 to 3 milliliters are placed on a mold. The mold is formed by placing strips of tape around the edges of a glass substrate as pictured in Fig. 6.8. The thickness of the tape is known and can be modified to adjust the resulting holographic film thickness. In this experiment 7 mil tape is used. A mold release agent, RainX, is applied to the mold to prevent the DCG film from sticking to the mold. Next, a glass cover plate is pressed against the mold and the gelatin mixture. The excess gelatin mixture is forced out of the corners of the mold. The mold and substrate are pressed together by placing clips along the edges. Next, the dichromated gelatin molds are placed in a refrigerator which is set at a temperature of 13^{o}C. The mold is kept in the refrigerator for 45 minutes or until the gelatin has a firm and rubbery texture. Finally, the mold

and the substrate are carefully separated and the process is successful if the DCG film adheres to the cover glass.

Table 6.1: Key parameters for the preparation of dichromated gelatin film using a mold coating process.

Deionized water	**25g**
Type-A 300 bloom gelatin	**3g**
Ammonium dichromate	**0.5g**
Gelling temperature	**13°C**
Gelling time	**45 minutes**
Curing time	**24 hours**

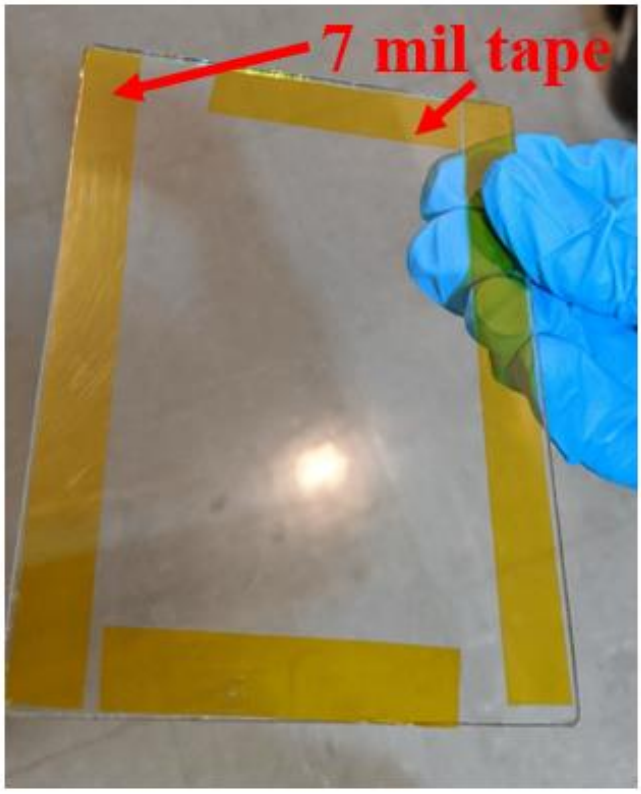

Figure 6.8: The dichromated gelatin mold consists of a 4" by 5" glass slab with strips of tape surrounding the edges. RainX is applied on the surface of the mold to prevent the film from sticking to the mold.

At this stage in the process the DCG film is still soft since it contains most of its initial water content. The next step in the film preparation process is drying the film to remove the excess water. Drying is accomplished by placing the samples in a "drybox" (Fig. 6.9). The drybox used in this experiment reduces the humidity to maintain a setpoint. However, if the humidity drops below the setpoint, the drybox is not able to increase the humidity to maintain the setpoint. To help regulate the humidity, a beaker of water is placed at the bottom of the box. The beaker of water slowly increases the humidity of the drybox until the setpoint is surpassed and the drybox starts regulating the humidity. The humidity can be controlled between 25% and 75% using this method. However, when the film is initially placed in the drybox, the local humidity inside increases rapidly and is not able to be regulated. An important technique for achieving good results is to crack the drybox open for the first several minutes so that some of the humidity escapes and the local humidity near the DCG sample can be maintained at the setpoint throughout the entire process. A fan is placed below the DCG film to provide air flow and is an essential part of the drying process. The film usually has high levels of scattering if there is not enough air flow during the film drying process. The film is left in the drybox for 24 hours before it is ready to be exposed. Each substrate is cut into four smaller sections before recording and up to three holograms are recorded on each sample.

Two groups of holograms are recorded with different lasers. In the first group, four sets of holograms are recorded with a 514nm argon laser with drying humidity setpoints of 20%, 35%, 45%, and 55%. Each set has 21 to 35 samples which are recorded with beam angles of 7.5^{o} and 31^{o} and an exposure energy of $200mJ/cm^2$. The beam angles are selected based on a reconstruction condition that accounts for film swelling that occurs during the chemical processing. The reconstruction condition is calculated so that normally incident light with a wavelength of 600nm is Bragg matched and has high diffraction efficiency. Unfortunately, the laser failed before samples

with higher humidity setpoints could be recorded. However, the first group still provides useful data for analysis and is compared alongside a second group fabricated with a 457nm DPSS laser. In the second group, six sets of holograms are recorded with drying humidity setpoints of 25%, 35%, 45%, 55%, 65%, and 75%. Each set has 10 to 16 samples which are recorded with beam angles of 8.9^{o} and 29.5^{o}. The beam angles are selected so that the K-vector of the second group of holograms matches the K-vector of the first group. The initial two sets are exposed with an energy density of 180mJ/cm^2. However, for the remaining sets of holograms the sensitivity to the exposure energy density increased so the energy density is reduced to 60 mJ/cm^2.

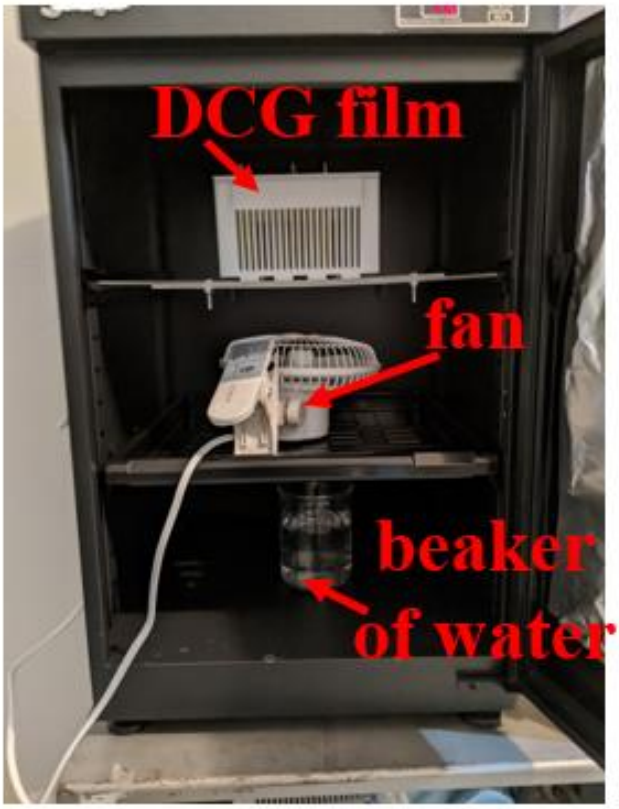

Figure 6.9: A drybox is set up for drying the DCG film and regulating the humidity. The DCG film is placed on the top rack, a fan is placed on the middle rack to provide air flow, and a beaker of water is placed on the bottom rack to gradually increase the humidity until the drybox begins to regulate the humidity.

After exposing the film, the samples are chemically processed to form the gratings. A diagram of the different steps used to process DCG is shown in Fig. 6.10. First, the samples are placed in a Kodak fixer bath for 90 seconds which removes dichromate from the null regions of the interference fringes. The removal of dichromate creates microscopic air bubbles, reduces the average index of refraction in the null areas, and results in a modulation of the index of refraction. A second property of the Kodak fixer bath is that it increases the strength, or "hardness" of the gelatin emulsion. This improves the optical transparency because in a weaker film the size of the microscopic air bubbles significantly increase and cause scattering in the film. Next, the film is placed in water for 60 seconds to wash out and remove the gelatin that was not chemically fixed with the Kodak fixer bath. The final three baths are filled with isopropyl alcohol (IPA)/water mixtures that have increasing IPA concentration from 50% to 99%. The IPA bathes are used to remove water from the gelatin film and can create high levels of stress in the film and cause light scattering. The gradual increase in IPA concentration reduces the stresses in the film and improves the optical transparency. After the IPA baths, the film is dried with compressed air and placed in a 60 ^{o}C temperature oven for 15 minutes to remove residual IPA and water content. The exposure and chemical processing are done in a partially controlled environment, with room humidity ranging between 20% and 30% and the room temperature ranging between 27^{o}C and 29^{o}C. A picture of three DCG holograms recorded in film dried at a humidity of 65% is shown in Fig. 6.11.

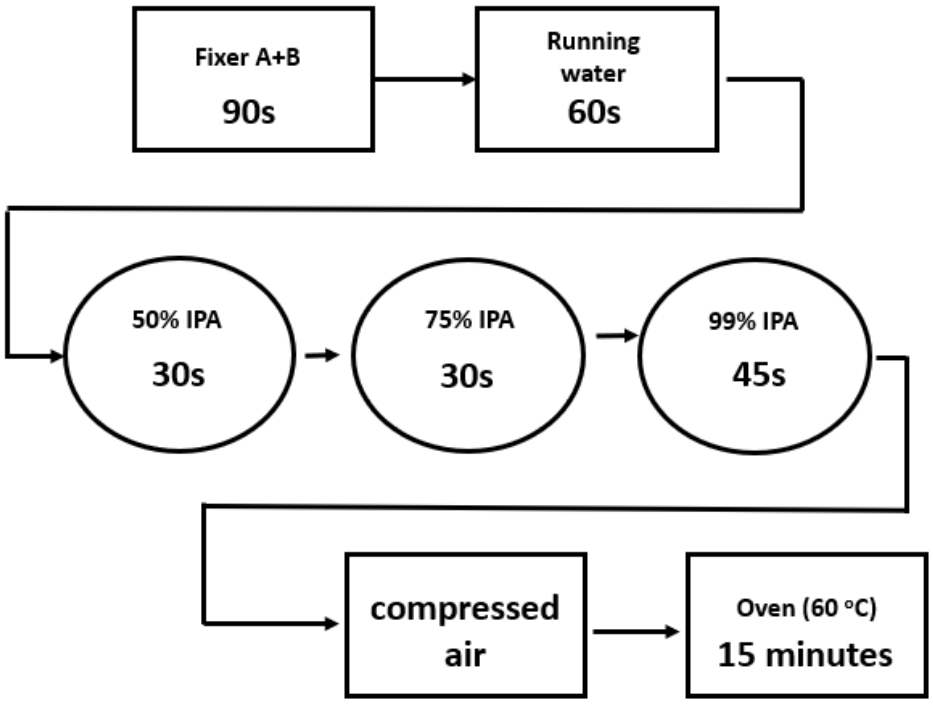

Figure 6.10: Process diagram for DCG chemical processing after the film exposure. First the sample is immersed in Kodak Fixer A+B, then placed in running water, and finally immersed three IPA baths with increasing concentration. All solutions are at room temperature. Lastly the sample is dried with compressed air and placed in an oven set at 60 ºC to remove residual moisture.

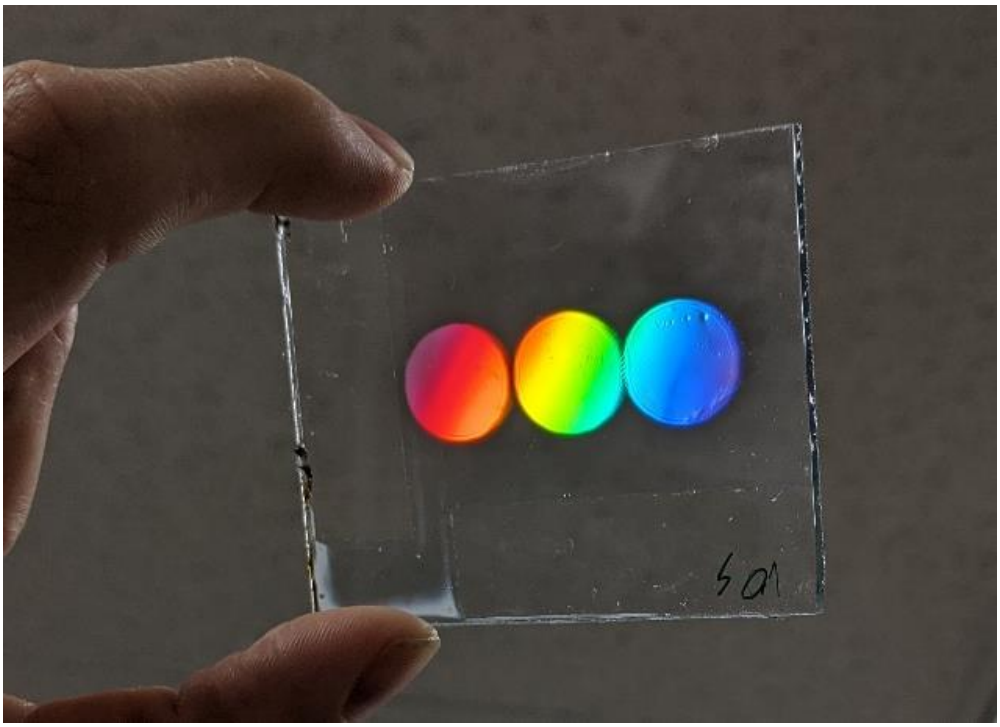

Figure 6.11: Three DCG holograms recorded in film dried at a humidity of 65%.

6.3.2 Effect of Humidity on Diffraction Efficiency

Each hologram is illuminated at normal incidence with light from a tungsten halogen lamp and the spectral transmittance $T(\lambda)$ is measured with an Ocean Optics USB2000+ spectrometer. The measurement is normalized for reflections by taking a reference measurement of light transmitted through the glass substrate. Each measurement is plotted in Fig. 6.12 for the first group and in Fig. 6.13 for the second group. A large degree of variation is observed between the samples with the lowest humidity setpoints (20% to 25%) and gradually decreases until it reaches a minimum for the samples with the higher humidity setpoints between 55% and 65%. The lowest variation is observed in group two for samples recorded in film that is dried with a humidity of 65%. The variation increases again for samples dried at a humidity of 75%. For this set of holograms, uneven structures resembling veins or waterways are observed across the surface and indicate the hologram is oversaturated with water.

Another way to analyze the data is by looking at the spectral diffraction efficiency $DE(\lambda)$ which is approximated using the following equation:

$$DE(\lambda) = 1 - T(\lambda) \tag{6.3}$$

Equation 6.3 is only an approximation since it does not account for the angular divergence of the illumination beam, polarization, higher order diffraction or absorption. However, this approach is much quicker than directly measuring the angular diffraction efficiency with a laser and is more suitable for measuring the large numbers of holograms that are necessary for a variability study.

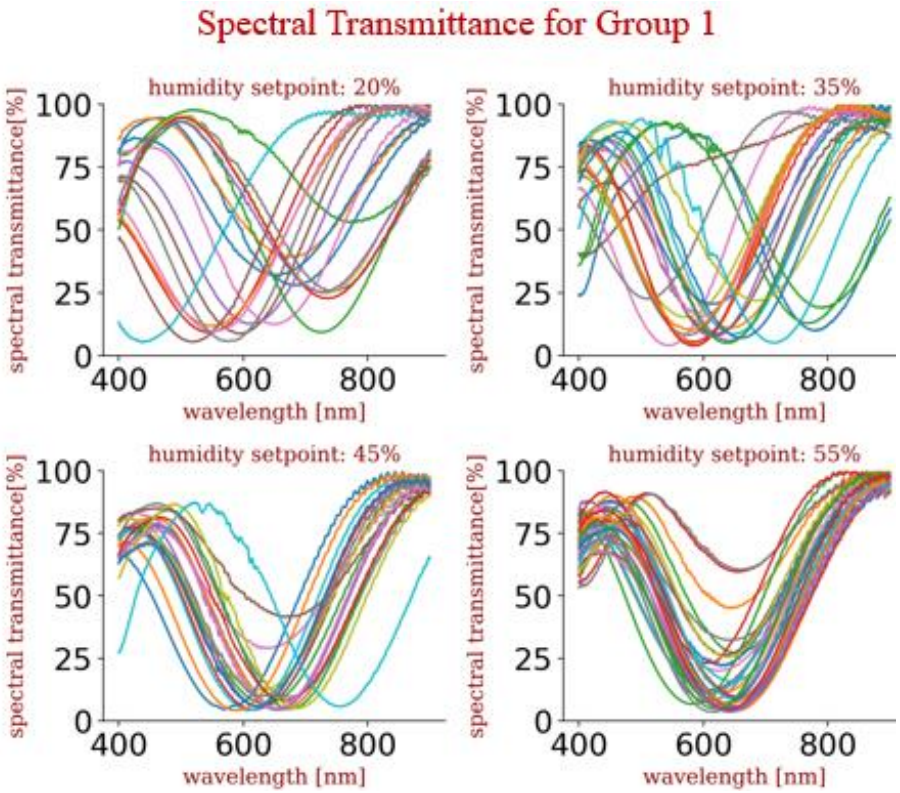

Figure 6.12: Spectral transmittance for each set of DCG holograms in the first group of samples. The first group of samples are recorded with a 514nm DPSS laser.

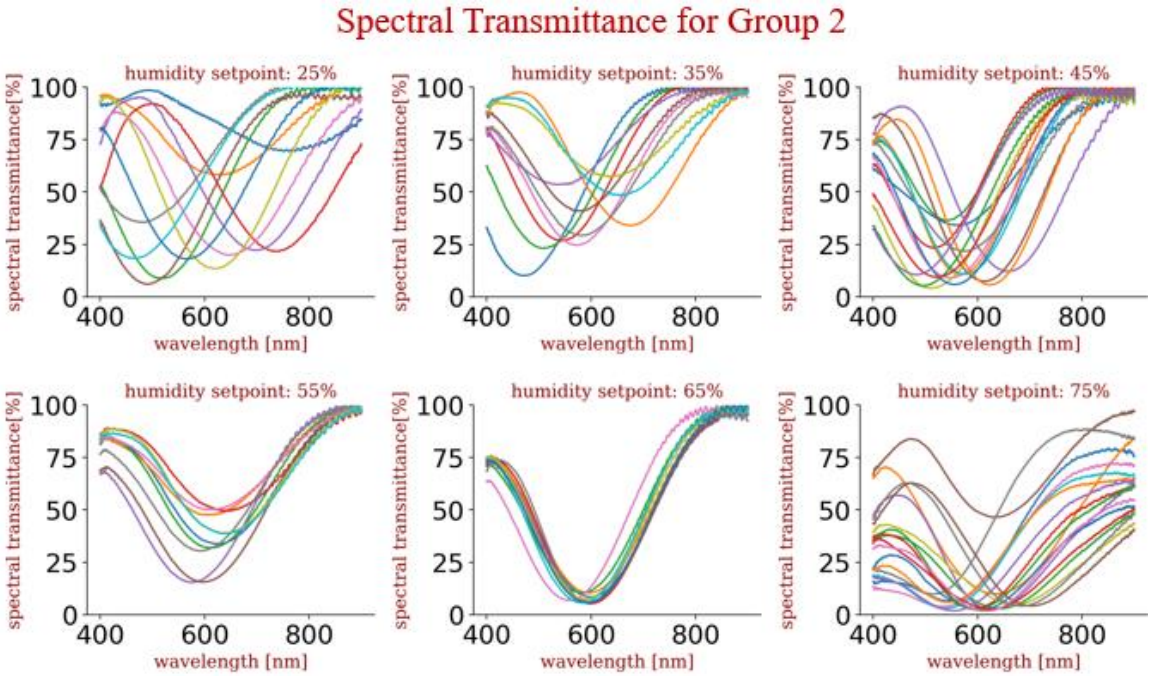

Figure 6.13: Spectral transmittance for each set of DCG holograms in the second group of samples. The second group of samples are recorded with a 457nm DPSS laser.

The variation in spectral diffraction efficiency is characterized by two variables. The first variable is the Bragg wavelength and the second variable is the maximum diffraction efficiency. The Bragg wavelength is the wavelength of maximum diffraction efficiency and the maximum diffraction efficiency is the value of greatest diffraction efficiency. The mean and standard deviation of these two variables is computed and plotted in Fig. 6.14 for each group. In the first group, the standard deviation in the Bragg wavelength decreases from +/-100nm for the 20% humidity samples to +/-20nm for the 55% humidity samples. However, the variation in diffraction efficiency (+/-12%) did not significantly change between the two humidity levels. In the second group, the standard deviation of the Bragg wavelength decreases from +/-100nm for the 25% humidity samples to +/-15nm for the 65% humidity samples. For this group of holograms, the variation in diffraction efficiency also decreases from +/-17% for DCG dried at a humidity of 25% to +/-2% for DCG dried at a humidity of 65%. Overall, the data shows that the variation in the spectral diffraction efficiency can be reduced by drying the film at a humidity of 65%.

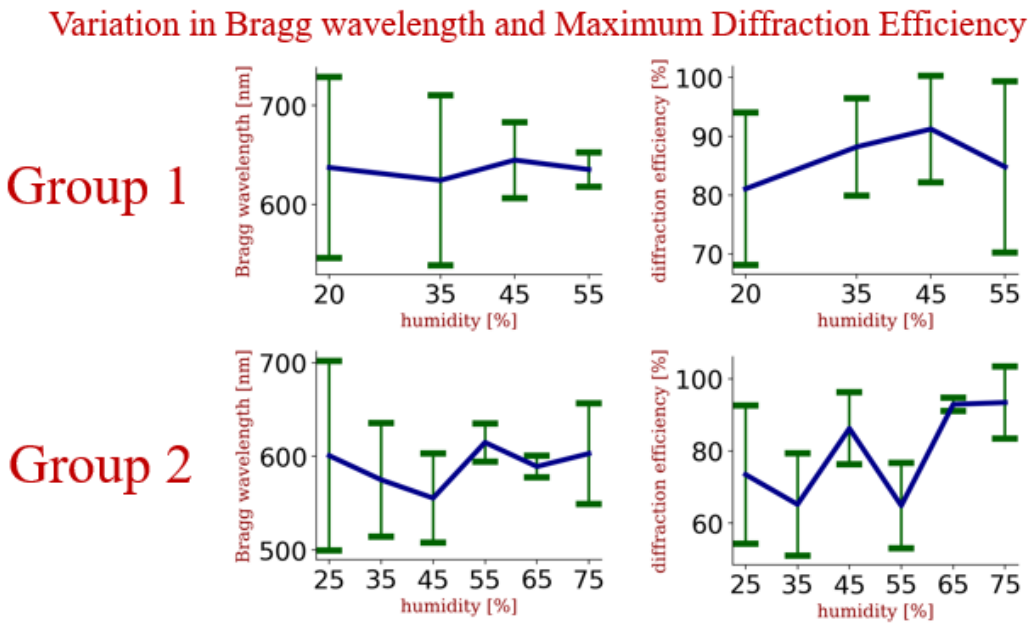

Figure 6.14: Plot of the Bragg wavelength and the maximum diffraction efficiency for each group of DCG samples. The blue line shows the mean value and the green error bars show the standard deviation.

6.3.3 Curve Fitting Analysis

The spectral transmittance and diffraction efficiency data from the previous analysis does not directly show which hologram parameters cause the measured variations. As discussed in Chapter 2, a volume hologram is characterized by the index modulation n_1, film thickness d, and K-vector $\vec{K}$. Therefore it is expected that these parameters must vary in order to cause the variations in the measured spectral transmittance. In this section, a curve-fitting algorithm is developed to estimate the hologram parameters for each of the samples.

The curve-fitting algorithm is designed to minimize the error between the measured spectral transmittance and the RCWA diffraction efficiency in the transmitted 0^{th} order. It is assumed that the lateral component of the K-vector K_x is fixed and can be calculated from the recording beam angles. Only the index modulation n_1, film thickness d, and grating slant angle ϕ are free variables to be determined so the error $\Delta_\lambda(n_1, d, \phi)$ is written as a function of these variables for a data point with wavelength λ. The error between a spectral transmittance data point T_λ and the RCWA diffraction efficiency for the 0^{th} order $\eta_{0,\lambda}(n_1, d, \phi)$ is:

$$\Delta_\lambda(n_1, d, \phi) = T_\lambda - \eta_{0,\lambda}(n_1, d, \phi) \tag{6.4}$$

The total error $\Delta(n_1, d, \phi)$ between the two functions is the root-mean-square of $\Delta_\lambda(n_1, d, \phi)$:

$$\Delta(n_1, d, \phi) = \sqrt{\sum_\lambda \Delta_\lambda(n_1, d, \phi)^2} \tag{6.5}$$

The error $\Delta(n_1, d, \phi)$ is minimized as a function of the free variables using the *optimize.minimize* function in the SciPy package of Python. For the algorithm to work reliably, each of the free parameters needs to be guessed before starting. The guess is determined based on

the construction angles in the recording setup, an assumed film thickness of 20μm, and an index modulation of 0.01. Each of the measured samples from the previous section are fitted using this algorithm. The free parameters are then used to compute the RCWA spectral transmission curves and plotted with the measured data in Fig. 6.15. The measured data from all samples in both groups are inspected and found to closely match the fitted curves.

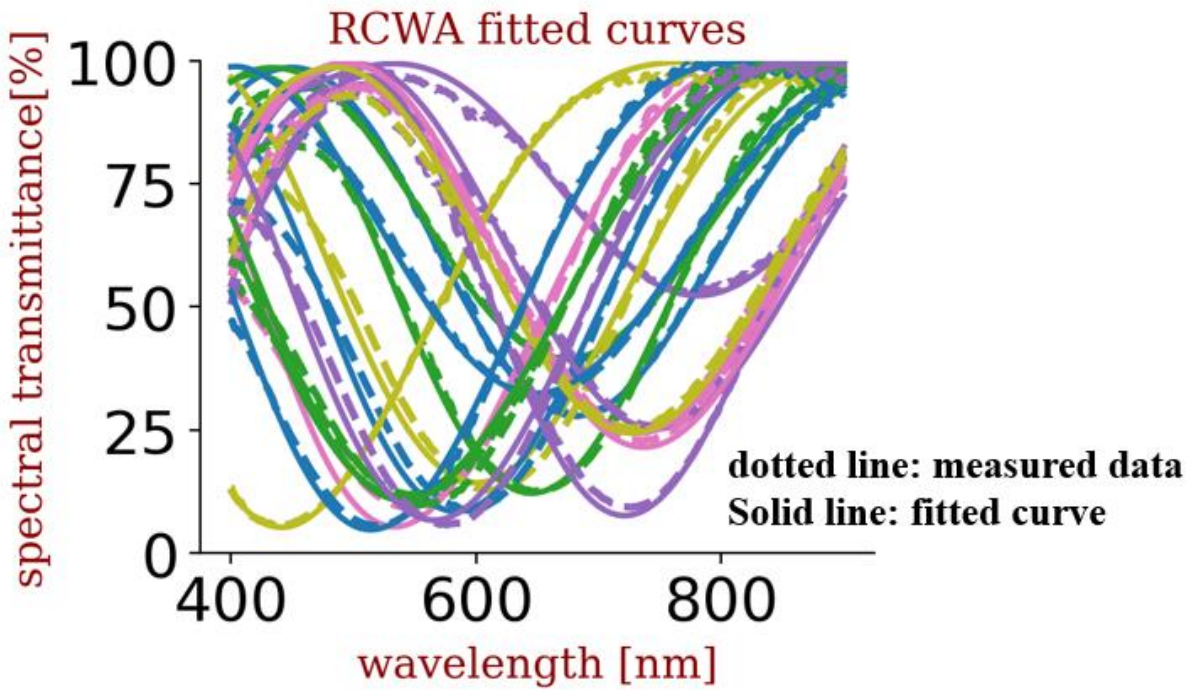

Figure 6.15: An example of the RCWA curve fitting algorithm for holograms in group 1 dried at a humidity of 20%. The spectral transmittance for the fitted curves are plotted with solid lines and the spectral transmittance for the measured curves are plotted in the same color with dotted lines.

The mean and standard deviation of the index modulation, film thickness, and slant angle are calculated and plotted in Fig. 6.16. In addition to the slant angle, the change in the longitudinal component of the K-vector ΔK_z from the initial value calculated from the recording beams $K_{z,0}$ is also calculated and plotted:

$$\Delta K_z = \frac{K_x}{\tan(\phi)} - K_{z,0} \tag{6.6}$$

Several characteristics of the holograms can be seen from the plotted data in Fig. 6.16. First, the mean index modulation ranges between 0.015 and 0.02 and has a standard deviation of 0.005. The mean film thickness is 16μm which is consistent with laboratory measurements made with a micrometer. The film thickness varies by +/-1μm for most sets of holograms but for some sets is as high as +/-3 μm. The mean film thickness is much lower (8μm) for the set dried with a humidity of 75%. For this set, the index modulation also increases to 0.035. As a result, the product of the index modulation and the film thickness stays consistent with other sets and still has high diffraction efficiency. The mean slant angle for the holograms ranges between 80.5^o to 82.0^o. In general, the standard deviation of the slant angle decreases from +/-1.5^o for the lower humidity samples until reaching a minimum of +/-0.25^o for the 65% humidity samples. The standard deviation increases again for the 75% humidity samples to +/-1.5^o. The mean value of ΔK_z is -30% and has a standard deviation of +/-10% for the low humidity samples (20% and 25%). The standard deviation for the high humidity samples (65%) is +/-2%.

Unlike the film thickness and index modulation, the standard variation in the slant angle has a clear relationship with the drying humidity that is confirmed in both groups of holograms. Based on this data it is concluded that the primary reason that the samples dried with a humidity ranging between 55% and 65% have better reproducibility than the lower humidity samples is because the variation in the slant angle of the fringes is reduced. Variations in the index modulation also play a role in the reproducibility of dichromated gelatin but aren't clearly correlated to the drying humidity. Fortunately, the effect of the index modulation on the reproducibility is not as great as the effect of the slant angle. Lastly, the variation of the film thickness is relatively small (16μm +/-1μm) and is comparable to the variation in Covestro Bayfol HX (16μm +/-2μm). Variations in the film thickness are therefore believed to have the least effect on reproducibility.

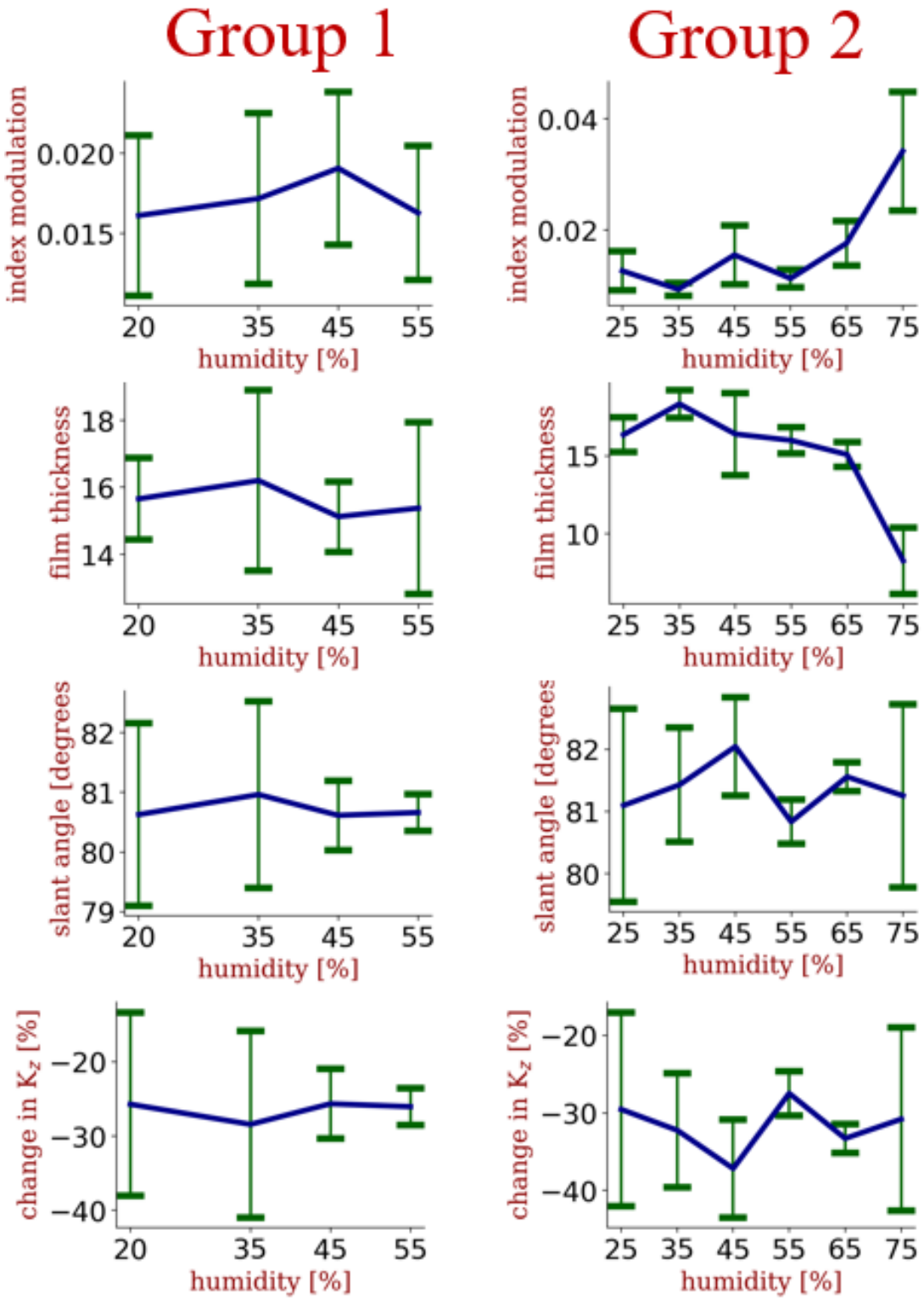

Figure 6.16: The index modulation, film thickness, slant angle, and change in the longitudinal component of the K-vector K_z are plotted as a function of humidity for each group of DCG holograms. The blue line is the mean value and the green error bars show the standard deviation.

Although a variation in the slant angle of +/-1.5° might seem small, it results in a spectral shift of the diffraction efficiency of +/-100nm. This can be confirmed by a theoretical analysis by calculating the Bragg wavelength λ_p for light incident at an angle θ as a function of the slant angle ϕ. A pair of equations are derived using K-vector closure methods [55]:

$$\frac{2\pi n}{\lambda_p} \cdot \left[\sin(\theta) - \sin\left(\phi - 90 - \frac{\theta_\delta}{2}\right)\right] = K_x \tag{6.7}$$

$$\frac{2\pi n}{\lambda_p} \cdot \left[\cos(\theta) - \cos\left(\phi - 90 - \frac{\theta_\delta}{2}\right)\right] = \frac{K_x}{\tan(\phi)}$$

Where θ_δ is the interbeam angle between the beam incident at angle θ and the Bragg-matched diffracted beam. These two equations are numerically solved for λ_p and θ_δ. The shift in the Bragg wavelength for normally incident light is plotted in Fig. 6.17 for a grating with the recording angles used in this experiment. Based on this plot, changes in the slant angle of +/-1.5° and +/-0.25° result in changes in the Bragg wavelength of +/-100nm and +/-15nm, respectively. This is consistent with the measured variation of the Bragg wavelength (Fig. 6.14) and the slant angle (Fig. 6.16) for the holograms in the 25% and 65% humidity sets. Overall, this confirms the role of the slant angle in causing the spectral shifts observed in the measured data.

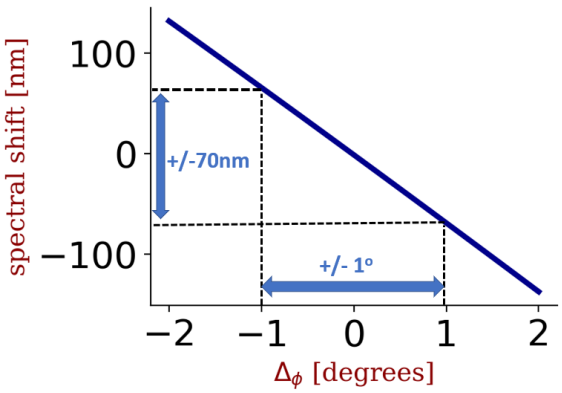

Figure 6.17: Plot showing the spectral shift in the Bragg wavelength for deviations in the slant angle from the nominal value of 81°. The grating has a grating period of Ω_x=1.36μm.

6.3.4 Film Swelling and Shearing

Another question that arises from this data is the cause of the rotation of the slant angle. Based on a calculation of the recording beam angles, the initial slant angle of the fringes is 77.5^o before processing. However, based on the curve-fitting data, the mean value of the slant angle ranges between 80.6^o and 81.9^o after processing. One effect that can rotate the slant angle is the swelling of the film (Fig. 6.18a). As the film swells the spacing between the fringes increases and the longitudinal component of the K-vector K_z decreases. This is consistent with Fig. 6.16 which shows that mean value of K_z decreases from the initial recording conditions by a value ranging from 26% to 37%. However, the film needs to swell by 35% to 59% to achieve a shift in slant angle this large (3.1^o to 4.4^o). Measurements of unslanted DCG reflection holograms indicate a swelling of 21.5% (Fig. 6.19). If the same swelling occurs in transmission holograms as in reflection holograms the slant angle would shift from 77.5^o to 79.7^o but would not shift to the range expected from the mesurements (80.6^o to 81.9^o). This suggests that another effect is present in the film that also causes the measured rotation of the slant angle. This effect could be lateral film shearing (Fig. 6.18b) [105]. In this effect, it is assumed that one side of the fringes are fixed on the substrate but the other end of the fringes are subjected to forces during the chemical processing and are free to rotate. Since the K-vector decreases for these holograms, the film shearing must rotate the fringes in the counter-clockwise direction as depicted in Fig. 6.18b. Since it is unlikely that the film swelling accounts for the entire 3.1^o to 4.4^o shift in the slant angle it is plausible that a combination of shearing and swelling cause the rotation of the slant angle.

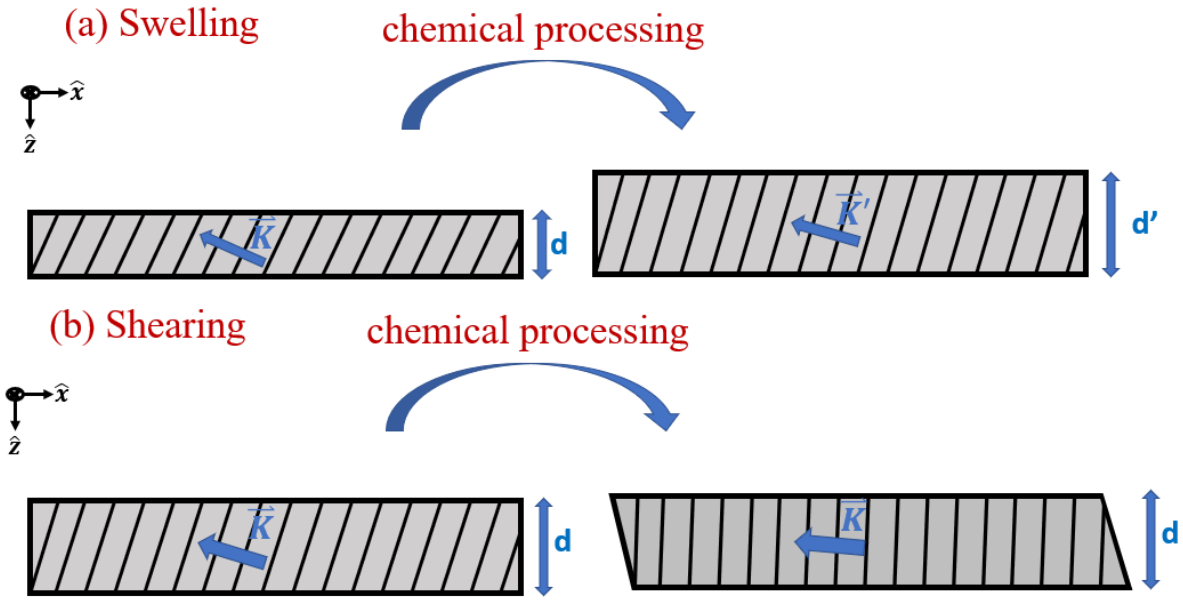

Figure 6.18: Two different mechanisms in DCG holograms that result in a rotation of the slant angle. (a) When a film swells the thickness increases from *d* before processing to *d'* after processing. (b) In film shearing the bottom surface is anchored to the substrate and the top edge is laterally translated.

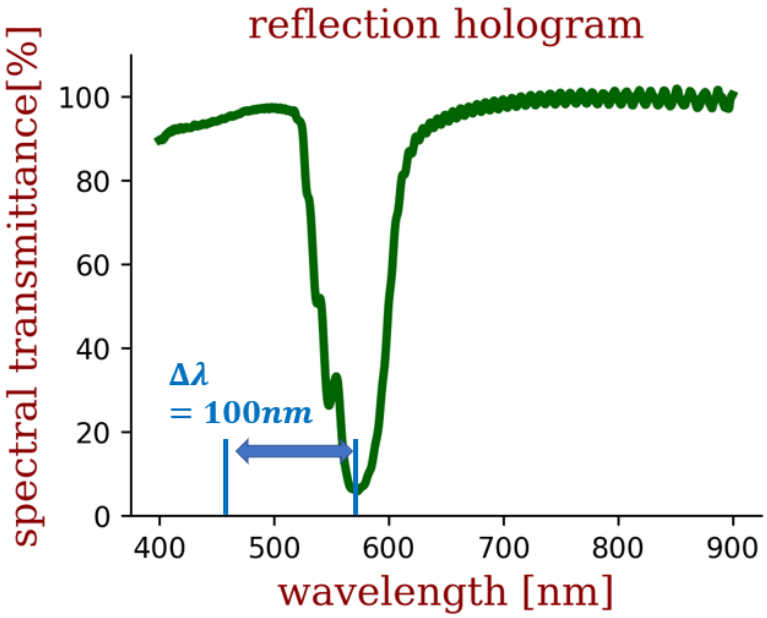

Figure 6.19: Spectral transmittance on an unslanted DCG reflection hologram measured at normal incidence. The hologram is fabricated with light from a 457nm laser with a beam angles of 10° and 170°. The DCG material is dried with a 65% humidity setpoint. The expected reconstruction wavelength without swelling is 465nm and the actual observed reconstruction wavelength is 565nm. This corresponds to a material swelling coefficient of 21.5%.

6.4 Conclusion

In this chapter the environmental stability and reproducibility of holographic materials for spectrum-splitting photovoltaic systems are investigated. It is found that Covestro Bayfol HX 102 degrades significantly after several weeks of exposure to sunlight. Dichromated gelatin withstood the outdoor testing until moisture began to diffuse from the edges of the seal and erase the hologram. However, with proper edge sealing dichromated gelatin holograms can be used in commercial solar photovoltaic systems as exemplified by Prism Solar Technologies [46]. The factors that cause irreproducibility in dichromated gelatin holograms are also studied. It is found that controlling the humidity during the drying stage of the film preparation process allows for increased repeatability in dichromated gelatin holograms. It is also shown that the variability in the film thickness +/-1μm is not a major factor in the reproducibility of dichromated gelatin. The variation of the index modulation (+/-0.005) does affect the reproducibility but is not responsible for the greatest variations. The greatest factor affecting the reproducibility is shown to be a variation in the slant angle of +/-1.5^{o} which causes spectral shifts of +/-100nm in the spectral diffraction efficiency. For the specific emulsion used in this study the variation is reduced to +/-15nm by regulating the humidity at 65% during the film drying process. Lastly, it is shown that a combination of swelling and shearing effects during the chemical processing is likely required to attain the measured rotation of the hologram fringes. In the next chapter, techniques for fabricating volume holographic optical elements are developed using the holographic materials discussed in this chapter.

Chapter 7

Fabrication Methods

In this Chapter, techniques for fabricating volume holographic optical elements are developed that are suitable for spectrum splitting photovoltaic systems. First, a volume holographic lens array is fabricated and used in a demonstration spectrum splitting system. One of the challenges identified during the fabrication process is the need for a replication system to quickly copy volume holographic lenses that have high diffraction efficiency and precisely spaced apertures. A replication technique is developed that has increased versatility, simplicity, and robustness compared with contact copy methods. In this technique, the object beam, reference beam, and hologram aperture are all recorded in a composite master hologram and reconstructed using a single beam at normal incidence. The technique is implemented and used to fabricate a 9.6cm by 6.0cm volume holographic lens array with 36 elements that each have greater than 95% diffraction efficiency.

7.1 Introduction

In previous chapters several spectrum splitting system are designed which use volume holographic lens (VHL) arrays to attain lateral spectral separation. The fabrication of large-format VHL arrays presents new challenges not addressed in literature. Two types of fabrication methods

exist for fabricating large-format holograms. The first method uses conventional optical elements such as lenses and mirrors to form the object and reference beam [98], [99]. For large format holograms, the dimensions of the lenses and mirrors are increased so that the aperture of the hologram fills the entire area of the holographic film. This method can be used for spatially varying elements, including VHLs, but is not suitable for hologram arrays which require smaller elements that are evenly spaced across a larger area. A second method that is widely used in commercial hologram replication systems uses a technique called contact-copy to form the object and reference beams in combination with roll-to-roll scanning to form a larger element. This method can be used to fabricate gratings that have arbitrarily large apertures [106]–[110]. However, it is most suitable for replicating gratings that do not have any spatial variation. This makes it difficult to use for volume holographic lenses. Additionally, it is difficult to fabricate master holograms with high quality that replicate gratings with high efficiency and repeatability.

In an initial fabrication attempt, a volume holographic lens array is formed using an "aperture-stitching" method in which conventional two-beam interference optical setups are reconfigured between exposures. Holograms fabricated with this method are used in a demonstration spectrum splitting system. However, the process for making VHL arrays in this way is time consuming, inaccurate, and difficult to repeat. A new technique is developed which improves upon these aspects. Many of the advantages of the technique stem from the use of a "composite" master hologram which, unlike contact-copy methods, generates both object and reference beams. In addition, the aperture of the object and reference beams is recorded in the master hologram itself. The master hologram can therefore be used to replicate holograms simply by illuminating it with a normally incident reference beam. By combining this replication method with a scanning system, a 9.6cm by 6.0cm volume holographic lens array is fabricated with 36 elements that each have

greater than 95% diffraction efficiency. Lastly, a modification is made in the replication system that makes the fabrication of the master hologram easier and is suitable for waveguide holograms.

7.2 Aperture-Stitching and Demonstration System

In this section a volume holographic lens array is fabricated using an "aperture-stitching" method and then implemented in a demonstration VHL spectrum-splitting system. The demonstration system uses a 1.1eV silicon cell and 1.4eV GaAs photovoltaic cell that both have dimensions of 50mm X 16mm. The VHL array is designed using the techniques in Chapter 2.

7.2.1 Aperture-Stitching

In the aperture-stitching technique, each VHL is fabricated using a conventional two-beam interference optical setup as pictured in Fig. 7.1. In this method, the VHLs are formed with a sequence of exposures. For each exposure, a cylindrical lens is placed in the object beam path and collimated light is used in the reference beam path. The aperture is formed by placing a mask directly on the holographic film. After making an exposure, the aperture mask is laterally translated to a new location on the film for the next exposure. The optical setup is reconfigured for the new construction angles and lens position. The optical setup is aligned in a dark room with a dim safety light and attention is paid to make sure to block the laser light from reaching the photopolymer. In this example, 16μm thick Covestro Bayfol HX 200 is used as the recording material.

First, a set of three VHLs are formed using the aperture-stitching method. Each VHL has the same transition wavelength of 633nm but has a different slant angle tuned for diffracting light in different spectral bands. The set of VHLs are illuminated with a HeNe laser in Fig. 7.2a. Diffracted light from each of the VHLs is observed to come to a focus along a line in one dimension. The

shadow from the two VHLs on the left are relatively dark since the VHLs are tuned for diffraction in a different spectral band. The diffraction of light with broadband illumination is seen in Fig. 7.2b. Different color shadows are observed underneath the VHLs since they are tuned for diffraction in different spectral bands. A rainbow of light is seen towards the right where the diffracted light is focused and dispersed.

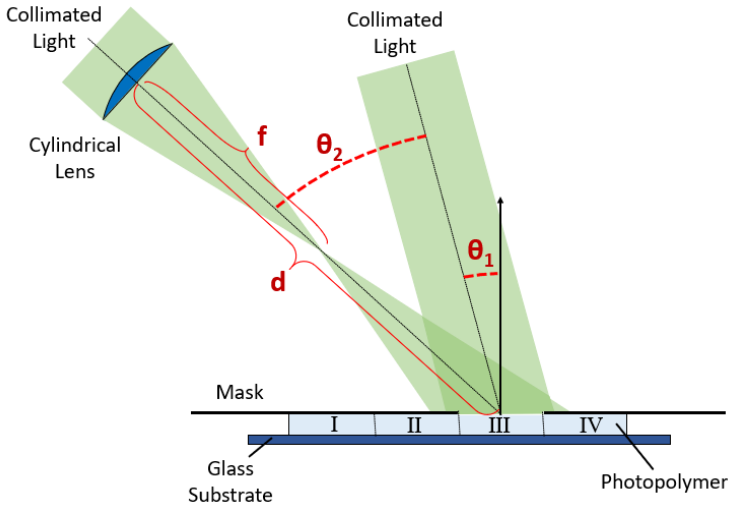

Figure 7.1: Diagram of the aperture-stitching setup for fabricating volume holographic lens arrays. In between exposures the mask is shifted to another location and the recording beams angles and lens positioning are adjusted for the design requirements in Table 7.1.

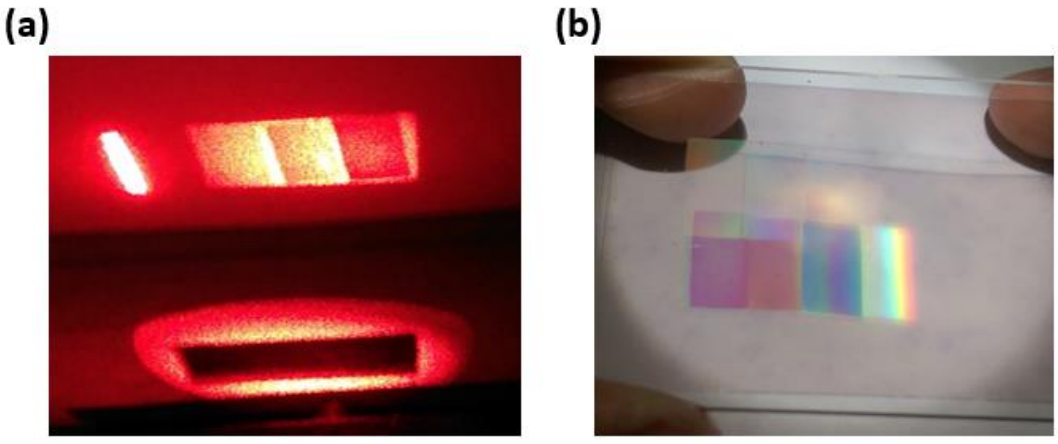

Figure 7.2: Three VHLs formed using the aperture-stitching methods that are designed to diffract 633nm wavelength light to a focus but are tuned for diffracting different spectral bands. (a) illumination with a 633nm HeNe laser, (b) illumination with a broad band Xenon-Arc lamp.

The aperture-stitching method is then used to fabricate a VHL array for a spectrum splitting system that divides the spectrum between silicon and GaAs photovoltaic cells. The VHL design parameters, construction angles, and lens position are determined for a construction wavelength λ_c = 514nm and a separation of t = 25cm in air between the photopolymer and the PV cells (Table 7.1). Each VHL has a dimension of 25mm in the vertical direction and a dimension of 8mm in the horizontal direction. Two VHL unit cells are fabricated on separate glass substrates. The substates for each unit cell are then cut at the edge of the aperture and arranged side by side to form two adjacent VHL unit cells as pictured in Fig. 7.3a. The spectral transmittance of the different VHLs is shown in Fig. 7.3b.

Although the diffraction efficiency and quality of the VHL apertures in Fig. 7.3 are suitable for an initial demonstration of the photovoltaic system it takes several hours to fabricate and many failed attempts are experienced before fabricating an array with high diffraction efficiency and accurately positioned apertures. The time-consuming nature of the process and the lack of repeatability is due to the reconfiguration of the optical setup between each exposure. Each time this happens there is a chance the newly positioned aperture is misaligned and overlaps with another VHL or leaves an unexposed area of the photopolymer. There is also a chance the beam angles or lenses are misaligned slightly and the VHL is detuned and has low diffraction efficiency.

Table 7.1: Design parameters for each volume holographic lens and their corresponding construction setups.

		Volume Holographic Lens			
		I	II	III	IV
Design	λ_t [nm]	875	875	875	875
	θ_t [deg]	38.7	25.6	-25.6	-38.7
	λ_p [nm]	650	1000	1000	650
Construction	θ_1 (in air) [deg]	-2.8	-7.0	7.0	2.8
	θ_2 (in air) [deg]	-24.6	-22.1	22.1	24.6
	d [mm]	125	100	100	125

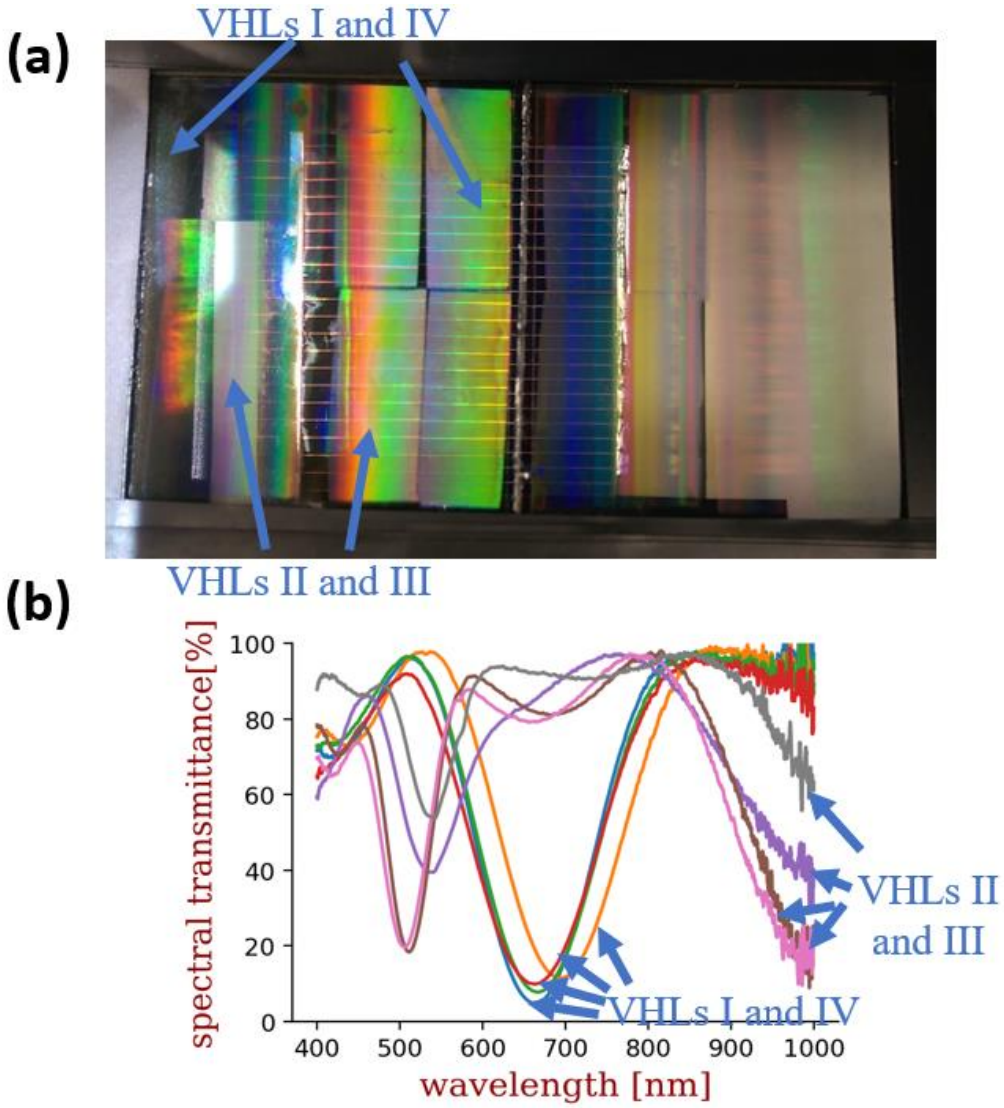

Figure 7.3: (a) A 2 X 8 volume holographic lens array designed for spectral separation with a 16mm silicon photovoltaic cell and a 16mm GaAs photovoltaic cell. (b) Spectral transmittance of eight VHLs. The VHLs on the left half of the array are measured. VHLs II and III have diffraction resonances greater than 1000nm and cannot be recorded by this spectrometer.

7.2.2 Experimental Setup and Metrics

Performance of the VHL system is evaluated using a power boost (PB) metric which is defined as the ratio of the combined power output of the two PV cells $P_{I,ss} + P_{II,ss}$ with spectrum splitting

(Fig. 7.4a) divided by the combined power output of the PV cells in a reference measurement $P_{I,r} + P_{II,r}$, without spectrum splitting (Fig 7.4b)

$$PB = \frac{P_{I,ss}+P_{II,ss}}{P_{I,r}+P_{II,r}} \tag{7.1}$$

During the reference measurement the VHL array is replaced with a photopolymer film that is laminated on a glass substrate. The photopolymer film is UV cured but does not have any recorded gratings. It is assumed that the Fresnel reflections and absorption are equal in the spectrum splitting and reference measurements.

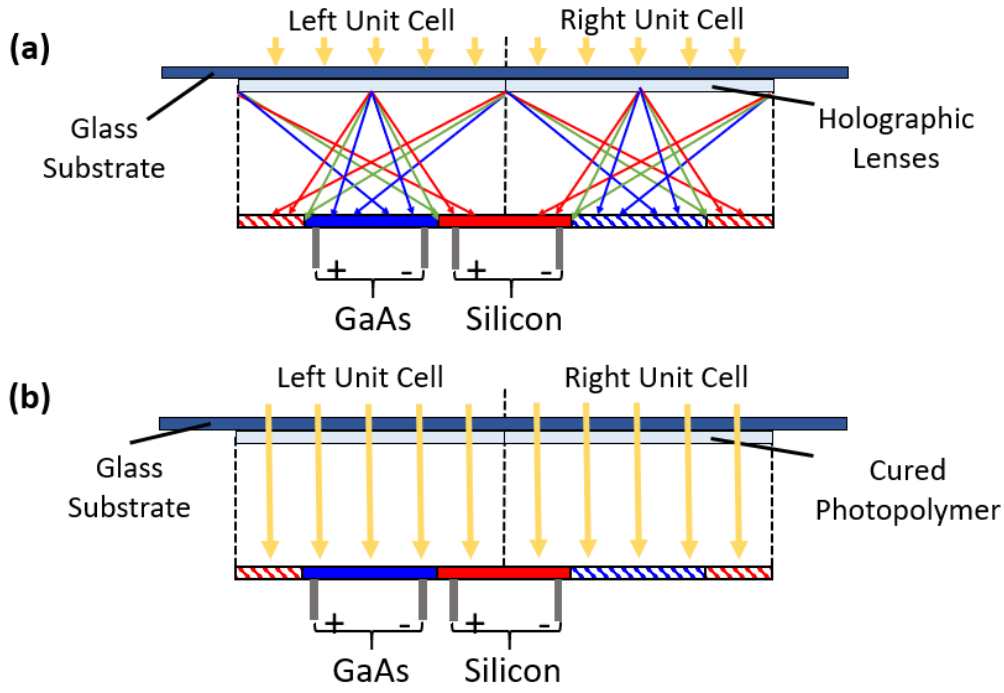

Figure 7.4: Depiction of two different measurements taken for a demonstration photovoltaic system with silicon and GaAs cells. (a) In a spectrum splitting measurement the volume holographic lens array is placed above the photovoltaic cells. (b) In a reference measurement, UV cured photopolymer film without any recorded holograms is placed above the photovoltaic cells.

The prototype VHL module is illuminated with a Xenon arc lamp solar simulator in Fig 7.5a and the diffracted light is pictured in Fig. 7.5b. The current-voltage (IV) curve is measured for both PV cells in the spectrum splitting and reference configurations. The IV curves are measured

in a 4-terminal configuration with a Keithley 2440 sourcemeter. The power output of the PV cells is determined by calculating the maximum power point of the IV curve. There is a reduction in power output of the silicon cell (-26.5%), and an increase in the power output of the GaAs cell (+36.9%). The net result is an increase in total power output of 8.5%. This value is less than the 22.9% increase that is expected for a combination of a silicon cell with a conversion efficiency of 20% and a GaAs cell with a conversion efficiency of 27%. A likely cause for the lower power output is because the silicon cell is not encapsulated in a glass material and has high levels of reflection. When viewed from an angle the cell even appears a white color indicating that light is reflecting in the visible spectrum. Unfortunately, the cell broke before taking more detailed measurements to confirm the exact cause of the lower-than-expected power output.

Regardless of the cause, the need for a more reliable, efficient, accurate, and quick fabrication method is clear. In the next section, a widely used replication method, contact copy, is discussed.

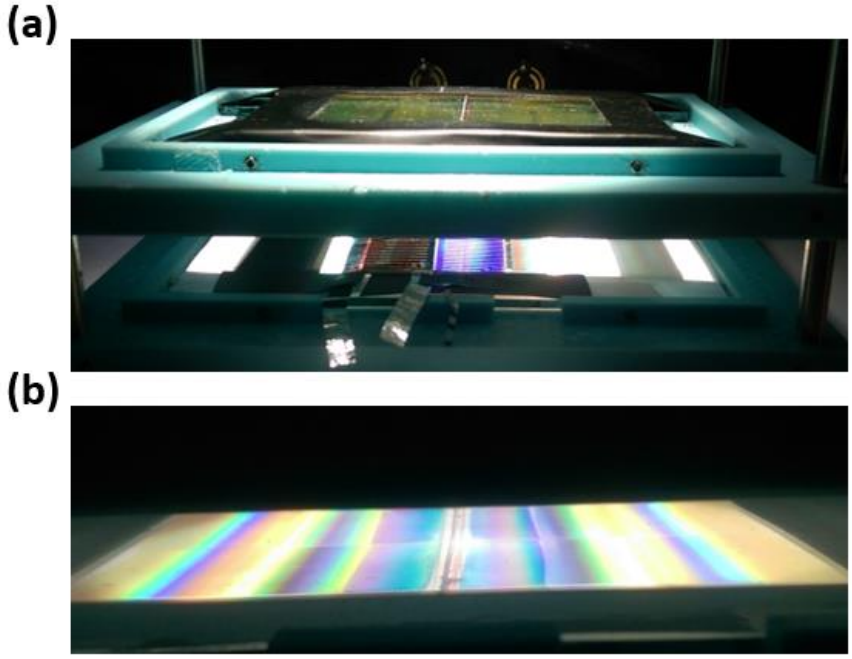

Figure 7.5: (a) The holographic lens elements were placed in a 3D printed mount and illuminated with a Xenon arc lamp solar simulator. (b) Photograph of diffracted light from the VHL array.

7.3 Contact-Copy Technique

Several hologram replication systems have been described in literature for applications in display systems, security, and photovoltaics [106]–[110]. Most of these systems are based on contact-copy methods that utilize a “master hologram” to generate the interfering wavefronts necessary to form a “copy hologram”. The master hologram is designed with the same lateral surface grating period as the copy hologram and has 50% diffraction efficiency. It is placed in direct or close contact with photopolymer material and illuminated with a reference beam. The master hologram diffracts the incident reference beam with 50% efficiency into the m = 1 diffraction order. The diffracted order and the transmitted reference beam act as the object and reference beams for the copy hologram exposure. One of the beneficial properties of the contact-copy technique is that the surface grating period of the copied element is always the same as the master hologram, regardless of the angle of incidence or wavelength.

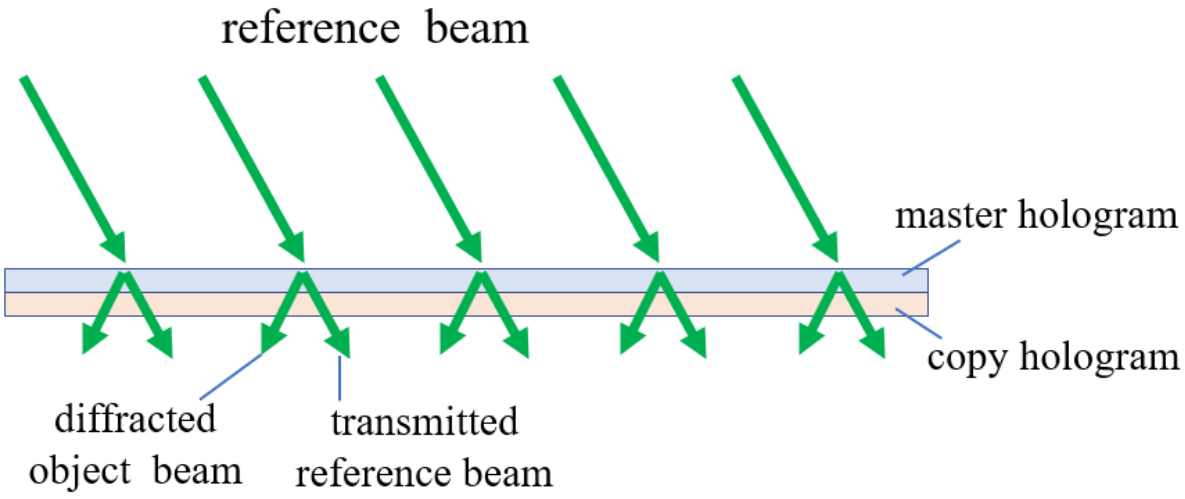

Figure 7.6: Diagram of the contact-copy technique. A master hologram is placed in direct contact with a copy hologram. The master hologram diffracts 50% of the incident light and the remaining light is transmitted. The transmitted and diffracted beams form an interference pattern in the copy hologram.

Contact-copy makes hologram replication systems more compact, robust, and simple compared with systems using conventional optical components. Contact copy systems are more compact since bulky optical components and mounts are eliminated. It has greater vibration stability since a single beam path is used. The alignment is simplified since only a single beam is used. Furthermore, the system is more versatile since the master hologram can be interchanged with only slight modifications that don't require changing the entire optical setup.

Although contact copy has useful properties for replication, there are several reasons why it is difficult to utilize for the fabrication of volume holographic lens arrays. The most important reason is that the slant angle of the fringes in the copy hologram depends on the angle of the reference beam illuminating the master hologram. Each VHL in the unit cell (Fig. 2.4) has reference beams with different incidence angles and in some designs the reference beams are also non-planar. Therefore, several reference beams are required and each need to be aligned with the master hologram. Instead of making the replication process simpler, contact copy may make it more complex and is not an ideal solution. A second reason that contact copy is difficult to utilize is due to the sensitivity of the master hologram to alignment and diffraction efficiency since the ratio of transmitted and diffracted beam powers should be equal to form a fringe pattern with high visibility. Reducing the fringe visibility results in a change in the diffraction efficiency of the copy hologram and reduces the repeatability of the method. The fringe visibility is calculated for a master hologram that is constructed with beams incident at 0^o and either 15^o, 30^o, or 45^o in the material ($n = 1.5$) and is plotted in Fig. 7.7. For a master hologram that diffracts normally incident light at an angle greater than 30^o the range of incidence angles with high visibility is less than 1^o. Furthermore, the sensitivity increases for master holograms with less than 50% diffraction efficiency. For a diffraction efficiency of 30% the maximum visibility is less than 90% even if it is perfectly aligned.

Any imperfections in the master hologram or misalignment of the reference beam will end up reducing the diffraction efficiency of the replication hologram. Overall, the contact copy method is useful for hologram replication but difficult to use for replicating volume holographic lenses with high repeatability.

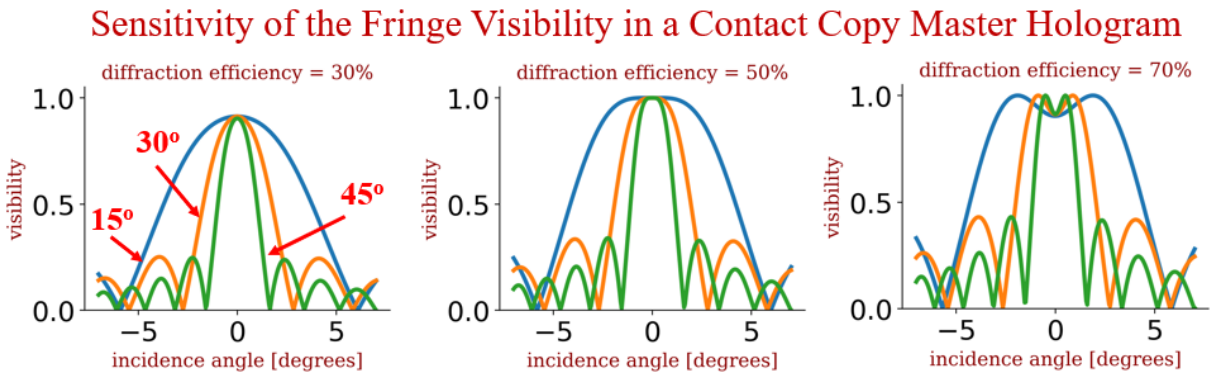

Figure 7.7: The fringe visibility of the interference pattern set up by the transmitted reference beam and diffracted object beam from a contact copy master hologram. The visibility is plotted for a master hologram constructed with a 0° reference beam and 15°, 30°, and 45° object beams (construction angles are in material n = 1.5 with a 457nm laser). The visibility is also plotted for master holograms with diffraction efficiencies of 30%, 50% and 70%.

7.4 Non-Contact Composite Master Hologram

In this section a novel replication system based on a composite master hologram is developed for fabricating volume hologram arrays. The technique has potential for use in mass-manufacturing and is well-suited for spectrum-splitting volume holographic lens (VHL) array fabrication and has a number of advantages over contact-copy techniques. In this technique, a composite master hologram is fabricated that forms the object and reference beams for the copy hologram when illuminated with normally incident light. In this particular implementation, the master hologram is placed in contact with a prism. The diffracted object and reference beams pass through the prism to the copy hologram and the light that isn't diffracted is reflected from total internal reflection

and directed away from the copy hologram. A replication system based on this technique is assembled and used to fabricate a 9.6cm by 6.0cm volume holographic lens array with 36 elements that each have greater than 95% diffraction efficiency.

7.4.1 Description of the Technique

Hologram array elements are fabricated based on a copy technique that uses a composite master hologram and a 45-45-90 prism to form a holographic exposure in the plane where the copy hologram is located. The optical setup is depicted in Fig. 7.8. A master hologram is placed in contact with a short face of the prism. An index matching oil or an optical adhesive fills the gap between the master hologram and the prism to reduce reflections. The long face of the prism is parallel to the surface of the copy hologram and separated by a distance 'z_0'. To form the holographic exposure, collimated light from a laser illuminates the master hologram at normal incidence. The object and reference beam holograms are located in separate regions of the master hologram and diffract light to form the object and reference beams for the holographic exposure. After diffraction, the object and reference beams propagate to the long face of the prism and are refracted out of the prism into air. They then propagate to the surface of the copy hologram where they overlap and form the holographic exposure for a VHL. Hologram arrays can be formed by 'stitching' together holographic exposures in different regions of the copy hologram using a step-and-repeat scanning method as depicted in Fig. 7.9. In the scanning method, the copy hologram is placed on a motorized stage and translated laterally in between holographic exposures to form an array.

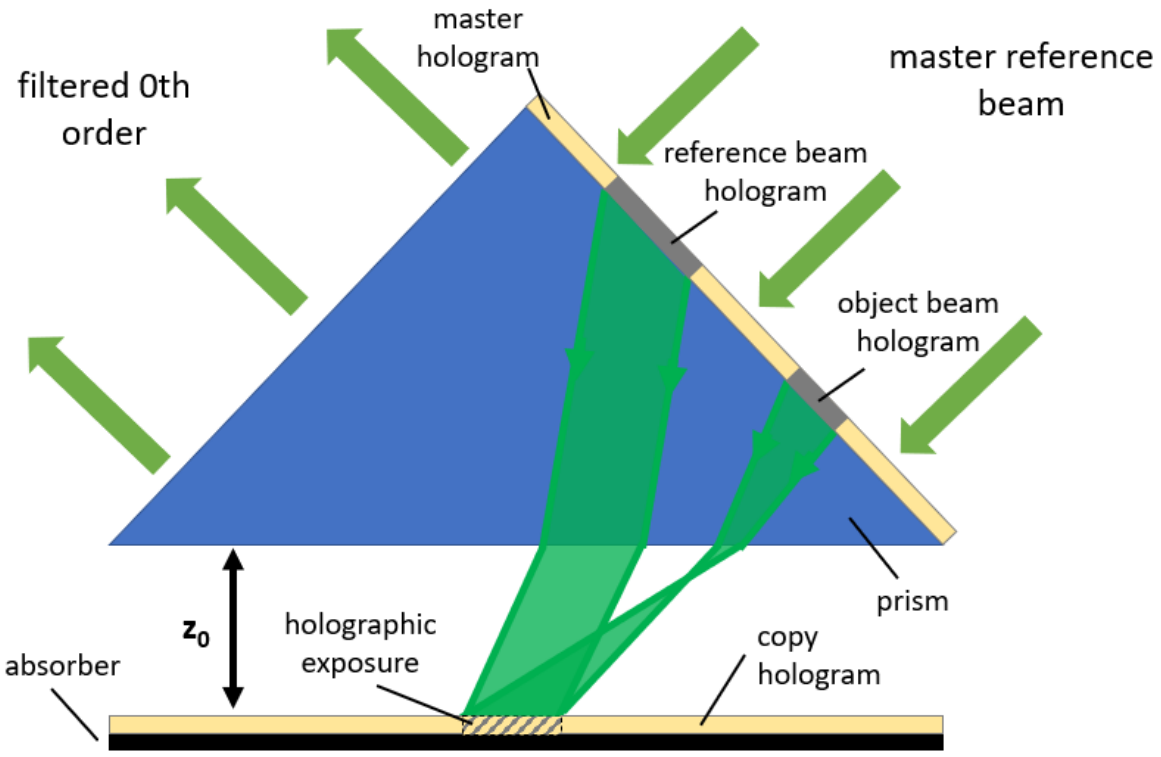

Figure 7.8: The object and reference beam for the copy hologram is formed by illuminating a composite master hologram with normally incident light. The light that is not diffracted by the master hologram is reflected from total internal reflection and filtered.

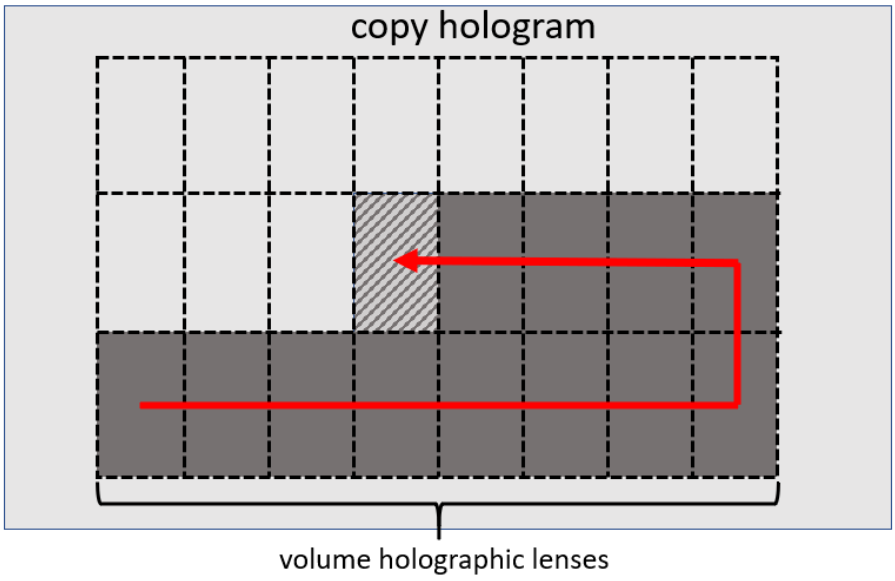

Figure 7.9: Depiction of a step-and-repeat scanning method. Each volume holographic lens is formed using the composite master hologram technique shown in Fig. 7.8 and then the hologram is laterally translated before making another exposure.

The composite master hologram used in the copy technique is fabricated in a two-step process. In the first step, the reference beam hologram is formed as depicted in Fig. 7.10a. The unexposed photopolymer is index-matched between the short face of the prism and an absorber. Interference fringes are set up in the photopolymer by exposing it with two beams. The first beam is the conjugate reference beam for the copy hologram. Before reaching the master hologram the conjugate reference beam first passes through an aperture placed at the working distance 'z_o'. No special calculations for the conjugate reference beam are required. Instead, the aperture can be illuminated with the same reference beam point source or beam angle that is used to form the desired copy hologram directly without the use of a replication system. The dimensions of the aperture are the same as the desired dimensions for the aperture of the copy hologram. For example, if a 1cm by 2cm aperture is desired for the copied VHL, then the aperture dimensions during fabrication of the master hologram should also have dimensions of 1cm by 2cm. The second beam that forms the reference beam hologram is the "master reference beam". This beam is normally incident on the other short face of the prism. It then reflects from total internal reflection and overlaps with the conjugate reference beam to form a holographic exposure. The master reference beam's spatial extent is limited by an adjustable window so that it overlaps with the conjugate reference beam without exposing the entire photopolymer film. The object beam hologram is formed using the same process and is depicted in Fig. 7.10b. The aperture set up at distance 'z_o' is unchanged and is illuminated with the conjugate object beam. Again, the exact same object beam is used as if the desired copy hologram is being fabricated directly without the use of a replication system. The window for the master reference beam is also adjusted so that it overlaps with conjugate object beam to form the object beam hologram. Once both exposures are made, the

master hologram is processed and used to form a hologram array using the methods described previously.

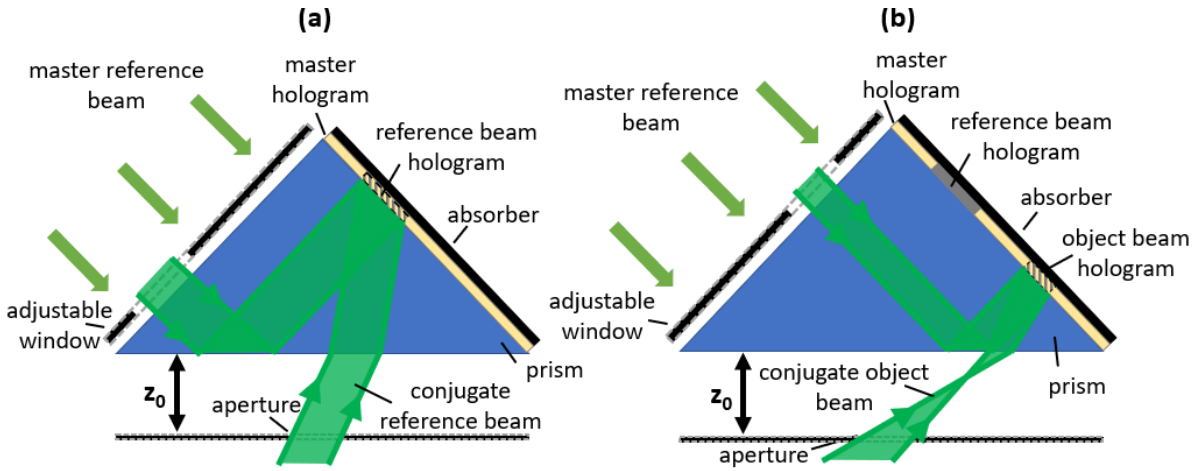

Figure 7.10: The optical setup for fabricating a master hologram. (a) First, a reference beam hologram is formed with the conjugate reference beam and master reference beam and (b) Second, an object beam hologram is formed with the conjugate object beam and master reference beam.

7.4.2 Design Procedure

A design procedure is developed to select values for the replication system parameters as depicted in Fig. 7.11: working distance 'z_0', aperture offset 'x_0', and prism face length 'l':

i. *Determine the desired reference and object beam wavefronts for the copy hologram.* This can be done using K-vector closure techniques [55] or using the point source optimization method described in Section 2.4. The aperture width 'w_0' used during the master hologram fabrication is equal to the desired array hologram width. The position of the point sources for a direct recording and for the recording of a master hologram are both shown in Fig. 7.11.

ii. *Select the working distance 'z_0', offset 'x_0', and prism face length 'l'.* Any value for these parameters is acceptable as long as two conditions are met. First, the extent of the conjugate object and reference beams do not overlap on the surface of the prism. Second, the spatial extent of the conjugate object and reference beams lies within the dimensions of the master hologram.

iii. *Determine optimal exposure energy for the coupling elements.* The spatial frequencies of the object and reference beam holograms are different, so the exposure energy should be optimized individually for each hologram. The optimal exposure energy can be determined by making several exposures with different energies and selecting the value that gives the highest diffraction efficiency.

iv. *Determine optimal exposure energy for the array element.* After fabrication of the master hologram, the last parameter that needs to be determined is the exposure energy for the copy hologram. Like done in step *iii* the exposure energy is determined by making several holograms with different exposure energies and using the value with the highest diffraction efficiency.

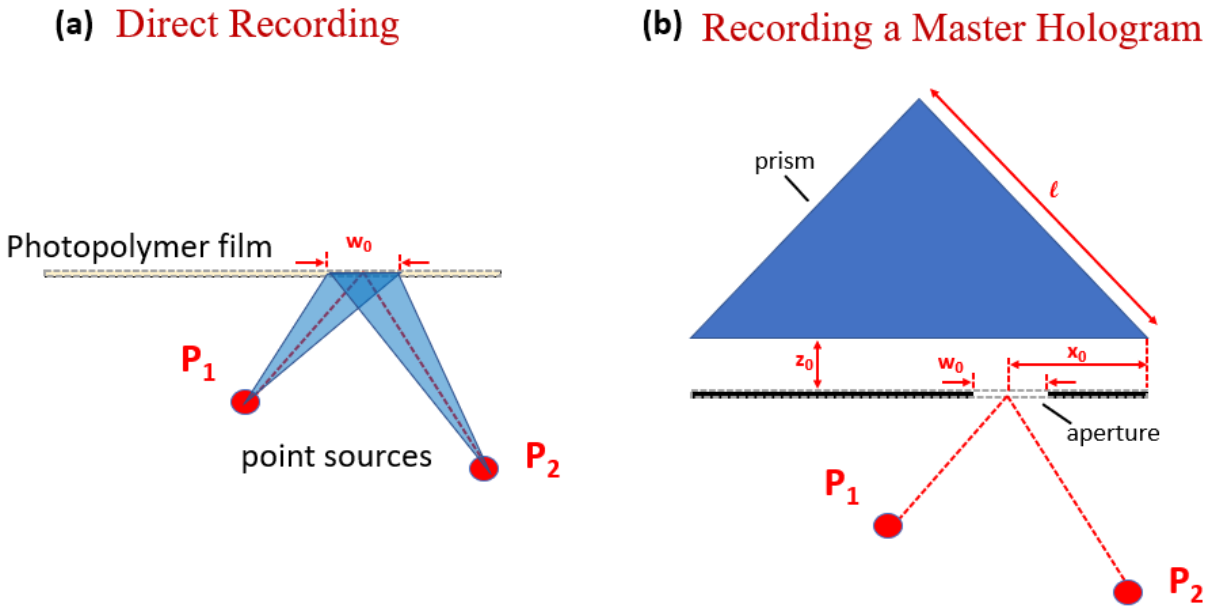

Figure 7.11: Depiction of the geometrical parameters for the master hologram fabrication. (a) First, the point sources (or beam angles for planar gratings) are determined using conventional design techniques as if the copy hologram is to be directly recorded. (b) Second, these point sources are used as the conjugate object and reference beams in fabricating the master hologram. The point sources are located relative to the center of the aperture.

7.4.3 Experimental Validation

The replication system is experimentally demonstrated and it is shown that it can be used to fabricate hologram arrays with high diffraction efficiency. In this example an array of volume holographic lenses is fabricated. The mounting hardware used for fabricating the master hologram and copy hologram is designed in Solidworks and fabricated with a 3D printer. Pictures of the experimental replication system and master hologram fabrication system are shown in Fig. 7.12.

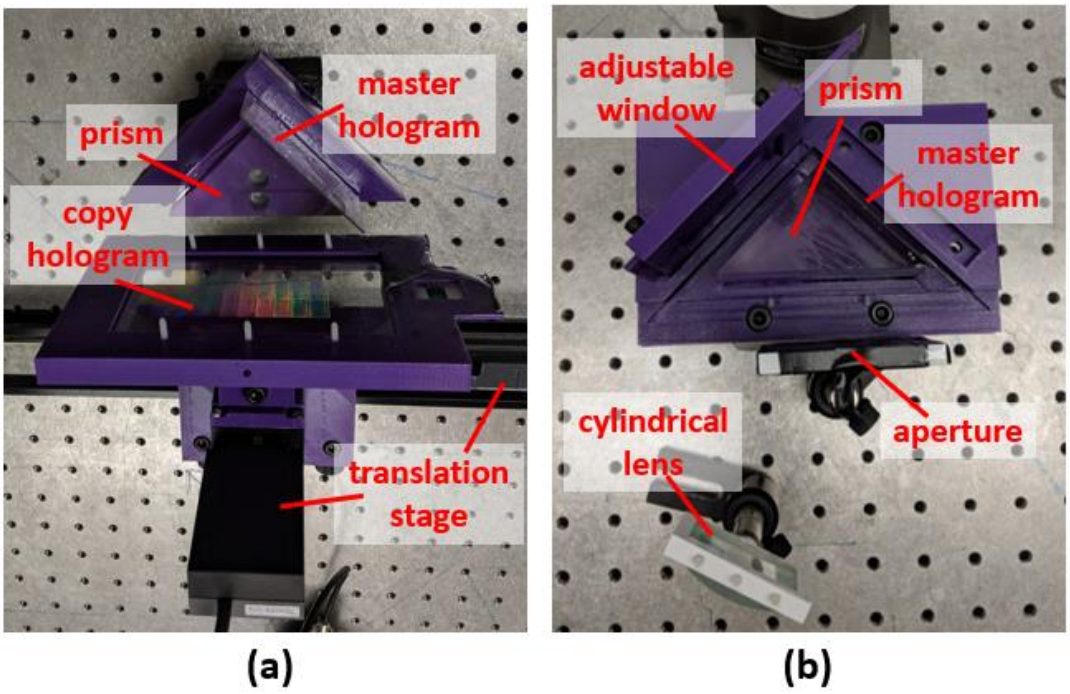

Figure 7.12: Optical setup for (a) fabricating the copy hologram and (b) fabricating the master hologram.

Table 7.2: Replication system parameters used for experimental demonstration.

w_0 [mm]	θ_1 [degrees]	θ_2 [degrees]	d [mm]	x_0 [mm]	z_0 [mm]	ℓ [mm]
8	2.5	25	115	20	30	55

The design procedure outlined previously is used to obtain the values of the experimental parameters that are listed in Table 7.2. A 532nm Verdi laser is used for the holographic exposures and both the master and copy holograms are fabricated in Covestro Bayfol HX 200 photopolymer [13]. The dimensions of the hologram array is 9.6cm by 6.0cm and there are 36 total copy holograms. After fabrication, the spectral transmittance of each holographic lens is measured using a tungsten halogen lamp and an Ocean Optics USB2000+ spectrometer. After correcting for Fresnel reflections and absorption with a reference measurement it is assumed that all light that is not transmitted in the 0^{th} order $\eta_0(\lambda)$ is diffracted in the 1^{st} order $\eta_1(\lambda)$:

$$\eta_1(\lambda) = 1 - \eta_0(\lambda) \tag{7.2}$$

The spectral diffraction efficiency for each volume holographic lens is plotted in Fig. 7.13. The VHL array has a median peak diffraction efficiency of 95.6% and a standard deviation of +/- 0.9%. The Bragg-matched wavelength for normally incident light is λ=675nm. A picture of the holographic lens array diffracting visible light is shown in Fig. 7.13.

Several other hologram arrays are fabricated using this replication system demonstrating the capability to replicate holograms quickly and with high repeatability. The first is an array of planar holograms designed for a "T-cap" holographic solar concentrator. A set of five hologram arrays for this project are shown on the left side of Fig. 7.15. A second volume holographic lens array is shown on the right in Fig. 7.15. Each VHL in this array has an aperture width of 5mm, compared with the 10mm aperture for the array shown in Fig. 7.14.

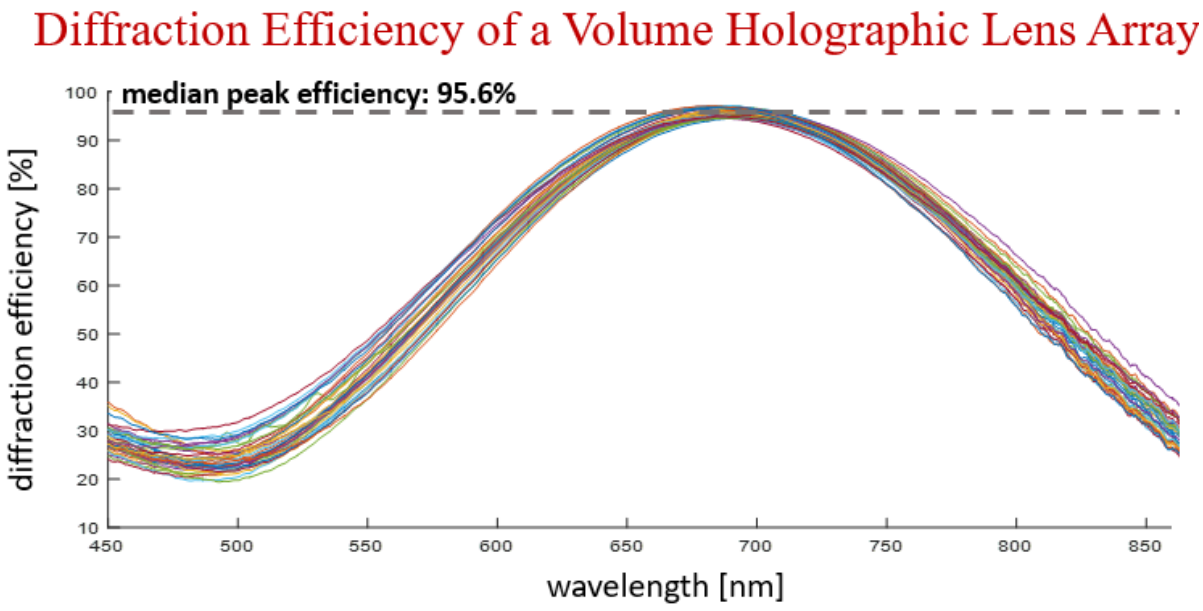

Figure 7.13: Measured spectral diffraction efficiency of each volume holographic lens in an array fabricated in Covestro Bayfol HX 200. The median peak diffraction efficiency was 95.6% with a variability of +/- 0.8%.

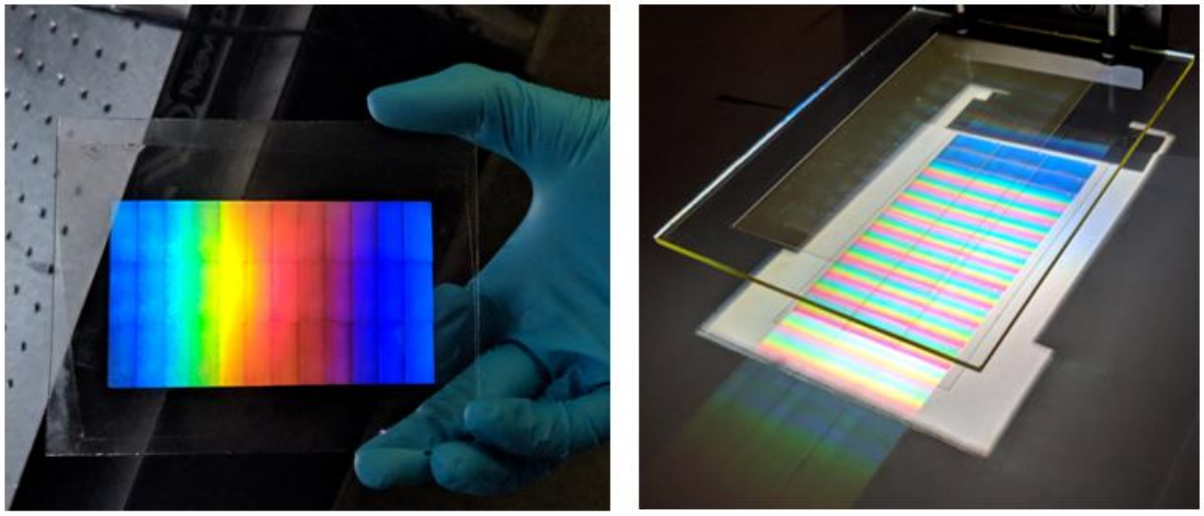

Figure 7.14: A 9.6cm X 6cm volume holographic lens array with 36 total array elements. In the picture on the left, the hologram array is diffracting light from a lamp located outside of the image towards the camera. In the picture on the right, the hologram is diffracting light from a solar simulator lamp onto a sheet of white paper. The diffracted light forms a periodic grid of colors.

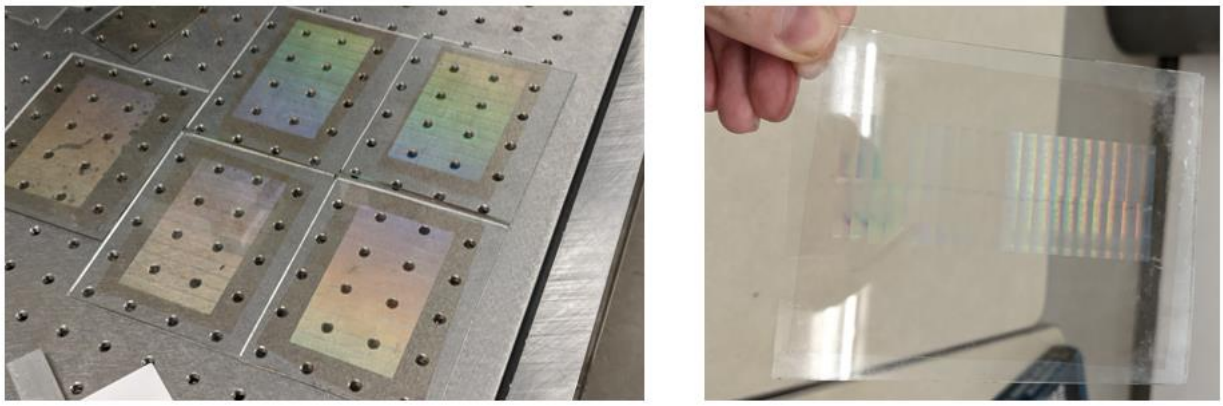

Figure 7.15: Several hologram arrays fabricated using the replication system. The five arrays on the left are planar gratings for a broadband solar concentrator. The array on the right is an array of holographic lenses with aperture widths of 5mm each.

7.5 Contact Composite Master Hologram

The replication technique described in the previous section has many useful properties stemming from the use of a composite master hologram with separate holograms for diffracting the object and reference beams. In the configuration that is discussed, the master hologram is

attached to a prism which is separated by a distance 'z_o' from the copy hologram. The separation distance is necessary so that the beam that is not diffracted by the master hologram is reflected from total internal reflection and filtered. The separation between the prism assembly and the copy hologram has a few advantages since no index matching fluid is required and the prism assembly does not exert any force on the copy hologram as it is laterally translated. However, the separation distance also has an important limitation in the ability to record waveguide holograms. Waveguide holograms require beam construction angles that are greater than the total internal reflection angle and cannot be fabricated using the setup described previously. In this section, a similar technique is described that also uses a composite master hologram but is capable of fabricating waveguide holograms. The modified configuration also has the additional benefit of using a composite master hologram in a reflection configuration. Reflection holograms are easier to fabricate and have potential for simplifying the process of fabricating a master hologram.

Hologram arrays can be manufactured using the setup shown in Fig. 7.16. A reflection-type composite master hologram is placed in between the long face of a prism and an absorber. The gaps are filled with an index matching fluid or optical adhesive. The horizontal face of the prism is placed in contact with an unexposed photopolymer roll and the gap is filled with an index matching fluid. For industrial manufacturing the photopolymer is placed on a roll-to-roll scanning machine and for laboratory applications the photopolymer can be mounted on a translation stage. A collimated "master reference beam" from a laser source propagates through an adjustable aperture window towards the vertical face of the prism. The beam is aligned at normal incidence and propagates towards the master hologram. Part of the light from the master reference beam is diffracted from the reference beam hologram and generates the reference beam for the holographic exposure. Another part of the light is diffracted from the object beam hologram and generates the

object beam. The remaining light is transmitted through the master hologram before being filtered by an absorber. The diffracted object and reference beams overlap on the surface of the copy hologram to form the holographic exposure.

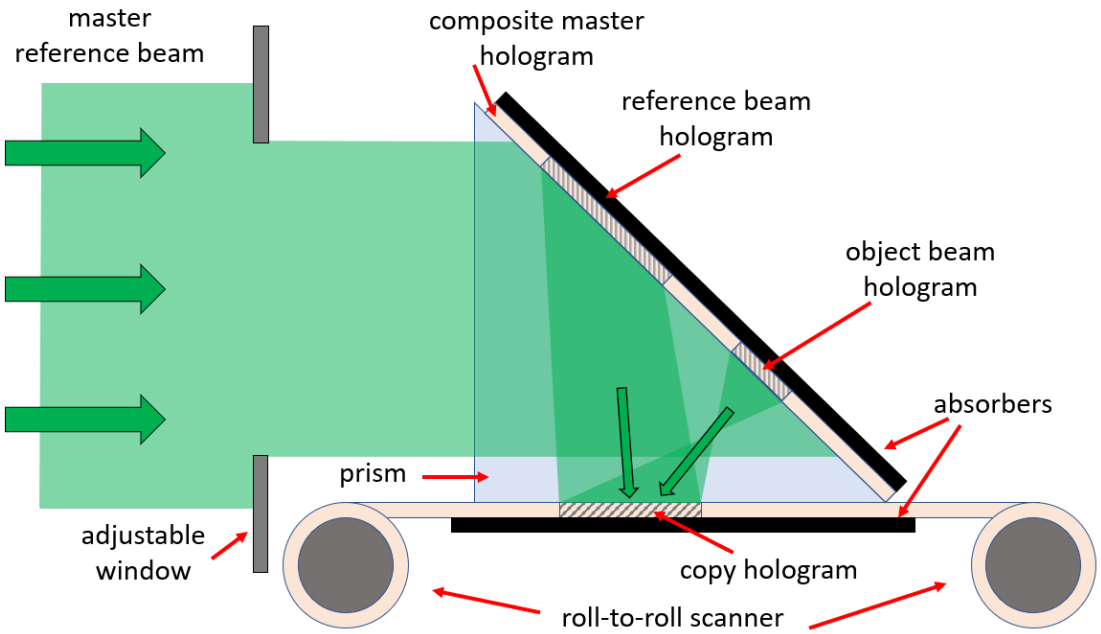

Figure 7.16: Replication technique for waveguide hologram arrays using a composite master hologram.

A technique for fabricating a reflection-type composite master hologram is shown in Fig. 7.17. First, unexposed photopolymer is placed in contact between two prisms and the gaps are filled with an index matching liquid. A master reference beam passes through an adjustable window and is aligned at normal incidence with respect to the vertical face of the upper prism. The beam transmits through the prism and propagates towards the unexposed photopolymer. The conjugate reference beam is transmitted through the replication hologram aperture on the horizontal face of the lower prism and propagates towards the photopolymer film. The conjugate reference beam and the master reference beam form the holographic exposure for the reference beam hologram. The adjustable window is then reconfigured for the second exposure. In a similar way, the master

reference beam and the conjugate object beam form the holographic exposure for the object beam hologram. The photopolymer film is then processed to form the reflection-type composite master hologram.

A prism or other optical element can be used to so that the angle of the conjugate reference beam or conjugate object beam exceeds the critical angle of the photopolymer (Fig. 7.17b). For many applications, only the reference beam or only the object beam exceeds the critical angle and the other beam is closer to normal incidence. In this situation there are challenges in using a conventional optical setup since a prism is required for one of the beams but a parallel face is needed for the other beam. Many of the solutions using conventional optics, such as combinations of prisms, limit the beam angles and beam sizes. An advantage of the technique described in this section is that the in-coupling prism only needs to be used for beam that exceeds the total internal reflection condition and can be removed for the beam that does not require it.

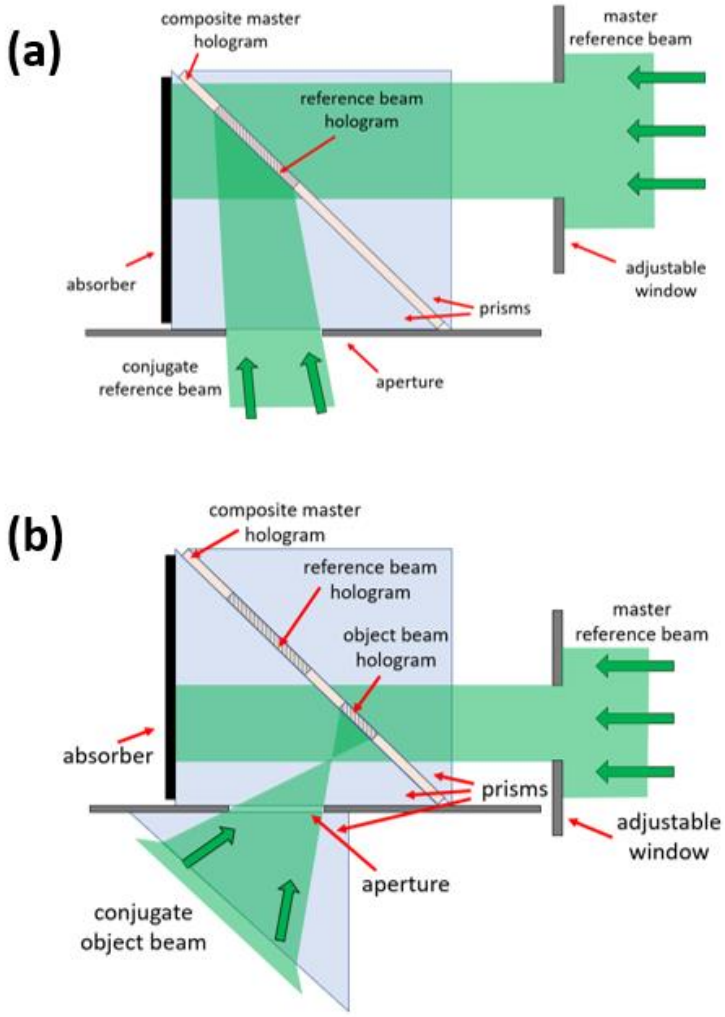

Figure 7.17: Depiction of a technique for fabricating a reflection-type composite master hologram. (a) Fabrication of the reference beam hologram. (b) Fabrication of the object beam hologram may require an in-coupling prism to couple light in past the total internal reflection angle.

7.6 Conclusion

In this chapter, a variety of replication techniques for volume holograms are discussed. The techniques are suitable for the mass-manufacturing of volume holographic lens arrays for the spectrum splitting designs discussed in previous chapters. One of the key developments is a composite master hologram in which the reference beam, object beam, and aperture of the copy hologram are recorded in a single element. The techniques are simple to use since they only require alignment of a single beam and the alignment is at normal incidence.

Appendix A

Cost Analysis

Most research and development in the field of photovoltaics (PV) is focused on developing technologies that have greater power conversion efficiency, energy yield, and durability or lower manufacturing costs. These metrics are frequently compared and reported since they are some of the most important factors in reducing the cost of the generated electrical energy. However, in many cases the proposed technology does not actually result in a lower cost of electrical energy when all aspects of the system are considered in a financial model. Since, in most cases, the cost of electrical energy needs to be equal to or less than other technologies to be commercially successful, it is important to analyze the cost of new photovoltaic cell technologies.

Two of the most common financial metrics for solar energy are the levelized cost of energy (LCOE) and the cost per watt (CPW or $/W). The LCOE is the more important of the two metrics since it takes into account more aspects of the system and represents the actual cost of electrical energy. The CPW is easier to calculate and more convenient when discussing the price of modules or the initial capital cost of an installation. In this section, the LCOE and the CPW are calculated for several of the systems discussed in Chapters 2 through 4 of this dissertation.

The following cost analysis provides a useful comparison between different photovoltaic technologies, but the reader should also understand the limitations of the results. First, cost models are very sensitive to each input, but many of the components used in these systems have not yet

been commercialized or tested. Therefore, many of the cost inputs are educated guesses based on industry or academic reports. Similarly, the power conversion efficiency and energy yield inputs are based on simulations and not from measured field data. Second, the values used in the model are as current as possible. However, it may be many years before any of the systems (besides silicon) in this analysis are commercialized and deployed. There is potential for any of the inputs to change significantly between now and the time of commercialization which could change the results of the model.

The Levelized Cost of Energy is calculated by entering the LCOE equations as described in the NREL online LCOE calculator documentation [111] into a Python script. In the following section, a baseline model is first described and then several variables are analyzed by adjusting the baseline model and recording the results. The results show that the LCOE for spectrum-splitting systems are cost-competitive with conventional silicon modules. However, the module with the lowest LCOE depends on many factors which each have high levels of uncertainty. In general, a 2-bandgap vertically-stacked all-perovskite module is projected to have the lowest LCOE and the 3-bandgap hybrid all-perovskite module is projected to have the second lowest LCOE.

Baseline

The inputs used in the baseline model are listed in Table A1. The efficiency of a conventional silicon cell is assumed to be $\eta = 19\%$ for consistency with NREL's online LCOE calculator [111]. Since this value is 74.2% of the value assumed in the body of the dissertation for this silicon ($\eta = 25.6\%$), the efficiency of all other systems are also scaled by this factor for equal comparison. For example, the efficiency of a single-bandgap perovskite cell is assumed to be 16% (compared with

the 21.6% efficient perovskite cell used in this dissertation [25]) and the efficiency of a 2-BG lateral, all-perovskite system is assumed to be 19.4% (compared with 26.1% in Chapter 2).

Another important consideration is the energy yield. The energy yield in Table A1 is normalized to the power of the module and is taken from NRELs online calculator for Phoenix, AZ [111]. The lower energy yield of the lateral and hybrid modules when illuminated with greater ratios of diffuse sunlight than specified in the standardized test conditions [51] is accounted for by multiplying the energy yield by a correction factor. The correction factor for lateral modules in Phoenix AZ is 98.7% and is determined based on Fig. 5.4 by taking the ratio of the energy conversion efficiency in Phoenix divided by the energy conversion efficiency under standard test conditions. The correction factor for hybrid modules (99.4%) is assumed to be halfway in between the correction factor of lateral modules (98.7%) and conventional or stacked modules (100%).

The cost of a 19% efficient silicon PV cell is assumed to be 34.4\$/m^2 based on the default entries in the NREL online calculator [111]. However, the cost of a perovskite cell is much lower (6.8\$/m^2) since it uses less energy intensive manufacturing processes [112]. Due to a lack of information, it is assumed that all perovskite cells have the same cost regardless of the bandgap energy.

The power-scaled balance of system (BOS) includes the cost of the inverter and scales as the power conversion efficiency of the module increases. The area-scaled BOS includes the cost of the solar tracking system and other installation hardware. The values for these parameters are taken from the NREL online LCOE calculator [111] by entering “single-axis tracked, utility scale” in the preset options. The operation and maintenance (O&M) is an important power-scaling recurring

cost each year the installation is maintained. The value of this parameter is taken from a 2021 NREL cost report [113].

The front and back layers include the cost of the glass. The default values from the NREL online calculator are used for the single-junction modules. For multiple bandgap systems, the cost of the front glass layer is doubled to account for additional glass material used in spectrum-splitting systems. The non-cell module costs account for a variety of module costs other than the photovoltaic cell itself and include the encapsulation, cell interconnection, junction boxes, leads, and connectors. In this analysis the single-junction modules use the default values from the NREL online calculator (18 $\$/m^2$) [111]. An additional 3 $\$/m^2$ is added for each additional bandgap to account for the increasing complexity of the electrical wiring of systems with multiple bandgaps.

The cost of a holographic optical element (HOE) is estimated to be $3\$/m^2$ based on conversations with Prism Solar Technologies [46]. Systems that use cascaded HOEs have double the cost since two layers are used.

The service life of the single-bandgap silicon cell is assumed to be 25 years based on the default assumption of the NREL online calculator [111]. However, the service life of each system with at least one perovskite cell is assumed to be 20 years. The lower service life is meant to account for the environmental stability challenges of perovskite cells [29]. The degradation rate of each module is assumed to be -0.7%/year based on a 2021 NREL industry report [113].

The discount rate and markup are assumed to be 6.3% and 15%, respectively, and are equal to the default values in the NREL online calculator [111].

The LCOE and CPW values for each system are shown in the bar charts in Fig. A1. The height of a given bar indicates the total cost for that system. Within the bar are several color-coded regions which correspond to the cost of individual components or services. The bars are then sorted from highest cost (left side) to lowest cost (right side). For the baseline model, the LCOE of a conventional silicon panel is 4.28¢/kw-hr. A vertically-stacked, all-perovskite module with 2-bandgaps has the lowest LCOE (4.13¢/kw-hr) followed closely by 3- and 4- bandgap hybrid all-perovskite modules (4.16¢/kw-hr, 4.23¢/kw-hr) and a 2-bandgap lateral, all-perovskite module (4.24¢/kw-hr). Each of the other modules has a higher LCOE than a conventional silicon module, including single-junction perovskite systems (4.37 ¢/kw-hr).

Service Life

One of the most difficult inputs to predict is the service life of perovskite cells. It is critical for the success of perovskite cells that researchers improve the service life to within several years of silicon. In this baseline model, it is assumed that the service life of all modules with at least one perovskite cell is equal to 20 years. In this section, the service life is also adjusted to 15 years and 25 years and plotted in Fig. A2. For a perovskite service life of only 15 years, conventional silicon modules have a lower LCOE. The break-even point is around 18 years. However, if the service life is made equal to silicon (25 years) then the all-perovskite modules have a great cost advantage over conventional silicon modules. For example, a 3-BG hybrid module with a 25 year service life has an LCOE that is nearly 10% lower than a conventional silicon module.

Location

The location of a module installation changes the energy yield and the LCOE of a module. The baseline model assumes the module is located in Phoenix AZ. The LCOE in San Antonio TX and Seattle WA are also calculated and plotted in Fig. A3. The initial value of the energy yield is taken directly from the NREL online calculator by entering the module location. The value is then adjusted for lateral and hybrid modules by multiplying by a location-specific correction factor as discussed in the previous paragraphs.

At each location, the 3-BG hybrid module and the 2-BG vertically-stacked module have the lowest LCOE. However, since San Antonio and Seattle have a greater ratio of diffuse sunlight than Phoenix, the LCOE is increased by a greater amount for lateral and hybrid modules than for single-junction and vertically-stacked modules. For example, a 2-bandgap lateral system has a lower LCOE than silicon in Phoenix, but a greater LCOE than silicon in San Antonio.

Conversion Efficiency

One of the most important inputs to the LCOE model is the conversion efficiency of the module. In the baseline assumption, the individual perovskite cells are less efficient than the silicon cells. However, the efficiency of perovskite cells has advanced rapidly in the last few years and it is possible that by the time of commercialization, the efficiency of perovskite cells will be greater than the values used in the baseline analysis. Two additional sets of efficiency values are considered and listed in Table A2: “Scaled to Silicon” and “Maximum”. The “Scaled to Silicon” values assume that the efficiency of any module with one or more perovskite cells is scaled from the simulated module efficiency values (Chapters 2 through 4) by a factor of 0.88. This value is selected so that the 21.6% efficient perovskite cell [25] matches the efficiency of the 19% efficient silicon cell. Lastly, the “Maximum” values use the efficiency values calculated in Chapters 2

through 4 without any scaling. In this scenario, many of the individual perovskite cells are actually slightly more efficient than the 19% silicon cell.

The results are plotted in Fig. A4 and show that the LCOE of the perovskite modules are significantly lower with the increased efficiency values. In fact, every single module has a lower LCOE than a conventional silicon module for both sets of efficiency values. For the "Scaled to Silicon" model, the 2-BG vertically-stacked all-perovskite module has an LCOE that is 11.5% lower than silicon and for the "Maximum" model, it has an LCOE that is 16.6% lower than silicon. These results show the importance of the conversion efficiency, and the potential for perovskite-based modules to have significantly lower LCOE than silicon-based modules after continued development.

Cell Cost

The last variable considered is the cost of the perovskite cells. Based on the cost analysis by Song et al. [112], the cost of a perovskite cell is 6.8\$/m^2 and is only about 1/5 the cost of silicon (34.4\$/m^2). However, it is difficult to accurately predict the actual costs of perovskite cells since they have not yet entered commercial production. The cost of perovskite cells is adjusted to 5\$/m^2 and 10\$/m^2 and plotted in Fig. A5. In both cases the 2-BG vertically-stacked, all-perovskite system has the lowest LCOE.

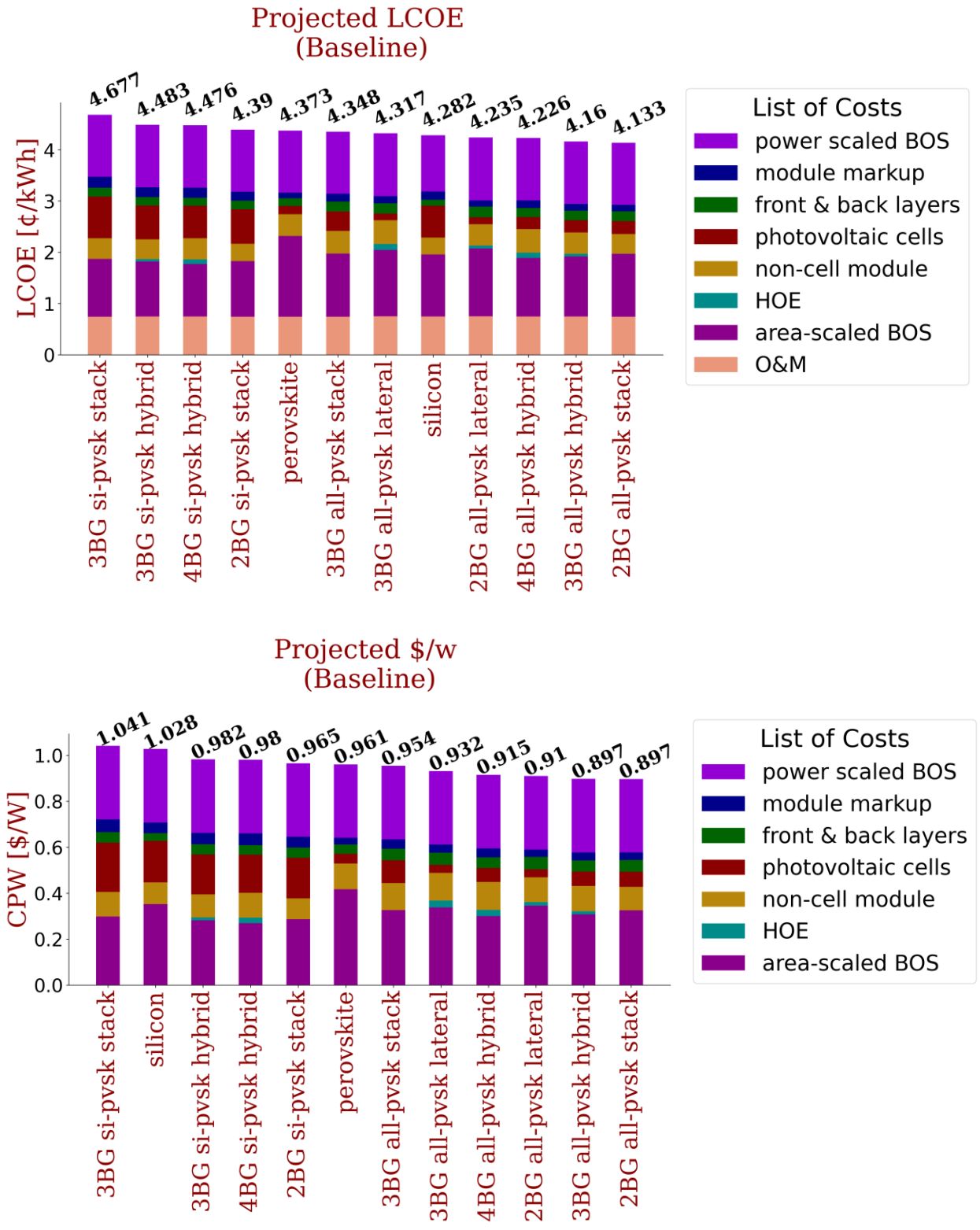

Figure A1: Bar charts showing the projected LCOE and CPW for several different system configurations assuming the "baseline" assumptions listed in Table A1.

Table A1: List of values used in the “baseline” cost analysis.

	silicon	**perovskite**	**all-pvsk lateral 2BG**	**all-pvsk lateral 3BG**	**si-pvsk hybrid 3BG**	**si-pvsk hybrid 4BG**	**all-pvsk hybrid 3BG**	**all-pvsk hybrid 4BG**	**si-pvsk stacked 2BG**	**si-pvsk stacked 3BG**	**all-pvsk stacked 2BG**	**all-pvsk stacked 3BG**
efficiency [%]	19	16	19.4	19.8	23.8	24.9	21.7	22.3	23.3	22.4	20.6	20.5
energy yield [kW-h/kW]	2488	2488	2440.7	2440.7	2464.4	2464.4	2464.4	2464.4	2488	2488	2488	2488
power scaled BOS [$/W]	0.3	0.3	0.3	0.3	0.3	0.3	0.3	0.3	0.3	0.3	0.3	0.3
module markup [%]	15	15	15	15	15	15	15	15	15	15	15	15
front and back layers [$/m^2]	6.4	6.4	10.4	10.4	10.4	10.4	10.4	10.4	10.4	10.4	10.4	10.4
photovoltaic cells [$/m^2]	34.4	6.8	6.8	6.8	41.2	41.2	13.6	13.6	41.2	48	13.6	20.4
non-cell module [$/m^2]	18	18	21	24	24	27	24	27	21	24	21	24
HOE [$/m^2]	0	0	3	6	3	6	3	6	0	0	0	0
area-scaled BOS [$/m^2]	66.9	66.9	66.9	66.9	66.9	66.9	66.9	66.9	66.9	66.9	66.9	66.9
OM [$/kW-year]	17.5	17.5	17.5	17.5	17.5	17.5	17.5	17.5	17.5	17.5	17.5	17.5
service life [years]	25	20	20	20	20	20	20	20	20	20	20	20
degradation rate [%/year]	0.7	0.7	0.7	0.7	0.7	0.7	0.7	0.7	0.7	0.7	0.7	0.7
discount rate [%]	6.3	6.3	6.3	6.3	6.3	6.3	6.3	6.3	6.3	6.3	6.3	6.3
CPW [$/W]	1.028	0.961	0.91	0.932	0.982	0.98	0.897	0.915	0.965	1.041	0.897	0.954
LCOE [$/kW-hr]	0.043	0.044	0.043	0.043	0.045	0.045	0.042	0.042	0.044	0.047	0.041	0.043

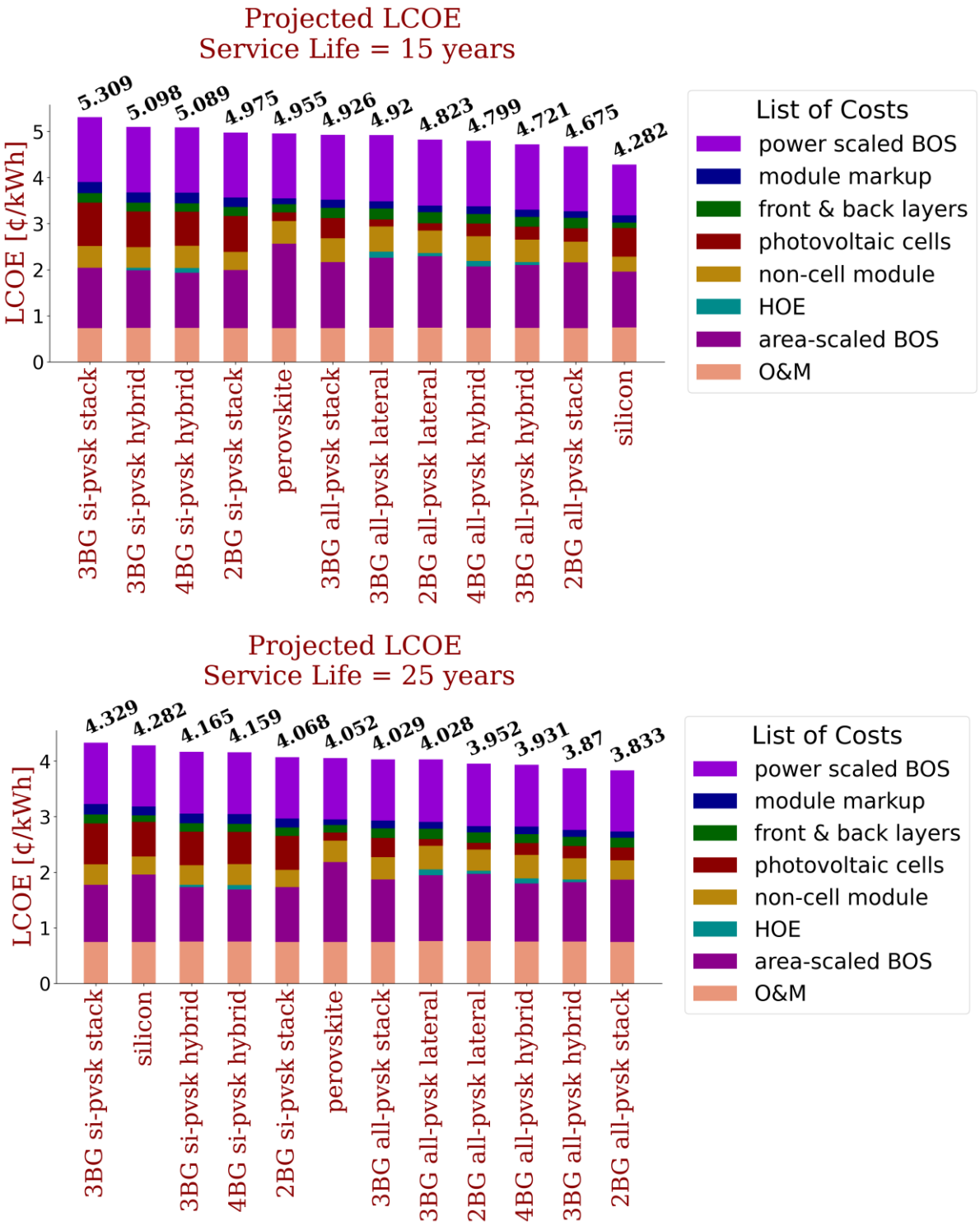

Figure A2: Bar charts showing the projected LCOE assuming the service life of any module with at least one perovskite cell is either 15 years (top) or 25 years (bottom). The baseline model assumes a perovskite service life of 20 years.

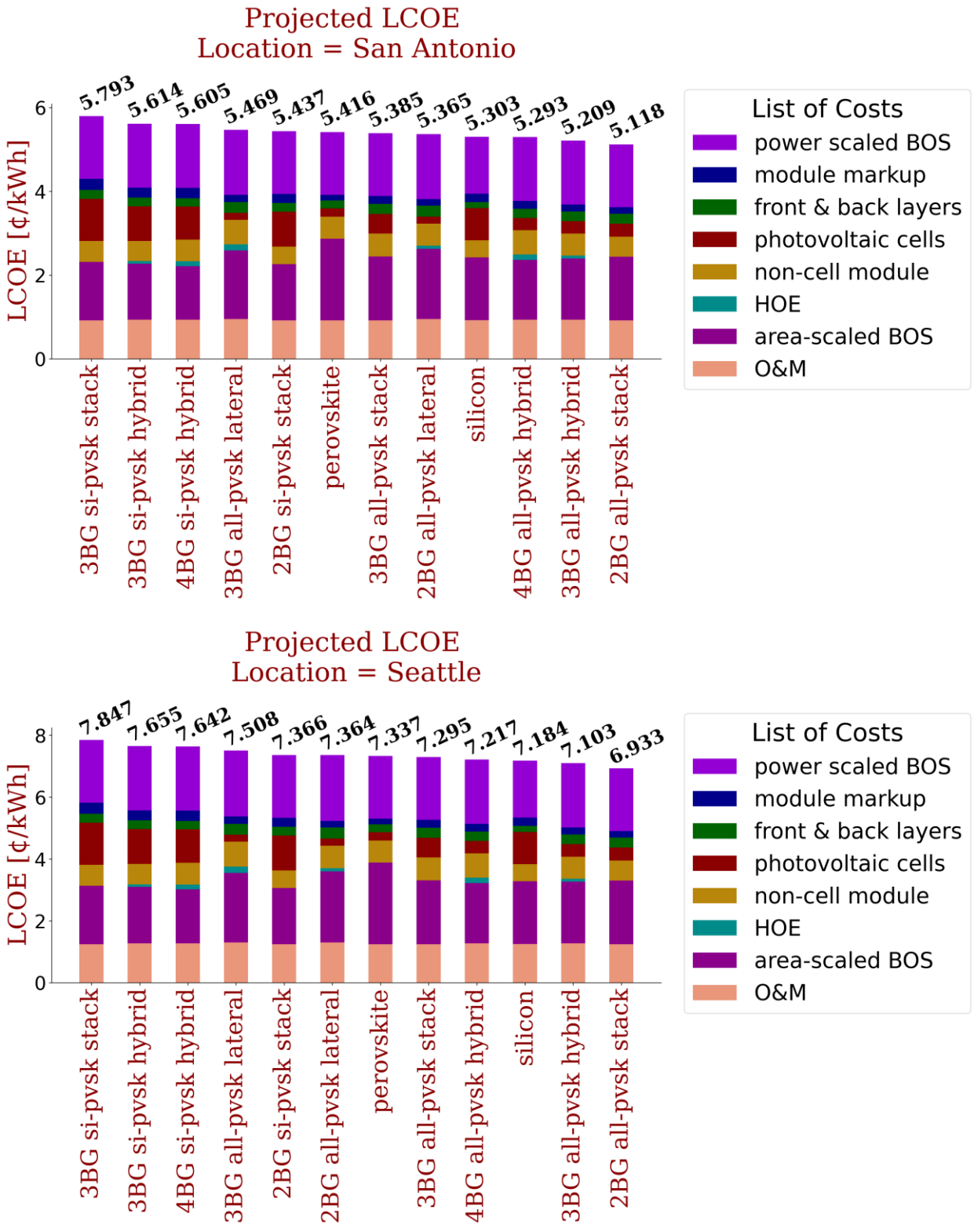

Figure A3: Bar charts showing the projected LCOE in San Antonio, TX (top) and Seattle, WA (bottom). The baseline model assumes the installation is located in Phoenix AZ.

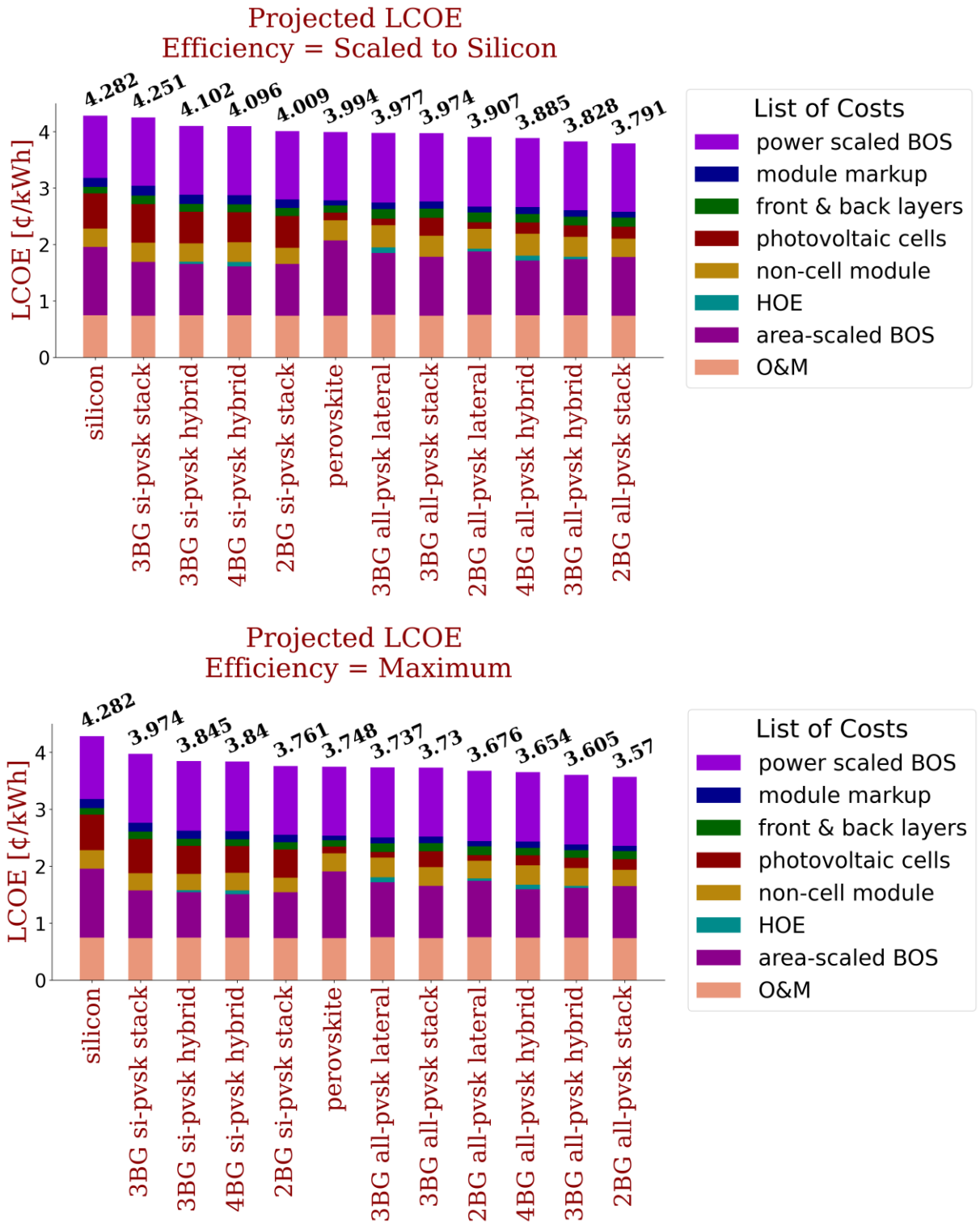

Figure A4: Bar charts showing the projected LCOE for different sets of module conversion efficiency values. Each set of module conversion efficiency values are listed in Table A2.

Table A2: List of efficiency values used in the "baseline", "Scaled to Silicon" and "Maximum" cost models that are plotted in Fig. A4. "Scaled to Silicon" means that the efficiency of each module containing at least one perovskite cell is scaled by a ratio of 0.88. This ratio is selected so that the efficiency of the single-junction perovskite cell is equal to the efficiency of the silicon cell. "Maximum Value" means that each module containing at least one perovskite cell is set equal to the module efficiency calculated in Chapters 2 through 4. In each case, the efficiency of the silicon cell is 19% and does not change.

	silicon	**perovskite**	**all-pvsk lateral 2BG**	**all-pvsk lateral 3BG**	**si-pvsk hybrid 3BG**	**si-pvsk hybrid 4BG**	**all-pvsk hybrid 3BG**	**all-pvsk hybrid 4BG**	**si-pvsk stacked 2BG**	**si-pvsk stacked 3BG**	**all-pvsk stacked 2BG**	**all-pvsk stacked 3BG**
efficiency [%], baseline	19	16	19.4	19.8	23.8	24.9	21.7	22.3	23.3	22.4	20.6	20.5
efficiency [%], scaled to silicon	19	19	23	23.5	28.1	29.5	25.8	26.4	27.6	26.6	24.4	24.3
efficiency [%], maximum value	19	21.6	26.1	26.7	32	33.5	29.3	30	31.4	30.2	27.7	27.6

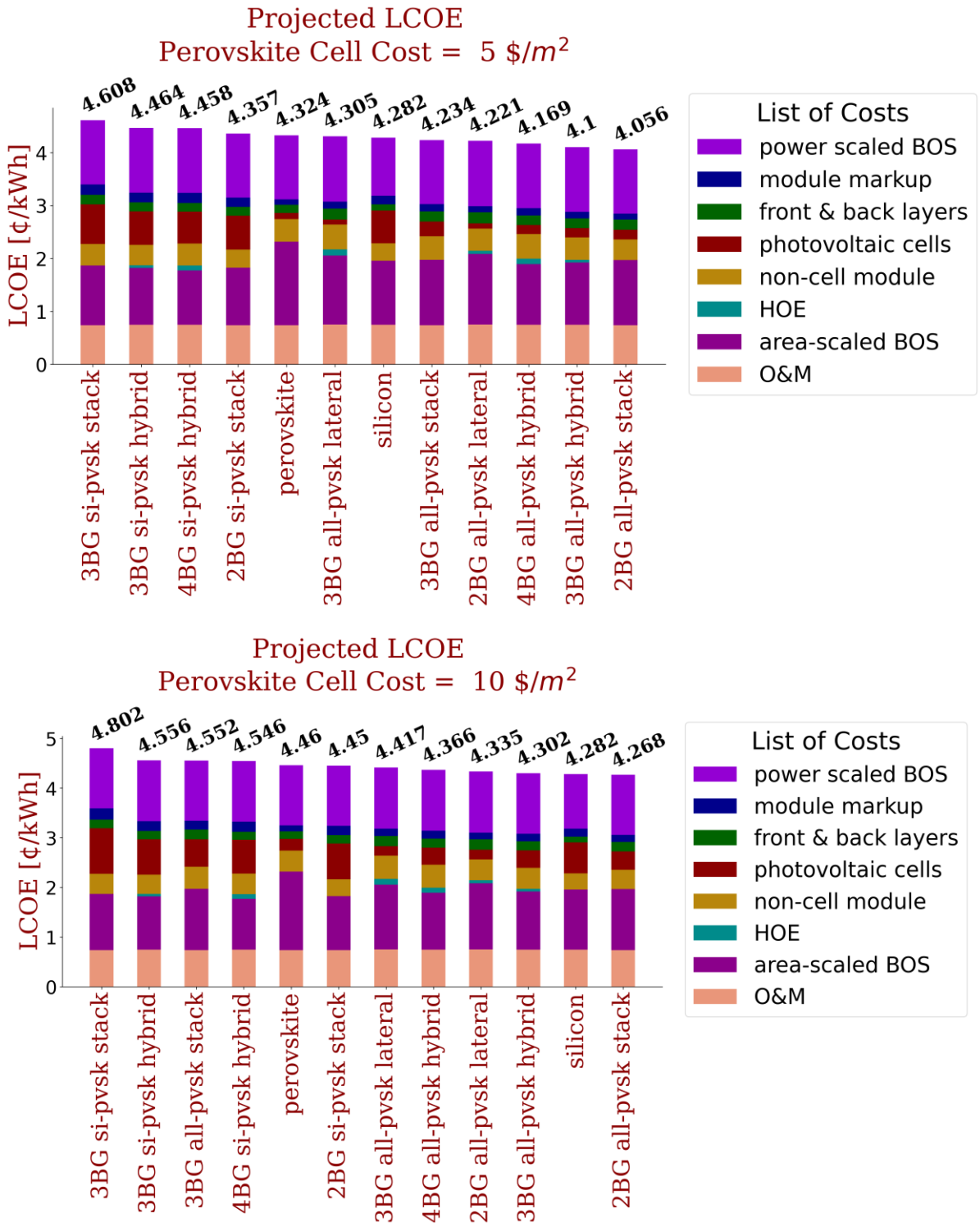

Figure A5: Bar charts showing the projected LCOE for modules with perovskite cell costs of 5$/m^2 and 10$/m^2. The baseline perovskite cell cost is 6.8$/m^2 and is taken from a cost analysis in the literature [25].

Appendix B

Table B1: Design and Construction Parameters for a two-bandgap spectrum splitting system with 1.25eV and 1.72eV perovskite cells. Assumes a thickness separation between the holograms and the PV cells of t = 10mm and a laser construction wavelength of $\lambda_c = 0.532nm$.

	Volume Holographic Lens Number			
	1	**2**	**3**	**4**
λ_B [μm]	0.53	0.8	0.8	0.53
λ_t [μm]	0.705	0.705	0.705	0.705
$\overrightarrow{R_f}$ [mm]	<6.25, 10.0>	<3.75, 10.0>	<-3.75, 10.0>	<-6.25, 10.0>
$\overrightarrow{R_1}$ [mm]	<7.24, 16.66>	<3.74, 10.56>	<-3.74, 10.56>	<-7.24, 16.66>
$\overrightarrow{R_2}$ [mm]	<-144.64, 190231.6>	<3.94, 56.97>	<-3.94, 56.97>	<144.64, 190231.6>
d [μm]	3	10	10	3
n_1	0.085	0.038	0.038	0.085
w [mm]	2.5	2.5	2.5	2.5

Table B2: Design and Construction Parameters for a two-bandgap spectrum splitting system with 1.1eV silicon cells and 1.72eV perovskite cells. Assumes a thickness separation between the holograms and the PV cells of t = 10mm and a laser construction wavelength of $\lambda_c = 0.532nm$.

	Volume Holographic Lens Number			
	1	**2**	**3**	**4**
λ_B [μm]	0.55	0.8	0.8	0.55
λ_t [μm]	0.705	0.705	0.705	0.705
$\overrightarrow{R_f}$ [mm]	<4.64, 10.0>	<2.14, 10.0>	<-2.14, 10.0>	<-4.64, 10.0>
$\overrightarrow{R_1}$ [mm]	<4.98, 14.65>	<2.14, 10.58>	<-2.14, 10.58>	<-4.98, 14.65>
$\overrightarrow{R_2}$ [mm]	<5.03, 914.88>	<2.18, 54.05>	<-2.18, 54.05>	<-5.03, 914.88>
d [μm]	5	18	18	5
n_1	0.054	0.023	0.023	0.054
w [mm]	3.57	1.43	1.43	3.57

Table B3: Design and Construction Parameters for a two-bandgap spectrum splitting system with 1.1eV silicon cells and 1.84eV GaInP cells. Assumes a thickness separation between the holograms and the PV cells of t = 10mm and a laser construction wavelength of $\lambda_c = 0.532nm$.

	Volume Holographic Lens Number			
	1	**2**	**3**	**4**
λ_B [μm]	0.55	0.8	0.8	0.55
λ_t [μm]	0.675	0.675	0.675	0.675
$\overrightarrow{R_f}$ [mm]	<4.64, 10.0>	<2.14, 10.0>	<-2.14, 10.0>	<-4.64, 10.0>
$\overrightarrow{R_1}$ [mm]	<4.93, 13.81>	<2.13, 10.07>	<-2.13, 10.07>	<-4.93, 13.81>
$\overrightarrow{R_2}$ [mm]	<5.02, 871.08>	<2.17, 51.59>	<-2.17, 51.59>	<-5.02, 871.08>
d [μm]	5	18	18	5
n_1	0.054	0.023	0.023	0.054
w [mm]	3.57	1.43	1.43	3.57

Table B4: Design and Construction Parameters for a two-bandgap spectrum splitting system with 1.1eV silicon cells and 1.4eV GaAs cells. Assumes a thickness separation between the holograms and the PV cells of t = 10mm and a laser construction wavelength of $\lambda_c = 0.532nm$.

	Volume Holographic Lens Number			
	1	**2**	**3**	**4**
λ_B [μm]	0.65	1.0	1.0	0.65
λ_t [μm]	0.875	0.875	0.875	0.875
$\overrightarrow{R_f}$ [mm]	<6.25, 10.0>	<3.75, 10.0>	<-3.75, 10.0>	<-6.25, 10.0>
$\overrightarrow{R_1}$ [mm]	<7.43, 19.34>	<3.78, 11.57>	<-3.78, 11.57>	<-7.43, 19.34>
$\overrightarrow{R_2}$ [mm]	<7.87, 212.74>	<3.93, 40.45>	<-3.93, 40.45>	<-7.87, 212.74>
d [μm]	3	18	18	3
n_1	0.1	0.027	0.027	0.1
w [mm]	2.5	2.5	2.5	2.5

Table B5: Design and Construction Parameters for a three-bandgap hybrid spectrum splitting systems with 2.3eV and 1.55eV perovskite cells and 1.1eV silicon cells. Assumes a thickness separation between the holograms and the PV cells of t = 10mm and a laser construction wavelength of $\lambda_c = 0.532nm$.

	Volume Holographic Lens Number			
	1	**2**	**3**	**4**
λ_B [μm]	0.47	0.67	0.67	0.47
λ_t [μm]	0.535	0.535	0.535	0.535
$\overrightarrow{R_f}$ [mm]	<5.0, 10.0>	<2.5, 10.0>	<-2.5, 10.0>	<-5.0, 10.0>
$\overrightarrow{R_1}$ [mm]	<5.12, 11.16>	<2.45, 8.63>	<-2.45, 8.63>	<-5.12, 11.16>
$\overrightarrow{R_2}$ [mm]	<-12992.95, 519143.89>	<2.54, 79.51>	<-2.54, 79.51>	<12992.95, 519143.89>
d [μm]	4	14	14	4
n_1	0.056	0.023	0.023	0.056
w [mm]	3.33	1.67	1.67	3.33

Table B6: Design and Construction Parameters for a three-bandgap hybrid spectrum splitting systems with 2.3eV, 1.63eV, and 1.25eV perovskite cells. Assumes a thickness separation between the holograms and the PV cells of t = 10mm and a laser construction wavelength of $\lambda_c = 0.532nm$.

	Volume Holographic Lens Number			
	1	**2**	**3**	**4**
λ_B [μm]	0.45	0.65	0.65	0.45
λ_t [μm]	0.535	0.535	0.535	0.535
$\overrightarrow{R_f}$ [mm]	<5.0, 10.0>	<2.5, 10.0>	<-2.5, 10.0>	<-5.0, 10.0>
$\overrightarrow{R_1}$ [mm]	<5.17, 11.55>	<2.46, 8.82>	<-2.46, 8.82>	<-5.17, 11.55>
$\overrightarrow{R_2}$ [mm]	<-10653.44, 322961.41>	<2.55, 93.3>	<-2.55, 93.3>	<10653.44, 322961.41>
d [μm]	4	12	12	4
n_1	0.054	0.027	0.027	0.054
w [mm]	3.33	1.67	1.67	3.33

Table B7: Design and Construction Parameters for a three-bandgap lateral spectrum splitting system with 2.3eV, 1.63eV, and 1.25eV perovskite cells. Assumes a thickness separation between the holograms and the PV cells of t = 10mm and a laser construction wavelength of $\lambda_c = 0.532nm$.

		Volume Holographic Lens Number					
		1	**2**	**3**	**4**	**5**	**6**
a	λ_B [μm]	0.65	0.425	0.85	0.85	0.425	0.65
	λ_t [μm]	0.535	0.535	0.76	0.76	0.535	0.535
	$\overrightarrow{R_f}$ [mm]	<5.63, 10.0>	<3.75, 10.0>	<-3.12, 10.0>	<3.12, 10.0>	<-3.75, 10.0>	<-5.63, 10.0>
	$\overrightarrow{R_1}$ [mm]	<5.08, 7.78>	<3.83, 11.63>	<-3.14, 11.08>	<3.14, 11.08>	<-3.83, 11.63>	<-5.08, 7.78>
	$\overrightarrow{R_2}$ [mm]	<6.05, 101.75>	<-21331.37, 647832.11>	<-3.26, 50.92>	<3.26, 50.92>	<21331.37, 647832.11>	<-6.05, 101.75>
	d [μm]	6	8	30	30	8	6
	n_1	0.049	0.027	0.014	0.014	0.027	0.049
	w [mm]	1.25	2.5	1.25	1.25	2.5	1.25
b	λ_B [μm]	0.45	0.85	0.65	0.65	0.85	0.45
	λ_t [μm]	0.535	0.76	0.535	0.535	0.76	0.535
	$\overrightarrow{R_f}$ [mm]	<-6.88, 10.0>	<6.25, 10.0>	<1.88, 10.0>	<-1.88, 10.0>	<-6.25, 10.0>	<6.88, 10.0>
	$\overrightarrow{R_1}$ [mm]	<-7.46, 12.36>	<6.29, 11.15>	<1.86, 8.92>	<-1.86, 8.92>	<-6.29, 11.15>	<7.46, 12.36>
	$\overrightarrow{R_2}$ [mm]	<18791.46, 403958.99>	<7.13, 58.87>	<1.89, 92.09>	<-1.89, 92.09>	<-7.13, 58.87>	<-18791.46, 403958.99>
	d [μm]	2	8	30	30	8	2
	n_1	0.1	0.049	0.01	0.01	0.049	0.1
	w [mm]	1.25	2.5	1.25	1.25	2.5	1.25

Table B8: Design and Construction Parameters for a three-bandgap lateral spectrum splitting system with 1.84eV GaInP cells, 1.4eV GaAs cells, and 1.1eV silicon cells. Assumes a thickness separation between the holograms and the PV cells of t = 10mm and a laser construction wavelength of $\lambda_c = 0.532nm$.

		Volume Holographic Lens Number					
		1	**2**	**3**	**4**	**5**	**6**
a	λ_B [μm]	0.775	0.55	1.0	1.0	0.55	0.775
	λ_t [μm]	0.675	0.675	0.875	0.875	0.675	0.675
	$\overrightarrow{R_f}$ [mm]	<5.63, 10.0>	<3.75, 10.0>	<-3.12, 10.0>	<3.12, 10.0>	<-3.75, 10.0>	<-5.63, 10.0>
	$\overrightarrow{R_1}$ [mm]	<5.5, 10.01>	<3.91, 13.36>	<-3.15, 11.54>	<3.15, 11.54>	<-3.91, 13.36>	<-5.5, 10.01>
	$\overrightarrow{R_2}$ [mm]	<6.23, 65.17>	<3.99, 836.78>	<-3.25, 39.71>	<3.25, 39.71>	<-3.99, 836.78>	<-6.23, 65.17>
	d [μm]	8	10	30	30	10	8
	n_1	0.045	0.027	0.016	0.016	0.027	0.045
	w [mm]	1.25	2.5	1.25	1.25	2.5	1.25
b	λ_B [μm]	0.55	1	0.775	0.775	1	0.55
	λ_t [μm]	0.675	0.875	0.675	0.675	0.875	0.675
	$\overrightarrow{R_f}$ [mm]	<-6.88, 10.0>	<6.25, 10.0>	<1.88, 10.0>	<-1.88, 10.0>	<-6.25, 10.0>	<6.88, 10.0>
	$\overrightarrow{R_1}$ [mm]	<-8.02, 15.73>	<6.32, 11.68>	<1.87, 10.31>	<-1.87, 10.31>	<-6.32, 11.68>	<8.02, 15.73>
	$\overrightarrow{R_2}$ [mm]	<-8.81, 1102.58>	<7.07, 45.47>	<1.9, 56.69>	<-1.9, 56.69>	<-7.07, 45.47>	<8.81, 1102.58>
	d [μm]	3	8	30	30	8	3
	n_1	0.087	0.056	0.014	0.014	0.056	0.087
	w [mm]	1.25	2.5	1.25	1.25	2.5	1.25

Table B9: Design and Construction Parameters for a four-bandgap hybrid spectrum splitting system. The cascaded volume holographic lens parameters are for splitting light between 2.3eV, 1.72eV, and 1.55eV perovskite cells. The bottom cell is either a 1.1eV silicon cell or a 1.25eV perovskite cell. The values assume a thickness separation between the holograms and the PV cells of t = 10mm and a laser construction wavelength of $\lambda_c = 0.532nm$.

		Volume Holographic Lens Number					
		1	**2**	**3**	**4**	**5**	**6**
a	λ_B [μm]	0.615	0.75	0.75	0.75	0.75	0.615
	λ_t [μm]	0.535	0.705	0.705	0.705	0.705	0.535
	$\overrightarrow{R_f}$ [mm]	<5.63, 9.5>	<6.25, 9.5>	<-3.12, 9.5>	<3.12, 9.5>	<-6.25, 9.5>	<-5.63, 9.5>
	$\overrightarrow{R_1}$ [mm]	<5.22, 7.93>	<6.41, 10.9>	<-3.15, 10.59>	<3.15, 10.59>	<-6.41, 10.9>	<-5.22, 7.93>
	$\overrightarrow{R_2}$ [mm]	<6.23, 143.69>	<7.35, 79.32>	<-3.29, 66.41>	<3.29, 66.41>	<-7.35, 79.32>	<-6.23, 143.69>
	d [μm]	4	6	30	30	6	4
	n_1	0.069	0.056	0.012	0.012	0.056	0.069
	w [mm]	1.25	2.5	1.25	1.25	2.5	1.25
b	λ_B [μm]	0.45	0.425	0.615	0.615	0.425	0.45
	λ_t [μm]	0.535	0.535	0.535	0.535	0.535	0.535
	$\overrightarrow{R_f}$ [mm]	<-6.88, 9.5>	<3.75, 9.5>	<1.88, 9.5>	<-1.88, 9.5>	<-3.75, 9.5>	<6.88, 9.5>
	$\overrightarrow{R_1}$ [mm]	<-7.53, 11.91>	<3.84, 11.1>	<1.86, 8.77>	<-1.86, 8.77>	<-3.84, 11.1>	<7.53, 11.91>
	$\overrightarrow{R_2}$ [mm]	<19188.91, 396224.41>	<-60164.54, 1742899.96>	<1.9, 125.03>	<-1.9, 125.03>	<60164.54, 1742899.96>	<-19188.91, 396224.41>
	d [μm]	3	8	30	30	8	3
	n_1	0.069	0.027	0.01	0.01	0.027	0.069
	w [mm]	1.25	2.5	1.25	1.25	2.5	1.25

References

[1] M. A. Green, “Photovoltaic technology and visions for the future,” *Progress in Energy*, vol. 1, no. 1, Jul. 2019, doi: 10.1088/2516-1083/ab0fa8.

[2] G. Kavlak, J. McNerney, and J. E. Trancik, “Evaluating the causes of cost reduction in photovoltaic modules,” *Energy Policy*, vol. 123, Dec. 2018, doi: 10.1016/j.enpol.2018.08.015.

[3] M. A. Woodhouse, B. Smith, A. Ramdas, and R. M. Margolis, “Crystalline Silicon Photovoltaic Module Manufacturing Costs and Sustainable Pricing: 1H 2018 Benchmark and Cost Reduction Road Map,” Golden, CO (United States), Feb. 2019. doi: 10.2172/1495719.

[4] W. Shockley and H. J. Queisser, “Detailed Balance Limit of Efficiency of *p-n* Junction Solar Cells,” *Journal of Applied Physics*, vol. 32, no. 3, Mar. 1961, doi: 10.1063/1.1736034.

[5] A. Richter, M. Hermle, and S. W. Glunz, “Reassessment of the Limiting Efficiency for Crystalline Silicon Solar Cells,” *IEEE Journal of Photovoltaics*, vol. 3, no. 4, Oct. 2013, doi: 10.1109/JPHOTOV.2013.2270351.

[6] K. Yoshikawa *et al.*, “Silicon heterojunction solar cell with interdigitated back contacts for a photoconversion efficiency over 26%,” *Nature Energy*, vol. 2, no. 5, May 2017, doi: 10.1038/nenergy.2017.32.

[7] E. C. Warmann, C. Flowers, J. Lloyd, C. N. Eisler, M. D. Escarra, and H. A. Atwater, “Design of photovoltaics for modules with 50% efficiency,” *Energy Science & Engineering*, vol. 5, no. 2, Apr. 2017, doi: 10.1002/ese3.155.

[8] A. de Vos, “Detailed balance limit of the efficiency of tandem solar cells,” *Journal of Physics D: Applied Physics*, vol. 13, no. 5, May 1980, doi: 10.1088/0022-3727/13/5/018.

[9] J. M. Gee and G. F. Virshup, “A 31%-efficient GaAs/silicon mechanically stacked, multijunction concentrator solar cell,” 1988. doi: 10.1109/PVSC.1988.105803.

[10] M. Yamaguchi, T. Takamoto, K. Araki, and N. Ekins-Daukes, “Multi-junction III–V solar cells: current status and future potential,” *Solar Energy*, vol. 79, no. 1, Jul. 2005, doi: 10.1016/j.solener.2004.09.018.

[11] J. F. Geisz *et al.*, “Six-junction III–V solar cells with 47.1% conversion efficiency under 143 Suns concentration,” *Nature Energy*, vol. 5, no. 4, Apr. 2020, doi: 10.1038/s41560-020-0598-5.

[12] N. Didato, F. Sodari, T. Stalcup, P. Strittmatter, and R. Angel, “REhnu dish based CPV: Performance and reliability improvements based on a year of field experience,” 2018. doi: 10.1063/1.5053492.

[13] S. P. Philipps, A. W. Bett, K. Horowitz, and S. Kurtz, “Current Status of Concentrator Photovoltaic (CPV) Technology,” Golden, CO (United States), Dec. 2015. doi: 10.2172/1351597.

[14] J. M. Russo, D. Zhang, M. Gordon, S. Vorndran, Y. Wu, and R. K. Kostuk, “Spectrum splitting metrics and effect of filter characteristics on photovoltaic system performance,” *Optics Express*, vol. 22, no. S2, Mar. 2014, doi: 10.1364/OE.22.00A528.

[15] M. V. Collados, D. Chemisana, and J. Atencia, “Holographic solar energy systems: The role of optical elements,” *Renewable and Sustainable Energy Reviews*, vol. 59, Jun. 2016, doi: 10.1016/j.rser.2015.12.260.

[16] N. Mohammad, P. Wang, D. J. Friedman, and R. Menon, “Enhancing photovoltaic output power by 3-band spectrum-splitting and concentration using a diffractive micro-optic,” *Optics Express*, vol. 22, no. S6, Oct. 2014, doi: 10.1364/OE.22.0A1519.

[17] D. Zhang, Y. Wu, J. M. Russo, M. Gordon, S. Vorndran, and R. K. Kostuk, “Optical performance of dichroic spectrum-splitting filters,” *Journal of Photonics for Energy*, vol. 4, no. 1, May 2014, doi: 10.1117/1.JPE.4.043095.

[18] N.-G. Park, “Perovskite solar cells: an emerging photovoltaic technology,” *Materials Today*, vol. 18, no. 2, Mar. 2015, doi: 10.1016/j.mattod.2014.07.007.

[19] T. Leijtens, K. A. Bush, R. Prasanna, and M. D. McGehee, “Opportunities and challenges for tandem solar cells using metal halide perovskite semiconductors,” *Nature Energy*, vol. 3, no. 10, Oct. 2018, doi: 10.1038/s41560-018-0190-4.

[20] E. H. Jung *et al.*, “Efficient, stable and scalable perovskite solar cells using poly(3-hexylthiophene),” *Nature*, vol. 567, no. 7749, Mar. 2019, doi: 10.1038/s41586-019-1036-3.

[21] M. A. Green, E. D. Dunlop, J. Hohl-Ebinger, M. Yoshita, N. Kopidakis, and X. Hao, "Solar cell efficiency tables (version 56)," *Progress in Photovoltaics: Research and Applications*, vol. 28, no. 7, Jul. 2020, doi: 10.1002/pip.3303.

[22] Z. Li *et al.*, "Cost Analysis of Perovskite Tandem Photovoltaics," *Joule*, vol. 2, no. 8, Aug. 2018, doi: 10.1016/j.joule.2018.05.001.

[23] J. Tong *et al.*, "Carrier lifetimes of >1 μs in Sn-Pb perovskites enable efficient all-perovskite tandem solar cells," *Science*, vol. 364, no. 6439, May 2019, doi: 10.1126/science.aav7911.

[24] W. S. Yang *et al.*, "Iodide management in formamidinium-lead-halide–based perovskite layers for efficient solar cells," *Science*, vol. 356, no. 6345, Jun. 2017, doi: 10.1126/science.aan2301.

[25] M. Saliba *et al.*, "Incorporation of rubidium cations into perovskite solar cells improves photovoltaic performance," *Science*, vol. 354, no. 6309, Oct. 2016, doi: 10.1126/science.aah5557.

[26] S. Gharibzadeh *et al.*, "Record Open-Circuit Voltage Wide-Bandgap Perovskite Solar Cells Utilizing 2D/3D Perovskite Heterostructure," *Advanced Energy Materials*, vol. 9, no. 21, Jun. 2019, doi: 10.1002/aenm.201803699.

[27] J. H. Heo, D. H. Song, and S. H. Im, "Planar $CH_3NH_3PbBr_3$ Hybrid Solar Cells with 10.4% Power Conversion Efficiency, Fabricated by Controlled Crystallization in the Spin-Coating Process," *Advanced Materials*, vol. 26, no. 48, Dec. 2014, doi: 10.1002/adma.201403140.

[28] L. Qiu, L. K. Ono, and Y. Qi, "Advances and challenges to the commercialization of organic–inorganic halide perovskite solar cell technology," *Materials Today Energy*, vol. 7, Mar. 2018, doi: 10.1016/j.mtener.2017.09.008.

[29] S. He, L. Qiu, L. K. Ono, and Y. Qi, "How far are we from attaining 10-year lifetime for metal halide perovskite solar cells?," *Materials Science and Engineering: R: Reports*, vol. 140, Apr. 2020, doi: 10.1016/j.mser.2020.100545.

[30] Z. Wang *et al.*, "Efficient and Air-Stable Mixed-Cation Lead Mixed-Halide Perovskite Solar Cells with n-Doped Organic Electron Extraction Layers," *Advanced Materials*, vol. 29, no. 5, Feb. 2017, doi: 10.1002/adma.201604186.

[31] G. Grancini *et al.*, "One-Year stable perovskite solar cells by 2D/3D interface engineering," *Nature Communications*, vol. 8, no. 1, Aug. 2017, doi: 10.1038/ncomms15684.

[32] S.-H. Turren-Cruz, A. Hagfeldt, and M. Saliba, "Methylammonium-free, high-performance, and stable perovskite solar cells on a planar architecture," *Science*, vol. 362, no. 6413, Oct. 2018, doi: 10.1126/science.aat3583.

[33] C. Yan *et al.*, "Cu2ZnSnS4 solar cells with over 10% power conversion efficiency enabled by heterojunction heat treatment," *Nature Energy*, vol. 3, no. 9, Sep. 2018, doi: 10.1038/s41560-018-0206-0.

[34] J. J. Becker *et al.*, "Monocrystalline 1.7-eV-Bandgap MgCdTe Solar Cell With 11.2% Efficiency," *IEEE Journal of Photovoltaics*, vol. 8, no. 2, Mar. 2018, doi: 10.1109/JPHOTOV.2017.2769105.

[35] C. D. Bailie *et al.*, "Semi-transparent perovskite solar cells for tandems with silicon and CIGS," *Energy & Environmental Science*, vol. 8, no. 3, 2015, doi: 10.1039/C4EE03322A.

[36] N. N. Lal, Y. Dkhissi, W. Li, Q. Hou, Y.-B. Cheng, and U. Bach, "Perovskite Tandem Solar Cells," *Advanced Energy Materials*, vol. 7, no. 18, Sep. 2017, doi: 10.1002/aenm.201602761.

[37] B. Dou *et al.*, "High-Performance Flexible Perovskite Solar Cells on Ultrathin Glass: Implications of the TCO," *The Journal of Physical Chemistry Letters*, vol. 8, no. 19, Oct. 2017, doi: 10.1021/acs.jpclett.7b02128.

[38] Y. Zhang *et al.*, "Fully Solution-Processed TCO-Free Semitransparent Perovskite Solar Cells for Tandem and Flexible Applications," *Advanced Energy Materials*, vol. 8, no. 1, Jan. 2018, doi: 10.1002/aenm.201701569.

[39] M. Schultes *et al.*, "Sputtered Transparent Electrodes (IO:H and IZO) with Low Parasitic Near-Infrared Absorption for Perovskite–Cu(In,Ga)Se $_2$ Tandem Solar Cells," *ACS Applied Energy Materials*, vol. 2, no. 11, Nov. 2019, doi: 10.1021/acsaem.9b01224.

[40] D. A. Jacobs *et al.*, "Light Management: A Key Concept in High-Efficiency Perovskite/Silicon Tandem Photovoltaics," *The Journal of Physical Chemistry Letters*, vol. 10, no. 11, Jun. 2019, doi: 10.1021/acs.jpclett.8b03721.

[41] M. F. Weber, "Giant Birefringent Optics in Multilayer Polymer Mirrors," *Science*, vol. 287, no. 5462, Mar. 2000, doi: 10.1126/science.287.5462.2451.

[42] J. D. McCambridge *et al.*, "Compact spectrum splitting photovoltaic module with high efficiency," *Progress in Photovoltaics: Research and Applications*, vol. 19, no. 3, May 2011, doi: 10.1002/pip.1030.

[43] M. A. Green, M. J. Keevers, I. Thomas, J. B. Lasich, K. Emery, and R. R. King, "40% efficient sunlight to electricity conversion," *Progress in Photovoltaics: Research and Applications*, vol. 23, no. 6, Jun. 2015, doi: 10.1002/pip.2612.

[44] D. Zhang, M. Gordon, J. M. Russo, S. Vorndran, and R. K. Kostuk, "Spectrum-splitting photovoltaic system using transmission holographic lenses," *Journal of Photonics for Energy*, vol. 3, no. 1, Jul. 2013, doi: 10.1117/1.JPE.3.034597.

[45] J. M. Castro, D. Zhang, B. Myer, and R. K. Kostuk, "Energy collection efficiency of holographic planar solar concentrators," *Applied Optics*, vol. 49, no. 5, Feb. 2010, doi: 10.1364/AO.49.000858.

[46] A. D. Cronin *et al.*, "Holographic CPV field tests at the Tucson Electric Power solar test yard," Jun. 2011. doi: 10.1109/PVSC.2011.6186423.

[47] Y. Wu and R. K. Kostuk, "Two-junction holographic spectrum-splitting microconcentrating photovoltaic system," *Journal of Photonics for Energy*, vol. 7, no. 1, Feb. 2017, doi: 10.1117/1.JPE.7.017001.

[48] Y. Wu, B. Chrysler, and R. K. Kostuk, "Design and fabrication of cascaded dichromate gelatin holographic filters for spectrum-splitting PV systems," *Journal of Photonics for Energy*, vol. 8, no. 01, Jan. 2018, doi: 10.1117/1.JPE.8.017001.

[49] S. D. Vorndran, B. Chrysler, B. Wheelwright, R. Angel, Z. Holman, and R. Kostuk, "Off-axis holographic lens spectrum-splitting photovoltaic system for direct and diffuse solar energy conversion," *Applied Optics*, vol. 55, no. 27, Sep. 2016, doi: 10.1364/AO.55.007522.

[50] K. Masuko *et al.*, "Achievement of More Than 25% Conversion Efficiency With Crystalline Silicon Heterojunction Solar Cell," *IEEE Journal of Photovoltaics*, vol. 4, no. 6, Nov. 2014, doi: 10.1109/JPHOTOV.2014.2352151.

[51] C. Gueymard, "SMARTS2: a simple model of the atmospheric radiative transfer of sunshine: algorithms and performance assessment," *NREL*, Dec. 1995.

[52] M. A. Green, Y. Hishikawa, E. D. Dunlop, D. H. Levi, J. Hohl-Ebinger, and A. W. Y. Ho-Baillie, "Solar cell efficiency tables (version 51)," *Progress in Photovoltaics: Research and Applications*, vol. 26, no. 1, Jan. 2018, doi: 10.1002/pip.2978.

[53] B. M. Kayes *et al.*, "27.6% Conversion efficiency, a new record for single-junction solar cells under 1 sun illumination," Jun. 2011. doi: 10.1109/PVSC.2011.6185831.

[54] M. A. Green, E. D. Dunlop, D. H. Levi, J. Hohl-Ebinger, M. Yoshita, and A. W. Y. Ho-Baillie, "Solar cell efficiency tables (version 54)," *Progress in Photovoltaics: Research and Applications*, vol. 27, no. 7, Jul. 2019, doi: 10.1002/pip.3171.

[55] H. KOGELNIK, "Coupled Wave Theory for Thick Hologram Gratings," in *Landmark Papers on Photorefractive Nonlinear Optics*, WORLD SCIENTIFIC, 1995. doi: 10.1142/9789812832047_0016.

[56] K. K. Kostuk, *Holography: Principles and Applications*. CRC Press, 2019.

[57] H. Chen, R. R. Hershey, and E. N. Leith, "Design of a holographic lens for the infrared," *Applied Optics*, vol. 26, no. 10, May 1987, doi: 10.1364/AO.26.001983.

[58] W.-H. Lee, "Techniques for recording holographic lenses for infrared wavelengths," *Optics Communications*, vol. 34, no. 1, Jul. 1980, doi: 10.1016/0030-4018(80)90152-2.

[59] "Chapter 24. The Method of Least Squares," in *The Probability Lifesaver*, Princeton University Press, 2017. doi: 10.1515/9781400885381-026.

[60] "scipy.optimize.minimize," *Scipy.org*, Apr. 26, 2021.

[61] C. G. Stojanoff, "A review of selected technological applications of DCG holograms," Feb. 2011. doi: 10.1117/12.874192.

[62] C. G. Stojanoff, "Review of the technology for the manufacturing of large-format DCG holograms for technical applications," Apr. 1997. doi: 10.1117/12.271375.

[63] S. Tropartz, O. Brasseur, R. Kubitzek, and C. G. Stojanoff, "Development and investigation of dichromated gelatin film for the fabrication of large-format holograms operating at 400-900," Sep. 1991. doi: 10.1117/12.47055.

[64] T. A. Shankoff, "Phase Holograms in Dichromated Gelatin," *Applied Optics*, vol. 7, no. 10, Oct. 1968, doi: 10.1364/AO.7.002101.

[65] Y. Luo, J. Castro, J. K. Barton, R. K. Kostuk, and G. Barbastathis, "Simulations and experiments of aperiodic and multiplexed gratings in volume holographic imaging systems," *Optics Express*, vol. 18, no. 18, Aug. 2010, doi: 10.1364/OE.18.019273.

[66] M. G. Moharam and T. K. Gaylord, "Rigorous coupled-wave analysis of planar-grating diffraction," *Journal of the Optical Society of America*, vol. 71, no. 7, Jul. 1981, doi: 10.1364/JOSA.71.000811.

[67] "DiffractMOD Product Overview."

[68] M. G. Moharam, T. K. Gaylord, E. B. Grann, and D. A. Pommet, "Formulation for stable and efficient implementation of the rigorous coupled-wave analysis of binary gratings," *Journal of the Optical Society of America A*, vol. 12, no. 5, May 1995, doi: 10.1364/JOSAA.12.001068.

[69] M. G. Moharam and T. K. Gaylord, "Three-dimensional vector coupled-wave analysis of planar-grating diffraction," *Journal of the Optical Society of America*, vol. 73, no. 9, Sep. 1983, doi: 10.1364/JOSA.73.001105.

[70] "FRED Optical Engineering Software."

[71] S. Wilcox, "National Solar Radiation Database 1991-2005 Update: User's Manual," Golden, CO, Apr. 2007. doi: 10.2172/901864.

[72] Z. J. Yu, K. C. Fisher, B. M. Wheelwright, R. P. Angel, and Z. C. Holman, "PVMirror: A New Concept for Tandem Solar Cells and Hybrid Solar Converters," *IEEE Journal of Photovoltaics*, vol. 5, no. 6, Nov. 2015, doi: 10.1109/JPHOTOV.2015.2458571.

[73] A. Hasan, J. Sarwar, and A. H. Shah, "Concentrated photovoltaic: A review of thermal aspects, challenges and opportunities," *Renewable and Sustainable Energy Reviews*, vol. 94, Oct. 2018, doi: 10.1016/j.rser.2018.06.014.

[74] D. Bouhafs, "Design and simulation of antireflection coating systems for optoelectronic devices: Application to silicon solar cells," *Solar Energy Materials and Solar Cells*, vol. 52, no. 1–2, Mar. 1998, doi: 10.1016/S0927-0248(97)00273-0.

[75] S. H. Zaidi, D. S. Ruby, and J. M. Gee, "Characterization of random reactive ion etched-textured silicon solar cells," *IEEE Transactions on Electron Devices*, vol. 48, no. 6, Jun. 2001, doi: 10.1109/16.925248.

[76] S. C. Baker-Finch and K. R. McIntosh, "Reflection of normally incident light from silicon solar cells with pyramidal texture," *Progress in Photovoltaics: Research and Applications*, vol. 19, no. 4, Jun. 2011, doi: 10.1002/pip.1050.

[77] "Pilkington Sunplus," *Pilkington Sunplus*.

[78] S. Darbe, M. D. Escarra, E. C. Warmann, and H. A. Atwater, "Simulation and partial prototyping of an eight-junction holographic spectrum-splitting photovoltaic module," *Energy Science & Engineering*, vol. 7, no. 6, Dec. 2019, doi: 10.1002/ese3.445.

[79] R. Lin *et al.*, "Monolithic all-perovskite tandem solar cells with 24.8% efficiency exploiting comproportionation to suppress Sn(ii) oxidation in precursor ink," *Nature Energy*, vol. 4, no. 10, Oct. 2019, doi: 10.1038/s41560-019-0466-3.

[80] J. Werner, B. Niesen, and C. Ballif, "Perovskite/Silicon Tandem Solar Cells: Marriage of Convenience or True Love Story? – An Overview," *Advanced Materials Interfaces*, vol. 5, no. 1, Jan. 2018, doi: 10.1002/admi.201700731.

[81] G. B. Ingersoll and J. R. Leger, “Optimization of multi-grating volume holographic spectrum splitters for photovoltaic applications,” *Applied Optics*, vol. 55, no. 20, Jul. 2016, doi: 10.1364/AO.55.005399.

[82] M. Fischer, “ITRPV 9th edition 2018 report release and key findings,” Penang, Malaysia, 2018.

[83] D. Lan and M. A. Green, “The potential and design principle for next-generation spectrum-splitting photovoltaics: Targeting 50% efficiency through built-in filters and generalization of concept,” *Progress in Photovoltaics: Research and Applications*, vol. 27, no. 11, Nov. 2019, doi: 10.1002/pip.3081.

[84] M. Theristis, V. Venizelou, G. Makrides, and G. E. Georghiou, “Energy Yield in Photovoltaic Systems,” in *McEvoy’s Handbook of Photovoltaics*, Elsevier, 2018. doi: 10.1016/B978-0-12-809921-6.00017-3.

[85] E. C. Warmann and H. A. Atwater, “Energy production advantage of independent subcell connection for multijunction photovoltaics,” *Energy Science & Engineering*, vol. 4, no. 4, Jul. 2016, doi: 10.1002/ese3.125.

[86] M. Kutzer *et al.*, “Ertragssteigerung durch bifaciale Modultechnologie.”

[87] S. A. Pelaez, C. Deline, S. M. MacAlpine, B. Marion, J. S. Stein, and R. K. Kostuk, “Comparison of Bifacial Solar Irradiance Model Predictions With Field Validation,” *IEEE Journal of Photovoltaics*, vol. 9, no. 1, Jan. 2019, doi: 10.1109/JPHOTOV.2018.2877000.

[88] X. Sun, M. R. Khan, C. Deline, and M. A. Alam, “Optimization and performance of bifacial solar modules: A global perspective,” *Applied Energy*, vol. 212, Feb. 2018, doi: 10.1016/j.apenergy.2017.12.041.

[89] J. E. Castillo-Aguilella and P. S. Hauser, “Multi-Variable Bifacial Photovoltaic Module Test Results and Best-Fit Annual Bifacial Energy Yield Model,” *IEEE Access*, vol. 4, 2016, doi: 10.1109/ACCESS.2016.2518399.

[90] A. Luque, E. Lorenzo, G. Sala, and S. López-Romero, “Diffusing reflectors for bifacial photovoltaic panels,” *Solar Cells*, vol. 13, no. 3, Jan. 1985, doi: 10.1016/0379-6787(85)90021-3.

[91] A. Cuevas, A. Luque, J. Eguren, and J. del Alamo, “50 Per cent more output power from an albedo-collecting flat panel using bifacial solar cells,” *Solar Energy*, vol. 29, no. 5, 1982, doi: 10.1016/0038-092X(82)90078-0.

[92] R. Guerrero-Lemus, R. Vega, T. Kim, A. Kimm, and L. E. Shephard, “Bifacial solar photovoltaics – A technology review,” *Renewable and Sustainable Energy Reviews*, vol. 60, Jul. 2016, doi: 10.1016/j.rser.2016.03.041.

[93] “International technology roadmap for photovoltaic (ITRPV) 2017 Results plus 2018 Maturity Report, 9th edition,” 2020.

[94] D. Zhang, “One-axis tracking holographic planar concentrator systems,” *Journal of Photonics for Energy*, vol. 1, no. 1, Jan. 2011, doi: 10.1117/1.3590943.

[95] F. Sallaberry, R. Pujol-Nadal, M. Larcher, and M. H. Rittmann-Frank, “Direct tracking error characterization on a single-axis solar tracker,” *Energy Conversion and Management*, vol. 105, Nov. 2015, doi: 10.1016/j.enconman.2015.08.081.

[96] F.-K. Bruder, T. Fäcke, and T. Rölle, “The Chemistry and Physics of Bayfol® HX Film Holographic Photopolymer,” *Polymers*, vol. 9, no. 12, Sep. 2017, doi: 10.3390/polym9100472.

[97] J. Marín-Sáez, J. Atencia, D. Chemisana, and M.-V. Collados, “Characterization of volume holographic optical elements recorded in Bayfol HX photopolymer for solar photovoltaic applications,” *Optics Express*, vol. 24, no. 6, Mar. 2016, doi: 10.1364/OE.24.00A720.

[98] P.-A. Blanche, “Volume phase holographic gratings: large size and high diffraction efficiency,” *Optical Engineering*, vol. 43, no. 11, Nov. 2004, doi: 10.1117/1.1803557.

[99] P.-A. Blanche, S. L. Habraken, P. C. Lemaire, and C. A. J. Jamar, “Large-scale DCG transmission holographic gratings for astronomy,” Feb. 2003. doi: 10.1117/12.456671.

[100] J. Crespo, M. A. Satorre, J. A. Quintana, and F. Ania, “Gelatin layers for holographic purposes: an X-ray diffraction study,” *Journal of Materials Science*, vol. 30, no. 24, Dec. 1995, doi: 10.1007/BF00369660.

[101] B. J. Chang, “Post-processing of developed dichromated gelatin holograms,” *Optics Communications*, vol. 17, no. 3, Jun. 1976, doi: 10.1016/0030-4018(76)90257-1.

[102] N. Kamiya, “Rigorous coupled-wave analysis for practical planar dielectric gratings: 2 Diffraction by a surface-eroded hologram layer,” *Applied Optics*, vol. 37, no. 25, Sep. 1998, doi: 10.1364/AO.37.005854.

[103] P.-A. Blanche, P. Gailly, S. Habraken, P. Lemaire, and C. Jamar, “Mosaiced and high line frequency VPH gratings for astronomy,” Sep. 2004. doi: 10.1117/12.548738.

[104] “Product Specification,” *Sigma-Aldrich*.

[105] N. Kamiya, “Rigorous coupled-wave analysis for practical planar dielectric gratings: 1 Thickness-changed holograms and some characteristics of diffraction efficiency,” *Applied Optics*, vol. 37, no. 25, Sep. 1998, doi: 10.1364/AO.37.005843.

[106] M. Okui, K. Wakunami, R. Oi, Y. Ichihashi, B. J. Jackin, and K. Yamamoto, “Copying of holograms by spot scanning approach,” *Applied Optics*, vol. 57, no. 15, May 2018, doi: 10.1364/AO.57.004117.

[107] F.-K. Bruder *et al.*, “Mass production of volume holographic optical elements (vHOEs) using Bayfol ® HX photopolymer film in a roll-to-roll copy process,” Apr. 2017. doi: 10.1117/12.2250933.

[108] D. F. Tipton, “New hologram replicator for volume holograms and holographic optical elements,” Mar. 1998. doi: 10.1117/12.304520.

[109] E. D. Aspnes, J. E. Castillo, P. S. Hausser, J. M. Russo, R. D. Courreges, and G. Rosenberg, “Volume hologram replicator for transmission type gratings,” 8,614,842, Dec. 2013

[110] J. M. Russo, S. A. Coe-Sullivan, M. Sanchez, J. Padiyar, and F. Dimov, “Manufacturable transparent holographic components for HUD applications,” in *Practical Holography XXXIII: Displays, Materials, and Applications*, Mar. 2019. doi: 10.1117/12.2510571.

[111] T. Silverman, M. Deceglie, and K. Horowitz, “NREL Comparative PV LCOE Calculator,” *http://pvlcoe.nrel.gov*, Mar. 2018.

[112] Z. Song *et al.*, “A technoeconomic analysis of perovskite solar module manufacturing with low-cost materials and techniques,” *Energy & Environmental Science*, vol. 10, no. 6, 2017, doi: 10.1039/C7EE00757D.

[113] D. Feldman, V. Ramasamy, R. Fu, A. Ramdas, J. Desai, and R. Margolis, “U.S. Solar Photovoltaic System and Energy Storage Cost Benchmark: Q1 2020,” Jan. 2021.